High-Coherence Hybrid Si/III-V Semiconductor Lasers

Thesis by

Christos Theodoros Santis

In Partial Fulfillment of the Requirements

for the Degree of

Doctor of Philosophy

California Institute of Technology

Pasadena, California

2013

(Defended May 24, 2013)

ii

For my parents and sister

Acknowledgements

My time in the U.S. and more importantly at Caltech as a Ph.D. student has been a life transforming experience. In the process, I had the chance to meet and interact with a number of people, people I would like to take the opportunity to acknowledge here.

First and foremost, I wish to thank my advisor Prof. Amnon Yariv for challenging me to overcome what I, for a long time, perceived as possible, to persist and persevere through adversity, to expand the boundaries of my abilities, in order to finally emerge on the other end stronger and more confident as both a researcher and individual.

I am grateful to Prof. Demetri Psaltis for giving me the opportunity to be at a special place like Caltech. I am greatly indebted to Prof. Bruno Crosignani for his genuine caring and thoughtfulness over the years.

I greatly appreciate the insightful comments and kind words of Profs. Bruno Crosignani, Oscar Painter, Axel Scherer, Kerry Vahala and Changhuei Yang, who took the time to be on my candidacy and thesis committees.

During my time in the Yariv group at Caltech, I had the opportunity to work and interact with a number of talented individuals. First of all, I wish to acknowledge my collaborator, Scott Steger, whose role in the work presented in this thesis has been critical and instrumental. Scott has also, with his relaxed attitude and positive outlook on life, been the best officemate of 5 years I could have asked for. Arseny Vasiliev and Yasha Vilenchik made significant contributions toward the successful fruition of this work, each in his respective area of expertise. I am thankful to Dr. Naresh Satyan, whom I always sought out for advice on matters scientific and beyond. In recent years, I enjoyed the company of Sinan Zhao, Mark Harfouche, Dongwan Kim

and Marilena Dimotsantou. They are all exceptionally bright and fun individuals and I wish them the best. I owe a special acknowledgement to Dr. Hsi-Chun Liu, for the long and stimulating discussions about research I had with him over the years. I thank Connie Rodriguez and Ali Ghaffari for their constant support and encouragement.

I am most thankful to my friends Ted Dikaliotis and Jacob Sendowski, for the fun and serious experiences we shared together. Their friendship has been unconditional and helped me through tough times. For that, I will always be grateful to them.

I am sincerely indebted to my Professor of Japanese at Caltech, Sensei Ritsuko Hirai. Meeting her has impacted my life in a profound way. Not only did she, with her charismatic teaching, impart to me a passion for learning, but she has also, with her effusion of warmth and kindness, been for me a priceless source of joy and happiness.

Last but most importantly, I thank my parents and sister, for their unwavering support, patience and thinking of me through the years.

Abstract

The relentlessly increasing demand for network bandwidth, driven primarily by Internet -based services such as mobile computing, cloud storage and video-on-demand, calls for more efficient utilization of the available communication spectrum, as that afforded by the resurging DSP-powered coherent optical communications. Encoding information in the phase of the optical carrier, using multilevel phase modulation formats, and employing coherent detection at the receiver allows for enhanced spectral efficiency and thus enables increased network capacity. The distributed feedback semiconductor laser (DFB) has served as the near exclusive light source powering the fiber optic, long-haul network for over 30 years. The transition to coherent communication systems is pushing the DFB laser to the limits of its abilities. This is due to its limited temporal coherence that directly translates into the number of different phases that can be imparted to a single optical pulse and thus to the data capacity. Temporal coherence, most commonly quantified in the spectral linewidth $\Delta\nu$, is limited by phase noise, result of quantum-mandated spontaneous emission of photons due to random recombination of carriers in the active region of the laser.

In this work we develop a generically new type of semiconductor laser with the requisite coherence properties. We demonstrate electrically driven lasers characterized by a quantum noise-limited spectral linewidth as low as $18\,\mathrm{kHz}$. This narrow linewidth is result of a fundamentally new laser design philosophy that separates the functions of photon generation and storage and is enabled by a hybrid Si/III-V integration platform. Photons generated in the active region of the III-V material are readily stored away in the low loss Si that hosts the bulk of the laser field, thereby enabling high-Q photon storage. The storage of a large number of coherent quanta

acts as an optical flywheel, which by its inertia reduces the effect of the spontaneous emission-mandated phase perturbations on the laser field, while the enhanced photon lifetime effectively reduces the emission rate of incoherent quanta into the lasing mode. Narrow linewidths are obtained over a wavelength bandwidth spanning the entire optical communication C-band $(1530 - 1575\,\text{nm})$ at only a fraction of the input power required by conventional DFB lasers. The results presented in this thesis hold great promise for the large scale integration of lithographically tuned, high-coherence laser arrays for use in coherent communications, that will enable Tb/s-scale data capacities.

Contents

List of Figures

Glossary of Acronyms

ADC   Analog to digital converter

ASIC   Application specific integrated circuit

BER   Bit-error rate

BP   Back(ward) propagation

BOA   Booster optical amplifier

BOE   Buffered oxide etch

BOX   Buried oxide

CD   Chromatic dispersion

CPS   Coupled phase shift

DFB   Distributed feedback (laser)

CMOS   Complementary metal-oxide-semiconductor

DSP   Digital signal processing

ECL   External cavity laser

EDFA   Erbium-doped fiber amplifier

FCA   Free carrier absorption

FEM   Finite element method

FSR   Free spectral range

FWHM   Full width at half maximum

FWM   Four-wave mixing

HDTV   High-definition television

IM-DD   Intensity modulation-direct detection

ICP-RIE   Inductively coupled plasma, reactive ion etching

ITLA   Integrated tunable laser assembly

LO   Local oscillator

MPS   Multiple phase shift

MQW   Multiple quantum well

MZI   Mach-Zehnder interferometer

NLPN   Nonlinear phase noise

OOK   On-off keying

OPLL   Optical phase-locked loop

OSA   Optical spectrum analyzer

PD   Photodiode

PDL   Polarization dependent loss

PEC   Perfect electric conductor

PMC   Perfect magnetic conductor

PMD   Polarization mode dispersion

PSD   Power spectral density

PSK   Phase shift keying

QAM   Quadrature amplitude modulation

QD   Quantum dot

QW   Quantum well

QWS   Quarter-wave shift

RBW   Resolution bandwidth

RF   Radio frequency

SA   Spectrum analyzer

SCL   Semiconductor laser

SCL   Separate confinement layer

SEM   Scanning electron microscope

SFL   Swept-frequency laser

SHB   Spatial hole burning

SMSR   Side mode suppression ratio

SNR   Signal to noise ratio

SOI   Silicon on insulator

SPM   Self-phase modulation

TE   Transverse electric

TEC   Thermo-electric cooler

TM   Transverse magnetic

VLSI   Very large scale integration

VOC   Vertical outgassing channel

VOD   Video-on-demand

WDM   Wavelength division multiplexing

XPM   Cross-phase modulation

Chapter 1

Overview

1.1 Introduction

The last 20 years have witnessed a dramatic transformation in the way we gener-
ate, store, and distribute information, and especially in the way we interface with it.
This profoundly cultural transformation is propelled by the ever-increasing ubiquity
of information-processing power in every aspect of life, whether in the form of a per-
sonal computer or laptop, a smartphone, or a high-definition TV (HDTV). Common
thread across the different manifestations of this information evolution is the ability to
access information beyond our immediate, physical reach, to communicate and share
it with people across the globe. This effective globalization is enabled and, at times,
augmented by the pervasive influence of the Internet on everyday life. The ability
to produce massive amounts of information, coupled with the need to transport it
around the world, are setting up the global communication network for a "perfect
storm".

At the eye of this storm lies the optical communication network. With the low-loss
optical fiber as its underpinning, optical communications have served as the backbone
of long-haul communications for over 30 years. For the bulk of its history, optical com-
munications have responded to the rising network traffic through increased channel
allocation (wavelength-division multiplexing, WDM) and faster carrier modulation
speeds. With the demand for bandwidth growing at a geometric rate, a staggering
estimated annual rate of 40%, driven by Internet-based services such as mobile com-

puting, cloud storage, HD video-on-demand (VOD), and music streaming, the limits of optical communications, as we know it, are being aggressively challenged. Dense WDM optical communications networks, as introduced in the mid-90s, operated at channel data rates of 2.5 Gb/s and employed intensity modulation with direct detection (IM-DD), also known as on-off keying (OOK), wherein 1 bit of information is encoded for every transmitted symbol. The growing demand for bandwidth was initially addressed by spectrum allocation and increase in channel data rates, taking advantage of advances in modulator speed technology and dispersion management (e.g., dispersion compensating fiber) [1]. Progress in DWDM network technology had, for years, been bottlenecked at 10 Gb/s, with fiber-induced impairments posing bounds on further increase of modulation rates, while the 10 THz bandwidth of the commercially useful part of the optical spectrum (C-band: 1530–1570 nm, L-band: 1570–1610 nm) was rapidly becoming fully utilized. With the growth in bandwidth demand relentless as ever, network operators are seeking ways to increase rates to 40 Gb/s and beyond. Networks operating at 40 Gb/s and 100 Gb/s are already commercially deployed, and the race toward Tb/s-scale capacities has just begun. The key technology enabling this information revolution is *coherent optical communications* [2–4].

1.2 DSP-Enabled Coherent Optical Communications

Unlike IM-DD communication systems, wherein detection is performed directly on the incoming optical signal via a square law-type photodetector, in coherent systems, beating of the incoming signal at the receiver with a local optical reference (local oscillator, LO) provides access to both the amplitude and the phase of the carrier, thus preserving the phase of the transmitted signal. This type of detection is referred to as *coherent detection* [5,6]. Depending on whether the LO operates at the transmitted carrier frequency or at an offset frequency, coherent detection is further distinguished

into homodyne and heterodyne detection respectively.

This is not the first time coherent communications are under the spotlight of the optical communication community. Coherent systems drew intense research efforts in the 80s, due to their inherently high receiving sensitivity and potential for long-distance unrepeated transmission. Despite proof-of-principle demonstrations using frequency-stabilized laser diodes [7, 8] in optical phase-locked loop (OPLL) configurations [9, 10], further progress was hampered by the relatively broad linewidth ($\sim 50\,$MHz) of communication lasers at the time, namely distributed-feedback semiconductor (DFB) lasers, that rendered the frequency and phase locking of the receiver laser to the incoming optical carrier, with the then existing analog carrier recovery technology, a challenging task [11–13]. More importantly even, commercial development in coherent systems was stalled in the 90s with the advent of the Erbium-doped fiber amplifier (EDFA), which provided a cheap and simple alternative for noise tolerance, enabling repeaterless long-haul transmission [14].

Mandated by the exhaustion of the available spectrum (C+L bands) and the fiber-imposed saturation in data rates under IM-DD, interest in coherent communications has since the mid 2000s started to resurge. In its second coming, interest in coherent systems is fueled by two particularly attractive attributes. First, its inherent compatibility with advanced modulation formats, such as multilevel phase shift keying (PSK) and quadrature amplitude modulation (QAM) [15]. By encoding information in the phase and/or the complex amplitude of the optical carrier, more bits per symbol can be transmitted, thus enhancing spectral efficiency (bits/s/Hz) and enabling superior utilization of the available bandwidth [16, 17]. Figure 1.1 illustrates the scaling of spectral efficiency over some basic phase/amplitude modulation formats. The aggregate capacity of a fiber link is given by the simple product:

$$C = S \times B \times W, \tag{1.1}$$

where C is the aggregate data rate of the link in [b/s], S the number of encoded bits per symbol, B the symbol or baud rate in [b/s], and W the number of utilized channels

or carrier wavelengths. From this simple expression, it becomes clear that increasing spectral efficiency via multilevel modulation offers an extra degree of freedom toward boosting the total capacity. Aggregate data rates can be improved without further increase in baud rates, which are the ones determining the tolerance of transmission against fiber impairments.
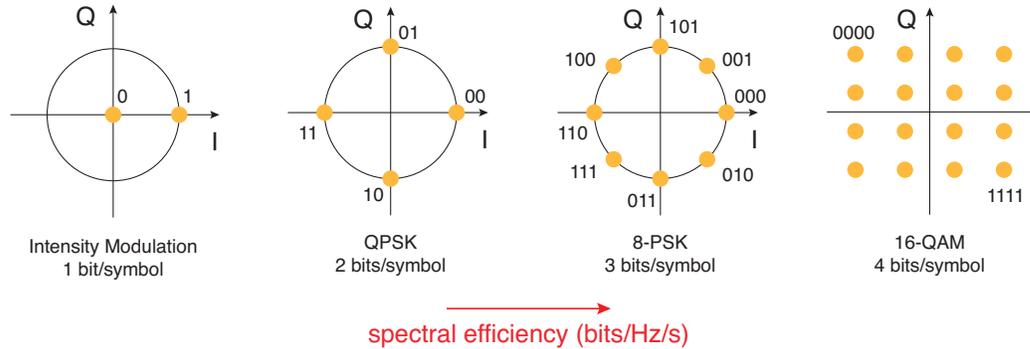
Figure 1.1. Phase constellation diagrams of some basic phase modulation formats.

The second compelling feature driving the resurgence of coherent communication systems is their special attributes with regard to distortion compensation, polarization demultiplexing and carrier recovery. These are afforded by the inherent nature of coherent systems, access to the optical electrical field (E-field) via coherent detection and enabled by digital signal processing (DSP) [18–21]. Working hand in hand with coherent detection, DSP is the mathematical tool through which the appropriate numerical transforms are applied to recover signals from impairments that are physically well understood, but were, until recently, electronically inaccessible. The major sources of degradation of the optical channel at regular power levels are linear and invertible with respect to the optical E-field. Coherent detection provides electrical signals that are predominantly proportional to the optical E-field, and so digital linear filters can be used to fully compensate the linear channel transfer functions [22–24]. Chromatic dispersion (CD), the primary signal impairment, is a linear degradation and can be inverted without penalty [25]. The polarization transfer function of the optical link can be tracked, allowing electronic domain compensation of polarization mode dispersion (PMD) and polarization dependent loss (PDL) [26, 27]. The capac-

ity of the communication link can further degrade at high enough launched powers under the effect of nonlinear impairments, such as self-phase modulation (SPM), cross-phase modulation (XPM), four-wave mixing (FWM) and nonlinear phase noise (NLPN) [28,29]. Coherent systems enable the digital compensation for such nonlinear impairments as well, by performing channel inversion via *backward propagation* in the electronic domain, either at the transmitter or the receiver [30–32].

In their current incarnation, coherent transceivers are more than just an assembly of optical components. They are essentially *digital coherent processors*, incorporating the processing power of DSP. Figure 1.2 presents a simplified schematic of the configuration of a coherent receiver, with the optical front end used for the downmixing of the optical carrier and the DSP back end employed for the the digital carrier recovery. Key factor contributing to the "marriage" between coherent communications and DSP is the substantial advancements in the area of very large scale integration (VLSI), specifically in the realization of high-speed analog-to-digital converters (ADC), that enable real-time digital processing at GHz baud rates. Digital fiber impairment compensation can be done either at the transmitter, prior to upconversion onto an optical carrier, or at the receiver, after the optical signal has been downconverted to the electronic domain. In both cases, provided the baseband signal in the electronic domain is sampled above the Nyquist rate, the digitized signal has the full information of the analog electric field, enabling DSP compensation to have no loss in performance compared to analog impairment compensation performed in either the optical or electronic domain. DSP has the advantage that signals can be delayed, split, amplified, and manipulated in other manner without degradation in signal quality. As baud rates, constellation size and transmission distances increase, more complex DSP algorithms are needed to sustain increasing capacities. This rapidly increasing processing complexity will require fully dedicated and specialized electronic circuits (ASICs), harnessing the ultimate in CMOS integration technology.

Optical Circuit

Electronic Circuit

Incoming carrier
(2 polarizations, each
with 4 phase states)

PBS

LO   PBS

AMZ   PD   ADC
AMZ   PD   ADC
AMZ   PD   ADC
AMZ   PD   ADC

DSP

A/D Converter
Adjustable Mach Zehnder
Digital Signal Processor
Local Oscillator
Photo Detector
Polarization Splitter
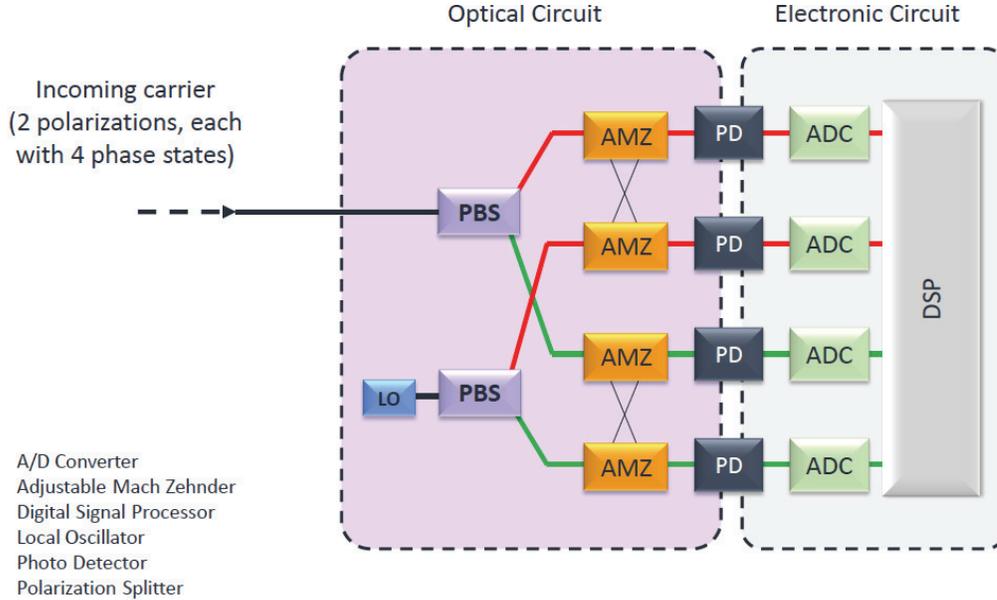
Figure 1.2. Schematic illustration of the configuration of a DSP-enabled coherent receiver. (Example shown for DP-QPSK).

1.3 Laser Phase Noise & Linewidth

Besides transmission medium impairments, the most fundamental nonideality affecting coherent communications is laser phase noise. A laser field undergoes random phase and amplitude fluctuations, that can be expressed as

$$\mathcal{E}(t) = \Re\{E_o(t)\exp(j\omega_o t + \theta(t)\}, \tag{1.2}$$

These fluctuations can be traced to a multitude of sources, but one in particular is of special importance. That is spontaneous emission, which is an effect fundamentally quantum mechanical in its origin. In a typical semiconductor laser, spontaneous emission is the result of random electron-hole recombination in the active region of the lasing medium. For every spontaneous emission event, a photon is added to the laser field. In addition to the obvious effect on the amplitude of the field, spontaneously emitted photons, not being in phase with the stimulated emitted coherent photons, represent phase perturbations on the coherent field.

Spontaneous emission occurs indiscriminately, below and above threshold, at a given temporal rate. Subject to this ever ongoing mechanism, the laser field's evolution deviates from that of a perfectly monochromatic field. Given the random nature of spontaneous emission, the laser field's excursion from perfect coherence emulates a "random walk" (i.e., Brownian motion), schematically illustrated in phasor space in figure 1.3. The coherent field is represented by a complex amplitude vector E_o of
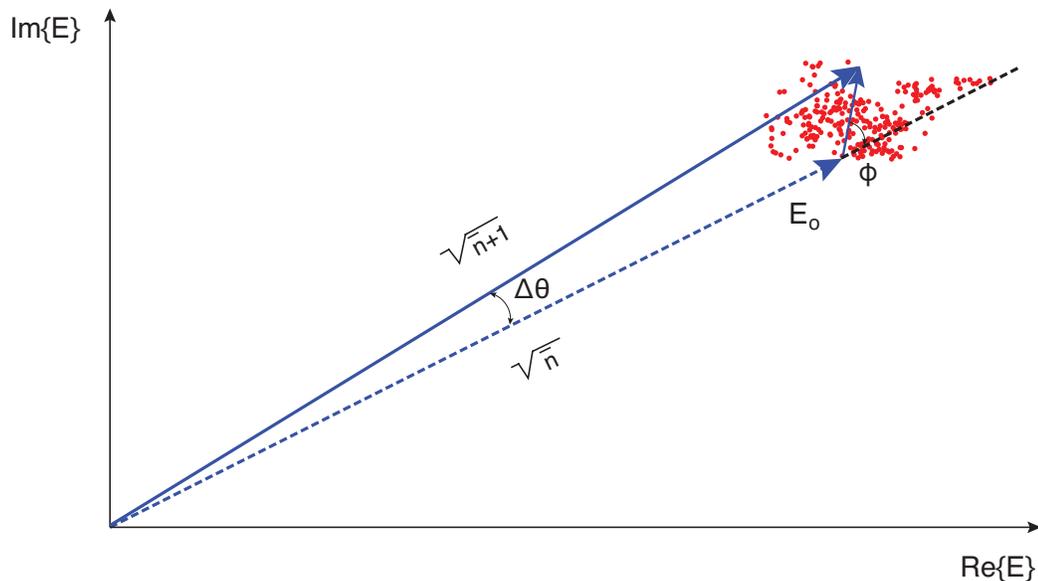
Figure 1.3. Phasor space representation of the effect of a single spontaneous emission event on the laser field.

length $\propto \sqrt{\bar{n}}$, where $\bar{n}$ is the average number of quanta in the mode. With every spontaneous emission event, one photon is added to the field, represented in the phasor space by a vector of unity length and a uniformly distributed random angle ϕ. Upon a large number of independent spontaneous emission events over time interval τ, the accumulated phase excursion obeys Gaussian statistics with probability distribution:

$$P(\Delta\theta) = \frac{1}{\sqrt{2\pi\sigma_{\Delta\theta}^2(\tau)}} \exp\left[\frac{-(\Delta\theta)^2}{2\sigma_{\Delta\theta}^2(\tau)}\right], \tag{1.3}$$

where $\sigma_{\Delta\theta}^2(\tau)$ is the variance of the phase excursion. For a single-mode semiconductor laser with ground and excited level populations N_1, N_2 respectively, this variance can

be expressed as [33]

$$\sigma^2_{\Delta\theta}(\tau) \equiv < [\Delta\theta(\tau)]^2 > = \frac{\eta}{2\bar{n}\tau_{ph}}\tau, \tag{1.4}$$

where $\eta = \frac{N_2}{(N_2-N_1)_{th}}$ is the population inversion factor at threshold and τ_{ph} the cold cavity (i.e., no pumping) photon lifetime in the laser resonator. The phase variance is proportional to the measurement time τ, with a proportionality factor that represents the diffusion constant of the phase diffusion process:

$$D_{\Delta\theta} = \frac{\eta}{2\bar{n}\tau_{ph}}. \tag{1.5}$$

The result of equation (1.4) is extremely insightful and we will refer to it again later on. The full width at half maximum (FWHM) of the phase diffusion is given in frequency units by

$$\frac{D_{\Delta\theta}}{2\pi} \equiv \Delta\nu = \frac{\eta}{4\pi\bar{n}\tau_{ph}}. \tag{1.6}$$

According to the Wiener-Khintchine theorem, the power spectral density (PSD) of a quantity subject to a random process, such as a laser field, is given by the Fourier transform of the autocorrelation function:

$$C_{\mathcal{E}}(\tau) \equiv < \mathcal{E}(t)\mathcal{E}(t+\tau), \tag{1.7}$$

$$S_{\mathcal{E}}(\omega) = \frac{1}{\pi} \int_{-\infty}^{+\infty} C_{\mathcal{E}}(\tau)\exp(-j\omega\tau)d\tau. \tag{1.8}$$

For a laser subject to quantum phase noise, the spectral density of the field can be shown to obey [33, 34]:

$$S_{\mathcal{E}}(\omega) = \frac{\langle E_o^2 \rangle}{2\pi} \frac{\frac{\eta}{4\bar{n}\tau_{ph}}}{\left(\frac{\eta}{4\bar{n}\tau_{ph}}\right)^2 + (\omega-\omega_o)^2}. \tag{1.9}$$

So, the spectrum of a laser field subject to spontaneous emission is a Lorentzian function centered about the lasing frequency ω_o, with a linewidth $\Delta\nu$, as defined in equation (1.6), through the phase diffusion constant $D_{\Delta\theta}$. The linewidth $\Delta\nu$, also known as the Schawlow-Townes linewidth [35], is a measure of the spectral pu-

rity of the laser emission. Although the Lorentzian lineshape can be, under certain circumstances, observed experimentally [36], a quantitative discrepancy was discovered early on [37], between the predicted Schawlow-Townes and the experimentally obtained linewidths. The broadened linewidths experimentally observed were consistent with fundamental oscillator noise theory predicting enhanced phase noise due to coupling between phase and intensity fluctuations [38], an effect later formulated as the amplitude-phase coupling factor, also known as Henry's linewidth enhancement factor α defined as [39–41]:

$$\alpha \equiv \frac{\partial \chi_r / \partial N}{\partial \chi_i / \partial N} = -\frac{4\pi}{\lambda} \frac{\partial n / \partial N}{\partial g / \partial N}, \tag{1.10}$$

where χ_r, χ_i are the real and imaginary parts respectively of the active medium's complex susceptibility, n and g the refractive index and gain of the active medium and N the carrier density in the active region. Under the effect of intensity fluctuations, the quantum phase noise-limited Schawlow-Townes linewidth is modified into

$$\Delta\nu = \frac{\eta}{4\pi\bar{n}\tau_{ph}}(1 + \alpha^2). \tag{1.11}$$

A rigorous semiclassical treatment (Van der Pol analysis) of semiconductor laser noise, accounting for linewidth enhancement due to index variations can be found in [42,43].

In practice, deviations from the Lorentzian spectral lineshape occur due to contributions from technical sources of noise (e.g., $1/f$ noise), such as the driving current source and temperature fluctuations. In addition to the deviation from the observed lineshape, technical noise also manifests itself in the form of a residual linewidth floor at the high power limit [44–48].

Phase-sensitive optical processing, as that involved in coherent communications, is demanding in terms of the degree of temporal (i.e., phase) coherence of the utilized light source. With regard to coherent communication systems, it is the high-offset (i.e., from carrier) frequency noise components due to spontaneous emission that predominantly factor into the phase noise and thus impair the performance [49]. This

is result of the high data rates of optical communications and the accordingly short symbol duration times. Under this assumption, the effect of phase noise in coherent communications can be quantified in [50]

$$\sigma^2_{\Delta\theta}(\tau) = 2\pi \left[(\Delta\nu)_{T_x} + (\Delta\nu)_{R_x} \right] \tau, \tag{1.12}$$

where $\sigma^2_{\Delta\theta}(\tau)$ is the phase variance over symbol time τ and $(\Delta\nu)_{T_x}, (\Delta\nu)_{R_x}$ are the spectral linewidths of the lasers at the transmitter and receiver respectively. The phase variance degrades the detection sensitivity, but most importantly, directly impacts the bit-error rate (BER) that is achievable at a given launched power or equivalently, the signal-to-noise ratio (SNR) required to achieve a given BER metric [11, 12, 21, 51, 52]. For optimal BER, the phase variance has to be kept low and this requirement becomes increasingly stringent as the constellation size and thereby the density of phases in the complex plane increases. For given laser linewidths $(\Delta\nu)_{T_x}, (\Delta\nu)_{R_x}$, the phase variance can be controlled by increasing the baud rate $(B = \frac{1}{\tau} [Gb/s])$. This way the linewidth requirement can be, to some degree, relaxed, especially given that with the use of DSP, the phase recovery is offset to the electronic domain. Indeed, DSP-enabled carrier synchronization, via for example feedforward recovery schemes [53–56], eliminates the necessity of phase-locking of the LO in the optical domain via OPLLs [57–59], thereby significantly increasing the phase noise tolerance on the utilized lasers [60, 61]. For instance, implementation of a $16-$QAM scheme with BER $= 10^{-3}$ and penalty on sensitivity of $1\,$db is possible with laser linewidths better than $150\,$kHz, using decision-directed, soft-decision phase estimation [60]. This requirement quickly tightens up for stricter BER and sensitivity target values. It also rapidly becomes prohibitive for higher level modulation formats, for example, linewidths on the order of $1\,$kHz would be needed for $64-$QAM with BER $= 10^{-4}$ and $2\,$db above sensitivity [61].

These stringent linewidth requirements are barely met by state of the art external cavity lasers (ECL) for the lower level modulation formats (e.g., QPSK, $8-$PSK, $16-$QAM), while higher level formats are prohibitive for existing semiconductor lasers

(SCL) [62–65]. ECLs are fairly expensive and do not lend themselves to dense, on-chip integration. In a multicarrier implementation for high capacity links, compact integration of laser assemblies is emerging as the most viable approach to improved performance and reduced cost. As much impetus the power of DSP has imparted to the resurgence of the field of coherent communications, the exponentially increasing algorithmic complexity in the functions required from DSP to perform is already testing the limits of high-speed CMOS technology. Boosting baud rates to relax linewidth requirements in turn, stops at the upper bound of about 80 GBaud possible with state of the art ADCs, while at the same time increases heat dissipation and power consumption.

For all of the above reasons, we believe that a major advancement in semiconductor laser's coherence is imperative, if the full potential of coherent communications is to be fulfilled. The distribute feedback laser (DFB) with its simple design, compact and robust size, single-mode operation and low cost, has been the workhorse of the optical communication technology for over 30 years [66–75]. With a temporal coherence limited at a few hundred kHz though, at best, the DFB falls short of the expectations of the coherent communication era. Retaining the unique features that made it so successful, while pushing the envelope on coherence, the *next generation* of the DFB laser could become the vehicle into the future of optical communications. In this work we set out to do exactly that, to rethink and redefine the design of semiconductor lasers on a new basis, with emphasis on spectral purity.

1.4   DFB Semiconductor Lasers — Overview

Historically, $\lambda/4$-shifted (quarter-wave shifted, QWS) DFB lasers have enjoyed a special place in communication laser commercialization, thanks to their simple design and manufacturing process. Key contributing features to their success has been their low thresholds and stable single-mode operation, housed in a compact package [76–82]. In terms of temporal coherence though, QWS DFBs have been limited to MHz-level linewidths, primarily due to the short photon lifetime τ_{ph} of their cavities, as factored

into the modified Schawlow-Townes linewidth formula repeated here for reference:

$$\Delta\nu = \frac{\eta}{4\pi\bar{n}\tau_{ph}}(1 + \alpha^2). \tag{1.13}$$

To improve on the coherence characteristics of QWS DFBs, researchers have resorted to a plethora of DFB laser variants. Increasing the length of the laser cavity and thereby the cavity photon lifetime has been the most straightforward approach [83–87]. Yet, The spectral characteristics of conventional QWS DFBs are extremely sensitive to changes of the cavity length and the strength of the grating, lumped into the dimensionless coupling coefficient κL [88–90]. Values of κL above certain critical thresholds quickly render QWS DFBs susceptible to spatial-hole burning (SHB), with ensuing mode instability and coherence degradation [91–93]. For long QWS DFB cavities to remain stable, the grating strength has to be reduced accordingly, a task of increasingly practical challenge, especially for gratings formed as part of a material growth process [94, 95]. Alternatively, longitudinal mode engineering is performed through the introduction of coupled phase-shift (CPS) or multiple phase-shift (MPS) sections into the grating, to flatten the intensity distribution and delay the onset of SHB, thus sustaining mode stability and allowing for further linewidth reduction [96–102].

In addition to optimizations of the longitudinal dependence of the laser field via optical mode engineering, linewidth reduction of SCLs has been pursued via more fundamental approaches of quantum mechanical nature. Specifically, the higher differential gain of low-dimensional nanostructures, such as quantum wells (QW), and its effect on the linewidth enhancement factor α [103–106] has been exploited to suppress the effective linewidth broadening due to intensity fluctuations above threshold [107–113]. Similarly, the dependence of the linewidth enhancement factor on the carrier density has been exploited via optimization of the number of quantum wells [114–117].Correlation between linewidth enhancement factor reduction due to quantum size effect in quantum confined structures (e.g., QWs) and suppression of SHB has also been drawn and utilized for linewidth reduction in multiple-QW (MQW)

DFB lasers [118–120]. Reduction of the effective linewidth enhancement and therefore, of the spectral linewidth, has also been established to occur with detuning of the laser emission to shorter wavelengths (i.e., blue detuning) with respect to the peak of the gain spectrum [121–125]. Further information on the measurement methodology of the linewidth enhancement factor can be found in [126,127], while a comprehensive overview of the evolution of the concept of the linewidth enhancement factor is given in [128].

1.5   High-Q Hybrid Si/III-V Semiconductor Lasers

Armed with the entire arsenal of methods and techniques outlined above, the state of the art in coherence for commercial DFB lasers lies in the neighborhood of a couple hundred kHz, a benchmark inadequate to fulfill the potential of coherent communications. In this work, we develop a new type of semiconductor laser with an order of magnitude improved temporal coherence over the state of the art. More than just a new device, we present a novel approach at laser design for high coherence. We do that by revisiting old and well-understood concepts, only this time around, with a fresh perspective. Our starting point is the phase diffusion-limited Schawlow-Townes linewidth:

$$\Delta\nu = \frac{\eta}{4\pi\bar{n}\tau_{ph}}(1 + \alpha^2). \tag{1.14}$$

It is critically insightful to recognize the role of two instrumental parameters in equation (1.14), the average number of quanta in the lasing mode $\bar{n}$ and the cavity photon lifetime τ_{ph}. First, the number of quanta $\bar{n}$, predominantly comprising stimulated emitted coherent photons above threshold, acts as an *optical flywheel* that enhances the coherent field's *inertia* to the phase diffusing effect of spontaneous emission. This is essentially a photon storage mechanism. The more stimulated quanta are stored in the cavity, the less susceptible the laser field becomes to spontaneous emission-mandated phase perturbations. Second, the cavity photon lifetime τ_{ph} acts as a *slowing factor* on spontaneous emission, effectively reducing the spontaneous

emission rate into the cavity mode. This becomes more evident if equation (1.14) is rewritten as

$$\Delta\nu = \frac{R}{4\pi\bar{n}}(1+\alpha^2),\tag{1.15}$$

where $R = \frac{\eta}{\tau_{ph}}$ is the spontaneous emission rate into the lasing mode. If the population inversion factor is interpreted as stating that for every electron available for a stimulated emission event there is η electron-hole pairs available for spontaneous recombination, then the effect of the photon lifetime is to suppress the rate at which these spontaneously emitted photons are added to the lasing mode by τ_{ph}. In other words, the number of incoherent photons emitted over a given period of time t is reduced by a factor of τ_{ph} ($N = Rt = \frac{\eta}{\tau_{ph}}t$).

We have identified two distinct mechanisms acting toward reducing phase noise, the storage of a large number of coherent quanta via $\bar{n}$ and the suppression of the spontaneous emission rate into the lasing mode via τ_{ph}. These two factors are both inherently linked to the laser cavity characteristics and specifically its loss rate. To make this more apparent, we recast (1.14) in an equivalent form, through manipulation of its constituent parameters:

$$\Delta\nu = \frac{2\pi h\nu_o(\Delta\nu_{1/2})^2\eta}{P}(1+\alpha^2),\tag{1.16}$$

where $\Delta\nu_{1/2} = \frac{1}{2\pi\tau_{ph}}$ is the linewidth of the passive cavity, that is without the effect of pumping and gain, and $P = \frac{\bar{n}h\nu_o}{\tau_{ph}}$ is the total power emitted by electrons in the active region. Drawing from resonator terminology, we define a quality factor Q to describe the temporal loss rate of the passive laser resonator:

$$Q \equiv \frac{\nu_o}{\Delta\nu_{1/2}},\tag{1.17}$$

and the laser linewidth then becomes

$$\Delta\nu = \frac{2\pi h\nu_o^3\eta}{Q^2P}(1+\alpha^2).\tag{1.18}$$

For a given total emitted power P or equivalently, at a given drive current above threshold $I - I_{th}$, the resonator Q incorporates information about both of the phase noise reducing mechanisms, the stored number of quanta and the photon lifetime. From a strictly laser resonator perspective therefore, the quality factor is the singularly most critical optimization parameter. The quality factor Q in equation (1.18) itself is the combined effect of the resonator's intrinsic loss and the external loss through the laser mirrors. In resonator terminology again, this is formulated as:

$$\frac{1}{Q} = \frac{1}{Q_i} + \frac{1}{Q_e}, \tag{1.19}$$

where Q_i is the resonator intrinsic quality factor, measure of its internal losses with no output, and Q_e the external quality factor, accounting for output coupling through the mirrors. The total Q is also known as the *loaded* quality factor of the resonator. In this work, we aim at maximizing the loaded Q to achieve improved laser coherence and to that end, we individually optimize both the intrinsic and external Q of the resonator. Enhancing Q_i pushes the bar for the potential in number of quanta and photon lifetime that can be harnessed higher, while Q_e serves as the control knob that determines the actual photon storage and lifetime, subject of course to considerations for the overall laser performance. We approach the laser design from a fundamentally new perspective, that of the optimal design of a passive resonator. The verbiage and nomenclature utilized hereafter in that process is accordingly of resonator origin, as opposed to the traditional laser design terminology.

A comprehensive resonator optimization involves the accurate identification of the sources of loss pertinent to the particular type of resonator and the targeted addressing of each one through elaborate design and refining of the fabrication process. Key enabling factor to that end is the choice of platform for the realization of a high-Q laser resonator. The platform utilized in this work is the hybrid Si/III-V semiconductor platform, schematically illustrated in figure 1.4. Hybrid integration of Si and III-V active materials has, in recent years, emerged as a technologically viable approach at incorporating active functionality in Si photonics [129–133]. The
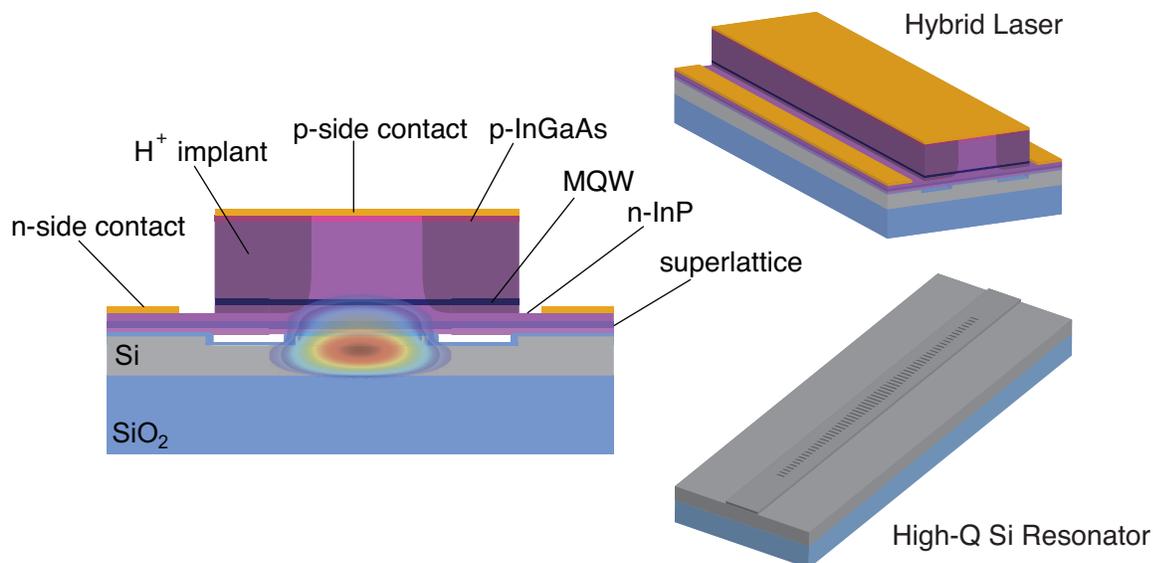
Figure 1.4. Device schematics of a high-Q hybrid Si/III-V semiconductor laser.

primary motivating factor behind those efforts had been the integration of a source of light on the otherwise poor at photon generation Si, via the implementation of hybrid Si/III-V lasers [134–142]. Besides the obvious added benefit of generating light on Si, these hybrid lasers have overall fallen short of the state of the art in semiconductor lasers and hybrid DFB variants specifically, have achieved subpar performance in coherence [143, 144].

The choice of the hybrid platform in this work though is distinctly different. We leverage Si as a low loss optical platform for the realization of a high-Q resonator. Si, in the form of a Si-on-insulator (SOI) die, serves as the host platform for the design and fabrication of an ultralow loss 1D waveguide grating. The Si waveguide and grating provide all of the mode guiding and control functionality. The evanescent tail of the mode interacts with the MQW active region of the bonded III-V die (InGaAsP/InP) to provide the necessary gain for lasing. The Si waveguide grating combined with the III-V counterpart of the optical mode, constitute a *hybrid resonator*, and it is the quality factor of this resonant hybrid entity that we aim at optimizing. Pivotal decision to that end, is the distribution of the optical mode between Si and III-V in such way that the minimum fraction of the mode resides in the

highly absorbing III-V material. This mode distribution can be formally expressed as

$$\frac{1}{Q_{ba}} = \frac{\Gamma_{Si}}{Q_{Si}} + \frac{\Gamma_{III-V}}{Q_{III-V}},\tag{1.20}$$

where Q_{ba} is the bulk absorption-limited quality factor of the hybrid resonator, Q_{Si}, Q_{III-V} the respective absorption-limited quality factors of Si and III-V and $\Gamma_{Si}, \Gamma_{III-V}$ mode confinement factors in the respective regions. Implicit in this dilution of the mode between Si and III-V is an effective separation between the processes of photon generation and storage. Photons are generated in the III-V active region over an effective interaction area that is optimally designed to supply the required gain, while at the same minimizing the detrimental effect of the III-V to the resonator's total quality factor. The generated photons are, in their vast majority, readily stored away in the low-loss Si part of the resonator. In this sense, high photon number storage with long photon lifetimes is enabled, with simultaneously efficient carrier injection and gain, a separation in degrees of freedom afforded by the hybrid platform.

1.6 Organization of the Thesis

This thesis is organized as follows. Chapter 2 introduces basic concepts of resonator theory and design, with emphasis on energy dissipation, characterized by the universally fundamental figure of merit of the quality factor Q. In the second half of chapter 2, the design and analysis of waveguide grating defect-mode optical resonators is presented, introducing concepts later utilized in the design of a high-Q resonator. Chapter 2 concludes with a break-down of the aggregate loss of a waveguide grating resonator on Si into its major constituent sources, an analysis essential for a targeted resonator optimization. Chapter 3 builds on the concepts introduced in chapter 2 to present the design of a high-Q resonator on Si, optimized for high photon-number storage and long photon lifetime. Chapter 4 adapts the design methodology introduced in chapter 3 for the design of a hybrid Si/III-V waveguide grating resonator

for laser cavity. While the first half of chapter 3 focuses on the design of the high-Q laser cavity from a resonator perspective, the second half reverts to more conventional laser design terminology, to describe a model that accounts for presence of gain and enables simulation of a semiconductor laser's fundamental physics. The model is based on spontaneous emission as optical seed and a constant external current drive as supply for carriers and is implemented using a finite-difference, time-domain method to account for the field's and carriers' spatial dependence. Chapter 5 reviews the experimental results obtained, during the first developmental phase, of high-Q resonators on Si and those, from the second phase, of high-Q hybrid Si/III-V semiconductor lasers. Special emphasis is given on the experimental setup and method utilized for the characterization of the temporal coherence of the lasers. Chapter 6 sums up the main contributions of this work and offers an outlook of the opportunities enabled by it. Finally, appendix A serves as a reference to the fabrication tools and techniques used for the fabrication of the passive Si resonators as well as for the hybrid integration of Si and III-V. Details on a Si process, developed and optimized for the fabrication of ultra-low loss grating resonators are presented.

Chapter 2

Waveguide Grating Defect-Mode Resonators

2.1 Resonator Fundamentals

2.1.1 Quality Factor of a Resonator

The fundamental figure of merit used to characterize a resonator in this work is the quality factor Q. For a resonator subject to various loss mechanisms, the quality factor is used to describe the temporal rate at which energy stored in the resonator is dissipated. Let us consider a generic resonator as the one shown in figure 2.1, with initial stored energy U_o at $t = 0$ that is let free to oscillate (un-driven) at a resonant frequency ω_o. The optical energy dissipation can then be described by a quality factor defined as

$$Q = \omega_o \frac{U(t)}{-\frac{dU}{dt}},$$ (2.1)

where $U(t)$ is the stored energy at time t and $\frac{dU}{dt}$ the rate at which the stored energy changes, with the minus sign indicating decay. By rearranging the terms in equation (2.1) and solving the differential equation for $U(t)$ we have

$$U(t) = U_o e^{-\frac{\omega_o t}{Q}}.$$ (2.2)

The quality factor itself is unitless, but the ratio $\frac{Q}{\omega_o}$ has units of time and corresponds to the time constant of the the stored energy's exponential decay (figure 2.2). The
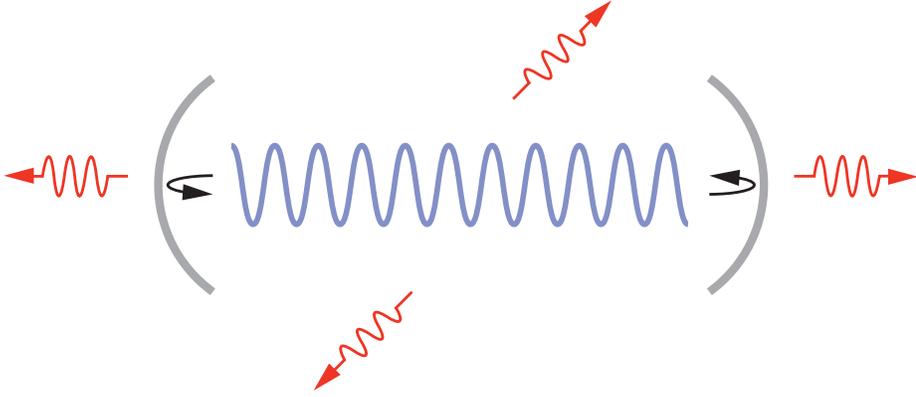
Figure 2.1. Generic model of an unloaded resonator.

time it takes for the energy to decay to e^{-1} of its initial value is given by

$$\tau_{ph} = \frac{Q}{\omega_o}. \tag{2.3}$$

This characteristic time, known as *photon lifetime*, is a measure of the time photons spend in the cavity before they are lost into various loss channels. The inverse of the photon lifetime, $\gamma = \frac{1}{\tau_{ph}}$, expresses the resonator's loss rate in frequency. The quality factor Q, the photon lifetime τ_{ph} and the loss rate γ can be interchangeably used to describe a resonator's loss characteristics.
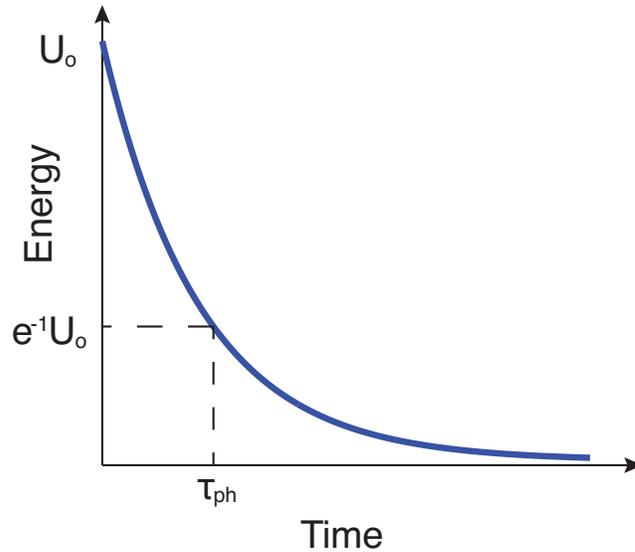
Figure 2.2. Exponential decay of the energy stored in a resonator.

For resonators that support more than one possible modes of oscillation, a unique set of Q, τ_{ph}, γ has to be defined for each mode and resonant frequency ω_o. Increasing the Q, thereby increasing the photon lifetime, enhances the interaction between light and matter, as photons spend longer time in a given material system. In combination with very small optical mode volumes V, this enhanced interaction can lead to a particularly interesting realm of quantum mechanically-mandated effects (Purcell effect, cavity QED, etc.).

While looking at the quality factor of a resonator in the time domain underscores the relevance of the photon lifetime, an alternative perspective can be gained by looking at the resonator in the frequency domain. By Fourier transforming the exponential decay function of a resonator's loss process, the frequency response is found to follow a Lorentzian distribution:

$$L(\omega) = \frac{1}{\pi} \frac{\frac{\Gamma}{2}}{(\omega - \omega_o)^2 + (\frac{\Gamma}{2})^2}, \qquad (2.4)$$

where Γ is the spectral linewidth (FWHM) of the Lorentzian lineshape for an optical mode with resonant frequency ω_o (figure 2.3). The quality factor Q is in this case defined as

$$Q \equiv \frac{\omega_o}{\Delta\omega} = \frac{\omega_o}{\Gamma}. \qquad (2.5)$$

Higher quality factor Q corresponds to narrower linewidth Γ. This view of an optical resonance reveals its function as a spectral filter. High quality factor resonant modes can thus be utilized as narrow-line optical filters on broadband signals, which are either incoming to the resonator (external drive) or internally generated via incoherent optical processes. Such case as the latter is the radiation of spontaneously emitted photons in a gain medium. Utilizing a high-Q resonance as the lasing mode in a semiconductor laser can provide an internal filtering mechanism of spontaneously emitted photons, thereby effectively narrowing the spontaneous emission spectrum and enhancing the coherence of the emitted light.
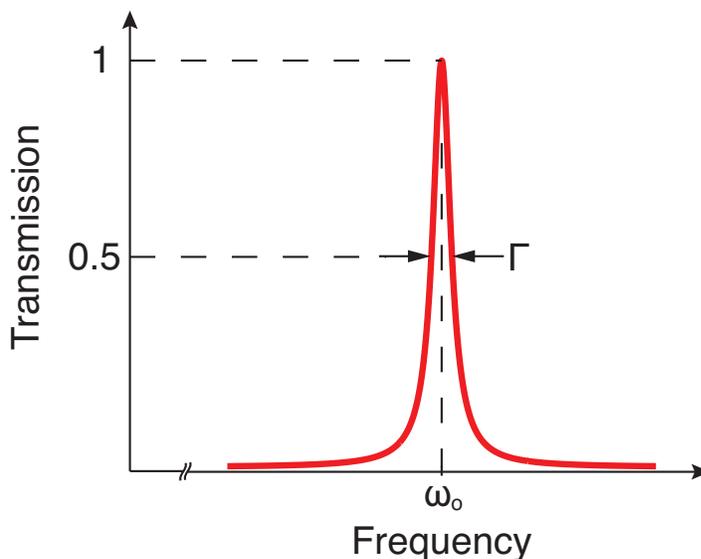
Figure 2.3. Lorentzian lineshape of a resonator's frequency response.

2.1.2 Resonator Loading

The resonator model described in the previous section was that of an isolated (stand-alone) resonator, indeterminately excited with initial stored energy U_o and left to oscillate subject only to its own internal loss mechanisms. The quality factor describing such a resonator is known as *intrinsic quality factor*, Q_i. In actual optical systems though, we need to be able to drive resonators externally and tap energy out of them. In other words, we have to establish a coupling path between the resonator and the outside world. This coupling path represents an additional channel of loss for the resonator and the operation of breaking the isolation of the resonator from the environment is known as *resonator loading*, schematically shown in figure 2.4. The coupling path itself represents the resonator's load. In the presence of the load, the quality factor of every resonant mode deviates from its intrinsic value to an effectively smaller one, known as *loaded quality factor*, Q_L. The relationship between intrinsic and loaded Q is described by the following equation:

$$\frac{1}{Q_L} = \frac{1}{Q_i} + \frac{1}{Q_e} \tag{2.6}$$
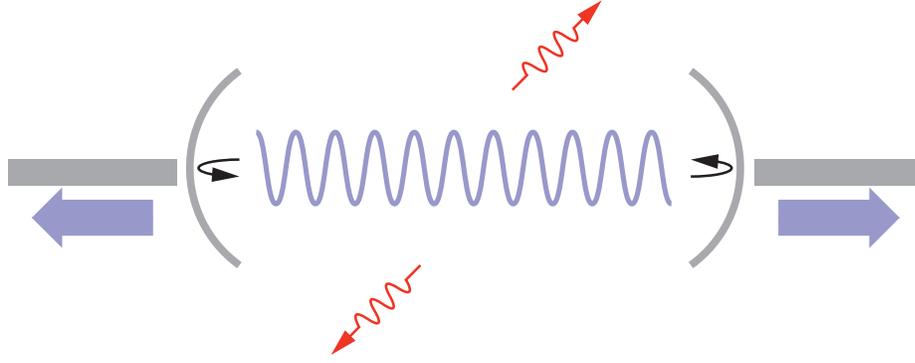
Figure 2.4. Generic model of a loaded resonator.

where Q_e is the *external* quality factor that accounts for the coupling of the resonator to the load. The coupling of energy to the load is nothing more than another loss channel for the resonator, "parallel" to the internal ones, therefore the parallel resistance type relationship between Q_L, Q_i, Q_e. Similarly to Q_i, an external loss rate, $\gamma_e = \frac{\omega_o}{Q_e}$, can be defined for the external coupling to the load. Practically, such coupling to a resonator is implemented via on-chip integrated waveguides or optical fiber tapers. For a laser cavity specifically, Q_e accounts for the lumped losses through the laser's mirrors.

The strength of the coupling between the resonator and the load is usually tuned by controlling the physical proximity of the two. Two distinct regimes of coupling arise based on the relative ratio between Q_i and Q_e. If $Q_e < Q_i$, the resonator is said to be *overcoupled* to the load, meaning that energy is dropped to the load at a rate faster than it is lost internally. If $Q_e > Q_i$, the resonator is said to be *undercoupled* to the load, with the internal loss rate dominating the total loss. In the extreme case of this regime, for $Q_e \gg Q_i$, the loaded quality factor is approximately equal to the intrinsic value. This situation is experimentally desirable as a means to ascertain the intrinsic quality factor of a resonator. The situation when $Q_e = Q_i$ is known as *critical coupling* and the resonator is then said to be "matched" to the load, similar to impedance matching in an electrical circuit. As such, the transfer of energy from the resonator to the load is then maximized. The loaded Q is half the intrinsic Q at critical coupling and therefore this case provides an alternative way of finding Q_i, although

tuning into critical coupling is not always easy under experimental conditions.

2.2 Waveguide Grating Resonators

2.2.1 Waveguide Gratings as Reflectors

An index perturbation on an optical waveguide can provide the coupling between the waveguides counterpropagating modes. This perturbation on chip is usually achieved by means of a surface corrugation on the waveguide using lithographic techniques. For simplicity, we consider a single mode waveguide that supports a mode of propagation constant β and transverse electric field distribution $E_o(x, y)$, patterned with a uniform grating of period a, as shown in figure 2.5. The coupling between the forward, $AEo(x, y) \exp[i(\omega t - \beta z)]$ and the backward, $BEo(x, y) \exp[i(\omega t + \beta z)]$, wave are described by the coupled-mode equations [33]:
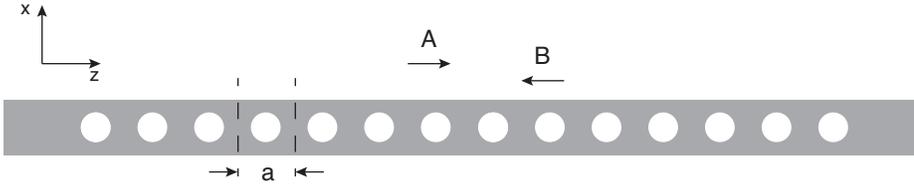
Figure 2.5. Schematic of a uniform waveguide grating.

$$\frac{dA}{dz} = -i\kappa B(z) \exp(i\Delta\beta z),$$
$$\frac{dB}{dz} = i\kappa^* A(z) \exp(-i\Delta\beta z), \tag{2.7}$$

where the coupling constant κ is given by

$$\kappa = \frac{\omega}{4} \iint E_o^*(x, y)\epsilon_m(x, y)E_o(x, y)dxdy. \tag{2.8}$$

The above equations are subject to the assumption of weak coupling, which is satisfied for a weak index perturbation. We consider the coupling via the grating's first order

Fourier component, therefore $m = 1$. The phase mismatch $\Delta\beta$ is given by

$$\Delta\beta = \beta - (-\beta) - \frac{2\pi}{a} \equiv 2(\beta - \beta_o), \tag{2.9}$$

where $\beta_o = \frac{\pi}{a}$. For the propagation constant β we can write

$$\beta = \frac{2\pi}{a} n_{eff} = \frac{\omega}{c} n_{eff}, \tag{2.10}$$

where n_{eff} is the effective index of the waveguide mode. The phase mismatch can then be written as

$$\Delta\beta = \frac{2n_{eff}}{c}(\omega - \omega_o). \tag{2.11}$$

The coupled-mode equations (2.7) can be solved analytically:

$$
\begin{aligned}
A(z) &= C_1 \exp\left(i\frac{\Delta\beta}{2}z - sz\right) + C_2 \exp\left(i\frac{\Delta\beta}{2}z + sz\right), \\
B(z) &= \frac{i}{\kappa}\frac{dA(z)}{dz},
\end{aligned}
\tag{2.12}
$$

where C_1 and C_2 are constants and s is given by

$$s = \sqrt{|\kappa|^2 - \left(\frac{\Delta\beta}{2}\right)^2}. \tag{2.13}$$

Assuming that there is no input wave at $z = L$, $B(L) = 0$, solutions (2.12) become

$$
\begin{aligned}
A(z) &= \exp\left(i\frac{\Delta\beta}{2}z\right)\frac{s\cosh s(L-z) + i\frac{\Delta\beta}{2}\sinh s(L-z)}{s\cosh sL + i\frac{\Delta\beta}{2}\sinh sL}A(0), \\
B(z) &= \exp\left(-i\frac{\Delta\beta}{2}z\right)\frac{-i\kappa^*\sinh s(L-z)}{s\cosh sL + i\frac{\Delta\beta}{2}\sinh sL}A(0).
\end{aligned}
\tag{2.14}
$$

The reflectance is given by

$$R = \left|\frac{B(0)}{A(0)}\right|^2 = \frac{|\kappa|^2\sinh^2 sL}{s^2\cosh^2 sL + \left(\frac{\Delta\beta}{2}\right)^2\sinh^2 sL}. \tag{2.15}$$

From (2.15) we find that maximum reflectance occurs when $\Delta\beta = 0$ and is given by:

$$R_{max} = \tanh^2 |\kappa| L. \qquad (2.16)$$

Reflectance is an increasing function of $|\kappa|L$. Figure 2.6 shows a typical reflectance spectrum of a uniform grating. Reflection occurs over the region where $-2|\kappa| < \Delta\beta < 2|\kappa|$. In this region, s is real and solutions (2.12) become exponential, indicating exchange of energy between the forward and backward propagating mode. Using
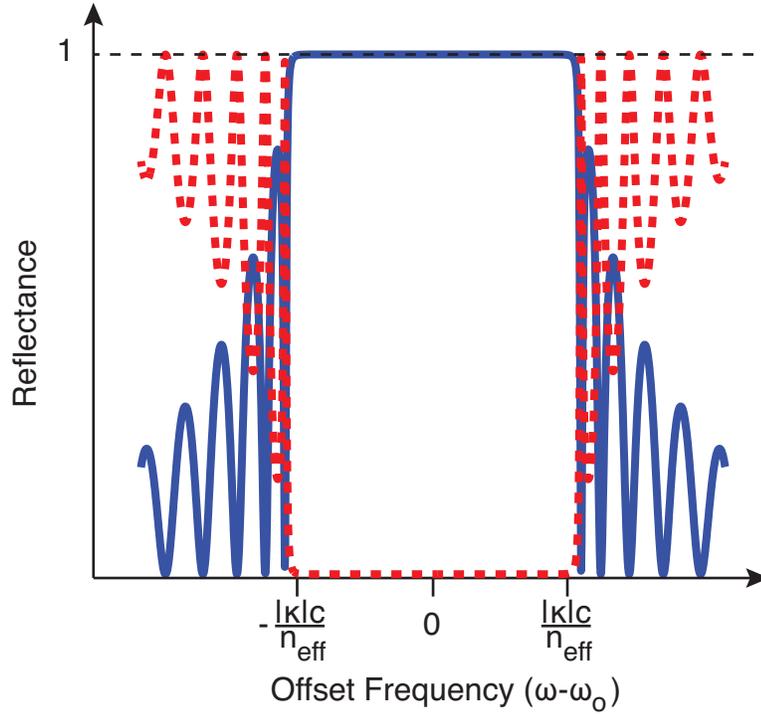
Figure 2.6. Reflectance (blue solid line) and transmittance (red dashed line) of a uniform grating.

equations (2.10), (2.11), this region can be expressed in frequency range as

$$-\frac{|\kappa|c}{n_{eff}} < \omega - \omega_0 < \frac{|\kappa|c}{n_{eff}}. \qquad (2.17)$$

The frequency range over which a grating reflects is known as *photonic bandgap* or *stopband* and is given by

$$\Delta\omega_{gap} = 2\frac{|\kappa|c}{n_{eff}}. \tag{2.18}$$

Oscillations outside the bandgap are due to Fabry-Perot-type reflections at the abruptly terminated ends of the grating. The general solution for the electric field in the grating can be written

$$E(z) = B_1 \exp(-i\beta'z) + B_2 \exp(+i\beta'z), \tag{2.19}$$

where B_1 and B_2 are constants and

$$\beta' = \beta - \frac{\Delta\beta}{2} \pm is = \frac{\pi}{a} \pm i\sqrt{|\kappa|^2 - [\beta(\omega) - \beta_o]^2}. \tag{2.20}$$

If we approximate $\beta(\omega)$ near its Bragg value $\frac{\pi}{a}$ by $\beta(\omega) \sim \frac{\omega}{c}n_{eff}$, then (2.20) becomes

$$\beta' = \frac{\pi}{a} \pm i\sqrt{|\kappa|^2 - \left(\frac{n_{eff}}{c}\right)^2 (\omega - \omega_o)^2}. \tag{2.21}$$

A plot of the real and the imaginary part of β' is shown in figure 2.7. The width of the forbidden zone is again given by (2.18). At the middle of the bandgap, where the Bragg condition is satisfied, $\omega = \omega_o$ and

$$\Im\beta'_{max} = |\kappa|. \tag{2.22}$$

The complex wavenumber β' is the Bloch wavenumber.

This behaviour of photons when travelling through a periodic structure is in direct analogy to the behaviour of electrons in periodic crystals. Electron wavefunctions in periodic potentials have a Bloch function form:

$$\Psi_i(\mathbf{r}, \mathbf{k}) = u_i(\mathbf{r}) \exp\left(-i\frac{E_i t}{\hbar} + i\mathbf{k_i} \cdot \mathbf{r}\right), \tag{2.23}$$

where i denotes the ith energy band and $\mathbf{k}, \mathbf{r}$ are reciprocal and real space vectors respectively. In periodic solid crystals, there exist regions electron energy E_i where
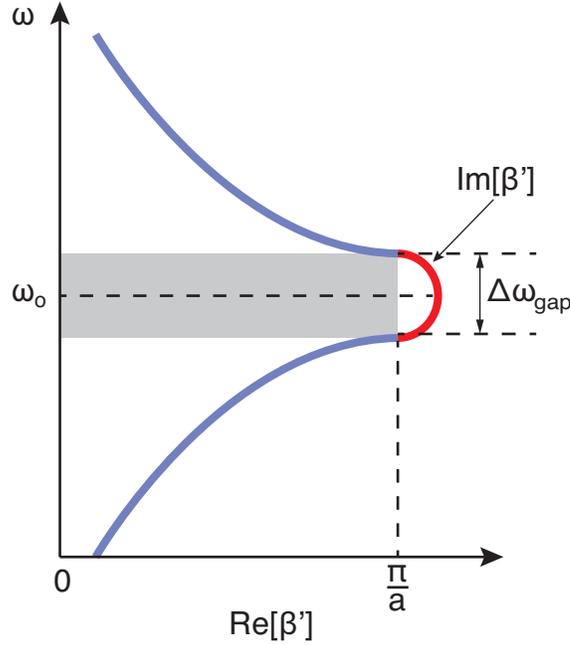
Figure 2.7. Dispersion diagram of a uniform grating showing the real (blue line) and imaginary (red line) part of the propagation constant β.

k is complex in every direction, thus electrons are forbidden to exist in those energy gaps. Unlike universal 3D bandgaps that occur in crystals naturally, 3D *photonic crystals* with complete photonic bandgaps is the objective of artificial engineering.

2.2.2 Waveguide Grating Defect-Mode Resonators

As we saw in the previous section, a grating acts as a reflector for frequencies inside its stopband with a set of transmission resonances on either side of it. Transmission within the stopband can be achieved by cascading two grating reflectors (i.e., mirrors) spaced by an appropriate distance L_d or equivalently by introducing a defect of size L_d into an originally uniform grating, as shown in figure 2.8. These stopband resonances can be made much narrower than the passband ones of the individual gratings since the reflectance of each grating is exploited at each maximum value. For lossless gratings with no intrinsic losses, arbitrarily narrowband resonances can be engineered for large enough $|\kappa|L$. The length of the spacing is such that phase-matching is
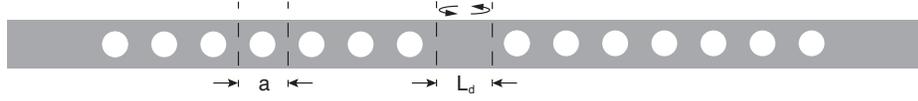
Figure 2.8. Schematic of a waveguide grating defect-mode resonator.

satisfied for a round-trip between the gratings:

$$2\beta L_d + 2\theta = 2m\pi, \qquad (2.24)$$

where θ is the reflection-induced phase change from each grating. At $\omega = \omega_o$, $\theta = \frac{\pi}{2}$ and the appropriate spacing L_d becomes

$$L_d = (2m - 1)\frac{\lambda}{4n_{eff}}, \quad m = 1, 2, 3, \ldots, \qquad (2.25)$$

where λ is the free space wavelength at $\omega = \omega_o$. The smallest allowable spacing is for $m = 1$ and it is $L_d = \frac{\lambda}{4n_{eff}}$. It accommodates one single resonance at the middle of the stopband, as shown in figure 2.9. When seen as a break in the periodic symmetry of a single grating, the split is often referred to as a *defect* and the corresponding resonance a *defect-mode*. Transmission through the resonator occurs via *resonant tunneling*, as opposed to transmission via propagation utilizing passband modes. This again bears analogy to defects in crystals in solid state physics and the respective defect states in forbidden gaps. A defect-mode is localized in space, since it is bounded by reflectors on either side. A quarter wavelength defect provides maximum confinement in space, as the mode at midgap experiences the highest reflection and thus penetrates into the mirrors the least distance. Therefore, defect-mode resonators of this type can be made extremely small, especially when combined with strong values of $|\kappa|$. A plot of the defect-mode's field distribution is given in figure 2.10. This profile corresponds to the slow-varying longitudinal envelope of the optical mode and represents a stark deviation from the Bloch function dependence. The implications of this phenomenon will be discussed in detail in a following section. If the two gratings comprising the defect-mode resonator are infinite or practically when $|\kappa|L \gg 1$, the resonator is said
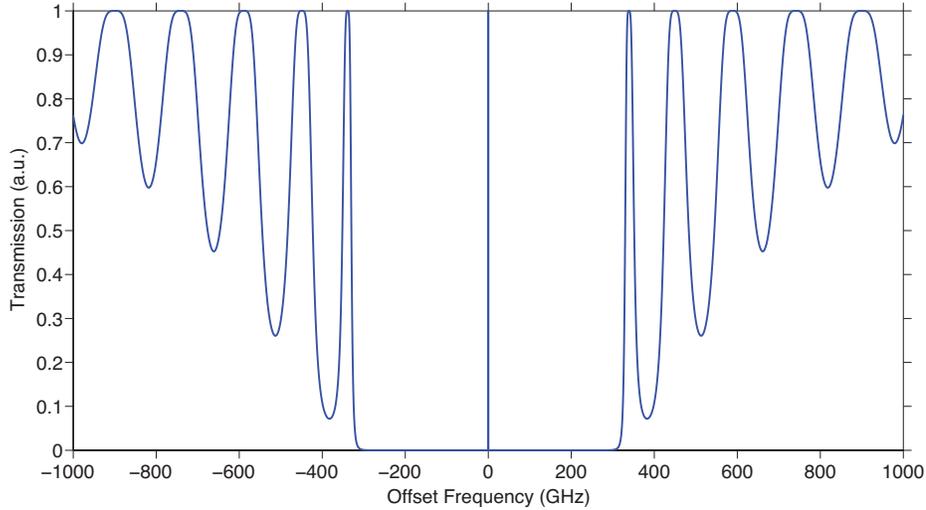
Figure 2.9. Transmission of a quarter-wave-shift grating resonator.
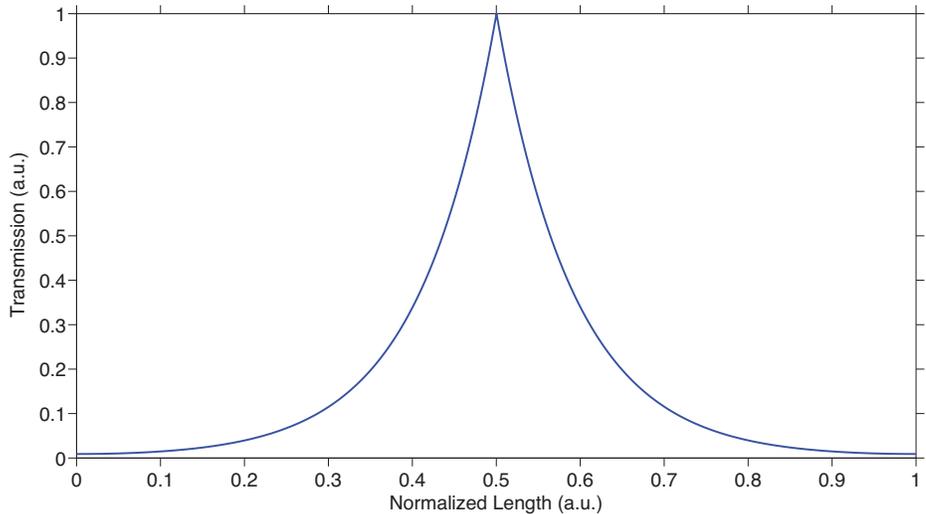
Figure 2.10. Field amplitude distribution in a quarter-wave-shift grating resonator.

to be unloaded in the sense that it was defined in section (2.1.1). The total Q is then equivalent with the intrinsic quality factor Q_i. In practice however, gratings are of finite length and therefore the resonator coupled to the waveguide, thus loaded, as defined in section (2.1.2). It is therefore useful to establish a connection between the grating's parameters and the external quality factor Q_e. Assuming lossless gratings and invoking energy conservation, the external quality factor due to each grating can

be expressed as [145]

$$Q_e = \frac{\pi c}{v_g \lambda |\kappa|} \exp(2|\kappa|L), \tag{2.26}$$

where v_g is the group velocity of the unperturbed waveguide mode. As can be seen from (2.26), an exponential increase with $|\kappa|L$ dominates over Q_e on resonance ($\omega = \omega_o$). The loaded Q can then be written as

$$\frac{1}{Q_L} = \frac{1}{Q_i} + \frac{2}{Q_e} = \frac{1}{Q_i} + \frac{2v_g \lambda |\kappa|}{\pi c} \exp(-2|\kappa|L). \tag{2.27}$$

The loaded Q can be made arbitrarily high only when intrinsic losses are ignored. Realistically, the actual Q and thereby the resonator linewidth are limited by Q_i. The mechanisms contributing to Q_i will be analysed in the next section.

2.3   Analysis of the Intrinsic Quality Factor Q_i

In the so far discussion about the quality factor of a resonator, the intrinsic Q has been treated as a given characteristic parameter, subject to the resonator's internal losses. The intrinsic quality factor represents an upper bound on the resonator's actual and usable Q, assuming that loading can be tuned arbitrarily, and the ultimate limit on the resonator's linewidth and thus spectral purity. Here, we will attempt to break down Q_i into the various mechanisms and sources of loss that contribute to it. Indeed, Q_i is an aggregate quality factor, comprising a range of parallel loss-inducing processes, lumped together into one characteristic quantity. These processes can vary in nature as substantially as does also their relative weight on the total Q_i. Both of these aspects are highly dependent on the specific type of resonator, material platform and method of implementation (i.e., fabrication). Therefore, the following analysis will focus on the resonator developed and utilized in this work, that is a 1D waveguide grating resonator on Silicon-on-Insulator (SOI). For such a resonator, Q_i can be broken down into the following components [146]:

$$\frac{1}{Q_i} = \frac{1}{Q_{rad}} + \frac{1}{Q_{sc}} + \frac{1}{Q_{ba}} + \frac{1}{Q_{sa}} + \frac{1}{Q_{dis}}, \tag{2.28}$$

where each Q on the right-hand side of (2.28) represents a quality factor limited by the respective process. Photon lifetimes and loss rates for each loss process can be defined accordingly and lumped into the intrinsic photon lifetime and loss rate respectively.

Radiation-limited quality factor ($\mathbf{Q_{rad}}$). This quality factor accounts for loss due to coupling of the resonant mode to leaky and radiation states that transfer energy to the outside world. But how does this coupling come about? A waveguide mode travelling through a grating with translational invariance (i.e., infinite length and uniform period), possess an extended Bloch-type spatial distribution and precisely prescribed wavevector. If the grating is designed to couple only counter-propagating guided modes, exchange of energy with radiation modes is forbidden, as phase-matching is strictly satisfied only for the guided modes. Yet, when we break the grating symmetry to create a localized defect-mode, the extended Bloch distribution is perturbed and the resulting mode assumes a spatial-limited profile. The localization of the mode in real space has as a result the delocalization of its Fourier components in reciprocal space (k-space). In other words, as the defect-mode becomes confined in space, it acquires a finite spread in k-space about the central wavevector (e.g., $\beta_o = \frac{\pi}{a}$). This spread is broader, the tighter the confinement in space. Furthermore, depending on the spatial profile of the mode distribution in real space, higher spatial frequency components (i.e., k-vectors) may rise. This effect is particularly pronounced at field profile discontinuities as those at the transition between the grating and defect section of the resonator. Abrupt field variations at structure discontinuities tend to give rise to high spatial frequencies. As a result, isolation from radiation modes is no longer guaranteed. The finite wavevector spread along with the high spatial frequencies can phase-match the resonant mode with leaky modes, thus the radiation-limited quality factor Q_{rad}. This energy leakage via radiation is further exacerbated by the lack of a complete photonic bandgap, that is the lack of a range of frequencies over which propagation is forbidden for all wavevectors in every direction in space. That would, in principle, be possible only in a 3D photonic crystal. In 2D photonic crystal slabs and 1D waveguide gratings, the lack of 3D confinement

provides a path for the defect-mode to couple to radiation, when the appropriate wavevector components for the phase-matching exist. The presence of this radiation path is represented schematically in the dispersion diagram of a waveguide grating with a triangular shaded area above a straight line, as shown in figure 2.11. The straight red line is known as the *light line*, and its slope, $\frac{\omega}{k}$, typically corresponds to the highest refractive of the waveguide's cladding or in general to the cutoff effective index of the guided mode. The dark-shaded grey above it represents a continuum of radiation states. From the above argument, it has become clear that the localization
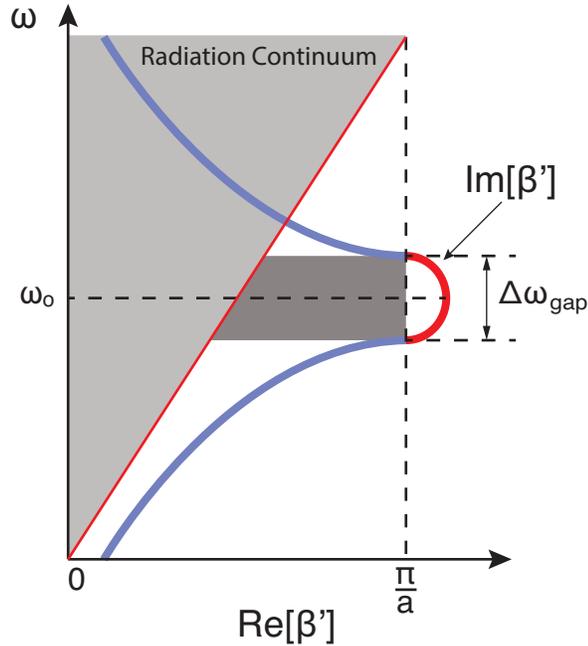
Figure 2.11. Dispersion diagram of a uniform grating with incomplete bandgap.

of light in space comes at the cost of radiation loss and, in fact, *the tighter the local-ization in real space, the broader the delocalization in k-space*, hence the smaller the Q_{rad}. There is a trade-off to be made between mode volume V and the the quality factor of a resonant mode. In the remainder of this chapter, we will present a design to optimize the Q_{rad} of a resonator intended for a laser cavity.

The radiation-limited Q defined above corresponds to a perfectly fabricated res-onator with no material imperfections. Yet, the actual intrinsic quality factor is still impaired by fabrication errors and material nonidealities. Therefore, the real experi-

mental Q_{iexp} can be expressed as

$$\frac{1}{Q_{iexp}} = \frac{1}{Q_{rad}} + \frac{1}{Q_{imp}}, \tag{2.29}$$

where Q_{imp} accounts for all imperfections of a real-world device. These imperfections are overviewed below.

Scattering-limited quality factor (Q_{sc}). This quality factor accounts for the energy radiated out of the resonator due to to scattering. Scattering occurs at structure discontinuities, that could be either inherent to the resonator design or unwanted artifacts of the fabrication process, as is the case of roughness-induced scattering. A scatterer of the latter type behaves as an additional dielectric perturbation, thereby inducing the generation of polarization currents when interacting with the electric field of mode. These current, in turn, act as pointlike sources of radiation. The aggregate effect of a large assembly of radiating sources is constructive and destructive interference and therefore the emission of energy into specific parts of the radiation spectrum.

Alternatively, viewing roughness as a random distribution of scatterers, one can treat it using its statistical properties. For that purpose, a spectral density function $\tilde{R}(\Omega)$ is introduced and related to an autocorrelation function $R(u)$ through the Fourier transform [147]:

$$\tilde{R}(\Omega) = \int_{-\infty}^{+\infty} R(u) \exp(i\Omega u) du. \tag{2.30}$$

The two functions can be fully defined using two parameters, the r.m.s. amplitude σ of the roughness, which corresponds to the mean square deviation from a flat surface and is a measure of the size distribution of the scatterers and a correlation length L_c, which describes their density distribution. The roughness amplitude is related to the autocorrelation function via

$$\sigma^2 = R(0). \tag{2.31}$$

The surface roughness of optical waveguides fabricated with standard lithographic

techniques is commonly modeled by either Gaussian or exponential autocorrelation functions:

$$R(u) = \sigma^2 \exp\left(-\frac{|u|^2}{L_c^2}\right),$$

$$R(u) = \sigma^2 \exp\left(-\frac{|u|}{L_c}\right). \tag{2.32}$$

An approximative, yet insightful expression for the exponential radiation loss coefficient α_{sc} of a slab waveguide due to roughness-induced scattering is given by [148]

$$\alpha_{sc} = \phi^2(d)(n_2^2 - n_1^2)^2 \frac{k_o^3}{4\pi n_1} \int_0^\pi \tilde{R}(\beta - n_2 k_o \cos\theta) d\theta, \tag{2.33}$$

where $2d$ is the width of the core, n_1, n_2 the refractive indices of the core and cladding respectively, $\phi(d)$ the electric field amplitude at the core-cladding interface and θ denotes the angle of propagation for a radiation wave component in space. Although the exact for the loss in a 3D waveguide can be quite different, the above formula offers some generic insight. The scattering loss increases strongly with the field amplitude at the waveguide boundaries and scales also very adversely with the index contrast between core and cladding. The importance of the correlation length L_c of the roughness is in that it selects the radiation components to which energy is preferentially coupled to. Given a scattering loss coefficient a_{sc} [cm^{-1}], the corresponding scattering-limited quality factor can be defined as:

$$Q_{sc} = \frac{\omega_o}{\upsilon_g a_{sc}}, \tag{2.34}$$

where υ_g is the group velocity of the guided mode.

Bulk absorption-limited quality factor (Q_{ba}). This quality factor accounts for loss due to absorption in the bulk of the material, also referred to as *material loss*. Absorption can be linear or nonlinear (i.e., at elevated optical power levels). Linear absorption arises from intrabandgap states due to doping or crystal defects. In Silicon, the primary cause of linear absorption is free-carrier absorption (FCA)

due to residual, electrons and holes in the conduction and valence band respectively. FCA is a function of the resistivity (i.e., doping level) of the wafer. For example, for a Si wafer of resistivity $\rho = 11.5\,\Omega\,\mathrm{cm}$ ($N_c = 1 \times 10^{15}\,\mathrm{cm}^{-3}$), the quality factor due to FCA is calculated to be well above 10^7 [146]. Yet, with the incorporation of III-V material in the optical platform, as in the case of a hybrid laser, free-carrier absorption contributes to loss significantly due to the increased doping of the III-V cladding layers.

Surface absorption-limited quality factor ($\mathbf{Q_{sa}}$). This quality factor accounts for loss due to absorption at the surfaces and interfaces of the optical structure. Although this loss component can be directly lumped into the total linear absorption, its physical origin is quite distinct from that of the bulk component. There are two major mechanisms that contribute to surface absorption. Absorption by water molecules adsorbed on surfaces, which can be particularly pronounced in the $1550\,\mathrm{nm}$ wavelength range ($Q_{water} \sim 4 \times 10^6$, based on one atomic layer of adsorbed water [146]), plus absorption due to surface electronic states. These states occur naturally at any abruptly terminated Si crystal as a result of unfulfilled valence bonds (i.e., dangling bonds). The density of these states can be further exacerbated on plasma-etched surfaces due to the physical damage incurred by the milling component of the etch process. The effect these incomplete bonds is the introduction of midgap states and an effective shrinking of the bandgap, thereby increasing the photon absorption.

Disorder-limited quality factor ($\mathbf{Q_{dis}}$). This quality factor accounts for loss to radiation induced by deviations from the theoretical resonator design due to fabrication imperfections. These imperfections, in the case of a waveguide grating, can be in the form of hole position and radii variation, period fluctuations, deviation from verticality of sidewalls among others [149]. Deviations in critical dimensions of features occur typically in the lithography step (e.g., e-beam lithography) of the patterning process and can be of both stochastic (i.e., random) and deterministic nature. Different mitigation techniques for each category of errors can be employed. Besides the absolute magnitude of such errors, the loss incurred by them on the resonant

mode depends also strongly on the strength of the interacting field at the disorder site. Therefore, an optimal resonator design can further suppress the disorder effect.

Chapter 3

High-Q Resonator for Ultracoherent Silicon Photonics

In this chapter we will present the design and analysis of a special type of waveguide defect-mode resonator on Silicon, designed to support a single, high-Q resonance and intended to be part of the cavity of a high-coherence, hybrid III-V/Si semiconductor laser. Although the present chapter focuses on the design of a passive resonator on Si, special considerations and choices for the passive platform itself are made, mandated by its eventual use as a laser cavity. We will begin by addressing those special issues and how they define the passive platform and then proceed to the discussion of the resonator design.

3.1 Waveguide Platform

A 1D optical waveguide provides a natural platform for an index-guided, edge-emitting laser. Unlike purely III-V semiconductor lasers where the III-V also serves as the mode guiding platform, the hybrid laser developed in this work is of the evanescent type, in that the bulk of the optical mode is hosted in Si and only a fraction of its evanescent tail reaches into III-V to interact with the gain medium. Due to the high average refractive index of the quaternary III-V material, in this case InGaAsP/InP ($n = 3.4$), the Si platform has to be adjusted appropriately for a mode to be confined primarily in Si. This is accomplished by increasing the thickness of the Si device layer of the Si-on-insulator (SOI) wafer, from a typical thickness of $220\,\mathrm{nm}$ to over $400\,\mathrm{nm}$

for optical confinement in Si of more than 60%. The second major choice with respect to the guiding platform pertains to the maximization of the scattering-limited quality factor Q_{sc}. Based on the analysis of section (2.3), we choose to use a rib-waveguide type of geometry to "bury" the mode into the Si slab and reduce the effective area of interaction of the mode with the roughness on the etched sidewalls. Specifically, a shallow-ridge rib-waveguide geometry is preferred, as shown in figure 3.1(a), with $\frac{h}{H} \ll 1$, where h is the etch depth of the ridge and H the total thickness of the Si slab. The profile of the fundamental TE mode of a waveguide of this type is shown in figure 3.1(b). The width of the ridge L_y normally has to be kept below the cutoff of the second-order transverse mode, a requirement particularly necessary for a laser cavity, yet we defer the discussion on the choice for L_y for a later section. Although even
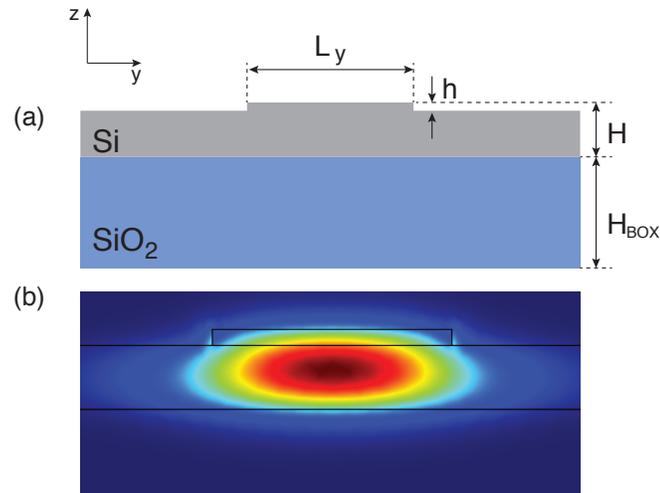
Figure 3.1. (a) Schematic of the Si waveguide 2D geometry. (b) Electric field distribution of the fundamental TE mode.

thicker Si layers, up to $800\,\mathrm{nm}$ have been previously used in similar hybrid structures, we limit the thickness in this work at $500\,\mathrm{nm}$, as we find that this choice allows us to satisfy the requirement for a shallow rib-waveguide and that for a weak, shallow grating in one lithography step, thus significantly simplifying the fabrication process.

3.2   High-Q Resonator Design

3.2.1   Introduction

With the waveguide platform defined in section (3.1), we now move on to the design of a high-Q resonator, based on a 1D waveguide grating. Starting from an originally uniform grating, a defect-mode is localized by perturbing the uniformity of the grating, as shown in figure 3.2 from top view and figure 3.3 from perspective view. The perturbation is physically implemented via the continuous modulation of a structural parameter of the grating, in this case of the transverse hole diameter W_y, that results in a corresponding modulation of the grating's bandgap. The origin of this concept can be traced back to the modegap-type photonic crystal resonators, first introduced in 2D photonic crystal slabs [150–153] and later adapted for 1D waveguide resonators [154–158].
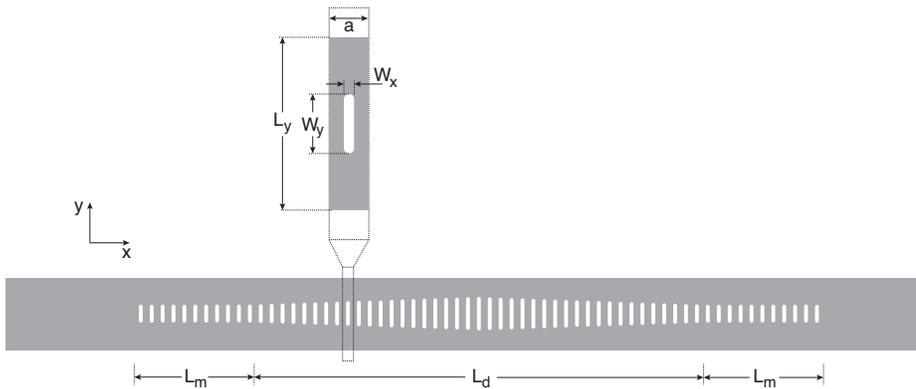
Figure 3.2. Top view of the high-Q grating resonator.

As opposed to a grating resonator with a phase shift (e.g., QWS), there is no such tyoe of defect here, as the period a is retained constant throughout the grating. Furthermore, the modulation scales slowly in space, spanning a length L_d, which represents the defect section of the resonator. The defect is bounded by uniform mirrors (i.e., reflectors) of length L_m. The purpose of the slow modulation is to avoid fast variations in the envelope of the field in real space and thereby to suppress high spatial-frequencies in the reciprocal space. The strength of the grating (i.e.,
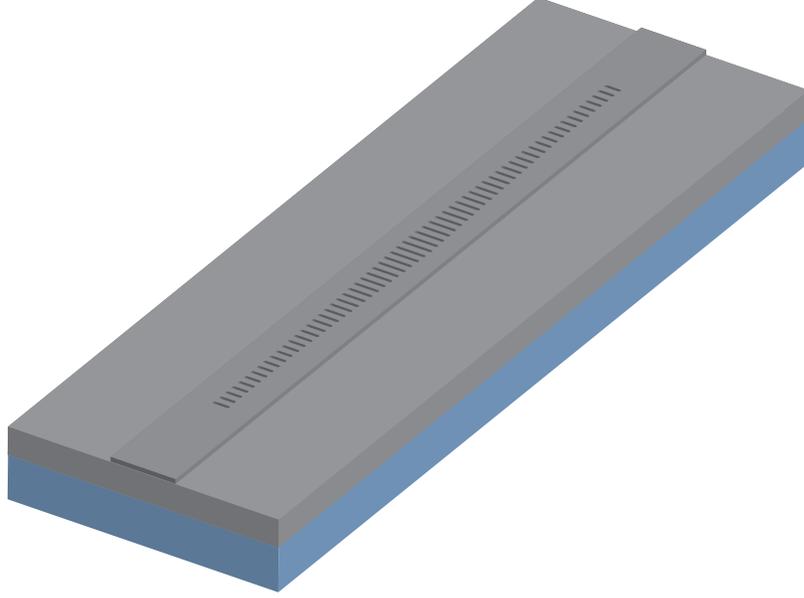
Figure 3.3. Perspective view of the high-Q grating resonator.

coupling coefficient κ) is also made to be small via a shallow etch, to allow the mode to spread out over a long distance. Keeping the total excursion of the modulated section from the mirror reference small makes the defect-mode "shallow" with respect to the bandgap of the uniform grating, thus forcing the mode to penetrate deeper into the mirrors. All of the above considerations aim at one goal, that is to spread the resonant mode out in real space, thus localizing it tighter in k-space, in order to minimize coupling to radiation modes and optimize the radiation-limited quality factor Q_{rad}. This choice also renders the resonator scalewise suitable for a large-scale laser cavity, necessary to generate appreciable amount of optical power.

3.2.2   Resonator Spatial Band Structure

Here, we define the resonator's spatial band structure as the variation of the upper and lower band edge frequencies at the local Bragg condition of each grating unit cell across the resonator, described by functions ω_c, ω_v, where the subscripts "c, v" stand for "conduction" band and "valence" band respectively, to illustrate the analogy of a unit cell's band structure to that of crystals in solid state physics. Engineering the spatial band structure allows us to control such properties as the resonator's defect-

mode capacity, as well as each mode's spatial profile. Therefore, it is important to be able to define the band structure in a deterministic manner. The modal behavior of a spatially modulated grating can be modeled by coupled-mode equations just as in the case of a uniform grating, with only slight change in notation:

$$\begin{aligned}
\frac{dA}{dx} &= -i\delta(x)A + i\kappa(x)B, \\
\frac{dB}{dx} &= -i\kappa(x)A + i\delta(x)B,
\end{aligned} \tag{3.1}$$

where $\delta = \beta - \beta_o$ is the detuning of the propagation constant $\beta(\omega)$ of a guided-wave component at frequency ω from the Bragg wavevector $\beta_o = \frac{\pi}{a}$ and the coupling coefficient κ is assumed to be real. Due to the spatial variation of the grating, both δ and κ become spatial-dependent functions $\delta(x), \kappa(x)$ respectively. Since we are interested in describing the spatial band structure as $\omega(x)$, we can express δ and κ as functions of frequency:

$$\delta = \frac{n_g(\omega - \omega_B)}{c}, \tag{3.2}$$

$$\kappa = \frac{n_g(\omega_c - \omega_v)}{2c}, \tag{3.3}$$

$$\omega_B = \frac{\omega_c + \omega_v}{2}, \tag{3.4}$$

where n_g is the group index of the unperturbed waveguide mode, ω_B the Bragg frequency of the local unit cell and ω_c, ω_v the upper and lower band edge frequencies of the local unit cell at $\beta_o = \frac{\pi}{a}$. Equations (3.2)–(3.4) are accurate within the realm of validity of the coupled-mode equations.

For each unit cell (figure 3.4(a)), the propagation constants of its supermodes can be found by solving for the eigenvalues of the coupled-mode equations (3.1):

$$K = \pm\sqrt{\delta^2 - \kappa^2}. \tag{3.5}$$

The supermodes in each unit cell propagate for $|\delta| > \kappa$ and exponentially decay and grow for $|\delta| > \kappa$. Since we are interested in frequencies near the band edge of the

uniform grating (figure 3.4(b)), we set the Bragg wavevector β_{vm} and frequency ω_{Bm} as universal reference levels for unit cells across the resonator, where the subscript "vm" denotes the lower band edge of the mirror grating. Equation (3.5) can then be rewritten as

$$K = \pm\sqrt{(\delta - \delta_B)^2 - \kappa^2},\tag{3.6}$$

where now $\delta = \beta - \beta_{vm}$ and $\delta_B = \beta_o - \beta_{vm}$. The detuning factor of resonant mode at frequency ω close to the lower band edge of the mirror can be expressed as

$$\delta = -\kappa + \delta_\omega,\tag{3.7}$$

where δ_ω is an offset from the lower band edge of the mirror. Substituting (3.7) into (3.6) and using $|\delta_\omega - \delta_B| \ll \kappa$, we get

$$K \approx \pm\sqrt{2\kappa(\delta_B - \delta_\omega)}.\tag{3.8}$$
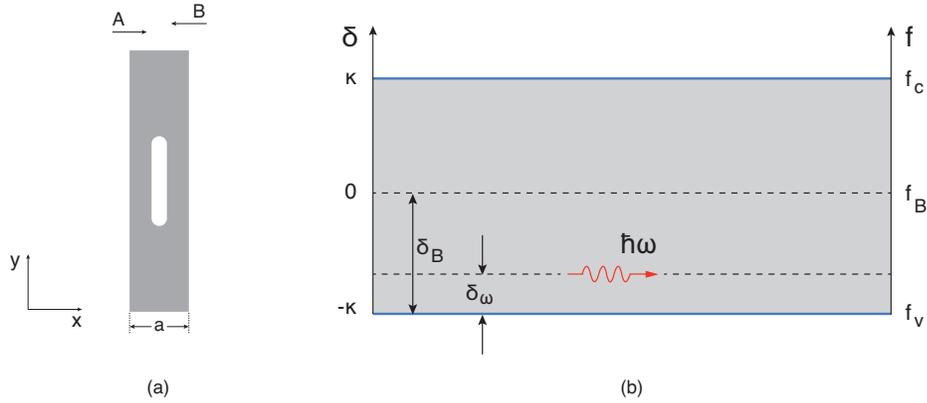
Figure 3.4. Grating unit cell: (a) Physical structure. (b) Spatial band structure.

Approximation (3.8) bears striking resemblance to the propagation constant of electron wavefunctions in a potential well, described by the 1D time-independent

Schrödinger equation:

$$-\frac{\hbar^2}{2m}\frac{d^2}{dx^2}\Psi(x) + [V(x) - E]\Psi(x) = 0, \tag{3.9}$$

where $\Psi(x)$ is the electron wavefunction, E the electron energy, $V(x)$ the spatial-dependent potential, m the electron mass and $\hbar$ Planck's constant. The eigenvalue of the electron wavefunction is given by

$$K = \sqrt{\frac{2m}{\hbar^2}[E - V(x)]}. \tag{3.10}$$

Comparing equations (3.8)–(3.10) the following association of parameters can be made

$$E = -\frac{\hbar^2\kappa}{m}\delta_\omega, \tag{3.11}$$

$$V(x) = -\frac{\hbar^2\kappa}{m}\delta_B(x). \tag{3.12}$$

Using equation (3.2) to replace wavevector detuning factors with frequency, we have

$$E = -\frac{\hbar^2\kappa n_g}{mc}(\omega - \omega_{vm}), \tag{3.13}$$

$$V(x) = -\frac{\hbar^2\kappa n_g}{mc}(\omega_B(x) - \omega_{vm}). \tag{3.14}$$

Based on the above correspondence, a direct analogy can be drawn between an electron potential well and a *photonic well* for photons. The offset of the frequency of photons in the resonant mode from the band edge reference frequency defines an effective energy for the photons in the localized state, and the offset of the local Bragg frequency for each unit cell from the same reference defines an effective local potential. By directly controlling the function $\omega_B(x)$, we can shape the photonic well at will and deterministically tailor the modal properties of the resonator. For example, we know that a parabolic potential well, which describes a quantum harmonic oscillator, gives rise to a Gaussian ground state electron wavefunction. In accordance with the above analogy, if we shaped the photonic well to be parabolic, we should expect a Gaussian-

like profile for the envelope of the fundamental resonant mode [159]. The Gaussian field profile has been shown to provide well-behaved distribution of spatial frequencies in the reciprocal space and is therefore attractive for optimizing the radiation-limited Q of a resonator [160, 161].
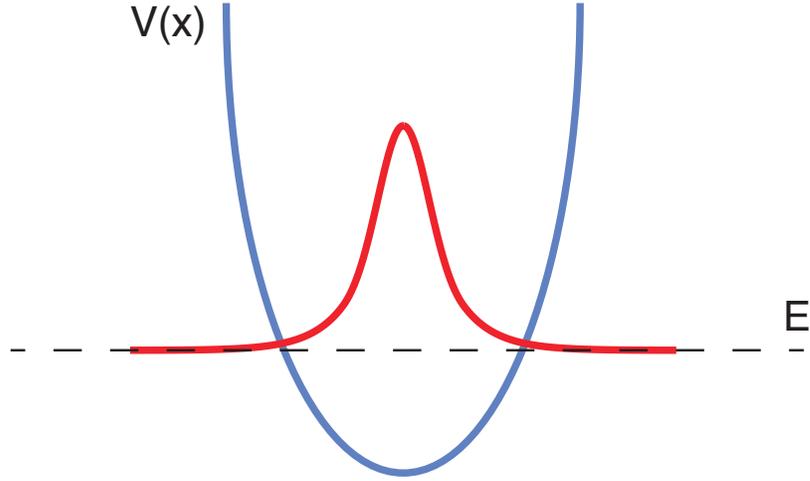
Figure 3.5. Quadratic potential well with a localized Gaussian ground state wave-function.

3.2.3 Design Methodology

By *a priori* defining the shape of the spatial band structure, the resonator design problem becomes of the *inverse* type, in that the structural design is no longer the input. Now, the band structure and thus the modal behavior constitute the input, while the physical design itself becomes the output of the problem. In this section we layout the steps of the design process.

We start by defining the fixed parameters of the design, the set independent and desired dependent variables. The waveguide platform is fixed via the thickness of the Si slab H, the ridge etch-depth h and the ridge width L_y. With respect to the grating, the period a and longitudinal hole diameter W_x are set in advance. The period is used to set the wavelength inside the desired window (e.g., 1550 nm), while W_x controls the duty cycle of the grating. We choose to work with W_x that corresponds to a duty

cycle of 40%−50%. Although both a and W_x can, in principle, be used as modulated parameters of a grating, they offer limited dynamic range for continuous modulation over an extended spatial scale. For dynamic range reasons as well as for simplicity, we choose to utilize the transverse hole diameter W_y as the only variable parameter. The last constraint to be set is the reference level ω_{cm}, ω_{vm} (f_{cm}, f_{vm}) for the spatial band structure, set by the mirror grating. By selecting a minimum hole diameter $W_{y_{min}}$, that reference level is defined. The choice for the absolute value of $W_{y_{min}}$ is based on practical considerations related to fabrication. We prefer to utilize smaller holes as they not only form weaker gratings, but also reduce the effective interaction area of light with the etched sidewalls.

The photonic well is designed according to the parabolic formula:

$$f_{c,v}(x) = A_{c,v}x^2 + B_{c,v}, \tag{3.15}$$

where $A_{c,v}$ and $B_{c,v}$ are constants defining the shape and position of the conduction and valence band edge. The sets (A_c, A_v) and (B_c, B_v) are mutually dependent. We choose to directly design the function $f_v(x)$ of the photonic well in the valence band edge. We use two basic parameters to define it, the depth V, expressed as an offset frequency in [GHz] from the mirror band edge and the width of the well L_d in µm. Given the two parameters, function $f_v(x)$ is written as

$$f_v(x) = \pm\frac{V}{(L_d/2)^2}x^2 + f_{vm} \mp V, \tag{3.16}$$

where $A_v = \pm\frac{V}{(L_d/2)^2}$ and $B_v = f_{vm} \mp V$. The $\pm$ sign in A_v controls the orientation of the parabola. For the positive sign the well in the valence band does not localize any modes and, in fact, behaves in antiresonant fashion (i.e., potential barrier). Instead, for the same choice of sign for A_v a localizing well is formed in the conduction band edge. The picture is reversed for negative A_v. Defect-modes of the former kind are known as *donor* modes, whereas of the latter kind, *acceptor* modes, in analogy to donor-, acceptor-type modes in semiconductors. We choose to design an acceptor-

type of mode, as that places it farther from the light line, thereby reducing the coupling to radiation modes. So, a photonic well in the valence band with frequency potential V and defect width L_d, as shown in figure 3.6, is described by

$$f_v(x) = -\frac{V}{(L_d/2)^2}x^2 + f_{vm} + V. \qquad (3.17)$$
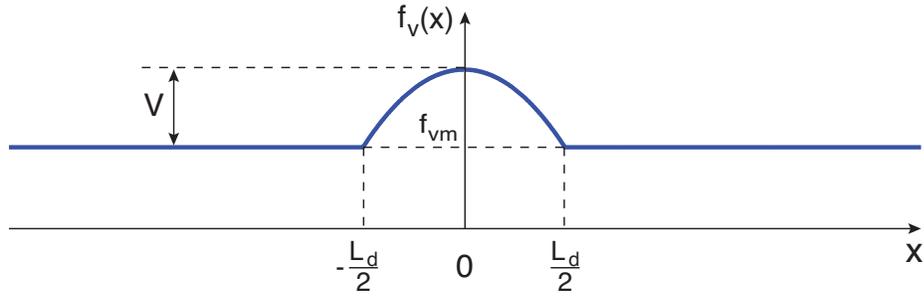
Figure 3.6. Parabolic photonic well in the valence band.

The problem to be solved can now be cast as

$$f_v(x) \Longrightarrow W_y(x). \qquad (3.18)$$

In other words, we need to find the structural design that yields the mandated frequency band edge profile. For that purpose, we seek to establish a connection between frequency and the structural parameter $W_y(x)$. For any given value of $W_y(x)$, the dispersion diagram $\omega - k_x$ of the corresponding uniform grating can be acquired by solving for the eigenfrequencies of a single unit cell with the appropriate periodic condition applied to it. This eigenfrequency analysis is carried out using the finite element method (FEM) over a 3D computation domain, represented by a slice cut out of a uniform grating, as shown in figure 3.7. A 1D Floquet periodic condition is applied to the two wide faces of the domain, while the unit cell is cut in half along the grating axis to reduce the computation time. Perfectly electric conductor (PEC) condition is applied to the cut boundary for the case even TE modes (e.g., TE_0, TE_2)
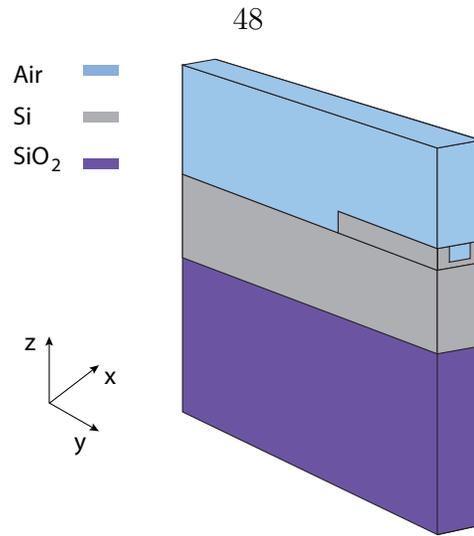
Figure 3.7. Finite element computation domain of a 3D unit cell.

and perfectly magnetic conductor (PMC) condition for odd modes (e.g., TE$_1$). A typical dispersion diagram for a Si resonator unit cell used in this work is shown in figure 3.8. The two blue lines represent the low and high frequency bands, $f_v(k_x)$
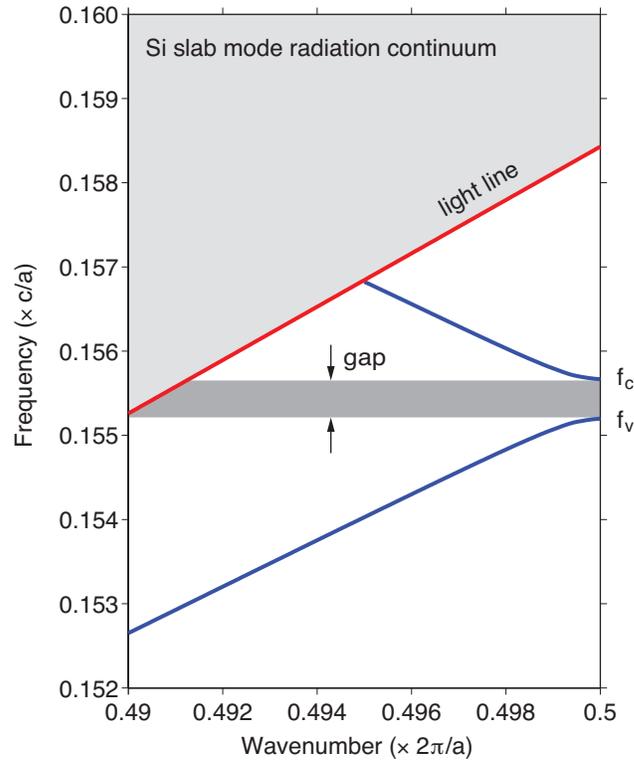
Figure 3.8. Dispersion diagram for a Si resonator unit cell.

and $f_c(k_x)$ respectively, of the fundamental TE mode. The red line denotes the light line, in this case defined by the cutoff effective index of the Si slab, and the shaded area above it the continuum of the Si slab radiation modes. Due to the low aspect ratio of the rib waveguide, this cutoff is very close to the effective index of the guided mode, thus making the Si slab mode continuum the predominant channel of radiation leakage. This proximity is also evident by how close the light line lies to the band edge at the end of the first Brillouin zone (only 1% of it shown in the diagram). The eigenfrequencies we are interested in are frequencies f_v and f_c at the two band edges of the unit cell, at the end of the first Brillouin zone, where the bandgap opens ($\beta_o = \frac{\pi}{a}$). Figures 3.9(a) and 3.9(b) show the 3D spatial distribution of the norm of the electric field for the fundamental TE mode at f_v and f_c respectively over the computation domain. Carrying this calculation out for a number of diameters W_y, we get sets of $f_v(W_y), f_c(W_y)$, plotted as blue lines in figure 3.10. Frequencies are cast on the vertical axis as offsets from a reference frequency f_{vm}. Figure 3.10 will be here-
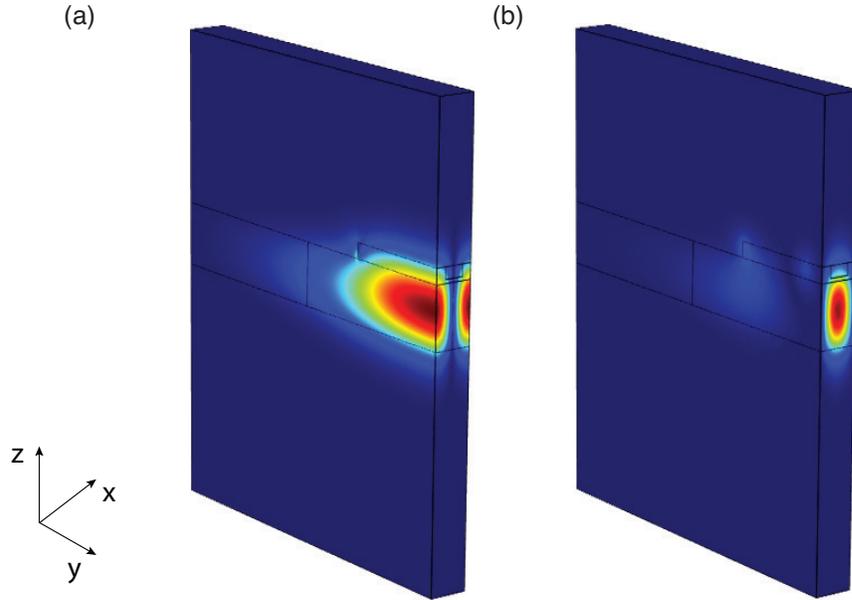
Figure 3.9. Spatial distribution of the norm of the electric field of TE_0 at (a) f_v, and (b) f_c ($\beta_o = \frac{\pi}{a}$).

after referred to as a *look-up table* as it provides the connection between frequency and the structural parameter W_y to be modulated. Indeed, once a valence band

edge frequency profile has been defined by setting V, L_d and $W_{y_{min}}$, projecting $f_v(x)$ through the $f_v(W_y)$ branch of the look-up table yields a corresponding distribution $W_y(x)$ on the horizontal axis. Similarly, projecting through the $f_c(W_y)$ branch yields a distribution $f_c(x)$. The utilized part of the two branches for a given design is shown in red. This way, a physical resonator design that delivers the desired frequency band edge profile is determined.
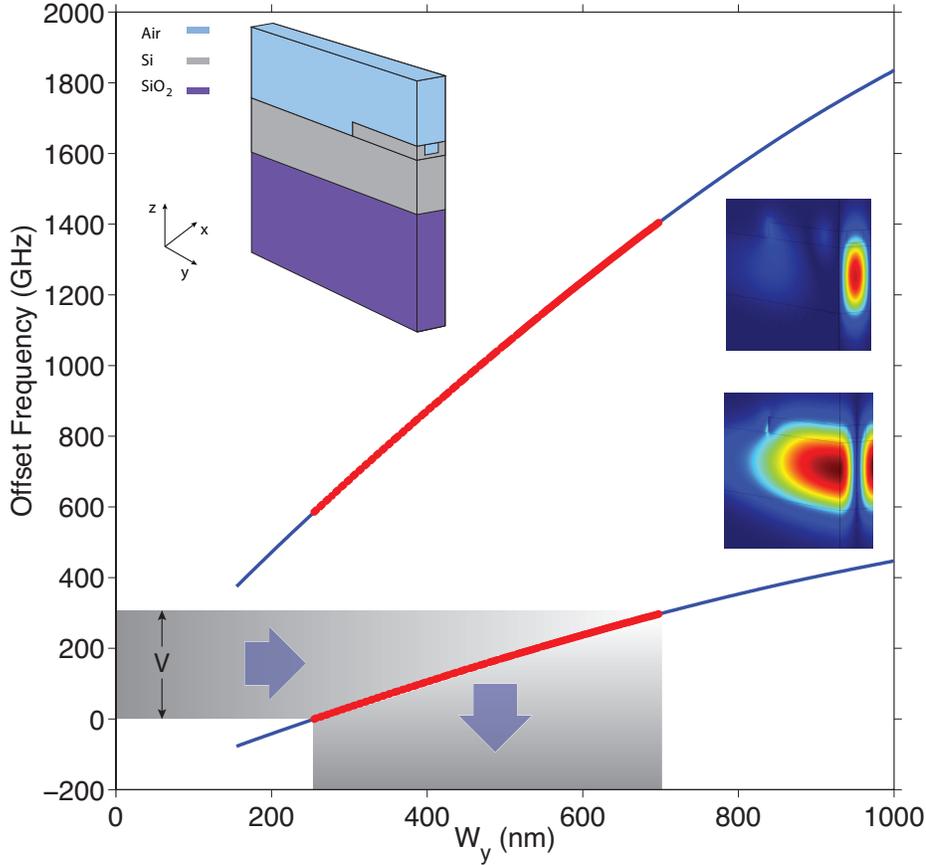
Figure 3.10. Typical look-up table for the design of a high-Q Si resonator.

3.3 Design Analysis

Having laid out the design methodology for the resonator in the previous section, we now move on to the analysis and study of its modal and spectral characteristics. Due to the sheer size of a resonator intended for a laser cavity, spanning several hundred

microns in length, solving it by a brute force approach (e.g., 3D electromagnetic simulation) constitutes a computationally formidable task. Instead, we trade off some accuracy for computation speed and simplicity by resorting once again to 1D coupled-mode equations:

$$\frac{dA}{dx} = -i\delta(x)A + i\kappa(x)B,$$
$$\frac{dB}{dx} = -i\kappa(x)A + i\delta(x)B. \tag{3.19}$$

What we have so far available for a given design, is a set of frequency spatial functions $f_v(x), f_c(x)$. Invoking the relative weakness of the grating, we employ conversion formulae (3.20)–(3.22) to attain the corresponding spatial distributions for the wavevector detuning $\delta(x)$ and the coupling coefficient $\kappa(x)$ at any operating optical frequency f.

$$f_B(x) = \frac{f_v(x) + f_c(x)}{2}, \tag{3.20}$$

$$\delta(x) = \frac{2\pi n_g}{c}\left[f - f_B(x)\right], \tag{3.21}$$

$$\kappa(x) = \frac{\pi n_g}{c}\left[f_c(x) - f_v(x)\right], \tag{3.22}$$

where f_B is the Bragg frequency of the local unit cell, n_g the group velocity of the guided mode and c the velocity of light in vacuum. Typical distributions for the derived Bragg frequency and coupling coefficient are plotted in figure 3.11 for the case of $V = 300\,\text{GHz}, L_d = 100\,\mu\text{m}, L_y = 1.5\,\mu\text{m}, h = 100\,\text{nm}, a = 245\,\text{nm}$. The detuning coefficient δ follows the same distribution as f_B.

With the derived sets of $\delta(x)$ and $\kappa(x)$ as input, the coupled-mode equations (3.19) are solved via a transfer-matrix approach along the resonator, for a range of frequencies f across the bandgap. The field amplitude distributions for components A and B are found, while for unity field input only from one end of the resonator (i.e., $A(0) = 1, B(L) = 0$) the normalized transmission spectrum $T(\omega) = \frac{A(L)}{A(0)}$ is also determined. Figure 3.12 shows a typical transmission spectrum for the case of $V = 300\,\text{GHz}, L_d = 100\,\mu\text{m}, L_y = 1.5\,\mu\text{m}, h = 100\,\text{nm}, a = 245\,\text{nm}$.
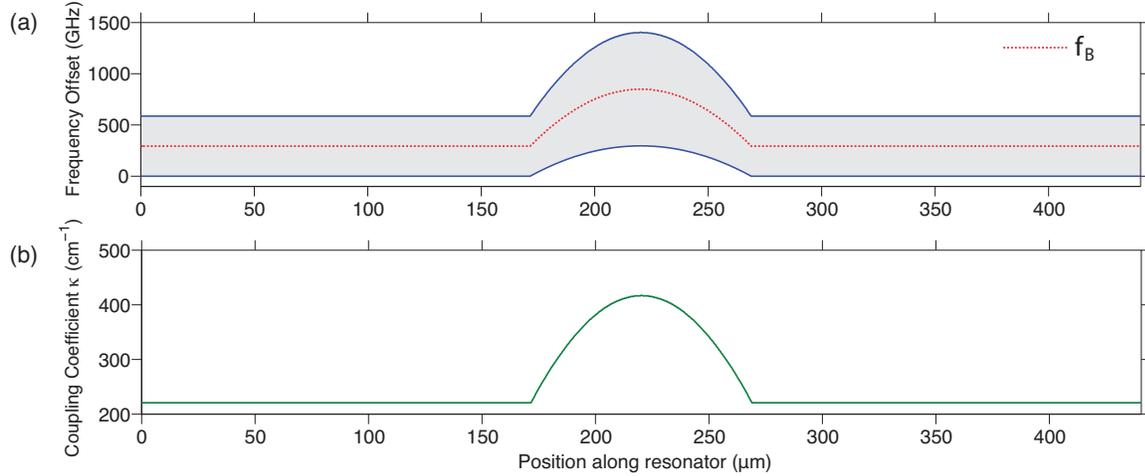
Figure 3.11. Design parameter distributions of a high-Q Si resonator (a) Spatial band structure $f_v(x)$, $f_c(x)$ and Bragg frequency $f_B(x)$. (b) Coupling coefficient $\kappa(x)$. ($V = 300\,\mathrm{GHz}$, $L_d = 100\,\mu\mathrm{m}$, $L_y = 1.5\,\mu\mathrm{m}$, $h = 100\,\mathrm{nm}$, $a = 245\,\mathrm{nm}$.)
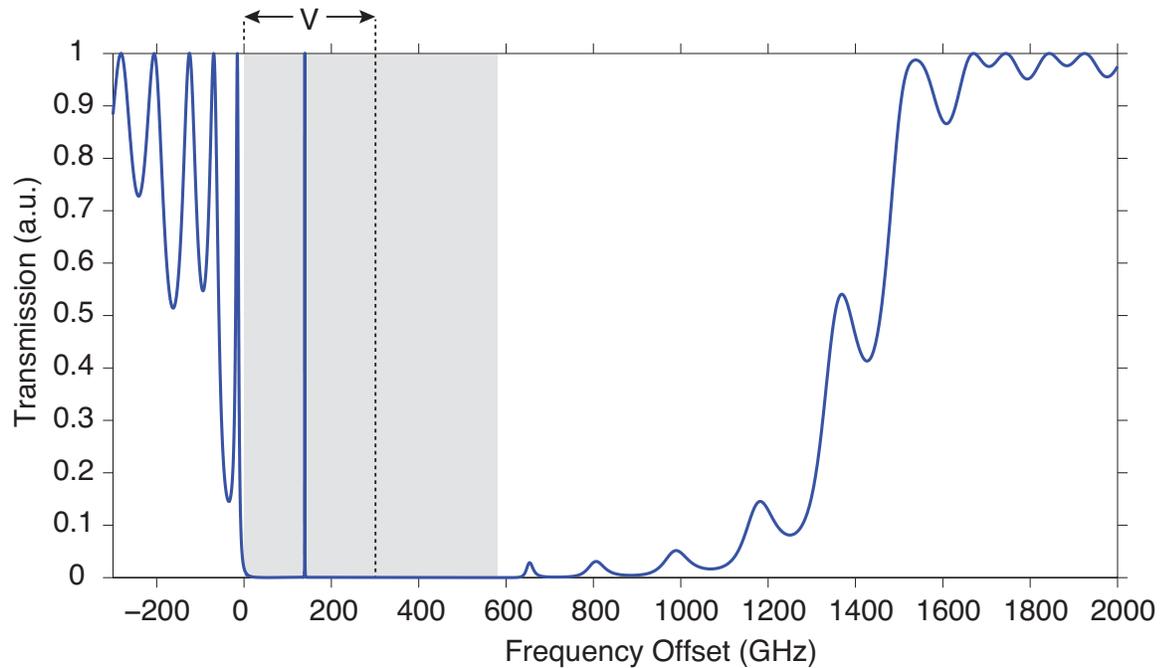
Figure 3.12. Transmission spectrum of a high-Q Si resonator. ($V = 300\,\mathrm{GHz}$, $L_d = 100\,\mu\mathrm{m}$, $L_y = 1.5\,\mu\mathrm{m}$, $h = 100\,\mathrm{nm}$, $a = 245\,\mathrm{nm}$.)

The grey-shaded area denotes the bandgap of the uniform grating mirrors, while the dashed line the extent of the photonic well in the valence band. Transmission

reaches unity at select frequencies, since the resonator is assumed to be free of any internal loss. The only loss accounted for is into the output waveguide through the finite mirrors. A more insightful reading of the spectrum is attained by plotting it against the designed spatial bandstructure, as shown in figure 3.13.
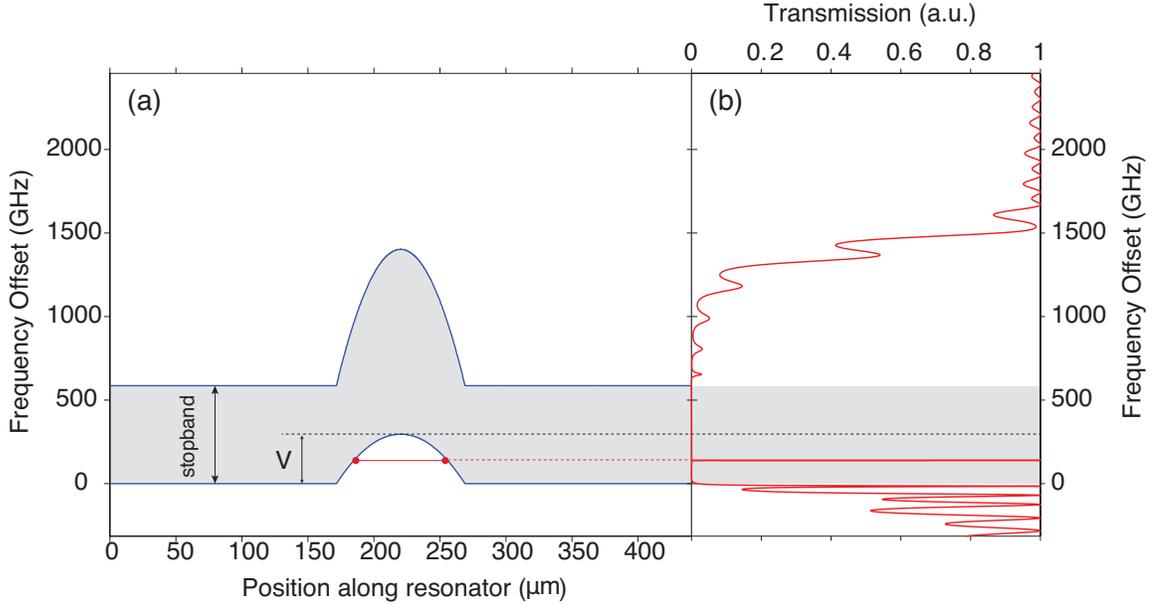
Figure 3.13. Transmission spectrum of a high-Q Si resonator plotted against its spatial band structure. (a) Spatial bandstructure. (b) Transmission spectrum. ($V = 300\,\text{GHz}$, $L_d = 100\,\mu\text{m}$, $L_y = 1.5\,\mu\text{m}$, $h = 100\,\text{nm}$, $a = 245\,\text{nm}$.)

The resonant defect-mode shows at about $120\,\text{GHz}$ into the well and is the only mode allowed in. A close-up of the transmission around the resonance, shown in figure 3.14, reveals the resonance's Lorentzian lineshape. The numerical example used in the figure is for mirror length $L_m = 200\,\mu\text{m}$ and the resonance wavelength is $\lambda_o = 1576.332\,\text{nm}$. The full width at half maximum (FWHM) corresponds to the linewidth $\Delta\lambda$, from which the quality factor of the resonance can be extracted as

$$Q_e = \frac{\lambda_o}{\Delta\lambda}. \tag{3.23}$$

Since the resonator is assumed to have no intrinsic losses, the resonance linewidth accounts exclusively for the waveguide coupling loss and the total Q is equal to the

external quality factor Q_e.

The transmission of wave components right above the high frequency band edge is suppressed, increasing progressively from zero to unity. This gradual increase spans the the frequency range of the corresponding modulation in the conduction band $f_c(x)$. While $f_v(x)$ acts as a mode localizing well in the valence band, $f_c(x)$ acts as barrier that attenuates the respective wave components over the length of the defect. As the barrier becomes thinner with increasing offset frequency, the attenuation these waves undergo decreases and their transmission across the resonator increases accordingly.
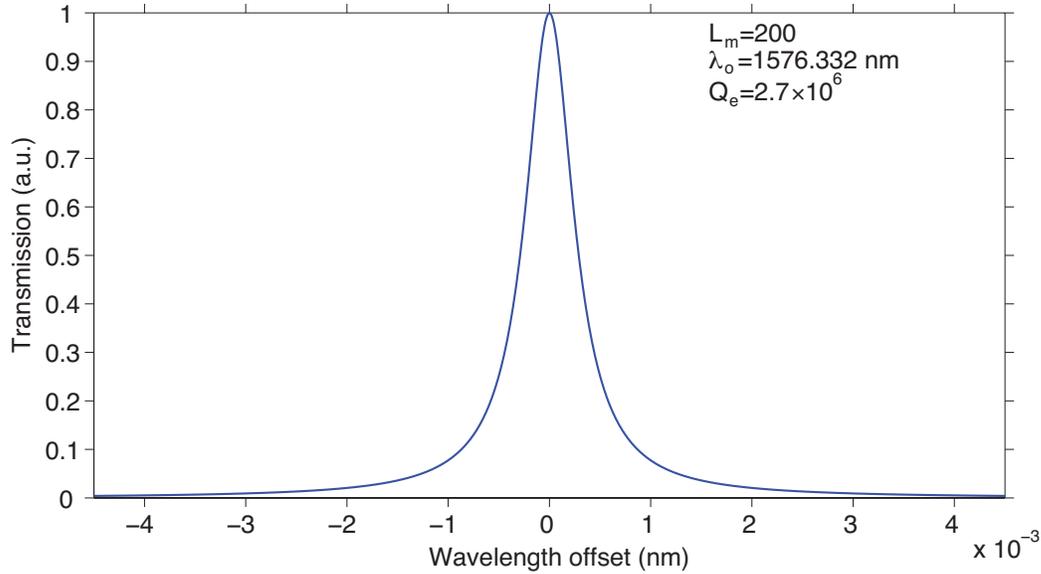
Figure 3.14. Lorentzian lineshape of the localized tranmission resonance of a high-Q Si resonator. ($V = 300\,\text{GHz}$, $L_d = 100\,\mu\text{m}$, $L_y = 1.5\,\mu\text{m}$, $h = 100\,\text{nm}$, $a = 245\,\text{nm}$.)

As already mentioned, the solution of the coupled-mode equations (3.19) also yields the distribution of the field amplitudes A, B along the resonator at any frequency f. Figure 3.15 depicts the normalized intensity distribution of the field component A at the resonant frequency f_o for the case of $V = 300\,\text{GHz}$, $L_d = 100\,\mu\text{m}$, $L_y = 1.5\,\mu\text{m}$, $h = 100\,\text{nm}$. The grey-shaded area represents the defect section. The field distribution deviates from that of a perfect Gaussian due to the finite depth of the well. The field shown in figure 3.15 is, in fact, best fit by a double Gaussian. The

field profile tends more to a single Gaussian, the deeper the resonant mode is localized from the valence band-edge. That would be satisfied for a well of substantial depth or width, except that in such case more modes would also be allowed into the well, a situation not desired for a laser cavity. Granted that a certain amount of deviation from a perfect Gaussian profile is inevitable for a single-mode defect, the potential V and defect width L_d are still chosen such that the single resonant mode is set the deepest from the band edge.
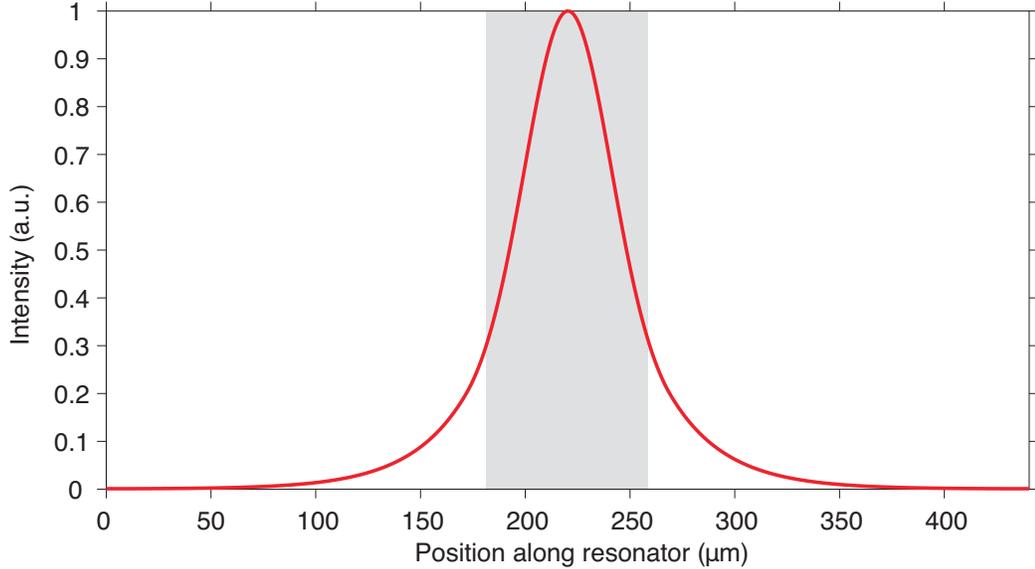
Figure 3.15. Field intensity distribution of the field of a high-Q Si resonator. ($V = 300\,\text{GHz}$, $L_d = 100\,\mu\text{m}$, $L_y = 1.5\,\mu\text{m}$, $h = 100\,\text{nm}$, $a = 245\,\text{nm}$.)

3.4   Fourier Space Engineering

The field distribution of figure 3.12 represents the slowly varying envelope of the field. If we now Fourier transform the spatially fast oscillating field amplitude, we acquire the field's Fourier component amplitudes $\tilde{E}(k_x)$ over a range of longitudinal wavevectors k_x of interest,

$$\tilde{E}(k_x) = \int \left[A(x)\exp(i\beta_o x) + B(x)exp(-i\beta_o x)\right]\exp(ik_x x)dk_x, \qquad (3.24)$$

where $\beta_o = \frac{\pi}{a}$ is the propagation constant at the Bragg frequency of the uniform mirror grating. An example of a Fourier amplitude distribution for a defect-mode on Si is given in figure 3.16 for the case of $V = 300\,\text{GHz}, L_d = 100\,\mu\text{m}, L_y = 1.5\,\mu\text{m}, h = 100\,\text{nm}, a = 245\,\text{nm}$. The two main peaks at $k_x = \pm\beta_o$ correspond to the forward and reverse propagating components of the resonant mode. The grey-shaded region represents the continuum of the Si slab radiation modes, previously defined in the dispersion diagram 3.8, which constitutes the dominant channel of loss on the specific waveguide platform. Wave components with wavevectors k_x inside the shaded region can couple to extended Si slab states and radiate energy away from the resonator. The boundary $\pm k_{rad}$ of the radiation region is set by the cutoff effective index of the continuum of the Si slab modes. The proximity of the continuum to the resonant mode's wavevectors is result of the rib waveguide's extreme aspect ratio ($h \ll H$). It is therefore imperative that the resonant mode be localized as tightly in k-space as possible, in order to minimize coupling to radiation and optimize the radiation-limited Q. This tight localization in k-space is achieved by conversely delocalizing the mode in real space, through the shallow photonic well design. In the example of figure 3.16, not only are resonant Fourier components sharply localized in k-space, at safe distance from the boundaries of the radiation continuum, but also all spatial frequency components across the continuum are highly suppressed, result of the well-behaved Gaussian-like field profile.

The Fourier analysis can be used to quantify the radiation loss by calculating Q_{rad}. In the limit of very high external quality factor Q_e (e.g., long mirrors), the integral of the intensity of the Fourier components over the radiation continuum is proportional to the energy stored in the resonator than can be potentially coupled to radiation. This result represents an approximate estimate, to the degree that the exact density of radiation states is not accounted for. The inverse of the normalized radiation integral represents an estimate of the radiation-limited quality factor Q_{rad},

$$Q_{rad} = \left[\frac{\int_{rad} \left| \tilde{E}(k_x) \right|^2 dk_x}{\int_{all} \left| \tilde{E}(k_x) \right|^2 dk_x} \right]^{-1} . \tag{3.25}$$
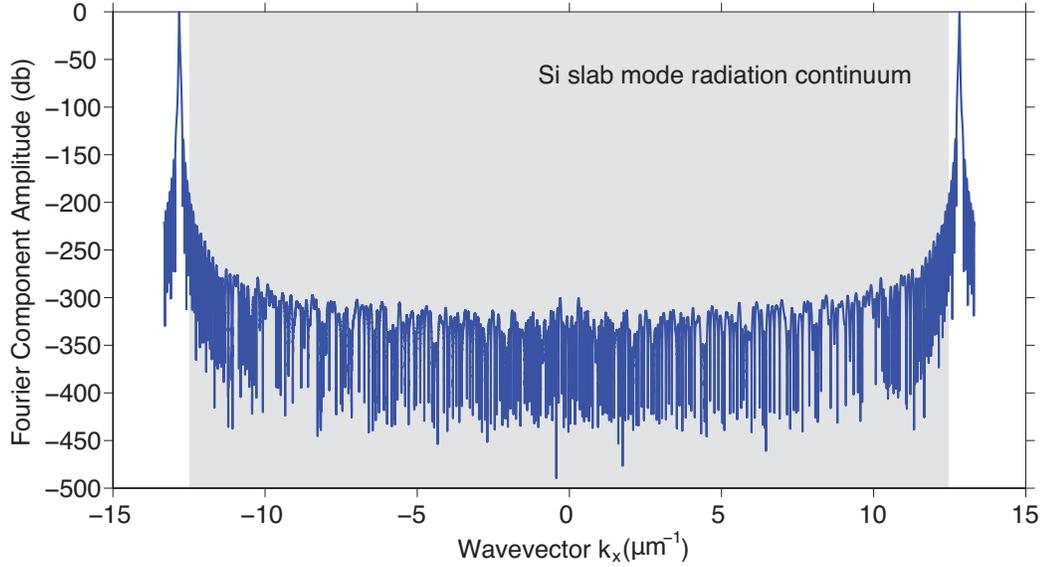
Figure 3.16. Normalized Fourier component amplitude distribution (log scale). ($V =$ 300 GHz, $L_d = 100\,\mu$m, $L_y = 1.5\,\mu$m, $h = 100$ nm, $a = 245$ nm.)

For equation (3.25) to be valid, the condition $Q_e \gg Q_{rad}$ has to be satisfied, typically $Q_e > 10^{12}$. With increasing Q_e, the fraction on the right-hand side of (3.25) converges to Q_{rad}. Engineering the resonant mode in Fourier space to tightly localize it and suppress radiation components is the primary tool employed for the optimization of the resonator's Q_{rad} [160–163].

3.5   Single-Mode Design Parameter Space

We have already underscored the importance of keeping the photonic well single-mode for use as a laser cavity. The mode capacity of the well is controlled by means of its parameters V and L_d. The design parameter set $V = 300$ GHz, $L_d = 100\,\mu$m, $L_y = 1.5\,\mu$m, $h = 100$ nm, $a = 245$ nm used in numerical examples so far, yields such a single-mode resonator. If we increase the potential depth V from 300 GHz to 450 GHz, then the well accommodates a second mode, as shown in the transmission spectrum of figure 3.17. The fundamental mode has now moved deeper into the well, at about 260 GHz from the band edge, while the second mode appears at 40 GHz. The same
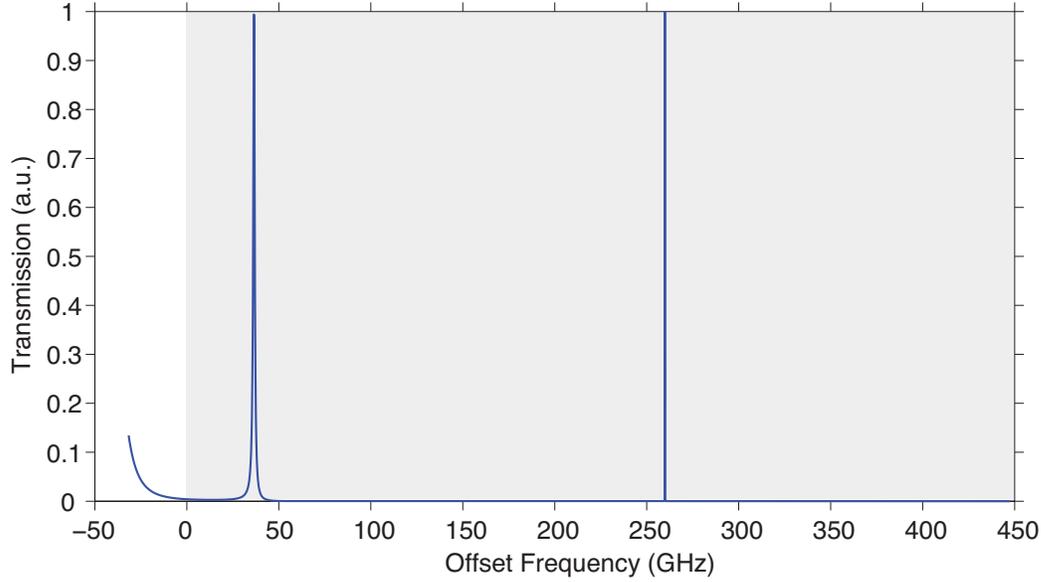
Figure 3.17. Normalized transmission spectrum of a high-Q Si resonator with a two-mode photonic well. ($V = 450\,\mathrm{GHz}$, $L_d = 100\,\mu\mathrm{m}$, $L_y = 1.5\,\mu\mathrm{m}$, $h = 100\,\mathrm{nm}$, $a = 245\,\mathrm{nm}$.)

effect to the mode capacity of the well is caused if the defect width L_d is increased instead. If the well is made either too shallow in depth or too narrow in width, then it can support no mode. We solve for the sets of $(V, L_d)_0$ and $(V, L_d)_1$ that correspond to the cutoff of the fundamental and second-order defect-mode respectively. The cutoff represents the set of (V, L_d) for which each of the two modes enters the well and is conventionally defined as the point where transmission at the valence band edge reaches unity. These cutoff sets form contours on the 2D (V, L_d) design space, denoted in figure 3.18 by red lines. The cutoff contours split the 2D space in three distinct regions, a region in the lower left corner wherein no mode fits in the well, a region in the upper right corner wherein at least two modes are accommodated and a region in between wherein only one mode is allowed in the well. The first two regions, shaded grey, are to be avoided for a single-mode laser cavity design. The middle region, shaded blue, is the region of interest and contains all the candidate design sets (V, L_d).
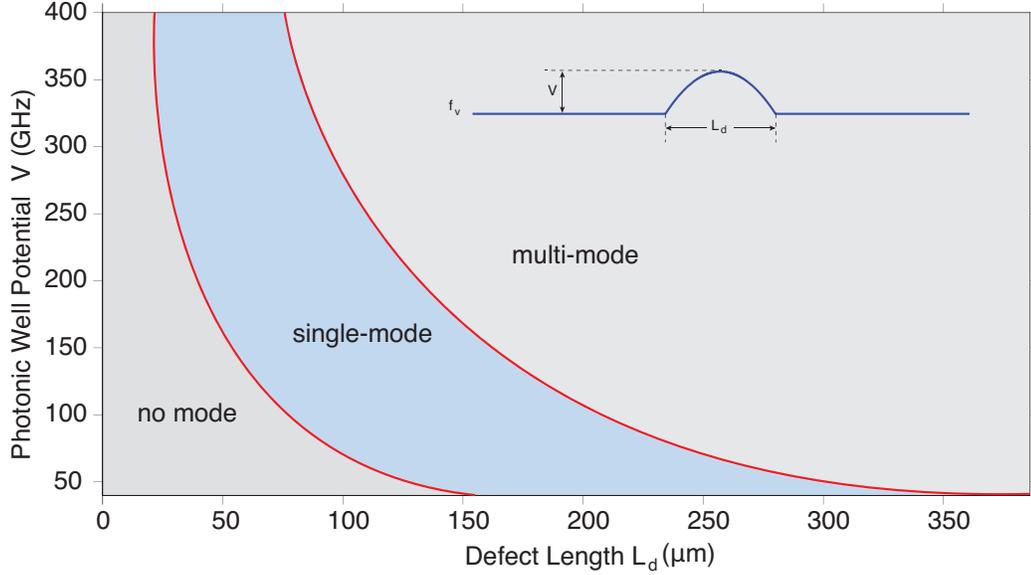
Figure 3.18. Single-mode design parameter space for a high-Q Si resonator. ($L_y = 1.5\,\mu m$, $h = 100\,nm$, $a = 245\,nm$.)

3.6 Q_{rad} Optimization Map

The single-mode design space defined in the previous section can be used as a grid to map various resonator metrics for optimization on. Here, we use it to map the radiation-limited quality factor Q_{rad}. Employing the Fourier analysis outlined in section 3.4, we calculate Q_{rad} for a number of design sets (V, L_d) in the single-mode design space of figure 3.18, with a resolution in V and L_d. The result is depicted in the form of a color map in figure 3.6 for the case of $L_y = 1.5\,\mu m$, $h = 100\,nm$, $a = 245\,nm$. The color scale corresponds to the decimal logarithm of Q_{rad}.

A trend for Q_{rad} can be readily inferred from figure 3.6. The radiation loss of the resonator decreases with decreasing V and increasing L_d. This behavior is to be expected, since shallower and wider wells feature defect-modes increasingly extended in real space, thus more confined in k-space. The longitudinal field distribution of these modes approaches more that of an infinitely extended Bloch mode of a uniform grating, which, for a waveguide with no intrinsic loss, would be rigorously lossless.

For a laser cavity, we will later on work with design sets closer to the cutoff of the
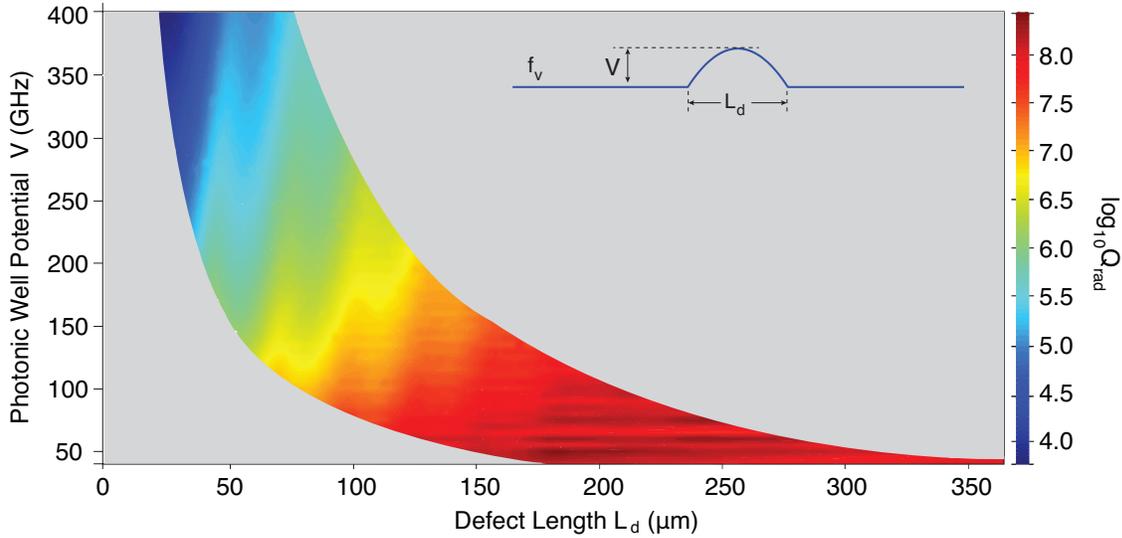
Figure 3.19. Q_{rad} optimization map. ($L_y = 1.5\,\mu m$, $h = 100\,nm$, $a = 245\,nm$.)

second-order defect-mode, as those, for a given well depth V, maximize the fraction of the mode's energy contained inside the well-behaved Gaussian-like region. This tailoring of the longitudinal mode profile not only enhances Q_{rad}, but also, as will be shown in the next chapter, has important implications with regard to laser operation.

3.7 Transverse Mode Allowance

In light of the grating design for the high-Q resonator presented in this chapter, we now reevaluate our choices for the waveguide geometry. Specifically, we reconsider the requirement for an absolutely single-transverse-mode waveguide. Allowing a second transverse to be guided would give us extra allowance in isolating the fundamental TE mode, which is to be utilized as the lasing mode, from the etched sidewalls to further reduce scattering loss.

The rib waveguide previously used in numerical examples in this chapter had a ridge width of $L_y = 1.5\,\mu m$, which yields a transversely single-mode waveguide. For $L_y = 1.5\,\mu m$ and $L_y = 2.5\,\mu m$, two and three TE transverse modes are supported by the waveguide respectively. Due to their unique spatial distribution, each mode

interacts with the grating differently. We repeat the design process followed previously for the fundamental TE_0 mode, this time for the two higher-order TE modes, TE_1 and TE_2, by building look-up tables for each one separately, thereby accounting for their unique interaction with the grating. Subsequently, for a set of $(V, L_d)_0$ that yields a single-defect-mode photonic well for TE_0, we derive the corresponding structural distribution $W_y(x)$. Once the universal $W_y(x)$ is defined, design and frequency sets $(V, L_d)_1, (f_v(x), f_c(x))_1$ and $(V, L_d)_2, (f_v(x), f_c(x))_2$ for TE_1 and TE_2 respectively are automatically also defined. Solving the 1D coupled-mode equations for each set individually, the transmission spectrum corresponding to each transverse mode is obtained. For $(V, L_d)_0 = (300\,\text{GHz}, 100\,\mu\text{m})$, the three transmission spectra are plotted in figure 3.20, with the respective transverse mode profiles superimposed as insets on top of each spectrum.
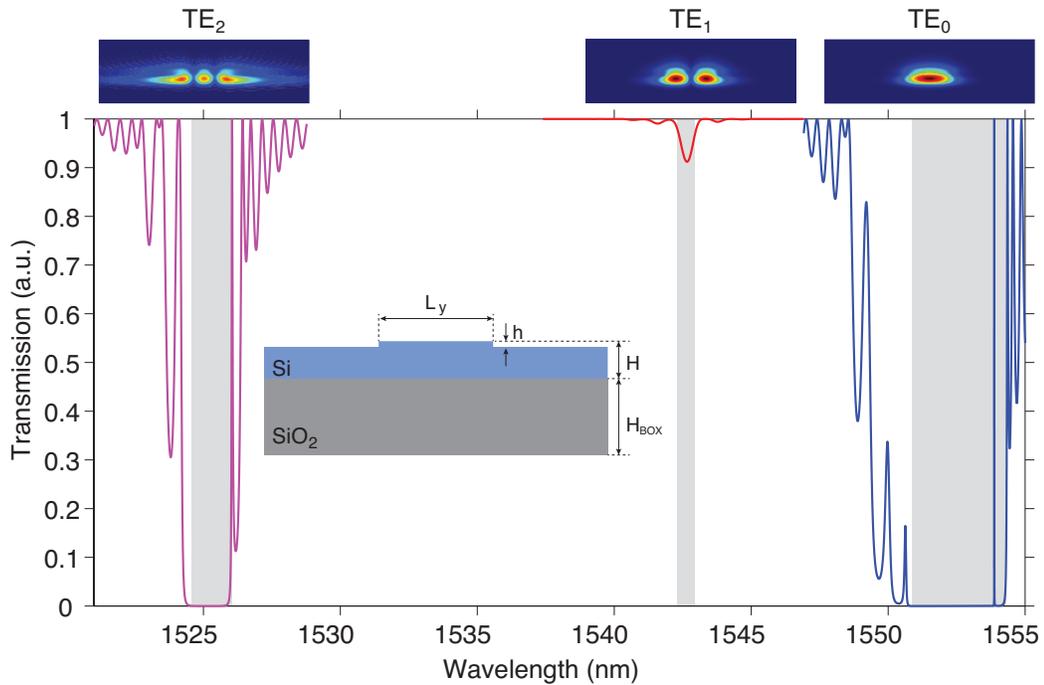
Figure 3.20. Transmission spectra of a high-Q Si resonator transverse guided modes TE_0, TE_1 and TE_2. ($V = 300\,\text{GHz}$, $L_d = 100\,\mu\text{m}$, $L_y = 2.5\,\mu\text{m}$, $h = 100\,\text{nm}$, $a = 245\,\text{nm}$.)

The fundamental TE mode interacts with the grating the strongest, therefore

experiences the largest bandgap. The familiar transmission spectrum for TE_0 that we have seen before, with a single resonant mode localized near the valence band edge, is represented in figure 3.20 by the blue line. On the contrary, due to the opposite spatial symmetry between the first odd TE mode and the grating, TE_1 sees an effectively much weaker grating. As a result, a bandgap barely opens for TE_1, manifested in a shallow dip in the transmission spectrum (red line), and thus no resonant defect-mode can be localized. Instead, for the second-order even TE mode, which possesses an antinode overlapping with the grating, an appreciable, although smaller than that for TE_0, bandgap opens and a resonant mode is starting to enter the well (magenta line). Therefore, TE_2 has to be cutoff, while TE_1 can be allowed to be guided. This result enables us to relax the restrictions on the waveguide dimensions, thus providing additional room to reduce scattering loss for the fundamental mode.

Chapter 4

Hybrid Laser Design and Modeling

In this chapter we present the design and modeling of a hybrid Si/III-V semiconductor laser, based on a high-Q hybrid Si/III-V resonator. The design of the laser cavity is primarily approached from the perspective of a passive resonator, following the methodology and analysis presented in chapter 3, while a model for the simulation of the basic laser physics in the presence of the gain and under pumping is later introduced.

4.1   Hybrid Laser Platform

The hybrid platform comprises a InGaAsP/InP-based III-V epiwafer bonded to SOI, the basic structure of which is schematically shown in figure 4.1(a). An ultralow loss grating on Si provides optical guiding and mode control, similar to the one described in chapter 3 is embedded in the SOI wafer (figure 4.1(c)).

4.1.1   III-V Epiwafer Structure

The first layer from the bottom in the epiwafer is a 10 nm n-InP bonding layer, intended to lattice match Si and InP. On top of it is a 30 nm n-InGaAsP/InP superlattice, designed to prevent lattice defects created at the bonding interface from propagating toward the quantum well region. A 110 nm n-InP cladding serves as the primary n-contact layer. The undoped active region consists of 5 quantum wells (MQW), grown to nominally emit at 1550 nm, alternately stacked with 4 barrier lay-
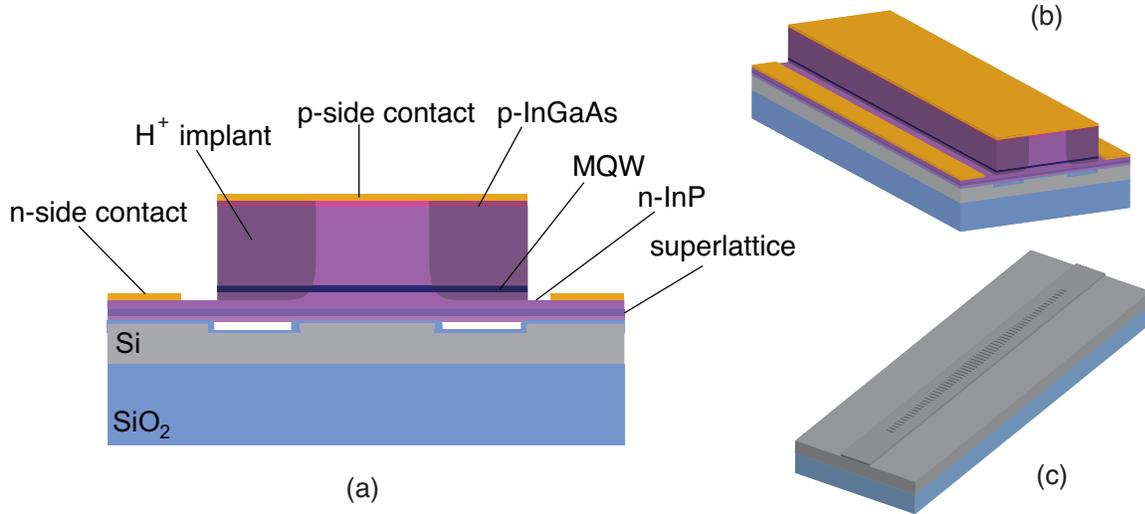
Figure 4.1. Hybrid laser device schematics: (a) Hybrid platform cross section. (b) Hybrid laser perspective view. (c) Embedded ultralow loss Si waveguide grating.

ers, comprising a total of $75\,$nm and with average refractive index of $n = 3.4476$. On either side of the MQW region is a two-step separate confinement layer (SCL), consisting of two graded energy gap, undoped InGaAsP layers of $40\,$nm thickness each and refractive indices $n = 3.33$ and $n = 3.3755$. The purpose of the SCL is to confine injected carriers in the vicinity of the MQW region, thereby enhancing their recombination rate, as well as their interaction with photons. In III-V only lasers, the SCL region is also used to enhance the confinement of photons, thanks to the relationship between energy gap and refractive index, yet, for hybrid lasers of the evanescent type, where photons predominantly reside in Si and only a fraction of light interacts with the gain medium, the role of SCL as a photon confining structure is greatly reduced. The active region is topped with a $1.5\,\mu$m p-InP cladding layer and a heavily doped, $200\,$nm p-InGaAs layer, serving as the primary p-contact. An InP buffer layer and the InP substrate are removed following wafer bonding. The p-mesa is patterned by wet chemical etching, while regions of the mesa on either side of the Si waveguide are implanted with protons (H^+) to increase their resistivity, thereby defining a confinement path for the injected carriers. Further details on the fabrication process can be found in appendix A.

4.1.2 Hybrid Waveguide

The hybrid laser designed here is an index-guided type of laser, with the guiding provided by the waveguide in Si. This is the same rib-type waveguide introduced in section 3.1. Due to the pulling of the mode up by the high index III-V, the hybrid mode overlaps with the grating more than in the Si-only case, thus making the grating effectively stronger on the hybrid platform. To maintain the grating strength at the same levels as on Si, the ridge etch depth is reduced from nominally $h = 100\,\text{nm}$ on Si to nominally $h = 50\,\text{nm}$ on hybrid.

Following the argument presented in section 3.7, the hybrid waveguide is also designed to accommodate two TE modes, the fundamental TE_0 and the first odd TE_1 mode, pictured in figure 4.2, with the latter not being resonant in the photonic well. Given the Si device layer thickness of $H = 500\,\text{nm}$, etch depth of $h = 50\,\text{nm}$ and the epiwafer structure as defined above, the two-transverse-mode criterion is satisfied with a ridge width of $L_y = 1.5\,\text{µm}$, keeping the second-order even mode TE_2 at safe distance below cutoff.

Given the above choices for the hybrid waveguide parameters, the effective index of the TE_0 mode in the unpatterned waveguide (i.e., no grating) is calculated to be $n_{eff} = 3.30$, its group velocity $n_g = 3.48$, while the cutoff effective index of TE_2 is found to be $n_c = 3.24$. It is this cutoff that sets the light line of the primary channel of loss, that is the continuum of Si slab radiation modes.

4.1.3 Confinement Factor

The overlap of the mode with the MQW region is quantified in the confinement factor

$$\Gamma_{\text{MQW}} = \frac{\iint_{\text{MQW}} |E(y,z)|^2 dydz}{\iint_{\text{all}} |E(y,z)|^2 dydz}, \tag{4.1}$$

where the two integrals are evaluated over the waveguide's cross section, for the MQW region and the entire cross section respectively. In classic laser terminology,

(a)

(b)
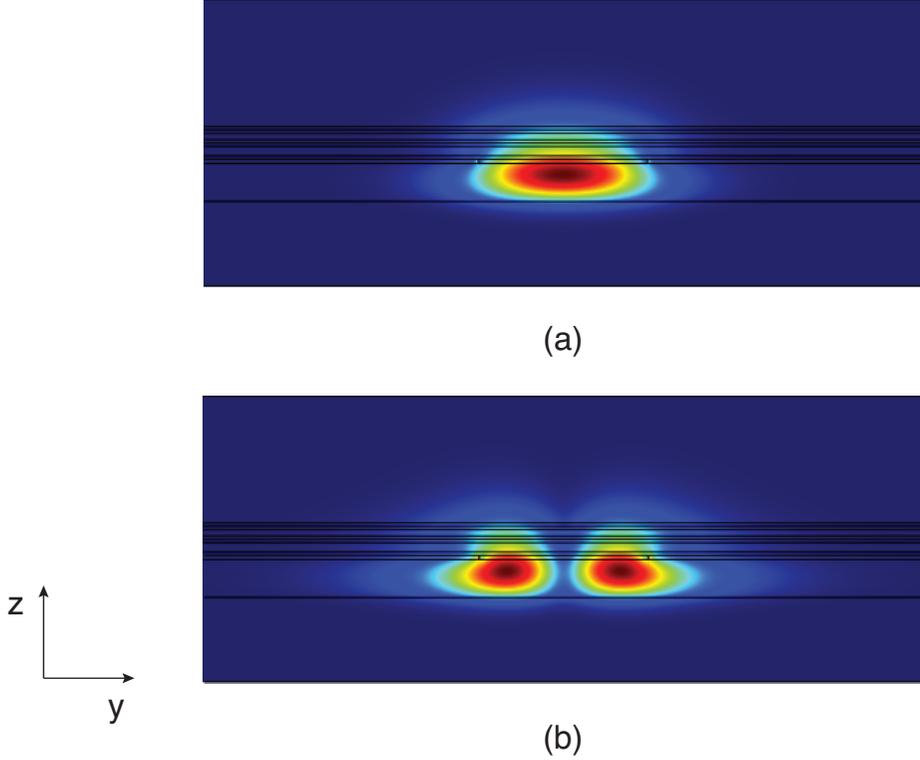
Figure 4.2. Hybrid waveguide: distribution of the norm of the electric field of (a) TE_0, (b) TE_1. ($H = 500\,\text{nm}$, $h = 50\,\text{nm}$, $L_y = 1.5\,\mu\text{m}$.)

the confinement factor enters the lasing threshold condition

$$\Gamma_{\text{MQW}} g_{\text{th}} = \alpha_i + \frac{1}{L} \ell n \left(\frac{1}{R_1 R_2} \right), \qquad (4.2)$$

where g_{th} is the material gain at threshold, α_i the laser cavity's internal loss rate in inverse length $[\text{cm}^{-1}]$, L the total cavity length and R_1, R_2 the mirror reflectivities. The internal loss can be further broken down into loss through radiation due to finite mode confinement, scattering loss due to roughness and fabrication imperfections, surface and bulk absorption, as analyzed in section 2.3. The predominant source of loss in III-V semiconductor lasers is free carrier absorption in the heavily doped contact and cladding layers of the epiwafer. The absorption rate is typically on the order of $\alpha_{\text{FCA}} = 10\,\text{cm}^{-1}$.

We seek to maximize the laser cavity's intrinsic quality factor as a means to reduce

the laser linewidth. We leverage Si platform as a low absorption optical platform, to reduce the otherwise high absorption in the III-V. For a given distribution of the hybrid waveguide mode, the total absorption rate can be expressed as:

$$\alpha_{ba} = \Gamma_{\text{III}-\text{V}}\alpha_{\text{III}-\text{V}} + \Gamma_{\text{Si}}\alpha_{\text{Si}}, \tag{4.3}$$

where Γ_{Si} is the mode's confinement in Si, defined as a fraction similar to (4.1) and α_{Si} the bulk absorption rate in Si, which is typically several orders of magnitude smaller than in III-V for high resistivity Si (e.g., $\rho > 10\,\Omega\,\text{cm}$). The absorption in III-V can be further divided into absorption in the p- and n-side of the epiwafer:

$$\alpha_{\text{III}-\text{V}} = \Gamma_n\alpha_n + \Gamma_p\alpha_p. \tag{4.4}$$

By "diluting" the mode between the III-V and Si, the effect of III-V FCA can be significantly reduced, thus enabling higher intrinsic Q than what is possible with conventional III-V-only lasers. At a first look at equation (4.2), it appears that this dilution comes at cost of increased material gain, for a given amount round-trip loss in the cavity. In fact, to the degree that the dilution of the mode into Si reduces the internal loss, through reduction in III-V absorption, the total modal gain required to overcome losses is also reduced and therefore, smaller confinements factors in III-V can be tolerated without increase of the material gain. This is especially true if the mirror losses are also kept low, as is the case for the undercoupled cavities utilized in this work. We therefore only need to retain sufficient amount of light in the III-V to overcome losses, while the majority of photons are stored in the low loss Si.

A minimum Si device layer thickness of 400 nm is needed to confine the mode in Si. On the other hand, too thick a Si layer would deplete the III-V of photons almost entirely, thus making photon generation highly inefficient. Furthermore, thicker layers require deeper etching to achieve a certain grating strength, thereby creating larger surfaces for scattering. An intermediate thickness of $H = 500$ nm is therefore chosen for the Si device layer of the SOI wafers used in this work. For the type of waveguide

defined in section 4.1.2, the calculated confinement factors are $\Gamma_{\mathrm{Si}} = 75\%, \Gamma_{\mathrm{MQW}} = 3\%, \Gamma_{\mathrm{III-V}} = 22\%$ in Si, active MQW region and III-V cladding respectively.

4.2 Hybrid Resonator Design

The design of the high-Q resonator on the hybrid platform follows the procedure outlined in chapter 3. It starts with the design of the valence band edge frequency distribution $f_v(x)$. Based on the analysis of chapter 3 and specifically the optimization of Q_{rad}, we choose an initial set of design parameters for the photonic well within the single-mode region and close to the cutoff of the second-order defect-mode, that is $(V, L_d)_{\mathrm{WD}} = (100\,\mathrm{GHz}, 200\,\mathrm{\mu m})$, as shown in figure 4.3. Along with the epiwafer parameters overviewed in section 4.1 and the hybrid waveguide parameters of section 4.1.2, this design will be referred to as the main working design parameter set. The period of the grating is fixed to nominally $a = 235\,\mathrm{nm}$, to set the operating wavelength around $1550\,\mathrm{nm}$.
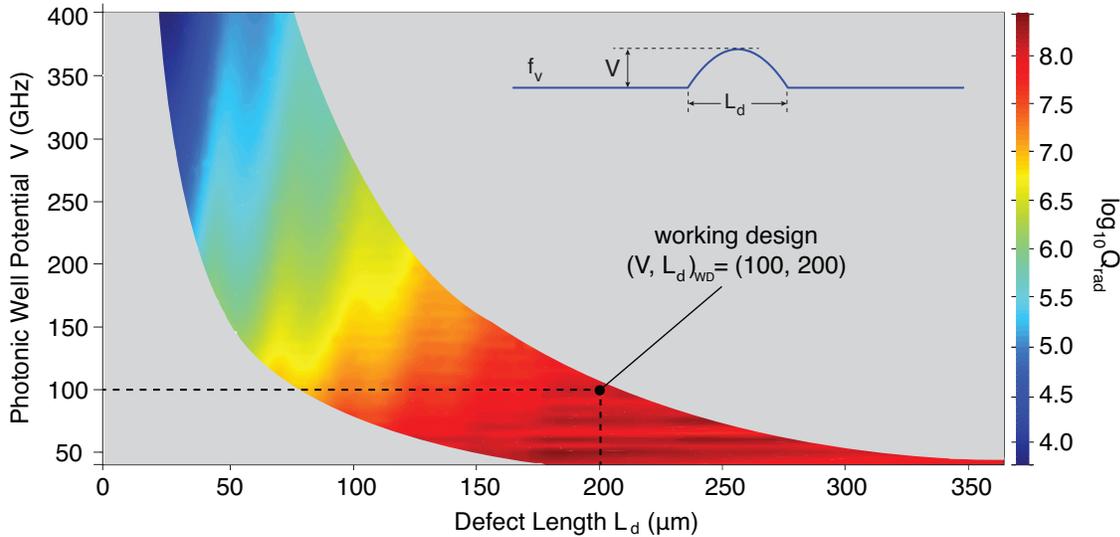
Figure 4.3. Q_{rad} optimization map for Si resonator, with working design set $(V, L_d) = (100\,\mathrm{GHz}, 200\,\mathrm{\mu m})$ marked for the hybrid resonator.

Although the map of figure 4.3 was derived for the Si-only platform, we expect

it to model the hybrid closely enough. The hybrid structure is rigorously accounted for by solving for the eigenfrequencies of the 3D hybrid unit cell and constructing the corresponding look-up table, shown in figure 4.4. The respective 3D hybrid unit cell mode distributions at the band edge frequencies f_v, f_c at the end of the first Brillouin zone are shown in figure 4.5.
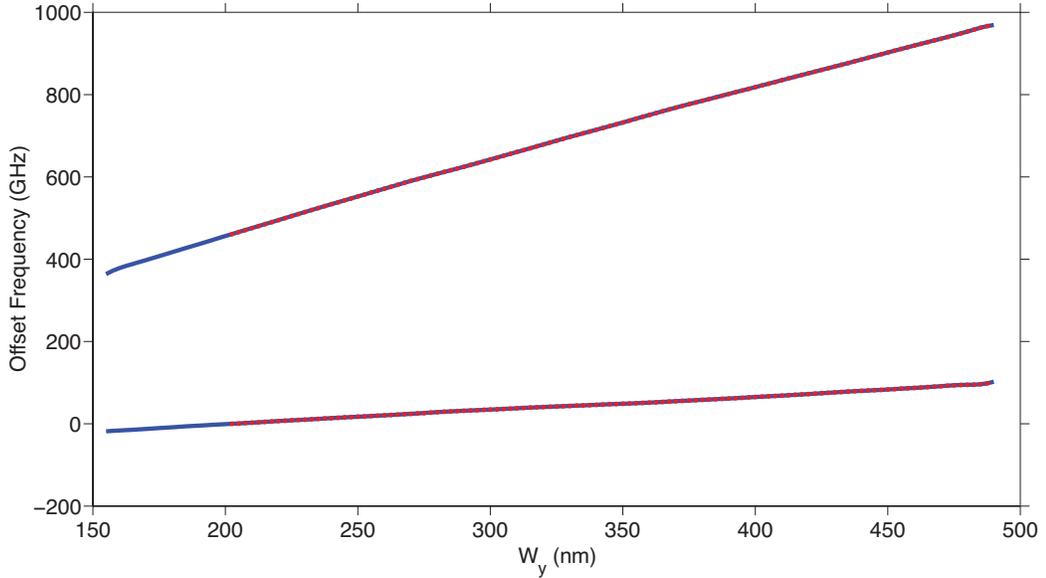
Figure 4.4. Look-up table for hybrid high-Q resonator with $V = 100\,\text{GHz}$ and $L_d = 200\,\mu\text{m}$. ($H = 500\,\text{nm}$, $h = 50\,\text{nm}$, $L_y = 1.5\,\mu\text{m}$, $a = 235\,\text{nm}$, $W_{y_{min}} = 200\,\text{nm}$, $W_x = 90\,\text{nm}$.)

The resonator's spatial band structure $f_v(x), f_c(x)$ is plotted in figure 4.6(a) for a mirror length $L_m = 320\,\mu\text{m}$. From $f_v(x), f_c(x)$, the corresponding detuning and coupling coefficient distributions in the wavelength range of interest are derived and the 1D coupled-mode equations are readily solved. It is noted that average grating strength on hybrid is similar to that on Si and more than an order of magnitude stronger than conventional DFB gratings (i.e., $10\,\text{cm}^{-1}$).

The hybrid resonator's transmission spectrum is plotted in figure 4.7. The bandgap is illustrated with the lighter grey-shaded area that spans about $568\,\text{GHz}$. The depth of the photonic well is represented with a darker grey-shaded area of width $V = 100\,\text{GHz}$. The resonant defect-mode is localized at $45\,\text{GHz}$ from the valence
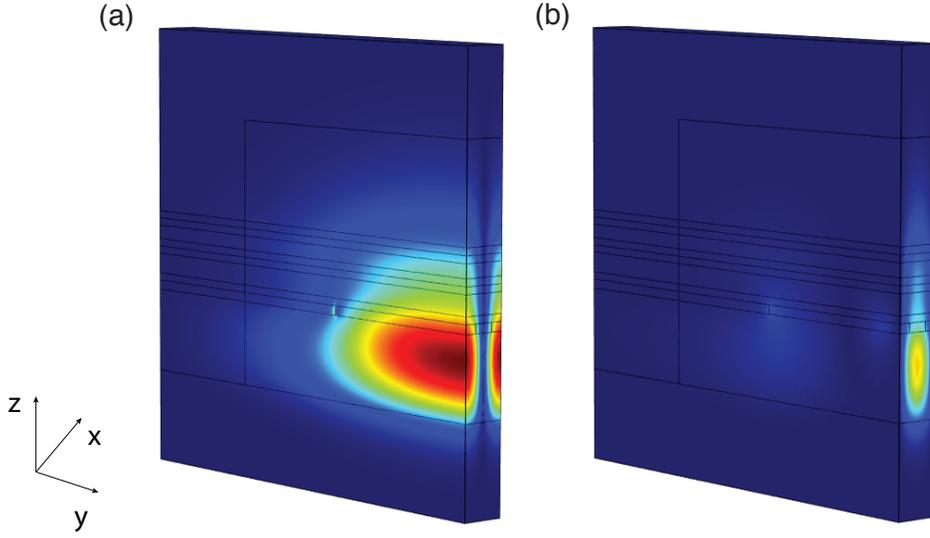
Figure 4.5. Hybrid 3D unit cell: distribution of the norm of the electric field of TE_0 at (a) f_v, (b) f_c. ($H = 500\,\text{nm}$, $h = 50\,\text{nm}$, $L_y = 1.5\,\mu\text{m}$, $a = 235\,\text{nm}$, $W_y = 250\,\text{nm}$, $W_x = 90\,\text{nm}$.)

band edge. The longitudinal field intensity profile of the resonant mode is shown in figure 4.8. The grey-shaded area corresponds to the extent of the photonic well. Due to the relative position of the design set $(V, L_d)_{\text{WD}}$ inside the single-mode space, that is near the cutoff of the second-order defect-mode, the resonant mode is primarily confined in the defect.

To estimate Q_{rad} for the resonant mode of the hybrid resonator, we Fourier transform the fast oscillating field for a mirror length $L_m = 940\,\mu\text{m}$ to ensure sufficient unloading from the waveguide. The corresponding external quality factor is $Q_e = 1.1 \times 10^{12}$. The distribution of the Fourier component amplitudes is plotted in figure 4.9. The resonant mode's wavenumber is found to be at $\beta_o = \frac{\pi}{a} = 13.37\,\mu\text{m}^{-1}$. The radiation mode continuum is illustrated by the grey-shaded area. The radiation light line is set by the cutoff effective index of the extended hybrid mode, which is
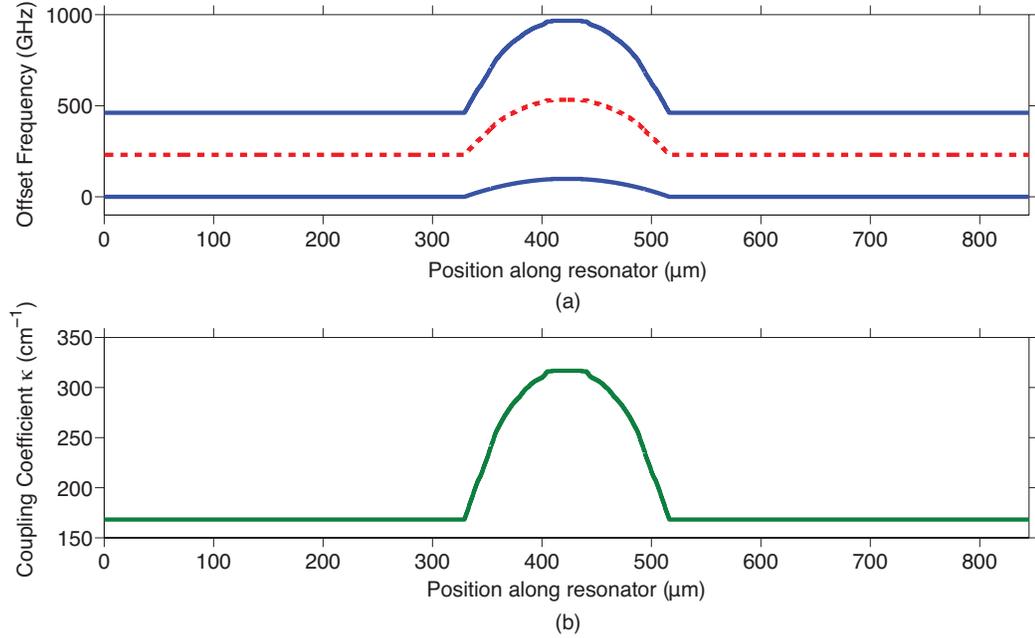
Figure 4.6. (a) Spatial band structure of a hybrid high-Q resonator with $(V, L_d) = (100\,\text{GHz},\ 200\,\mu\text{m})$, $L_m = 320\,\mu\text{m}$, $f_v(x), f_c(x)$ (blue solid lines), f_{Bragg} (red dashed line). (b) Coupling coefficient distribution $\kappa(x)$.
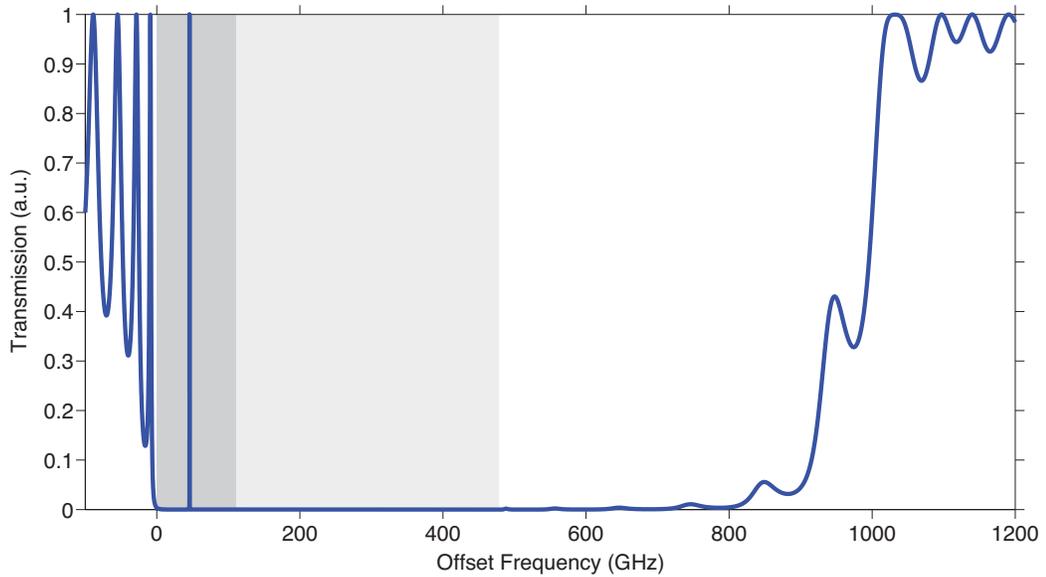
Figure 4.7. Transmission spectrum of a hybrid high-Q resonator with $(V, L_d) = (100\,\text{GHz},\ 200\,\mu\text{m})$, $L_m = 320\,\mu\text{m}$.
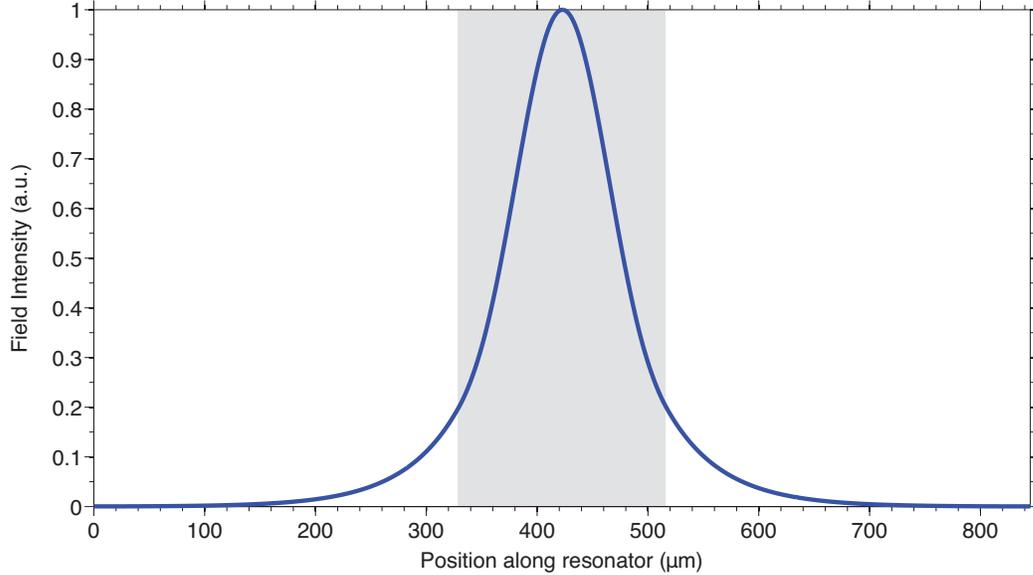
Figure 4.8. Longitudinal field intensity profile of the resonant mode of a hybrid high-Q resonator with $(V, L_d) = (100\,\mathrm{GHz}, 200\,\mu\mathrm{m})$, $L_m = 320\,\mu\mathrm{m}$.

primarily confined in the Si slab. This effective index is found to be $n_c = 3.24$ and the corresponding radiation mode cutoff wavenumber $k_{rad} = 13.13\,\mu\mathrm{m}^{-1}$. Integrating the area under the Fourier amplitude distribution across the radiation continuum and normalizing by the total area under the line yields an estimate of the resonator's radiation-limited quality factor, here calculated to be $Q_{rad} = 4.8 \times 10^7$, a value very close to the estimate based on the Si platform's Q_{rad} optimization map.

4.3   Hybrid Laser Modeling

We have so far approached the design of the hybrid laser from a largely resonator optimization perspective. The resonator platform has thus been assumed to be passive. To predict the behavior of the actual laser though, we now seek to find out how the designed high-Q resonator fares in the presence of gain. To account for the laser's fundamental physics, we will revert to a more traditional laser terminology.
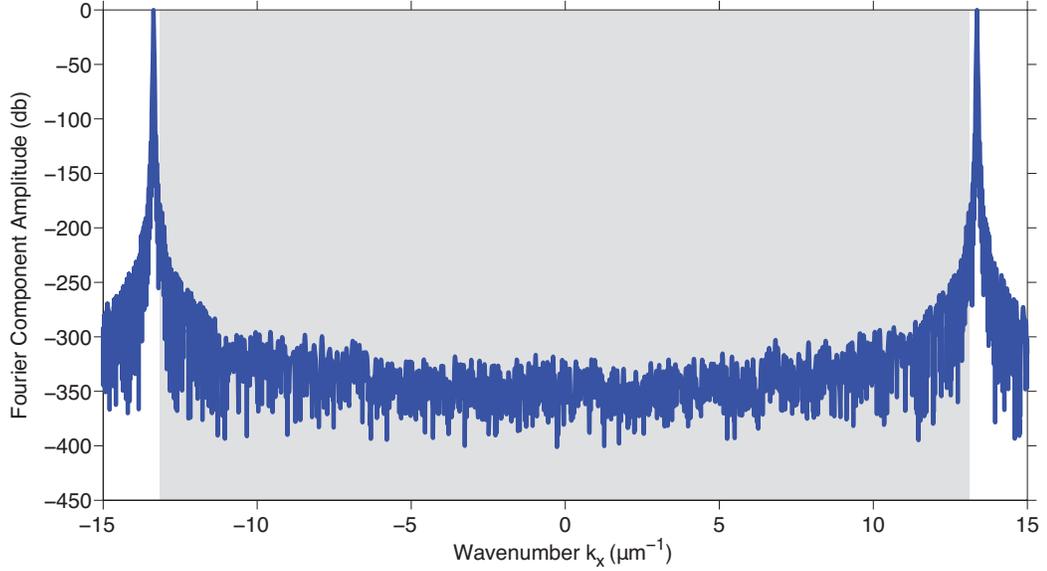
Figure 4.9. Fourier component amplitude distribution of the resonant defect-mode of a hybrid high-Q resonator with $(V, L_d) = (100\,\text{GHz}, 200\,\mu\text{m})$, $L_m = 940\,\mu\text{m}$.

4.3.1 Rate Equations

The simplest of laser modeling approaches is based on the concepts of particle and energy conservation with regard to photon/electron interaction. Accounting for absorption and emission of photons, as well as the recombination of electrons and holes, a balance between photon generation and carrier recombination has to be kept at any point in time. This is accomplished using the *photon/carrier rate equations*. For a spatially uniform density distribution of photons S occupying an optical volume $V = AL$ and interacting with an accordingly uniform density distribution of electrons N over an interacting volume $V_{int} = \Gamma V$, the rate equations are written as

$$\frac{d(VS)}{dt} = \Gamma V G_m(N)S - \frac{VS}{\tau_i} - \frac{VS}{\tau_e} + \beta_{sp}\Gamma\frac{VN}{\tau_{sp}}, \tag{4.5}$$

$$\frac{d(\Gamma V N)}{dt} = \frac{I}{e} - \Gamma V G_m(N)S - \frac{\Gamma V N}{\tau_r}, \tag{4.6}$$

where equation (4.5) describes the temporal rate of change of the number of photons in the cavity and equation (4.6) that of carriers.

The first term on the right-hand side of (4.5) gives the rate of stimulated emission

of photons, where $G_m(N)$ is the gain coefficient per unit time. The confinement factor Γ, defined in section 4.1.3 as the fraction of the optical mode in the active region, accounts for the fact that only photons in the active region contribute to stimulated emission. The second and third term account for photon loss internally (e.g., absorption, scattering, radiation) and through the finite laser mirrors respectively, with τ_i and τ_e representing the intrinsic and external photon lifetimes respectively and associated with quality factors Q_i and Q_e, as defined previously. The last term of (4.5) describes the change of the photon density due to spontaneously recombining electron-hole pairs. The coupling factor β_{sp} accounts for the fact that only specific frequencies and directions of the spontaneous emission continuum contribute to the photon density of a particular mode ($\beta_{sp} \sim 10^{-5}$).

The first term on the right-hand side of equation (4.6) describes the change of the carrier density via a constant external current injection. The second term is the counterpart of the first term in (4.5) and accounts for the loss of carriers in photon-induced recombination. The third term represents the total spontaneous carrier recombination rate, accounting for both radiative and nonradiative processes. This rate can be further broken down as

$$\frac{N}{\tau_r} = AN + B(NP) + C'(N^2P) + C''(NP^2), \tag{4.7}$$

where N, P are electron and hole densities respectively ($N \sim P$ under laser operation) and A, B, C', C'' characteristic constants. The first term in (4.7) is linearly proportional to the electron density and is usually nonradiative. The second term corresponds to bipolar radiative recombination (i.e., spontaneous emission). The third and fourth term describe nonradiative Auger recombination.

4.3.2   Field Equations

The rate equations provide a phenomenological description of the laser's basic physics, but fail to give any explicit information about the frequency of oscillation. They also do not allow for spatial nonuniformities to be accounted for, nor do they account for

the field's phase. Spatial dependencies and phase information are parameters critical for the modeling of lasers based on distributed feedback mechanisms. In such cases, a rigorous modeling of the waves' evolution in time and space is necessary, accounting for both propagation in the laser cavity and interaction with the grating.

Let's first consider a wave propagating in a uniform waveguide with gain. The electric field distribution can be expressed as

$$E(y,z) = F(x,t)u(y,z)\exp(i\omega_o t - i\beta_o x) + R(x,t)u(y,z)\exp(i\omega_o t + i\beta_o x), \quad (4.8)$$

with β_o the propagation constant at ω_o and $u(y,z)$ the mode's transverse distribution, taken to be constant over the length of the cavity for an index-guided laser. $F(x,t)$ and $R(x,t)$ represent the forward and reverse propagating, slowly varying envelope functions of the field, which can vary both in time and space under laser operation. The counterpropagating components are, for now, assumed to be uncoupled. For a small range of optical frequencies around ω_o, these slowly varying functions are modeled as wavepackets propagating at the group velocity $v_g = \frac{d\omega}{d\beta}\big|_{\omega_o}$, which is also the field's energy velocity of propagation. The wavepacket's evolution in time and space is described by an advection-type of equation as

$$\frac{\partial F}{\partial x} + \frac{1}{v_g}\frac{\partial F}{\partial t} = (\Gamma g_m - \alpha_m)F, \quad (4.9)$$

$$-\frac{\partial R}{\partial x} + \frac{1}{v_g}\frac{\partial R}{\partial t} = (\Gamma g_m - \alpha_m)R, \quad (4.10)$$

where Γg_m and a_m are the modal gain and total loss per unit length respectively. With the right-hand side of (4.9) set to zero, the wavepacket propagates with no gain or loss at the group velocity v_g.

The laser field excitation is driven by spontaneous emission, which is incorporated

into the field's evolution by means of random field amplitudes i_{spf}, i_{spr}:

$$\frac{\partial F}{\partial x} + \frac{1}{v_g}\frac{\partial F}{\partial t} = gF + i_{spf}, \tag{4.11}$$

$$-\frac{\partial R}{\partial x} + \frac{1}{v_g}\frac{\partial R}{\partial t} = gR + i_{spr}, \tag{4.12}$$

where $g = \Gamma g_m - \alpha_m$ now represents the net field gain. Spontaneous emission field amplitudes i_{spf}, i_{spr} are uncorrelated in time and space. Factored into i_{spf}, i_{spr} is the spontaneous emission coupling coefficient β_{sp} that accounts for the fraction of spontaneous emission coupled to a particular lasing mode, as well as a spontaneous emission confinement factor Γ_{sp}, similar to the gain confinement factor, that defines the fractional volume over which recombining carriers contribute to spontaneous emission.

Let us now assume that a grating of period a couples F and R. This situation was addressed before for a passive grating in chapter 3. Introducing the spatial coupled-mode formalism of chapter 3 in equations (4.11), (4.12), we have

$$\frac{\partial F}{\partial x} + \frac{1}{v_g}\frac{\partial F}{\partial t} = (g - i\delta)F + i\kappa R + i_{spf}, \tag{4.13}$$

$$-\frac{\partial R}{\partial x} + \frac{1}{v_g}\frac{\partial R}{\partial t} = (g - i\delta)R + i\kappa F + i_{spr}, \tag{4.14}$$

where δ is the detuning of the wave's propagation constant β_o at the central frequency ω_o from the grating's Bragg wavenumber and κ the grating's coupling coefficient for the particular mode. Equations (4.13), (4.14) are essentially enhanced versions of the photon rate equation (4.5). They model the photon number's change due to stimulated, spontaneous emission and internal loss, with the added information of the field's phase, the coupling through the grating and accounting for the field's spatial dependence. Hence, the advection field equations (4.13), (4.14), along with the carrier rate equation (4.6), provide the formalistic basis for the laser model.

4.3.3 Gain Saturation

The material gain per unit time G_m or unit length g_m introduced above, are functions of the electron density, usually modeled as

$$G_m(N) = G'_m(N - N_{tr}), \tag{4.15}$$

$$g_m(N) = g'_m(N - N_{tr}), \tag{4.16}$$

where G'_m, g'_m are differential gain coefficients and N_{tr} is the electron density at transparency. Higher-order fitting models (e.g., parabolic) for the gain-electron density dependence can be constructed, yet the linear model of (4.15), (4.16) is adequate for practical value ranges of the electron density.

Although we would, in principle, expect the gain to increase indefinitely with electron density, it is, in fact, experimentally observed that it starts to saturate and even decrease upon stronger pumping. This effect, known as *gain saturation*, is the result of decrease of population inversion at elevated optical intensities in the laser. As the drive current is increased, the ever increasing stimulated emission depletes the medium of carrier at regions in the cavity with high field intensity, leading to a reduction of the electron density and thereby of the gain. This process effectively limits the maximum available material gain at levels achieved with relatively low optical powers. In that range of gain values, the linear model of (4.15), (4.16) provides acceptable accuracy. Yet, equations (4.15), (4.16) have to be modified to account for saturation. This is done by introducing a gain saturation coefficient ϵ as in

$$G_m(N) = \frac{G'_m(N - N_{tr})}{1 + \epsilon S}, \tag{4.17}$$

$$g_m(N) = \frac{g'_m(N - N_{tr})}{1 + \epsilon S}, \tag{4.18}$$

with $\epsilon \sim 10^{-17}\,\mathrm{cm}^3$ representing a scale for semiconductor lasers. The product ϵS of the the gain saturation coefficient with the photon density S in $[\mathrm{cm}^{-3}]$ is dimensionless.

4.3.4 Spontaneous Emission Modeling

The optical seed for any laser-emitted light is spontaneously emitted photons due to random electron-hole recombination, funneled into a continuum of guided and radiation modes, the spectral signature of which is dictated by the active medium's gain spectrum. Spontaneous emission channeled into resonant modes of the laser cavity gets amplified, once intrinsic losses are overcome (i.e., above threshold), resulting in the set up of a coherent field in the cavity, with a well-prescribed modal distribution and frequency of oscillation. This coherent field, even well above threshold, remains subject to the ever ongoing spontaneous emission process. Under the effect of this inherently random process, the lasing field is forced into a "random walk" in the complex amplitude space.

The semiclassical approach at modeling this process starts with a coherent field of prescribed frequency and complex amplitude

$$A(t) = a \exp(j\phi) \exp(j\omega_o t) \tag{4.19}$$

where $a \exp(j\phi) = a_x + ja_y$ is the complex field amplitude. Added to this field is then a random complex field amplitude $\tilde{A}_{sp}(t)$, so that the aggregate field becomes

$$A(t) = [a \exp(j\phi) + \tilde{A}_{sp}(t)] \exp(j\omega_o t), \tag{4.20}$$

where $\tilde{A}_{sp}(t) = A_{spx}(t) + jA_{spy}(t)$ and $A_{spx}(t), A_{spy}(t)$ are random Gaussian and mutually uncorrelated field distributions. The effect of Gaussian-distributed white noise on a coherent field is simulated and illustrated in figure 4.10(a). Each red dot represents a sequential snapshot in time of the instantaneous complex field amplitude $A(t)$, relative to the steady phasor $\exp(j\omega_o t)$, with the blue vector denoting the mean of all of the events. The frequency domain representation of this process is found by Fourier transforming the time-evolved field and is pictured in figure 4.11(a). The narrow-line peak at the frequency origin corresponds to the coherent component of the field, superimposed on the white noise background. To simulate the actual physical

process, we still need to introduce a spectral noise bandwidth that emulates the finite bandwidth of spontaneous emission due to the finiteness of the gain spectrum. This is achieved numerically by filtering (e.g, Lorentzian filter) the net random field of equation (4.20), upon which the "random walk" of the coherent field in the phase plane is retrieved, as illustrated in figure 4.10(b). This is again represented in frequency domain as a coherent field peak, superimposed this time on a band-limited noise background.

4.3.5 Laser Numerical Model

The model developed here aims at revealing the unique static characteristics, spatial and spectral, of the designed hybrid laser. The results will be used to assess the performance of the resonator as an active entity and, if necessary, as feedback to the redesigning and further optimization of the resonator. Given the mathematical formulation of the field equations (4.13), (4.14) and carrier rate equation (4.6), the model is numerically implemented using a 1D finite-difference scheme in time and space [164]. The only two inputs are a constant feed of carriers, through an externally injected current I, and the field-seeding spontaneous emission, through the random field amplitudes i_{spf}, i_{spr}. The driving current is turned on at time $t = 0$ and the spontaneously generated fields are evolved in time and space, under the influence of feedback, provided by the special cavity design, ultimately reaching a steady state, at which point the static picture is revealed.

Schematically, the laser cavity is spatially sampled by splitting it up into a large number of segments, as shown in figure 4.12. Each segment has a length of $s = m * a$, where m is an integer and a the period of the grating. The modelling equations are
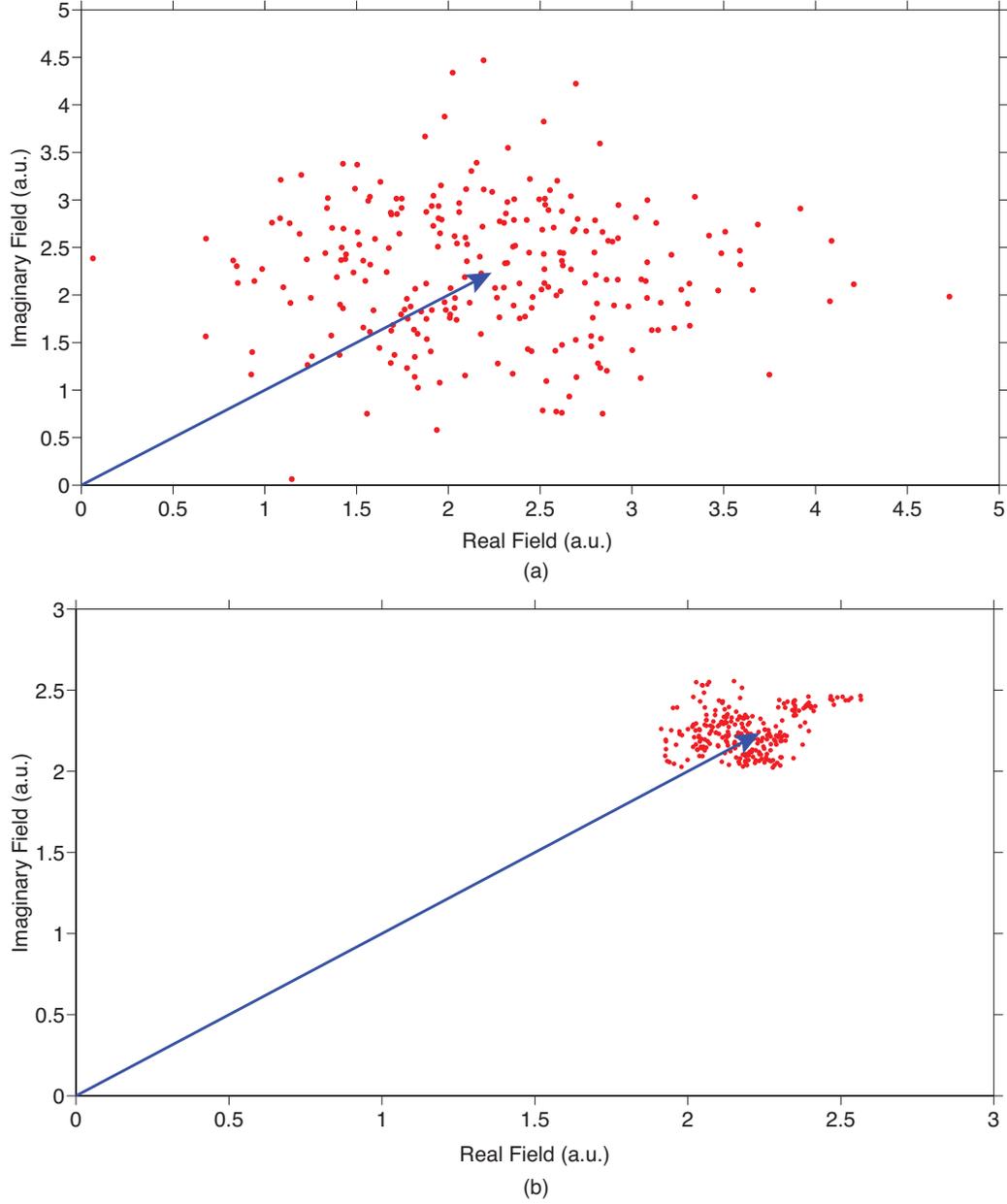
Figure 4.10. Effect of spontaneous emission noise on the complex amplitude of a coherent field: (a) Gaussian white noise. (b) Lorentzian-filtered white noise.

then written for each segment separately as

$$s\frac{\partial F}{\partial x}\bigg|_{\substack{x=x_i\\t=t_i}} + s\frac{1}{v_g}\frac{\partial F}{\partial t}\bigg|_{\substack{x=x_i\\t=t_i}} = j(\kappa s)_i R + [\Gamma(g_m s)_i - j(\delta s)_i - (\alpha s)_i]F + (si_{spf})_i, \quad (4.21)$$

$$s\frac{\partial R}{\partial x}\bigg|_{\substack{x=x_i\\t=t_i}} + s\frac{1}{v_g}\frac{\partial R}{\partial t}\bigg|_{\substack{x=x_i\\t=t_i}} = j(\kappa s)_i F + [\Gamma(g_m s)_i - j(\delta s)_i - (\alpha s)_i]R + (si_{spr})_i, \quad (4.22)$$

$$\frac{dN}{dt}\bigg|_{\substack{x=x_i\\t=t_i}} = \frac{I}{e\Gamma s\mathcal{A}L} - \frac{2g_m v_g}{\mathcal{A}}\frac{F^*F + R^*R}{v_g}\bigg|_{\substack{x=x_i\\t=t_i}} - \frac{N}{\tau_r}, \quad (4.23)$$
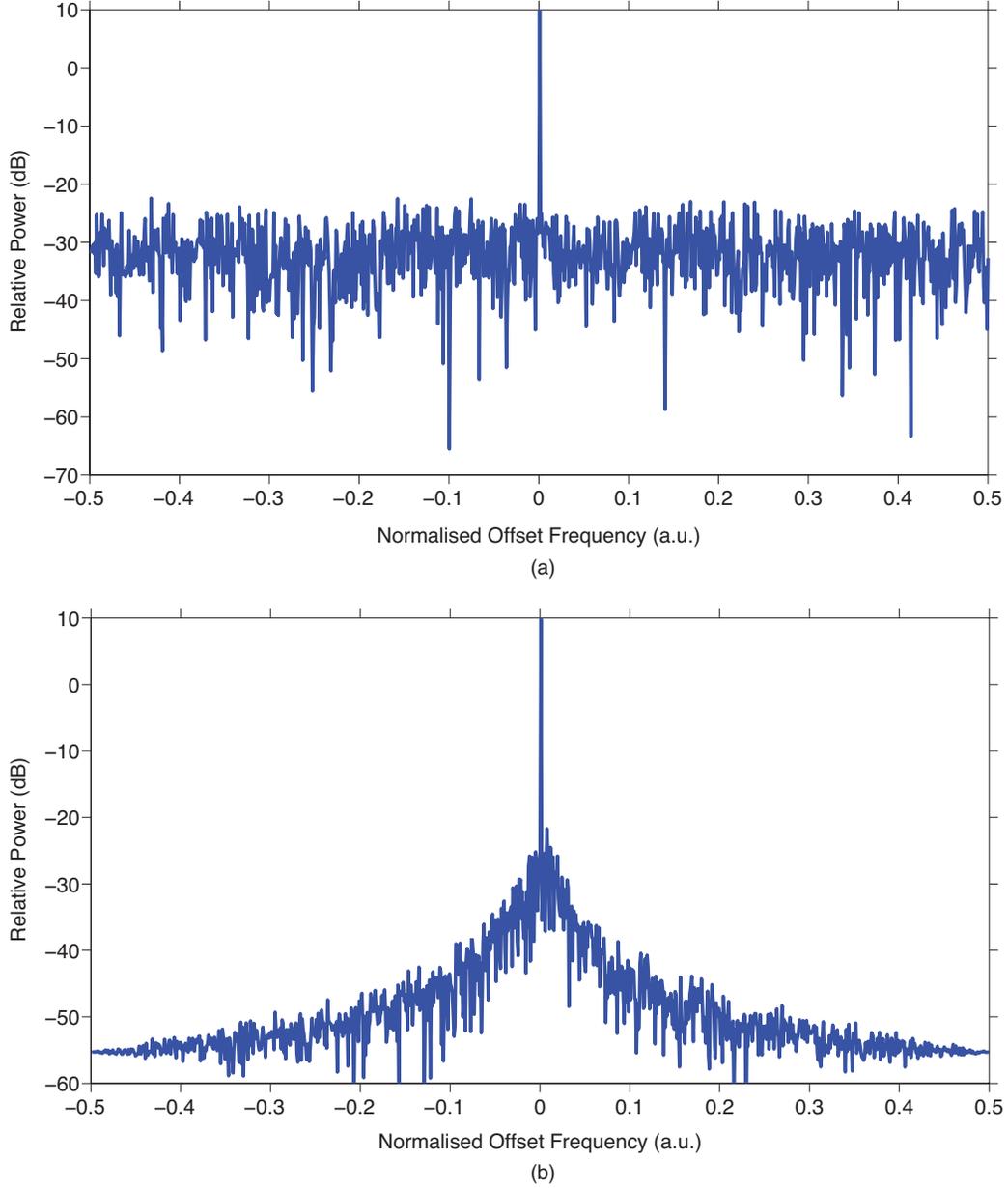
Figure 4.11. Effect of spontaneous emission noise on the frequency spectrum of a coherent field: (a) Gaussian white noise. (b) Lorentzian-filtered white noise.

where $\frac{F^*F + R^*R}{v_g}$ is the total photon density per unit length at a local position along the laser. Parameters κ, g_m, δ and α are assumed to be constant over each segment, but are allowed to vary from segment to segment. This is essential for not only capturing the spatial dependence of such parameters as the gain, but also for accounting for the spatial grating modulation. The electron density N also varies between segments
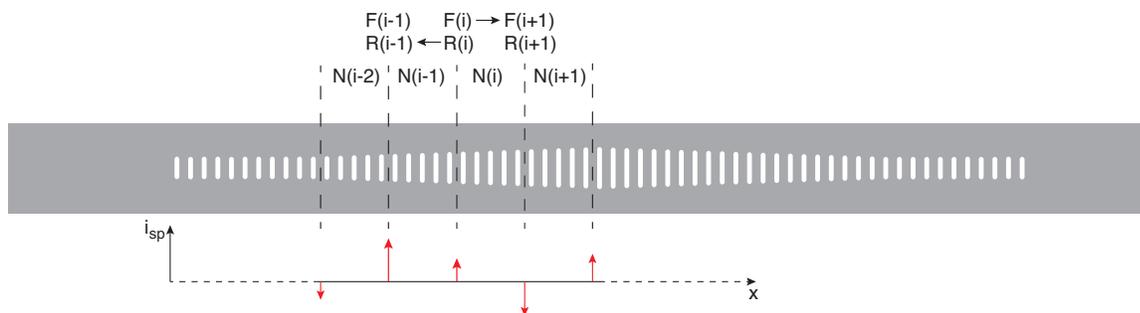
Figure 4.12. Laser numerical modeling schematic.

and is coupled to the photon density through the carrier rate equation (4.23).

For a computation in time-domain, there is no longer a well prescribed operating frequency. The detuning factor in equations (4.21), (4.22) becomes now a measure of how the central Bragg grating frequency deviates from the central gain peak. The role of δ in the model is dual. First, it allows for the modeling of a phase change $j\alpha_H \Delta g_m$, due to gain increase with electron density and the associated gain-phase coupling through Henry's factor α_H. Second, it enables to account for the change of the local grating Bragg frequency due to the grating's spatial-dependent band structure. These two effects lead to a complex material gain $s(g_m - j\delta)$ over each segment s, with δ incorporating a phase change due to gain and structural variations.

The field amplitudes F and R are evolved in time and space according to the field equations (4.21), (4.22), over a large number of time steps. Due to the relatively faster temporal variation of fields, compared to that of the electron density, a second-order central-difference scheme with the use of Lax averaging [165] is used for the discretization of (4.21), (4.22) for greater accuracy and stability, as opposed to a simple forward finite-difference scheme used for the carrier rate equation (4.23). The finite-difference discretization of (4.21), (4.22) over one sample length s can be cast in matrix form as

$$
\begin{bmatrix} F\{(T+1,(X+1)\} \\ R\{(T+1),X\} \end{bmatrix} = \exp\{(g-j\delta)s\} \begin{bmatrix} \cos\theta & j\sin\theta \\ j\sin\theta & \cos\theta \end{bmatrix} \begin{bmatrix} F\{(T,X)\} \\ R\{T,(X+1)\} \end{bmatrix},
$$

(4.24)

where T and X are integers denoting the Tth and Xth step in time and space re-

spectively, such that $t = T\frac{s}{v_g}$ and $x = Xs$. Spontaneous emission has been omitted from (4.24).

Spontaneous emission fields are added at each step (T, X) as

$$si_{spf}(T, X) = \mathcal{R}_f r_{sp} \tag{4.25}$$

for the forward field component and accordingly for the reverse one, schematically represented in figure 4.12 by red vectors. $\mathcal{R} = \mathcal{R}_{xf} + j\mathcal{R}_{yf}$ are normalized, normally distributed random numbers and r_{sp} is the spontaneous emission magnitude, proportional to the square of the product of the carrier densities NP. $\mathcal{R}_{xf}, \mathcal{R}_{yf}$ are generated separately for each point in space and refreshed for every time step, to ensure that there is no correlation between spontaneous emission fields at any two points of space and time. Given the linear dependence of r_{sp} on the electron density, we associate the spontaneous emission field injected at any point in space with the local electron density on the spatial samples on either sides of the injection point:

$$i_{spf}(T, X) \propto \frac{1}{2}[N(T, X) + N\{T, (X-1)\}], \tag{4.26}$$

where the proportionality factor is included in the explicit expression for the magnitude r_{sp}:

$$r_{sp}^2 = \frac{\lambda^2 v_g}{8\pi\epsilon_{rreff}\Delta_{sp}f}\Gamma_{sp}BNP, \tag{4.27}$$

where ϵ_{rreff} is the guided mode's effective permitivity, $\Delta_{sp}f$ the spontaneous emission bandwidth, Γ_{sp} the spontaneous emission confinement factor and B the bipolar recombination rate.

4.3.6 Lorentzian Filtering

With regard to laser modeling, there are at least two cases where the use of a Lorentzian filter can prove helpful. Shaping the gain spectrum experienced by the fields and spectral-band-limiting the spontaneous emission noise. Assuming a maximum gain value $g(\omega_o)$ at a center frequency ω_o, the frequency-domain expression of

a Lorentzian gain filter is given by

$$g(\omega) = \frac{g(\omega_o)}{\sqrt{1 + \tau^2(\omega - \omega_o)^2}}, \qquad (4.28)$$

where τ is a relaxation time constant. The Lorentzian spectral filter is expressed in time-domain through a first-order relaxation equation:

$$(1 + \tau \frac{d}{dt})S_{out} = S_{in}, \qquad (4.29)$$

where S_{in}, S_{out} are temporal input and output signals respectively. Equation (4.29) is implemented in a finite-difference scheme by use of central differences and Lax averaging as

$$S_{out}(T + 1) = \frac{K - 1}{K + 1}S_{out}(T) + \frac{1}{K + 1}(S_{in}(T + 1) + S_{in}(T)), \qquad (4.30)$$

where $K = \frac{2\tau v_g}{s}$ and $T, (T + 1)$ represent successive steps in time.

4.3.7   Laser Modeling Results

Using the model described in the previous sections, we present here simulation results of high-Q hybrid lasers. We start with the main working design $(V, L_d) = (100\,\text{GHz}, 200\,\mu\text{m})$, analyzed in its passive form in section 4.2. Figure 4.13 repeats the transmission spectrum of the passive resonator from the preceding analysis (figure 4.13(a)), contrasted against the simulated emission spectrum of the laser (figure 4.13(b)). The results of figure 4.13 are based on a resonator with total mirror length $L_m = 480\,\mu\text{m}$, corresponding to an external Q of 7×10^5. For the active simulation, the intrinsic Q of the laser cavity (i.e., internal loss) was set to $Q_i = 5 \times 10^5$, representing near critical coupling, while the driving current to $4\times$ transparency.

The grey-shaded region denotes the bandgap, as defined in the passive transmission spectrum. The reference frequency in both spectra is taken at the main resonant peak. The laser emits single-mode, with the lasing peak positioned inside the bandgap

at the expected location, based on the passive resonator spectrum, that is approximately 60 GHz from the low frequency band edge. The bandgap manifests itself in the laser emission in the form of pronounced power suppression in the spectrum, result of the strong grating coupling coefficient ($\kappa \sim 200\,\mathrm{cm}^{-1}$). The exact span of it can be discerned by satellite side mode features about the lasing peak. The dominant side mode appears, as expected, right off the high frequency edge of the bandgap. The respective side mode in the passive spectrum, as pointed out before, appears highly suppressed due to the antiresonant effect of the photonic well in the conduction band. Due to the significant attenuation undergone through the well, the blue side mode appears greatly suppressed in the emission spectrum as well, with a side mode suppression ratio (SMSR) of 43 db.

Figures 4.14(a) and 4.14(b) show the field intensity distribution in the passive and active resonator respectively. As opposed to the field in the passive resonator, which is plotted for a well-prescribed frequency (i.e., resonance frequency), the field distribution in the case of the laser represents the total field built up in the cavity, result of the broadband spontaneous emission and the resonator action. Given that the laser emits single-mode with high SMSR, this aggregate field follows the exact same Gaussian-like profile as the resonant mode in the passive resonator. The laser field is also largely contained within the resonator's defect section, indicated by the grey-shaded region. Random fluctuations superimposed on the field are due to spontaneous emission-induced amplitude fluctuations.

Figure 4.15 presents the electron density distribution for the same laser. The suppression in electron density over the cavity's center region is result of stimulated emission-induced carrier depletion over the region of high photon density, also commonly referred to as *spatial hole burning* (SHB). The carrier distribution is flat over the defect section (grey-shaded region) and remains relatively flat over a distance longer than actual physical extent of the defect, before it finally starts to rise toward the mirror ends. This surplus of carriers at the two laser ends is available to modes on the high frequency edge of the bandgap, which primarily reside in the ends of the cavity, feeding them with gain. This explains why the the mode at the high frequency
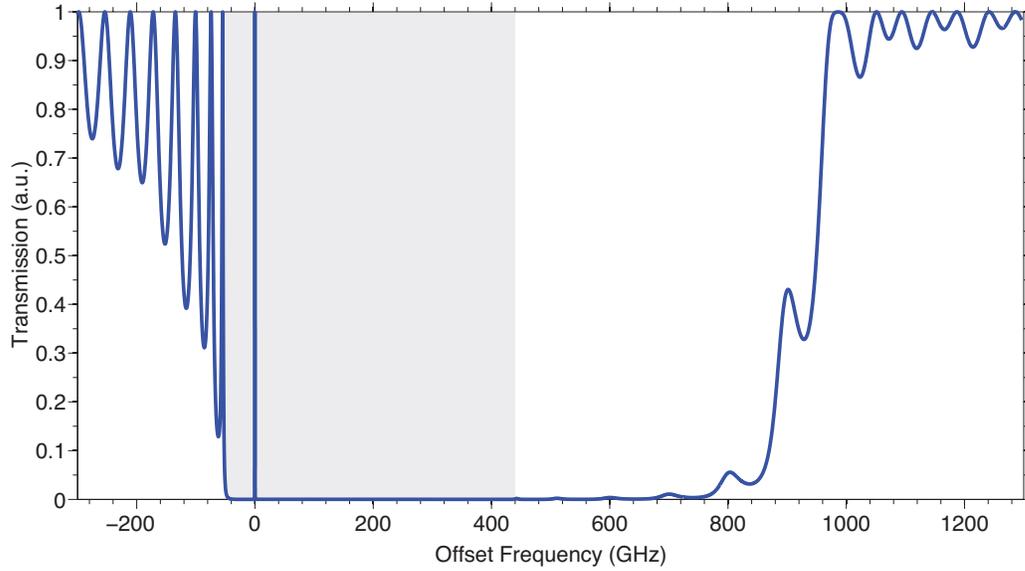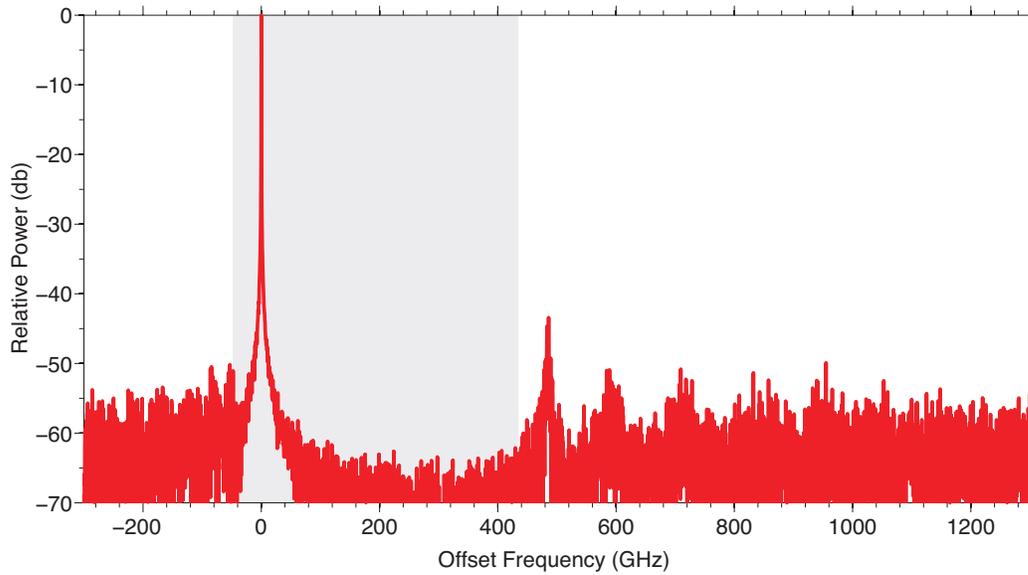
Figure 4.13. Relative frequency spectra of a high-Q hybrid resonator with $(V, L_d) = (100\,\text{GHz}, 200\,\mu\text{m})$, $L_m = 480\,\mu\text{m}$: (a) Transmission spectrum of passive resonator. (b) Emission spectrum of active resonator.

band edge appears as the dominant side mode in the lasing spectrum.

The extent of this overlap becomes increasingly favorable for the side mode as spatial hole burning grows bigger, for instance, upon increased pumping or elongation
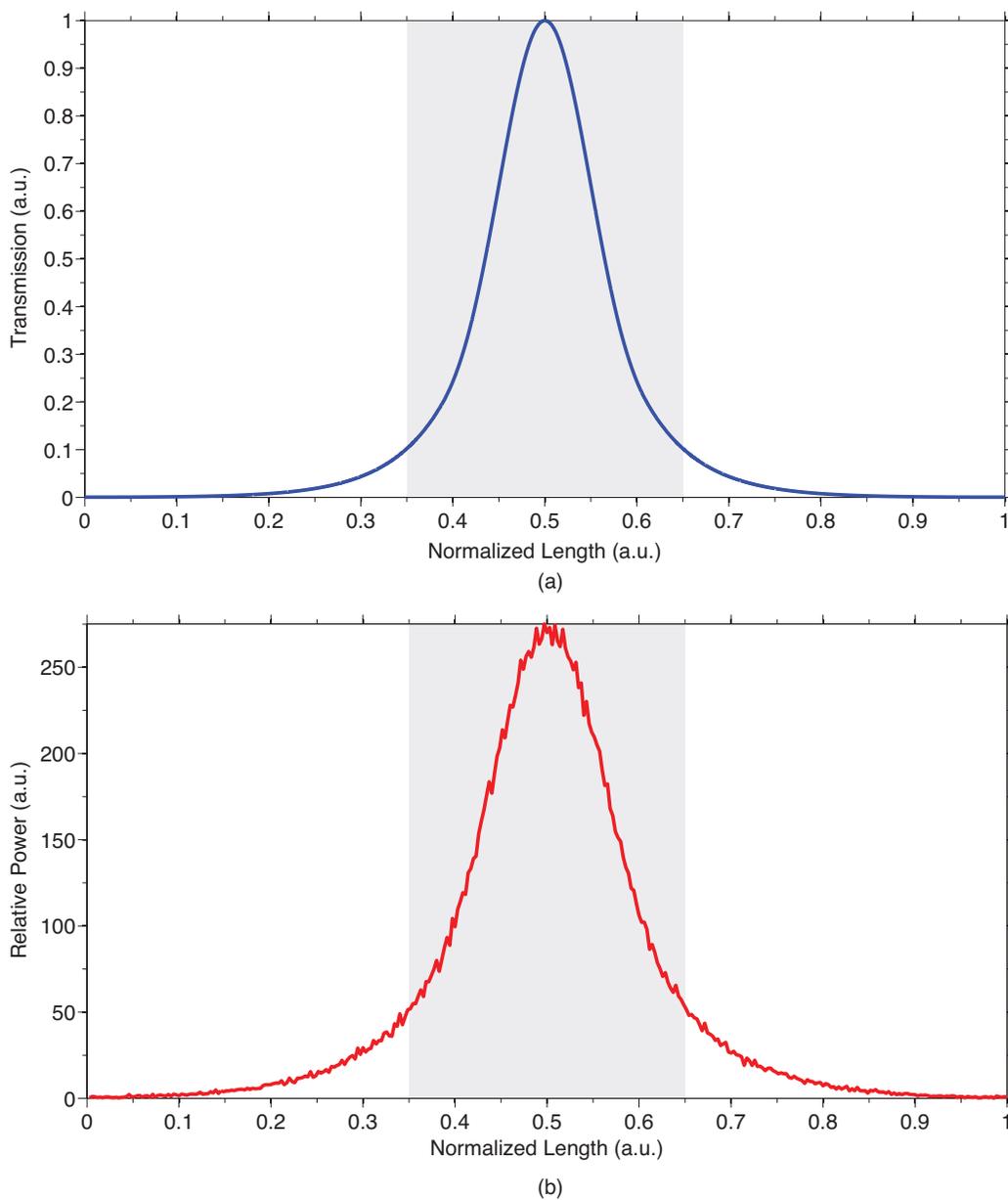
Figure 4.14. Field distribution for a high-Q hybrid resonator with $(V, L_d) = (100\,\text{GHz}, 200\,\mu\text{m})$, $L_m = 480\,\mu\text{m}$: (a) Field intensity distribution of passive resonator. (b) Photon density distribution of active resonator.

of the mirrors. In such cases, severe SHB results in mode instability [97, 166] and ultimately degradation of the laser's coherence (i.e., linewidth broadening) [91, 93]. SHB is clearly directly correlated with the field's spatial uniformity, which is why substantial efforts have been devoted in flattening the field's longitudinal profile, as
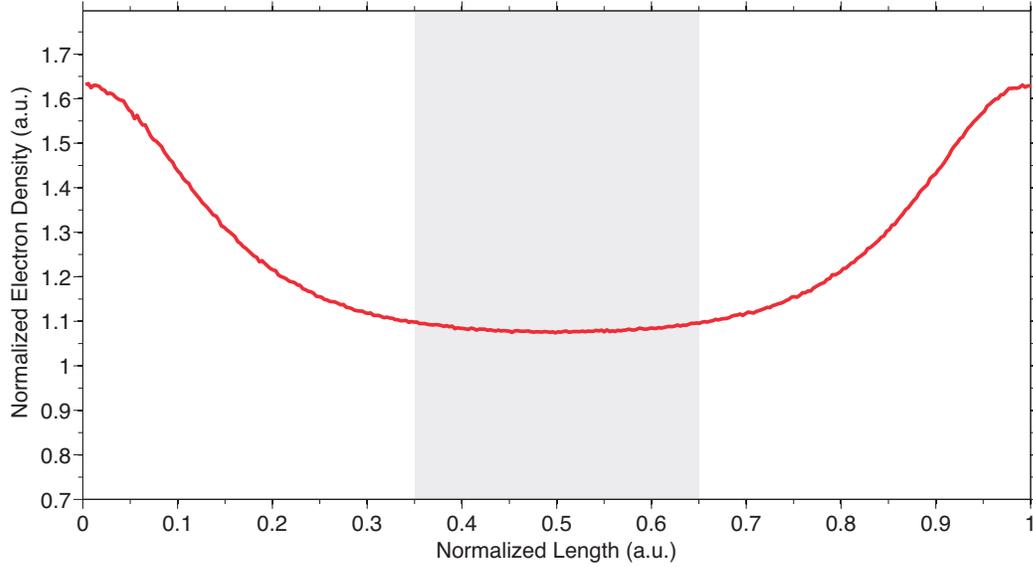
Figure 4.15. Electron density distribution for a hybrid laser with $(V, L_d) = (100\,\text{GHz},$ $200\,\mu\text{m})$, $L_m = 480\,\mu\text{m}$.

a means to enable further linewidth reduction. This has been demonstrated with the use of multiple phase-shift (i.e., coupled phase-shift) gratings [96, 98–101, 167, 168], nonuniform current injection [169] and active medium (e.g., MQW) optimization [120]. An alternative field-flattening approach, based on structural modulation of the grating [170], is conceptually similar to the photonic well design developed in this work.

Given the importance of SHB with regard to the laser's stability and coherence, we will now use the model to probe how the high-Q hybrid laser fares against SHB. First, for a given laser resonator design $((V, L_d) = (100\,\text{GHz},\ 200\,\mu\text{m}),\ L_m = 480\,\mu\text{m})$, we change the driving current over a range $2 - 12 \times I_{tr}$, where I_{tr} is the transparency current. Figures 4.16, 4.17, and 4.18 present the evolution of the emission spectrum, the photon and electron density distribution respectively, as a function of the the driving current.

The critically coupled (i.e., $Q_i \sim Q_e$) laser exhibits high mode stability, with single-mode emission and SMSRs well above 40 db throughout the entire pump range. This is despite the increasing nonuniformity in the photon density distribution and
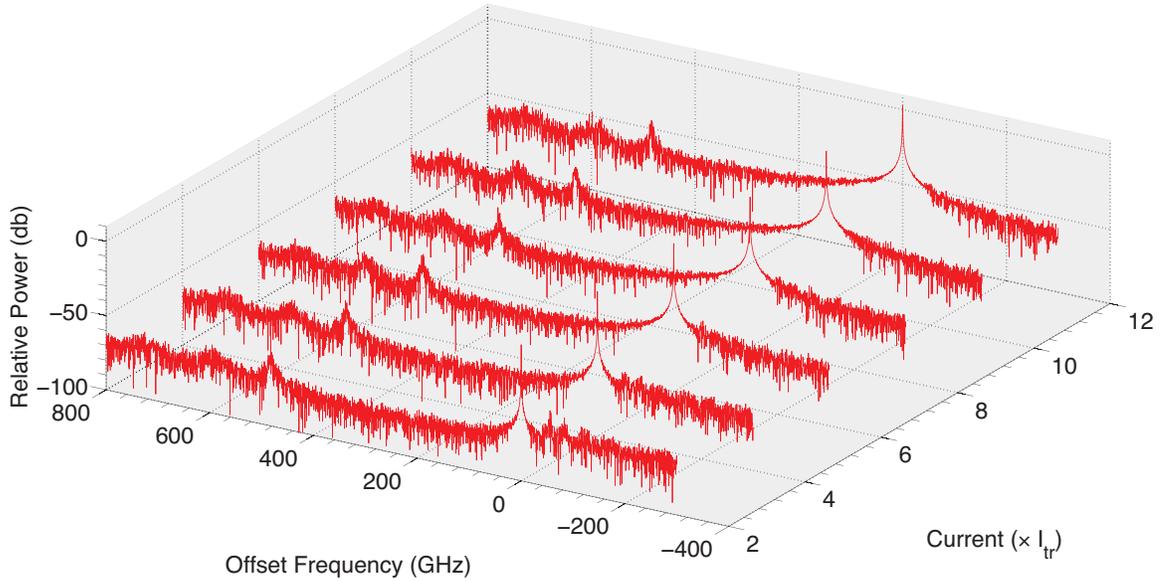
Figure 4.16. Emission spectrum as a function of the driving current for a high-Q hybrid laser with $(V, L_d) = (100\,\text{GHz}, 200\,\mu\text{m})$, $L_m = 480\,\mu\text{m}$.
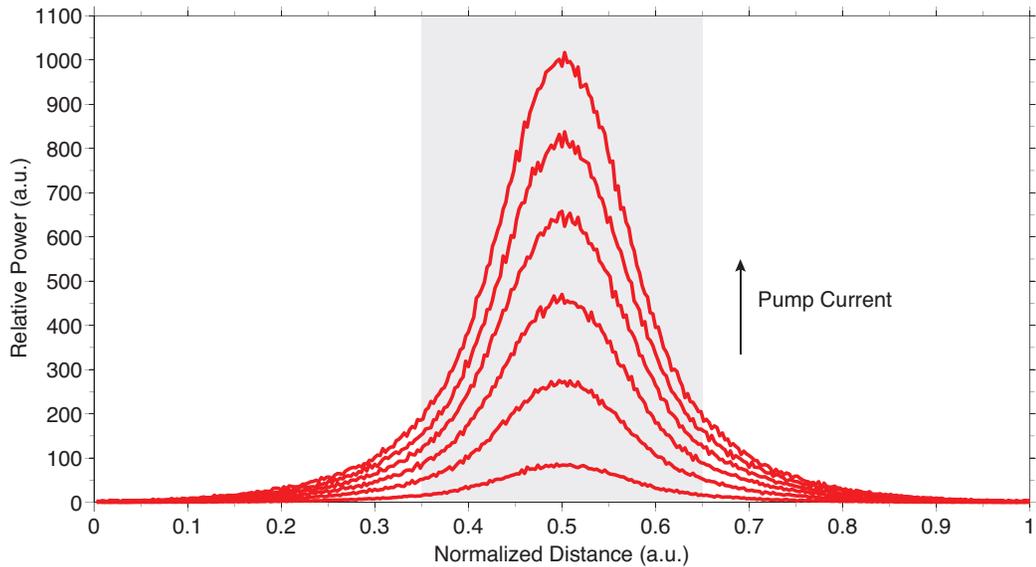
Figure 4.17. Photon density distribution as a function of the driving current for a high-Q hybrid laser with $(V, L_d) = (100\,\text{GHz}, 200\,\mu\text{m})$, $L_m = 480\,\mu\text{m}$.

the simultaneously increasing spatial-hole burning in the electron density distribution. The electron density near the mirror ends increases, but not enough to feed considerable gain to the side mode. The photon density at the center of the cav-
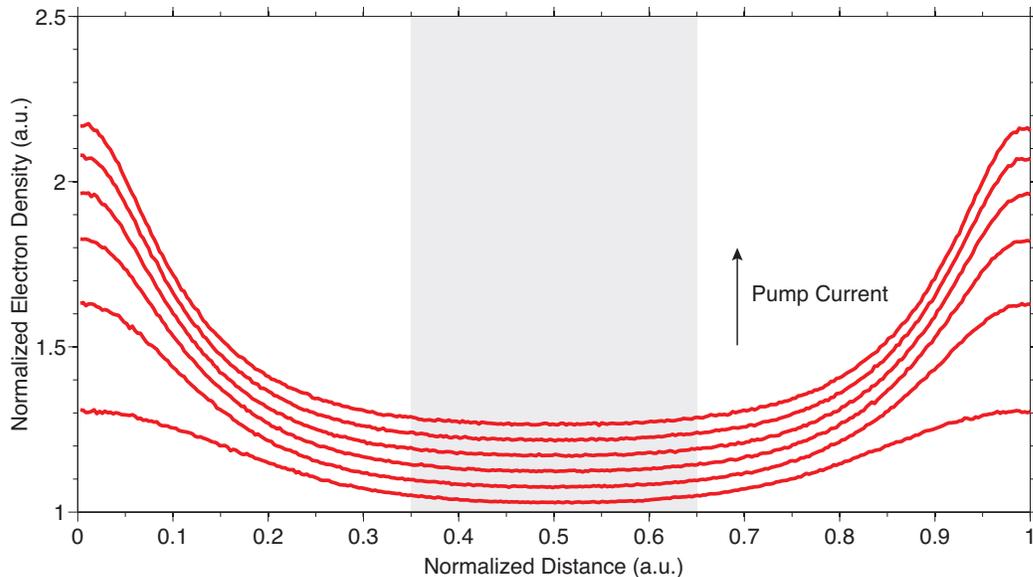
Figure 4.18. Electron density distribution as a function of the driving current for a high-Q hybrid laser with $(V, L_d) = (100\,\text{GHz}, 200\,\mu\text{m})$, $L_m = 480\,\mu\text{m}$.

ity increases linearly with the current, as a result of the fundamental lasing mode experiencing minimal competition from the side mode. The critically coupled laser therefore is quite robust against against strong pumping. For maximum linewidth reduction, we wish to utilize the maximum possible fraction of the available intrinsic Q and the way to do that is by undercoupling the resonator. We now check how the laser's stability holds up against resonator undercoupling.

Figures 4.19, 4.20, and 4.21 present the evolution of the emission spectrum, the photon and electron density respectively, as a function of the total mirror length L_m, where $L_m = 480$–$670\,\mu\text{m}$ in increments of $50\,\mu\text{m}$. The respective external Qs are 7.3×10^5, 1.2×10^6, 1.9×10^6, 3.0×10^6, and 4.8×10^6. The SMSR is over $40\,\text{db}$ for $L_m = 480\,\mu\text{m}$ and $530\,\mu\text{m}$, drops to $30\,\text{db}$ for $L_m = 580\,\mu\text{m}$, before it starts to degrade rapidly thereafter. For $L_m = 630\,\mu\text{m}$ the SMSR has dropped at $15\,\text{db}$, while for $L_m = 680\,\mu\text{m}$, the two modes lase with equal power. With regard to the photon distribution, the photon density at the center of the cavity progressively saturates with the mirror length, as the main contributor to that density, the fundamental lasing mode, experiences increasing competition from the side mode. In turn, the side mode
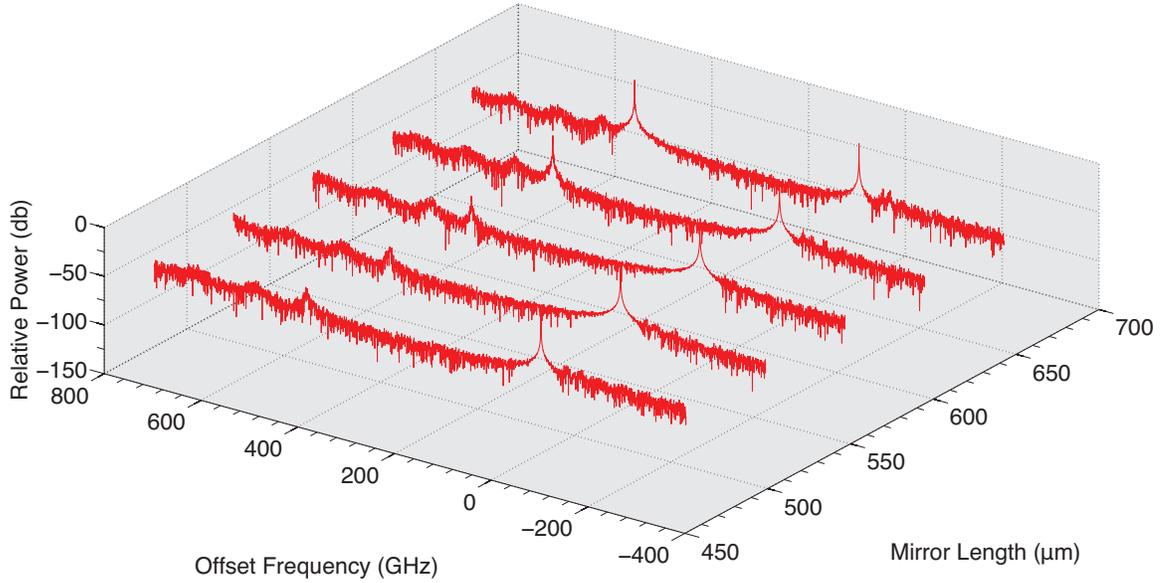
Figure 4.19. Emission spectrum as a function of the mirror length for a high-Q hybrid laser with $(V, L_d) = (100\,\text{GHz}, 200\,\mu\text{m})$, at driving current $I = 4 \times I_{tr}$.
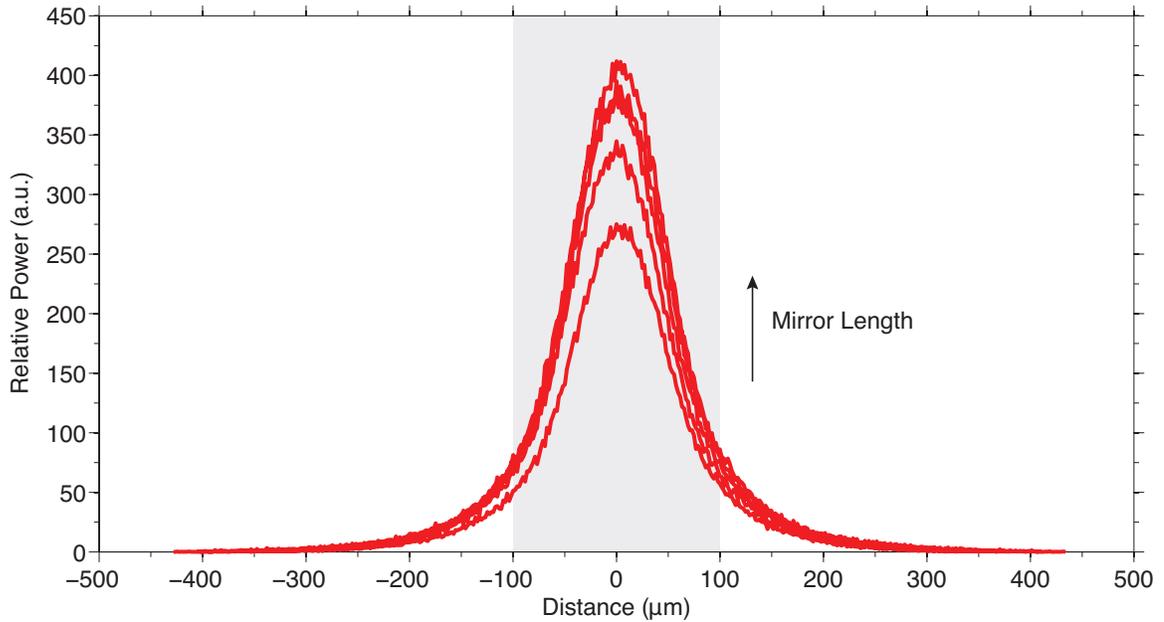
Figure 4.20. Photon density distribution as a function of the mirror length for a high-Q hybrid laser with $(V, L_d) = (100\,\text{GHz}, 200\,\mu\text{m})$, at driving current $I = 4 \times I_{tr}$.

receives increasing gain with the elongation of the mirror sections. Undercoupling on the order of $Q_e = 2 \times Q_i$ provides adequate protection against SHB. The final choice,
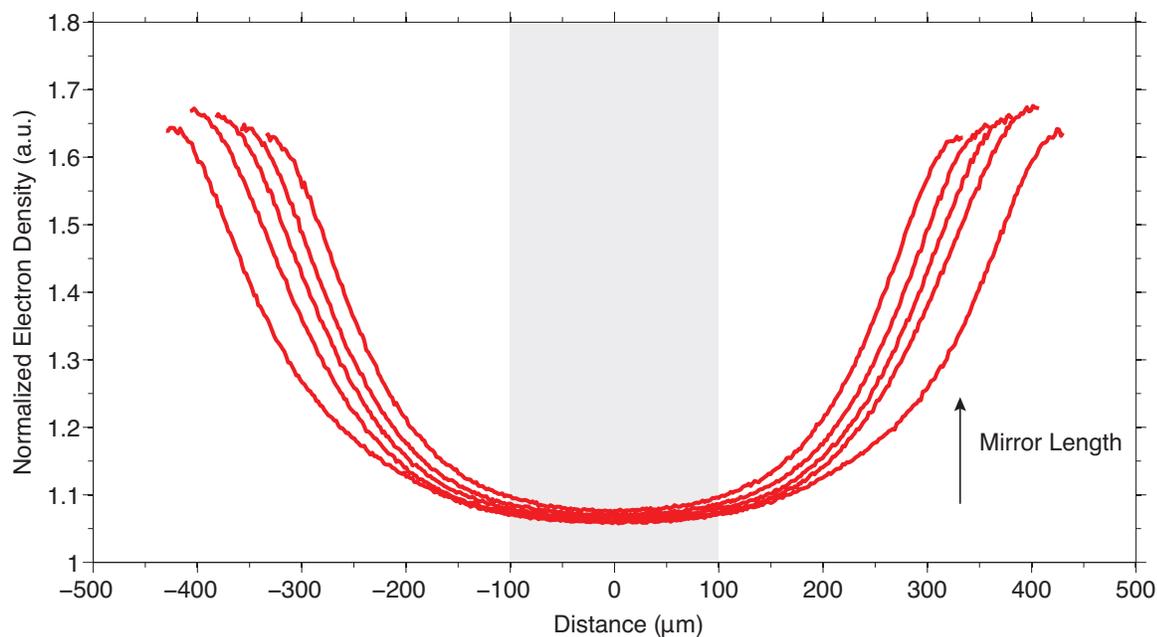
Figure 4.21. Electron density distribution as a function of the mirror length for a high-Q hybrid laser with $(V, L_d) = (100\,\text{GHz}, 200\,\mu\text{m})$, at driving current $I = 4 \times I_{tr}$.

of course, also depends on the desired level of output power. For strictly linewidth reduction purposes, maximum undercoupling is desired. The above analysis was based on the assumption of a laser resonator with intrinsic $Q_i = 5 \times 10^5$, but the derived rule of the thumb for the choice of the degree of undercoupling holds for any choice of the intrinsic Q.

Upon further elongation of the mirrors, the laser enters a regime of severe SHB, the effects of which are illustrated in figures 4.22, 4.23, and 4.24. The blue side mode takes over as the main lasing mode, while the red side mode on the low frequency band edge starts to grow now, eventually to rise on par with the blue. The photon density at the middle of the cavity starts to grow again, this time under the contribution from the red mode. The blue mode itself contributes pedestals in the wings of the photon density distribution.
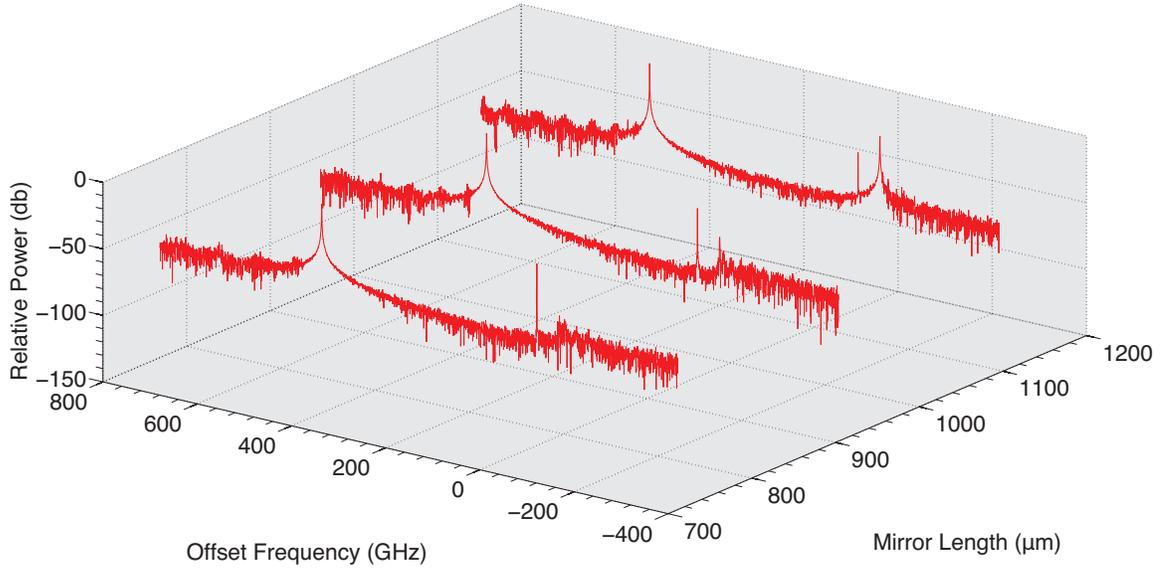
Figure 4.22. Emission spectrum as a function of the mirror length, under the effect of extreme SHB, for a high-Q hybrid laser with $(V, L_d) = (100\,\text{GHz}, 200\,\mu\text{m})$, at driving current $I = 4 \times I_{tr}$.
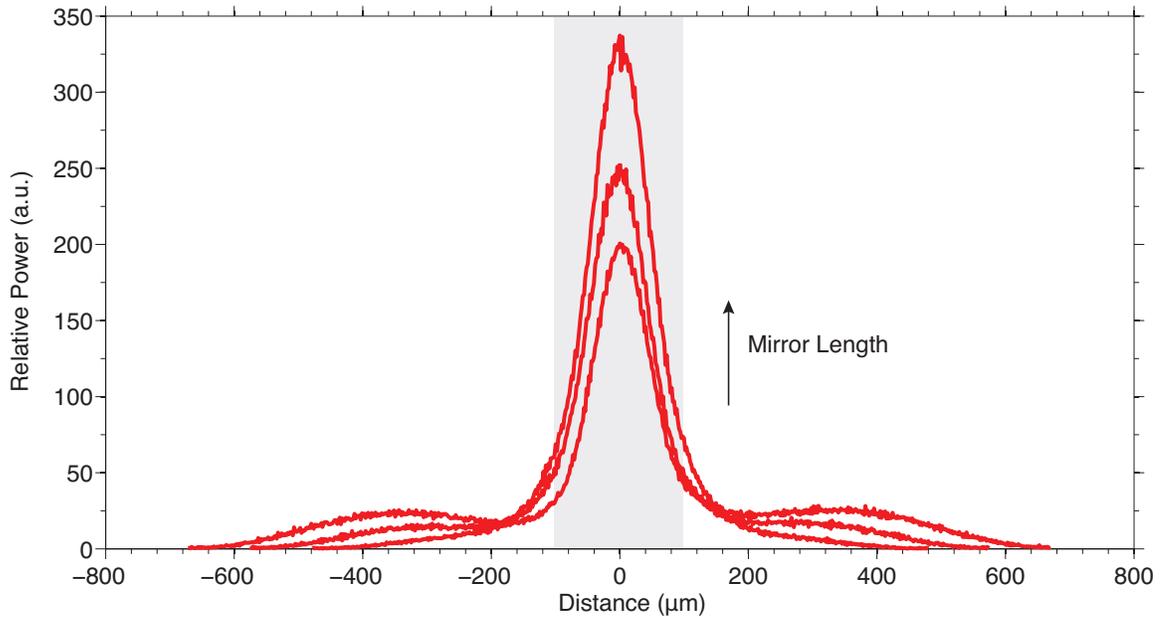
Figure 4.23. Photon density distribution as a function of the mirror length, under the effect of extreme SHB, for a high-Q hybrid laser with $(V, L_d) = (100\,\text{GHz}, 200\,\mu\text{m})$, at driving current $I = 4 \times I_{tr}$.
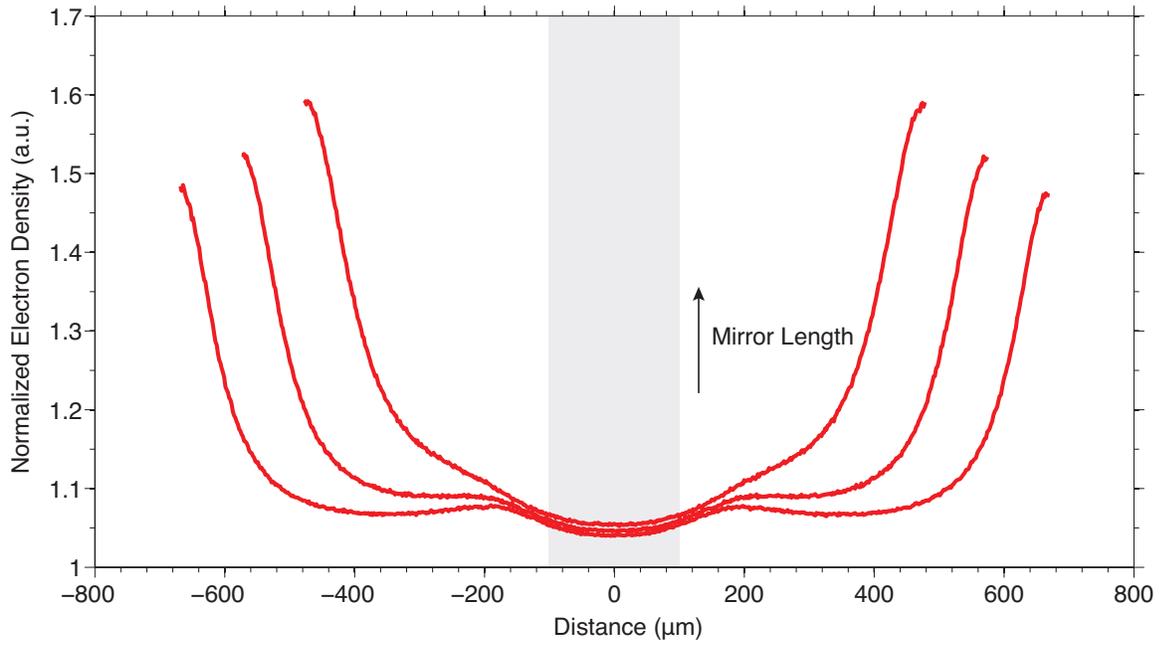
Figure 4.24. Electron density distribution as a function of the mirror length, under the effect of extreme SHB, for a high-Q hybrid laser with $(V, L_d) = (100\,\text{GHz},\ 200\,\text{µm})$, at driving current $I = 4 \times I_{tr}$.

Chapter 5

Experimental Results

In this chapter, we will present results of fabricated devices, passive Si resonators and hybrid Si/III-V lasers. In the timeline of the project, passive resonators on Si were developed first, to validate the grating design and analysis methodology. The quality of passive resonators was assessed directly by measuring their loaded quality factors, without the complication of the absorbing III-V medium of the hybrid structure. In this first part of the project, important parameters of the fabrication process were also tuned. Resonator design parameters were experimentally evaluated, serving as useful input for the design and fabrication of the hybrid laser resonators. Here, we will briefly present representative results of Si resonators before we move on to the experimental characterization of hybrid lasers. Details on the fabrication process of both resonators and lasers can be found in appendix A.

5.1 High-Q Si Resonators

Passive resonators were fabricated on the SOI platform, previously described in chapter 3, and repeated here for reference in figure 5.1. The Si device layer has a thickness of $H = 500\,\mathrm{nm}$, while that of the buried oxide is $H_\mathrm{BOX} = 1.0\,\mu\mathrm{m}$. Rib waveguides were patterned on Si, with typical ridge widths of $L_y = 1.0\text{--}2.5\,\mu\mathrm{m}$ and etch depths of $h = 50\text{--}100\,\mathrm{nm}$.

To couple light into and out of the waveguides, grating couplers were designed and fabricated on each waveguide end, as shown in figure 5.2. The coupling grating was

uniform with nominal period of 600 nm, designed to couple to free space beams at an angle of 30° and center wavelength around 1575 nm. The experimentally observed 3 db coupling efficiency bandwidth was 20–30 nm. The coupler pads were 10 µm wide and connected to the main waveguide via "slow" tapers approximately 250 µm long, to suppress the excitation of higher-order transverse modes.
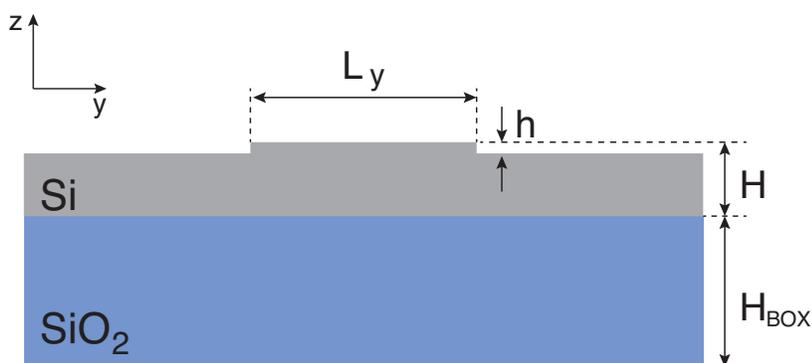
Figure 5.1. Schematic cross section of the SOI waveguide platform.

Figure 5.2. Top view schematic of a high-Q Si resonator with grating couplers.

Figure 5.3 shows different views of a fabricated high-Q Si resonator, taken with a scanning electron microscope (SEM). Due to the sheer scale of the structure, a single frame image of the full structure could not be obtained. Instead, different sections of the grating (e.g., mirror, defect) are shown. Besides, the modulation of the grating in true scale is so slow, that is difficult to discern in any snapshot. Resonator lengths varied from approximately 500 µm to slightly over 1 mm, using the length of the mirrors to tune the external loading (Q_e).

Passive resonators were characterized by measuring their frequency response in transmission mode. An incoming wave of varying frequency is coupled via the grating couplers to the waveguide's fundamental guided mode and transmitted through the resonator. The transmitted light, coupled out through the second coupler, is collected at a photodetector and its intensity is plotted as a function of frequency (or
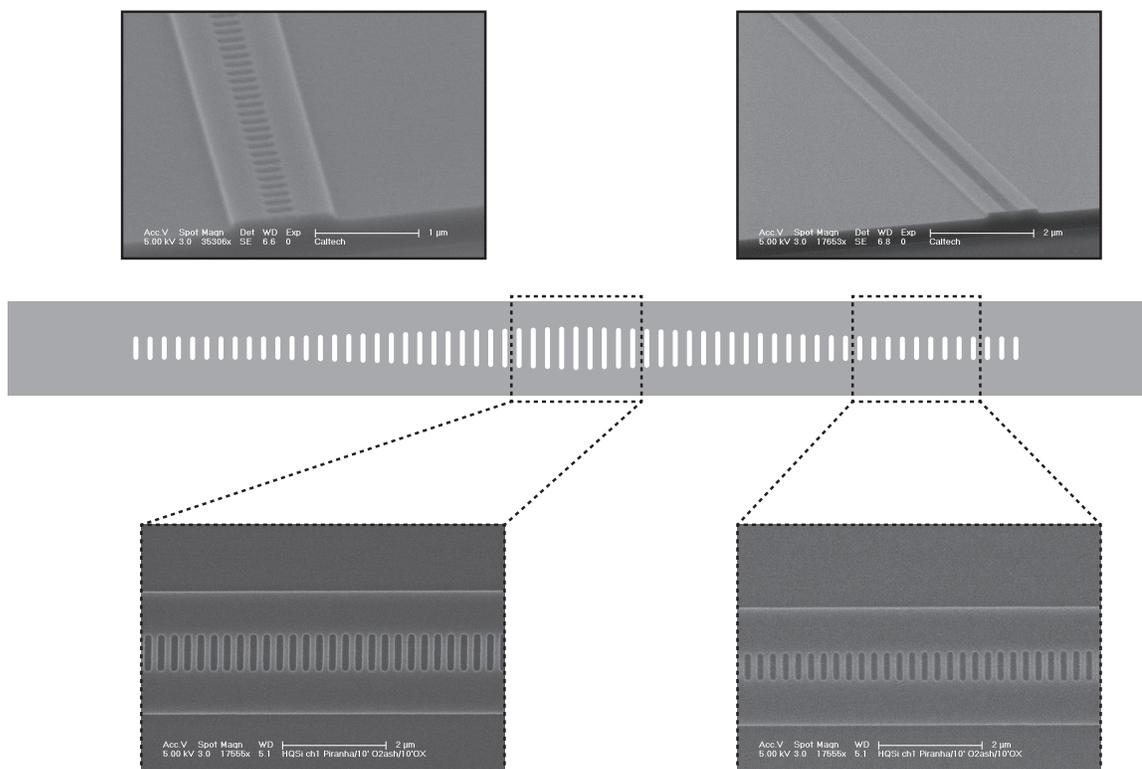
Figure 5.3. Scanning electron microscope (SEM) images of a fabricated high-Q Si resonator.

wavelength), revealing the transmission spectrum of the resonator. To be able to resolve narrow-line resonances (e.g., $Q > 2 \times 10^5$), the scanning resolution in frequency has to be sufficiently fine, at least a few times finer than the targeted resonance linewidths. This corresponds to wavelength scanning resolution better than 1 pm. Frequency scanning using standard tunable laser sources relies on the piezo-activated tuning of the length of an external cavity, a process generally slow and with inherent hysteresis. Narrow-line resonances are susceptible to thermal drift over the timescale of one scan, thus making the accurate determination of the linewidth challenging.

To speed up data acquisition and improve accuracy, we implemented an electronically controlled frequency-sweeping scheme, in the configuration shown in figure 5.4. A commercial tunable laser (Santec TSL-510) is externally modulated to produce a fast frequency sweep in time around a given frequency set point. The wavelength span of the sweep is limited by the maximum applied voltage to about 80 pm. For
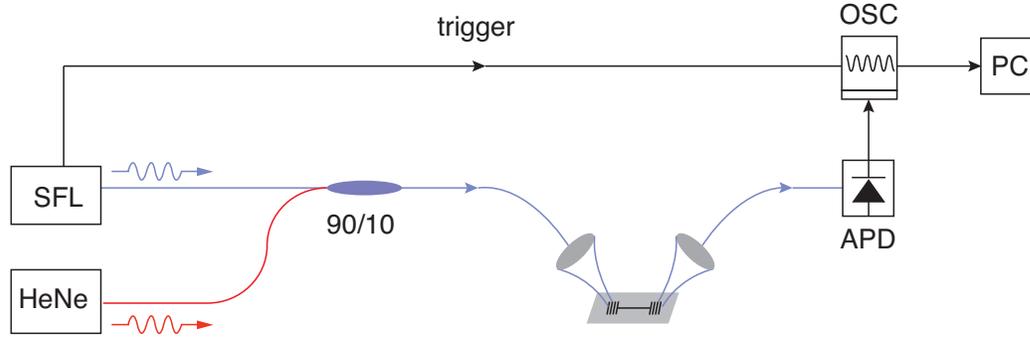
Figure 5.4. Frequency-sweeping configuration for the measurement of high-Q Si resonators.

every set point, the swept frequency output of the tunable laser is coupled into the resonator and the transmission is monitored by an oscilloscope (OSC), with timing triggered by the sweep-generating module. To calibrate the frequency sweep, part of the laser output is transmitted through a Mach-Zehnder interferometer, the output of which is also monitored by the oscilloscope. This way, a connection between the resonator's transmission in time and its spectrum is established. We further locked the swept-frequency laser (SFL) via a feedback loop, thereby linearizing the sweep and making the calibration more straightforward. For more details on the implementation of a swept-frequency laser, the reader is referred to [171–173].

Due to the limited frequency scan window and in order to avoid the use of a preliminary broadband sweep, *a priori* knowledge of reference features in the resonator's transmission spectrum was found to be useful. As one such feature, for example, serves the bandgap of the resonator, which is usually searched for at the beginning of every measurement. Then, expecting the resonant mode to be located near the low frequency band edge, the tunable laser is manually tuned until the resonance enters the scan window. The recorded oscilloscope signal is then grabbed by a computer (PC) and mapped from time onto frequency space. This mapping provides us with only a relative frequency scale for the transmission spectrum, which is, however, all we need to extract the resonance's linewidth. An absolute frequency reference point, within a certain uncertainty range, is available through the laser's frequency

setpoint. Scanning across a resonance in this fast manner provides a practically instant snapshot of the resonator's transmission signature, removed from environmental perturbations. Furthermore, as the scanned light spends significantly reduced time on resonance, thermal effects are greatly suppressed.

To increase the power coupled into waveguides through the grating couplers, fibers terminated with focusing lens modules were used. Red light laser (HeNe) was also employed to facilitate alignment with the couplers. To obtain a linewidth as close as possible to the intrinsic, resonators were increasingly unloaded from the waveguides by increasing the mirror length. This comes at the expense of transmitted power, which decays exponentially with mirror length. For increasingly longer mirror sections the SNR at the output degrades significantly, setting a sensitivity-imposed limit on the highest loaded Q that can be resolved. To push this limit higher, a high-gain, low noise photodetector (Newport InGaAs 2153) was used, featuring femtoWatt level sensitivity.

Figure 5.5 shows a typical transmission spectrum of a high-Q resonance. The blue line corresponds to the experimental trace and the red one to the Lorentzian fit, from which the quality factor is extracted. Loaded Qs as high as 1 million were obtained. The showcased result of figure 5.5 corresponds to a resonator with photonic well parameters $V = 200\,\text{GHz}, L_d = 100\,\mu\text{m}$, waveguide width $L_y = 2.0\,\mu\text{m}$, etch depth $h = 100\,\text{nm}$ and longitudinal hole diameter $W_x = 105\,\text{nm}$. Given the degree of unloading of the particular resonator, the measured loaded Q represents a close approximation of the resonator's intrinsic quality factor.

5.2   High-Q Hybrid Laser

Having validated the resonator design on Si platform, we then embarked on the integration with III-V for the realization of hybrid lasers. This was done by die-scale bonding of the two material platforms. Details on the hybrid integration process can be found in appendix A. Waveguide gratings were patterned on SOI and subsequently bonded to III-V. The grating in Si along with the III-V part of the platform constitute
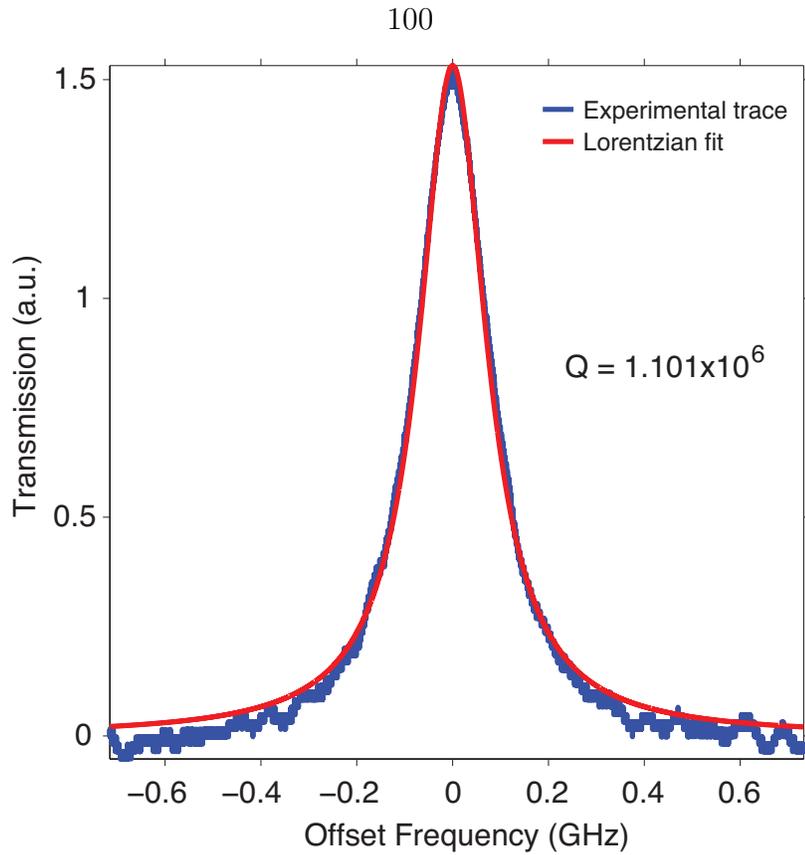
Figure 5.5. High-Q resonance. Experimental trace (blue line), Lorentzian fit (red line).

a composite hybrid Si/III-V resonator, as described and analyzed in chapter 4.

The hybrid structure and basic device configuration are shown in figure 5.6. We fabricated hybrid lasers based on the design parameter set analyzed in chapter 4. That is, $V = 100\,\mathrm{GHz}$, $L_d = 200\,\mu\mathrm{m}$ for the photonic well, waveguide width of $L_y = 2.0\,\mu\mathrm{m}$ that guides TE_0 and TE_1 and etch depth of $h = 50\,\mathrm{nm}$.

5.2.1 Light-Current Characteristics (L-I)

Hybrid lasers were mounted on a temperature controlled stage, based on an electronically controlled thermo-electric cooler (TEC). External pumping was provided by a laser diode driver. Continuous-wave lasing at room temperature ($20\,^{\circ}\mathrm{C}$ in this work) was achieved for all lasers tested. Lasers on a given chip were arrayed in four groups of three devices each. The period of the grating was lithographically tuned
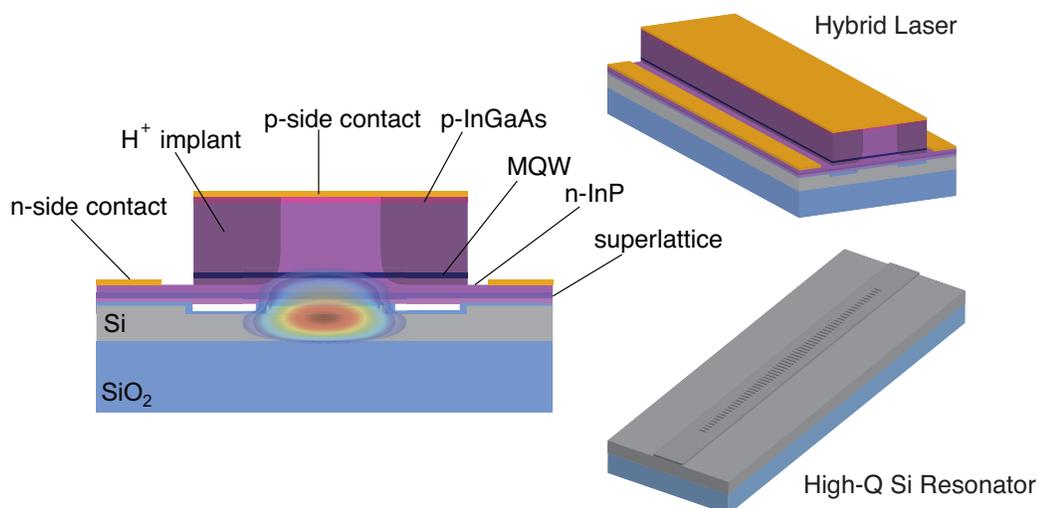
Figure 5.6. High-Q hybrid laser device schematics.

between groups, thereby tuning the emission wavelength. All lasers were otherwise designed to be identical. The period was tuned in the range of $a = 230\text{--}240\,\text{nm}$, in steps of $2.5\,\text{nm}$, translating to a respective wavelength tuning range of $1530\text{--}1575\,\text{nm}$, in increments of $15\,\text{nm}$. From optical spectrum measurements (see section 5.2.2), the peak of the gain spectrum under pumping was found to redshift from the nominal quantum well (QW) emission wavelength of $1550\,\text{nm}$ to approximately $1575\,\text{nm}$. This is mainly due to the energy gap shrinking with carrier injection.

Figure 5.7 presents representative power versus current characteristics (L-I) for four lasers from a single chip. Each trace in this figure corresponds to one laser from each wavelength group. Lasing up to $45\,\text{nm}$ away from the gain peak was attained. The particular devices featured relatively small slope efficiencies, as the resonators they were based on, were intentionally designed to be undercoupled ($Q_e > Q_i$) to maximize Q for linewidth reduction. The average cavity length was $1.1\,\text{mm}$. The measured power was collected from one end of the cavity by a large-aperture photodetector. The amount of collected power depended primarily on the insertion loss in the coupling into free space through the laser facet. The quality of the facet varied significantly from device to device, largely due to the coarse nature of the laser bar cleave, thus making even identical lasers to differ significantly in power output.

The observed L-I curves are subject to this randomness and, as a result, a reliable trend for the slope efficiency could not be derived.
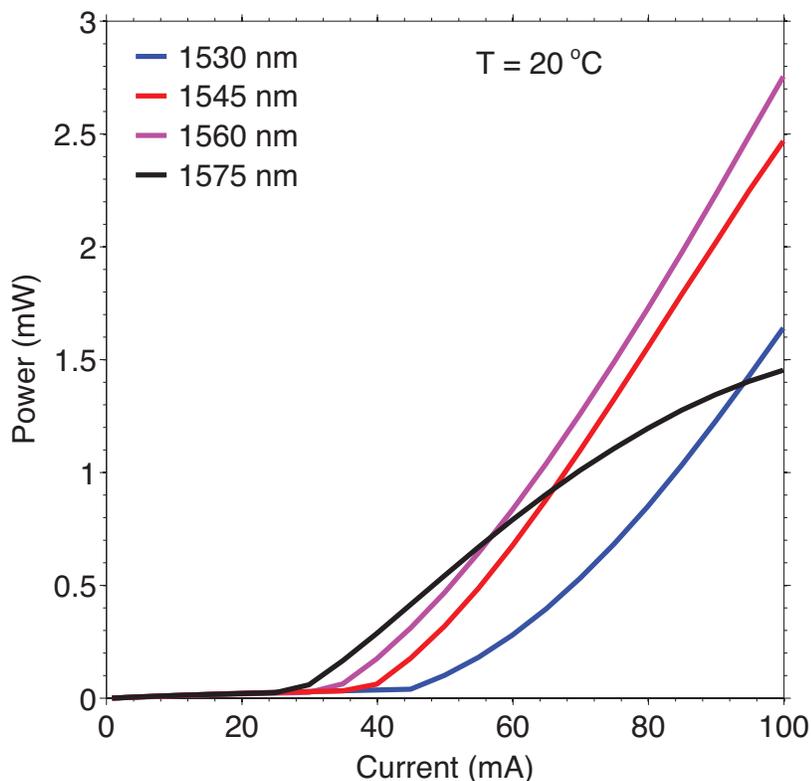
Figure 5.7. L-I characteristics of four high-Q hybrid lasers from a single chip, with lithographically tuned emission wavelength.

The behavior exhibited by the black trace of figure 5.7 is representative of the thermal roll-off effect, often encountered in these hybrid lasers. As the active region heats up, carriers localized in the QWs become increasingly thermalized and escape confinement, thus reducing the recombination rate, manifesting itself as a power roll-off in the L-I curve. The onset of this thermal effect on the hybrid platform occurs at relatively lower pump currents, than for conventional all-III-V lasers. This is due to the poorer heat dissipating capability of the hybrid structure. Heat generated in the III-V medium (mostly on the p-side of it) has to diffuse downward, through the SOI part of the structure, toward the heat sink. The presence of the low thermal conductivity buried oxide layer creates a thermal buffer that slows down the heat

extraction from the III-V. As a result, hybrid lasers tend to heat up faster and to reach the thermal roll-off threshold sooner than conventional III-V lasers.

Simultaneously with the output power, the voltage drop across the laser was also recorded as a function of the pump current. Figure 5.8 presents representative I-V characteristics of measured hybrid lasers. All lasers from a single chip showed I-V dependence that followed one of the two traces of figure 5.8. The distribution of
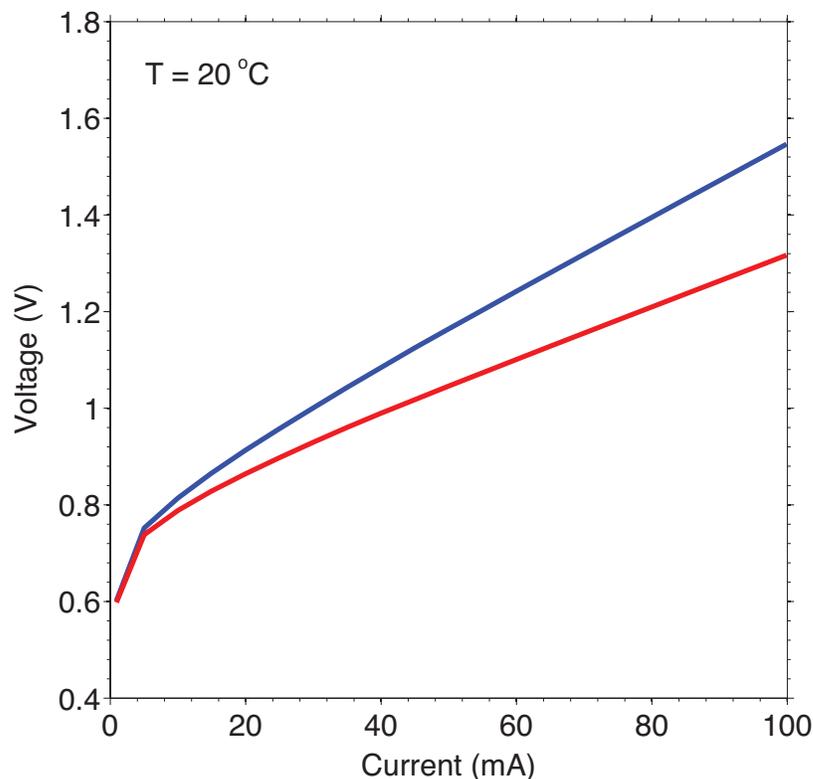
Figure 5.8. I-V dependence of all twelve high-Q hybrid lasers from a single chip.

devices between the two traces did not seem to follow a trend with the emission wavelength. Overall, the electrical behavior was consistent, with minor deviations attributed to processing-induced variations across the chip.

While output power tended to vary significantly between devices, threshold currents exhibited a much more consistent trend. Threshold currents for devices in the same emission wavelength group were extremely repeatable, while a clear trend with detuning from the peak of the gain spectrum was also established. Figure 5.9 shows L-I curves of three lasers with the same emission wavelength. Unlike the variation in

slope efficiency, all three feature the same threshold, in this case 35 mA at 1545 nm. Similar consistency was observed for all four wavelength groups. Thresholds as low as 27 mA were measured for lasers with emission wavelength closest to the gain peak and cavity lengths of 1.1 mm. This low threshold for the given cavity length is attributed to the enhanced intrinsic Q and the undercoupled laser cavities.
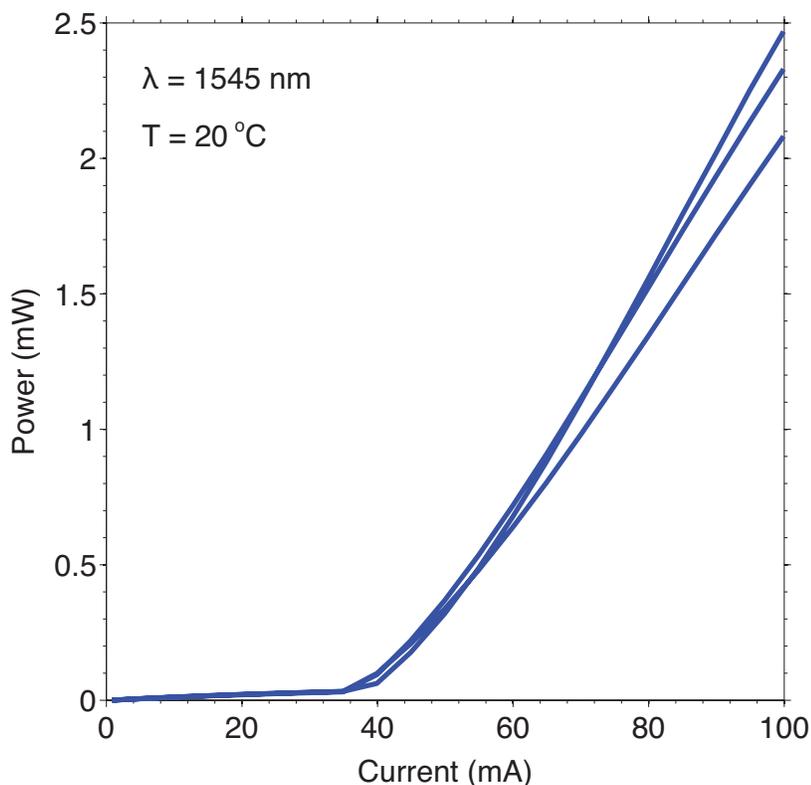
Figure 5.9. L-I characteristics of three high-Q hybrid lasers with same emission wavelength.

Figure 5.10 presents the dependence of threshold current on the emission wavelength offset from the gain peak $(\lambda-\lambda_o)$, with the latter, as mentioned above, observed at $\lambda_o = 1575$ nm. Thresholds as high as 45 mA were measured for the maximum detuning of 45 nm from the gain peak. The trend line (red line) of figure 5.10 corresponds to a double exponential fit and it appears to be modeling the trend closely over the specific wavelength range.

To facilitate heat sinking, as well as to perform temperature-dependent measure-
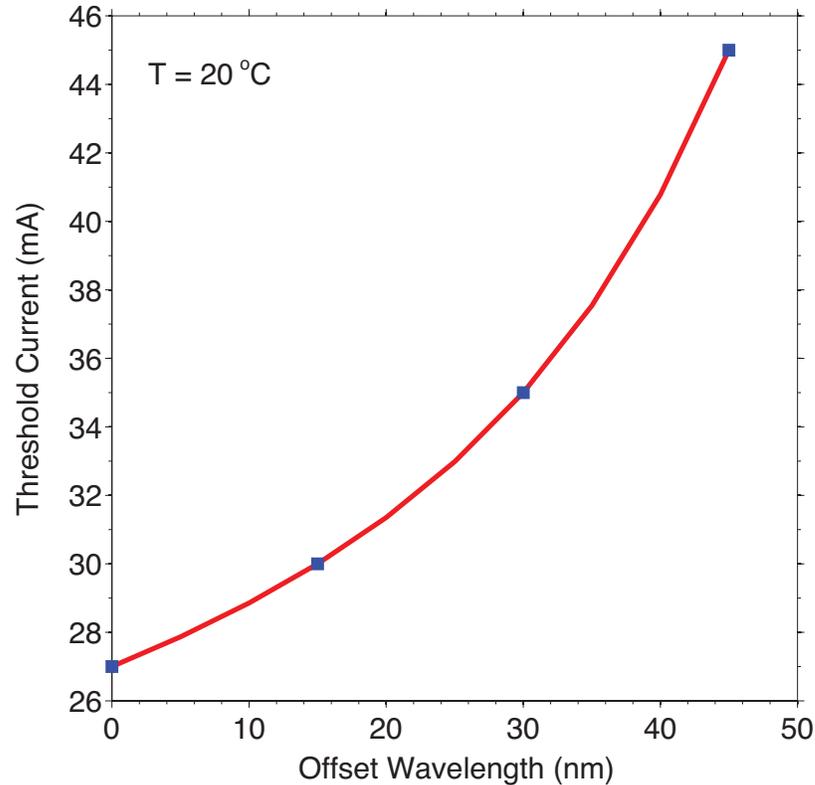
Figure 5.10. Threshold current as a function of offset emission wavelength from the gain peak ($\lambda_o = 1575\,\text{nm}$).

ments, the same laser bar, results from which were presented above, was die bonded to improve thermal contact with the temperature-controlled stage. The chip was also flipped around and L-I measurements were retaken from the opposite laser facet. Significant discrepancies between measured output powers from the two facets of a given laser were found, confirming the variation in facet quality. Figure 5.11 shows L-I and I-V characteristics of a laser emitting at 1545 nm. In addition to the increased power output at 100 mA, compared to the output at the same pump current from the other facet, this time the laser could also be pumped harder, up to 150 mA, thanks to the reduced heating effect. A record-high, among the lasers tested in this work, output power of 9 mW was measured for this particular laser. This result shows promise for the potential of these lasers for high-power operation. With the use of a commercial-grade packaging process (e.g., dicing, polishing, AR-coating, fiber-coupling) can be

greatly improved. Furthermore, tuning the resonator loading (i.e., reduced undercoupling) to increase slope efficiency, can also be used boost the output power.
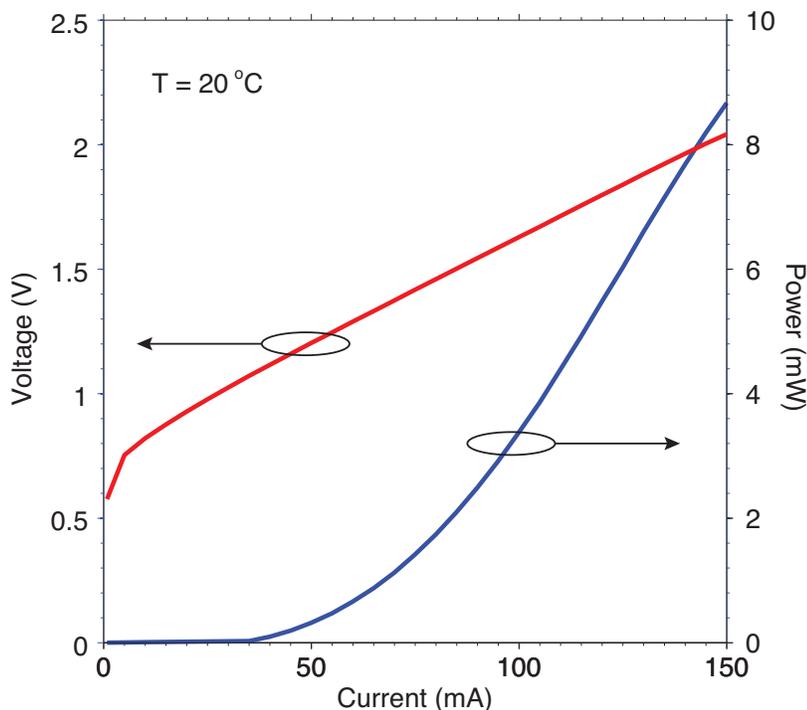
Figure 5.11. L-I and I-V characteristics of a die-bonded high-Q hybrid laser.

We tested the lasers' light output characteristics as a function of temperature. Tuning the TEC setpoint, we measured the power output as a function of the pump current at different temperature setpoints. This was done on the already die bonded chip. Figure 5.12 presents the change of a hybrid laser's L-I characteristic with temperature in the range 10–70 °C. Continuous-wave lasing up to 70 °C was attained. As carriers spread out in energy with increasing temperature, higher carrier densities are needed to reach transparency (N_{tr}). Higher carrier densities in turn, lead to increased absorption (e.g., Auger absorption) and reduced carrier lifetime, particularly through the increase of nonradiative carrier recombination [175]. The decrease in slope efficiency with temperature has been found to be modeled closely by an increase in internal absorption losses, primarily between the split-off and heavy-hole valence bands [176–178].

Figure 5.13 presents the dependence of threshold current on temperature. Thresh-
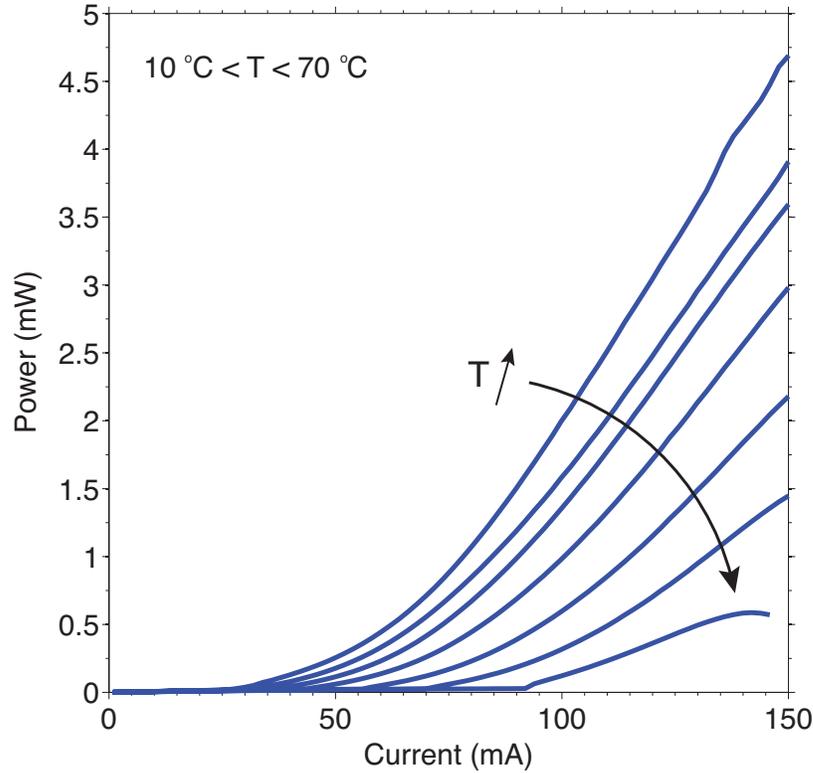
Figure 5.12. L-I characteristic of a hybrid laser as a function of operating temperature.

old current (or density) grows exponentially with temperature and is often modeled as

$$I_{th} = I_o \exp\left(\frac{T}{T_o}\right), \tag{5.1}$$

where T_o is a characteristic temperature, measure of the threshold current's sensitivity to temperature. The lower T_o, the more sensitive threshold current is to temperature. As both the carrier density and gain to reach transparency increase with temperature, so does the threshold current. This increase is slower at lower temperatures (e.g., 280–300 K), but quickly starts to grow at higher temperatures, as nonradiative processes (e.g., Auger recombination) and internal losses (e.g., intervalence absorption) increase with carrier density. In the case of the hybrid laser of figure 5.13, we split the measurement range in three regions of gradually increasing sensitivity to temperature. The characteristic temperature extracted from fitting to equation (5.1) are 77 K, 42 K and 30 K for the temperature ranges 280–300 K, 300–330 K, and 330–350 K respec-

tively. These characteristic temperatures are typical of InGaAsP/InP QW lasers at 1.55 μm.
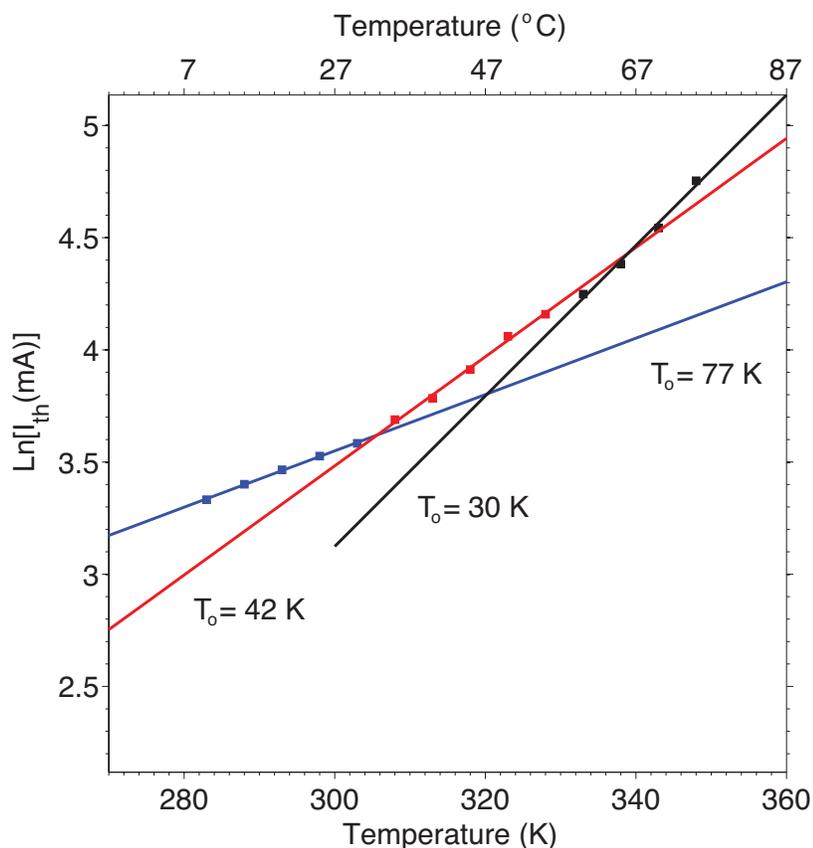
Figure 5.13. Threshold dependence on temperature for a high-Q hybrid laser.

The emission wavelength was recorded on a wavemeter over the temperature range 10–70 °C and its dependence is presented in figure 5.14. Over the given range, the wavelength tunes by approximately 5 nm, a shift that corresponds to a wavelength sensitivity with temperature of about 0.089 nm/K. Although QW-based lasers typically exhibit sensitivities on the order of 0.3 nm/K, this dependence is usually reduced in DFB lasers at the levels of 0.07 nm/K, due to the wavelength selectivity provided by the grating. Overall, the temperature-dependent characteristics seem to be III-V material dictated and to have carrier over to the hybrid laser.
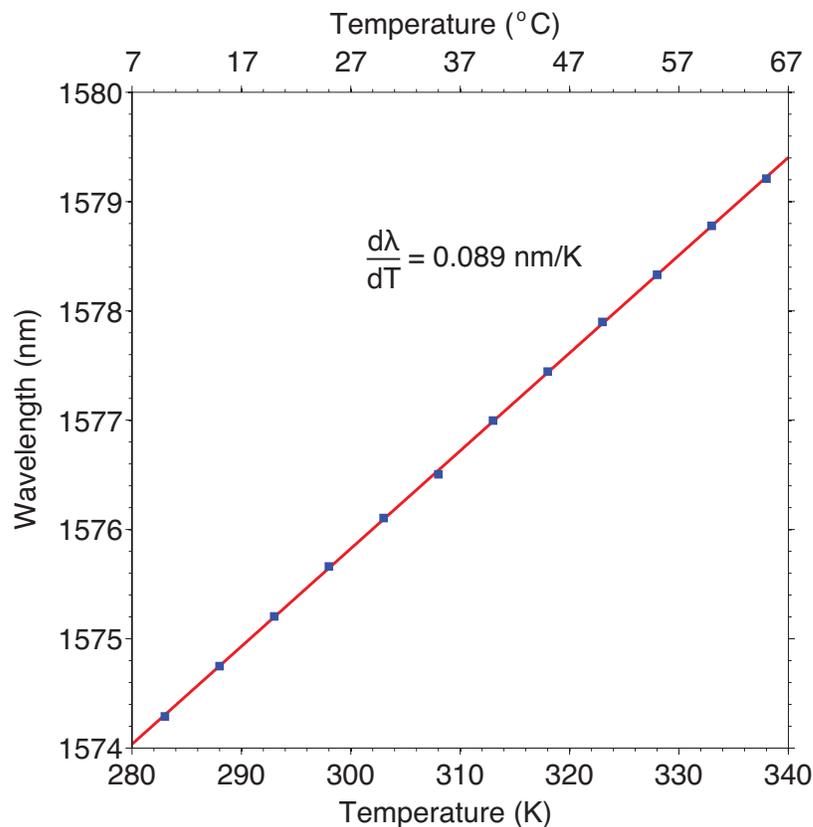
Figure 5.14. Emission wavelength dependence on temperature for a high-Q hybrid laser.

5.2.2 Optical Spectrum

Analysis of the optical emission spectrum is an important aspect of the hybrid laser's characterization, given that its features are directly dictated by the resonator design. Figure 5.15 presents a representative optical spectrum of a high-Q hybrid laser, taken with an optical spectrum analyzer (OSA). The particular device features the main working design parameter set ($V = 100\,\text{GHz}, L_d = 200\,\mu\text{m}$) and was taken at $20\,°\text{C}$ and pump current of $120\,\text{mA}$. The threshold current for the specific laser was $35\,\text{mA}$ and the emission wavelength $1546\,\text{nm}$. This laser, just like all hybrid lasers tested, was single-mode over the entire wavelength range accessible with the OSA (1450–$1650\,\text{nm}$).

The grey-shaded region of figure 5.15 denotes the extent of the bandgap. The

lasing peak appears inside the bandgap, right off the low frequency band edge. The linewidth of the lasing peak is limited by the resolution of the OSA ($\sim 0.08\,\mathrm{nm}$). Side mode suppression ratios (SMSR) over $45\,\mathrm{db}$ were consistently obtained for the hybrid lasers over their entire operating current range.
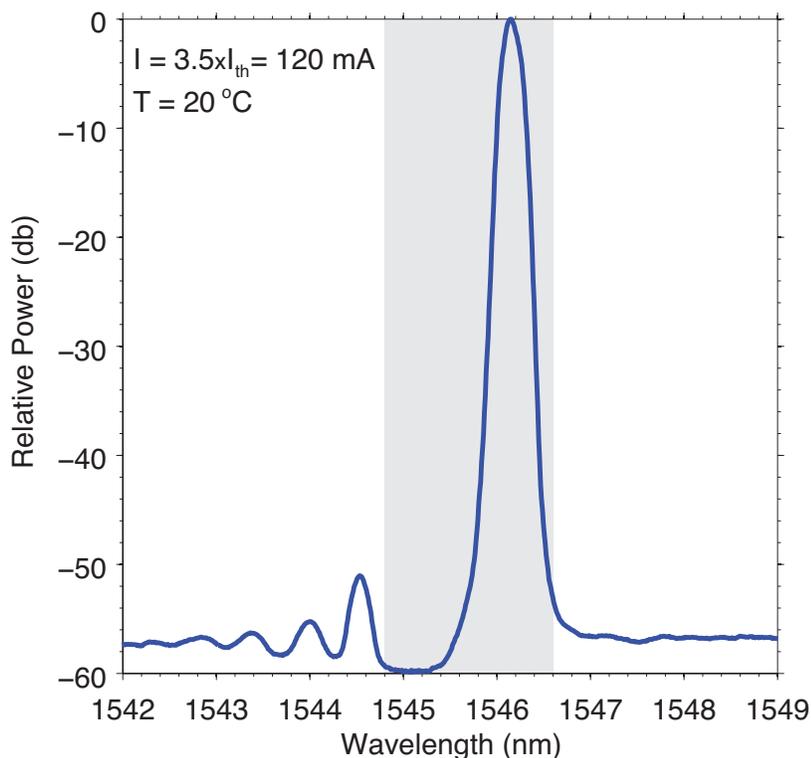
Figure 5.15. Optical spectrum of a high-Q hybrid laser. ($V = 100\,\mathrm{GHz}$, $L_d = 200\,\mu\mathrm{m}$.)

Figure 5.16 shows traces of the optical spectrum taken below and at threshold for a hybrid laser emitting at $1575\,\mathrm{nm}$. The spectrum below threshold corresponds to that of spontaneous emission, which is essentially representative of the gain spectrum, offset in wavelength under the effect of pumping. The offset gain peak is found at approximately $1575\,\mathrm{nm}$, from nominally $1550\,\mathrm{nm}$ for the nonpumped medium. The pronounced notch in the spontaneous emission spectrum is the bandgap, also evident at threshold as a deep negative spike. The gratings utilized for the hybrid resonators are, on average, 20–30 times stronger ($\kappa \sim 200\text{–}300\,\mathrm{cm}^{-1}$) than gratings in traditional DFB lasers ($\kappa \sim 10\,\mathrm{cm}^{-1}$).

At this point, it is interesting to contrast the experimentally observed optical
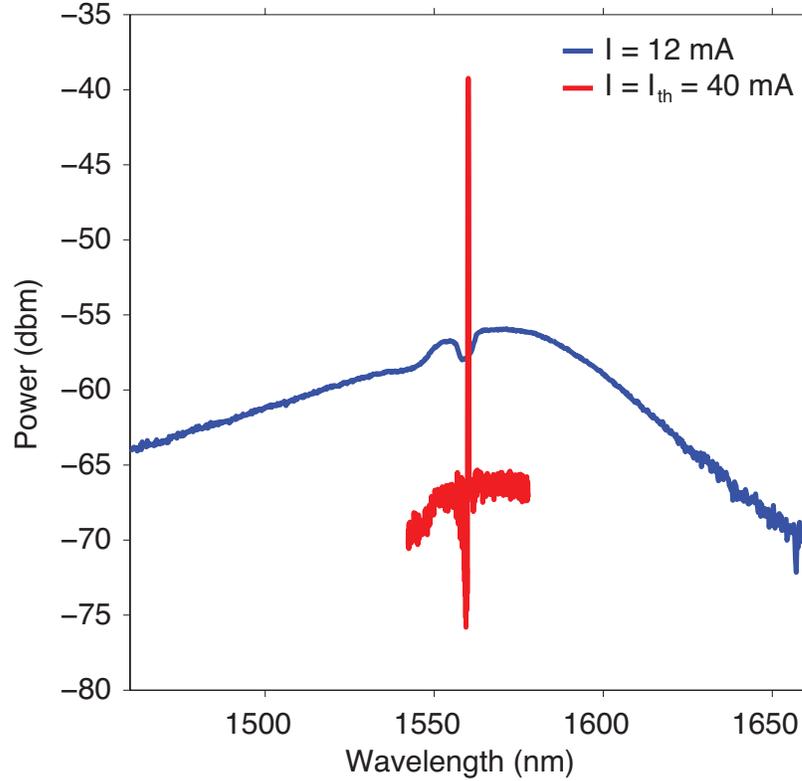
Figure 5.16. Optical spectrum of a high-Q hybrid laser below (blue line) and at threshold (red line). ($V = 100\,\text{GHz}$, $L_d = 200\,\mu\text{m}$.)

spectrum with the theoretically designed one. Figure 5.17 presents the theoretical transmission spectrum of the passive resonator (figure 5.17(a)), the theoretically modeled emission spectrum of an active resonator (i.e., with gain, figure 5.17(b)) and an experimental laser spectrum (figure 5.17(c)). To facilitate the direct comparison, all spectra are plotted on a relative frequency axis with respect to a common reference point, taken at the lasing peak. All three spectra are based on a high-Q resonator with $V = 100\,\text{GHz}$, $L_d = 200\,\mu\text{m}$. In the experimental spectrum, the lasing peak appears at approximately $70\,\text{GHz}$ from the low frequency band edge, although the exact location of the edge is difficult to identify, due to the lack of a strong side mode on that side of the bandgap. In the passive resonator's transmission and the active model's emission spectrum, the resonant mode and lasing peak respectively, also appear about $50\,\text{GHz}$ from the band edge. The dominant side mode experimentally appears, as expected
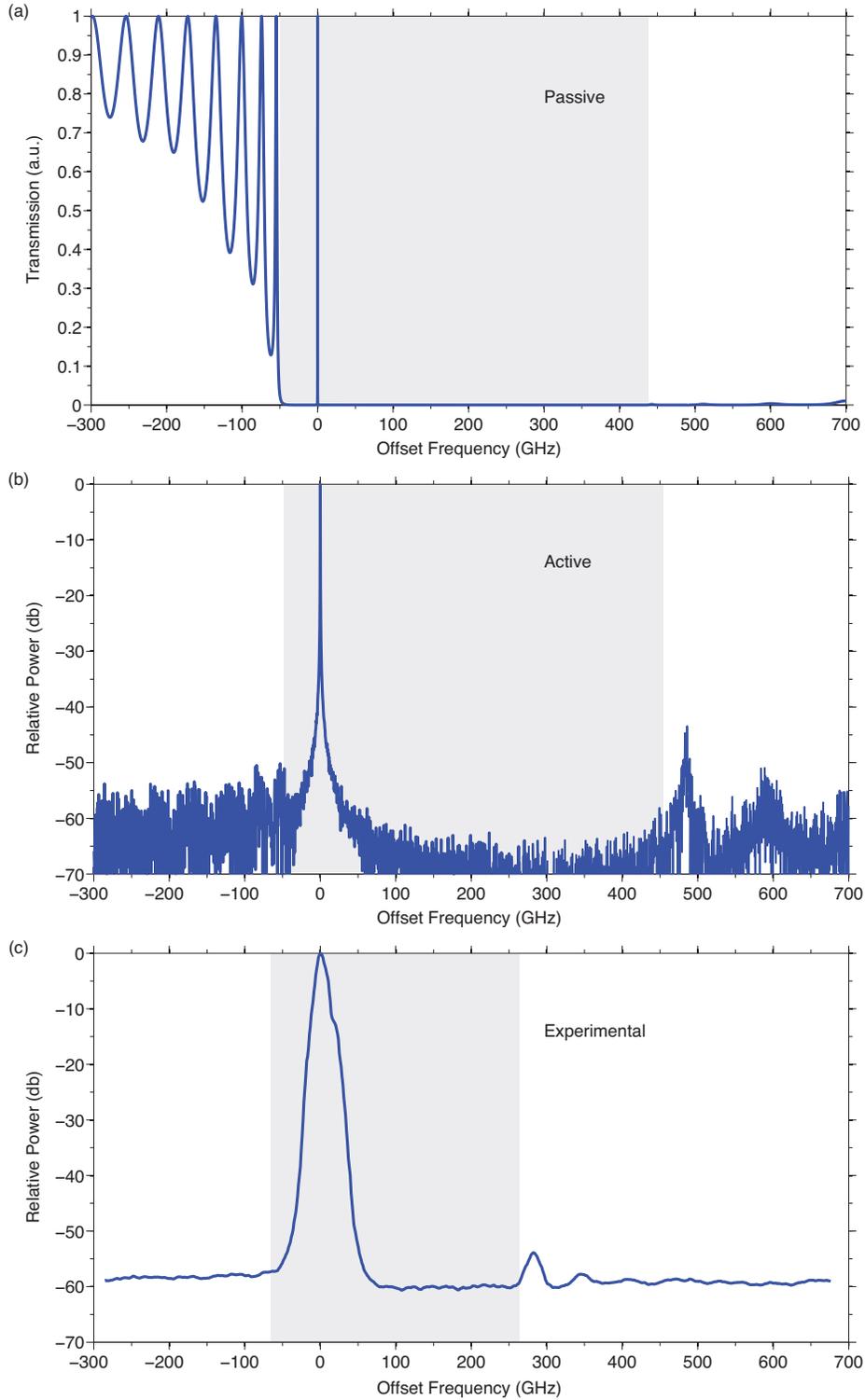
Figure 5.17. Optical spectrum of a (a) passive hybrid resonator, (b) active hybrid resonator (with gain) and (c) fabricated hybrid laser. ($V = 100\,\mathrm{GHz}$, $L_d = 200\,\mu\mathrm{m}$.)

from the design and model, off the high frequency band edge. Side mode suppression ratios are in all cases over 45 db. A distinct discrepancy between experiment and theory is the actual size of the bandgap. The experimentally identifiable bandgap appears to be about 300 GHz, much smaller than the roughly 560 GHz of the theoretically designed resonator. This is, most likely, due to a deviation in the etch depth of the fabricated grating from the theoretical depth of $h = 50$ nm that rendered the actual grating effectively weaker.

To further illustrate the effect of the etch depth on the size of the bandgap, we compare spectra of lasers from two different chips. The SOI dies for the two hybrid chips were etched back to back, with one etched 6 nm deeper relative to the other. Lasers represented in figure 5.18 with a blue and red trace were on the deeper etched chip, while a laser from the shallower etched one is represented with the purple trace. The bandgap on the spectra of the deeper etched gratings appears approximately 90 GHz wider. The relative position of the lasing peak in the bandgap does not seem to have been significantly affected (70 GHz from band edge). The three lasers of figure 5.18 have all the same period ($a = 240$ nm), yet their emission wavelengths differ by roughly 5 nm, with the lasers on the deeper etched die being longer. This result seems counterintuitive if only the etch depth is taken into account. Yet, with the change in etch depth, there is also a shift in the vertical position of the mode. The mode in the deeper etched waveguide shifts upward, toward the higher refractive index III-V, thus causing a net redshift of the emission wavelength (blue and red traces), compared to the laser on the shallower etched die (purple trace).

Each one of the lasers of figure 5.18 is also based on a grating with different longitudinal hole diameter W_x, 105, 125, and 90 nm for the blue, red and, purple trace respectively. Lasers on the same chip but with different W_x exhibit almost identical optical spectra, in terms of both the size of the bandgap and the emission wavelength.

As mentioned earlier, the emission wavelength of hybrid lasers on a given chip was lithographically tuned, by varying the period of the grating between 230–240 nm. Figure 5.19 presents representative optical spectra of a laser of each wavelength group,
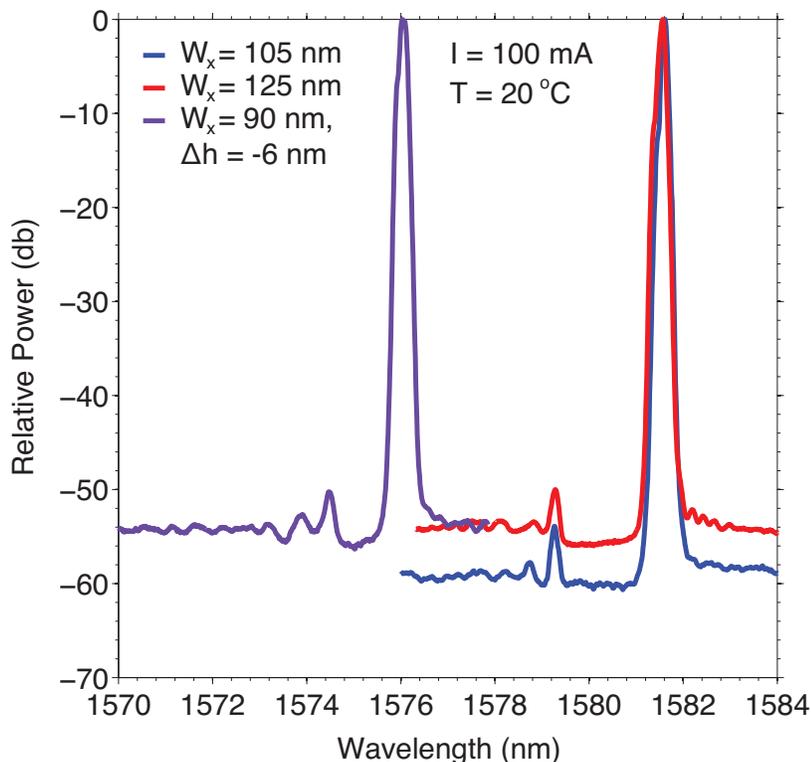
Figure 5.18. Effect of grating etch depth h and hole diameter W_x on the bandgap. ($V = 100\,\mathrm{GHz}$, $L_d = 200\,\mathrm{\mu m}$.)

all from the same chip. Emission was lithographically tuned over a total range of 45 nm, with single-mode lasing over the entire observable bandwidth achieved in every case. In the inset of figure 5.19, the position of each lasing peak relative to the spontaneous emission spectrum below threshold is shown. The longest of the emitted wavelengths lines up roughly with the peak of the pumped gain spectrum, while the tuned emission spans up to 45 nm on the blue side of the gain peak. Side mode suppression ratios on the order of 50 db were recorded in all cases.

For a given laser, the tuning of the emission wavelength with the pump current was monitored. Figure 5.20 shows optical spectra taken at 1.7 and 4 times threshold. Measured with the OSA, a tuning range of 0.6 nm (75 GHz) is found. Measured more accurately with a wavemeter, a total tuning range of about 1.1 nm (138 GHz) is recorded from threshold up to the maximum operating current. The limited tuning with current is manifestation of the resonator's resonance-dictating function, as
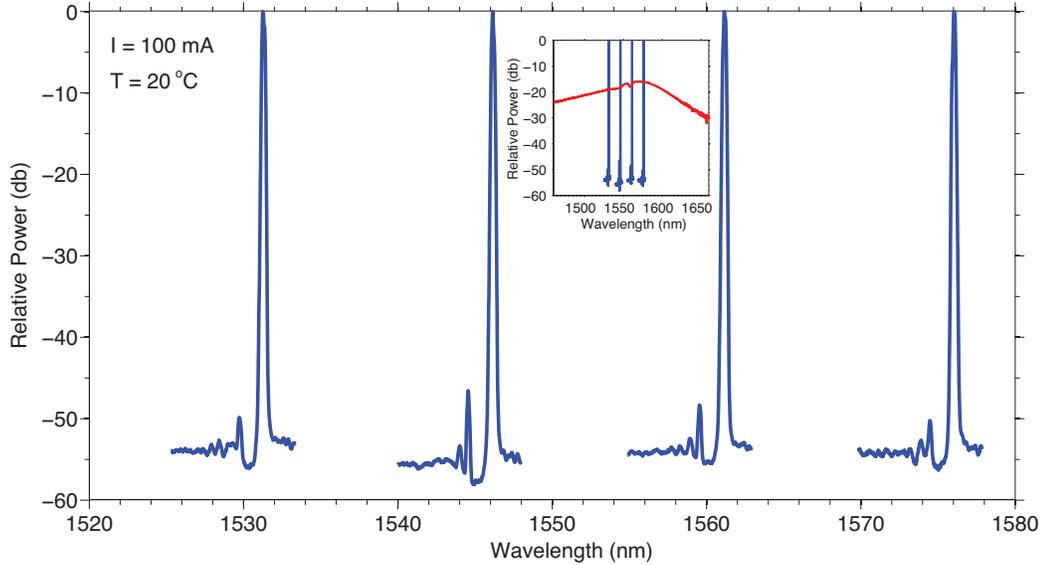
Figure 5.19. Optical spectra of lithographically tuned high-Q hybrid lasers. Inset: optical spectra relative to the spontaneous emission spectrum. ($V = 100\,\mathrm{GHz}$, $L_d = 200\,\mathrm{\mu m}$.)

well as of the active medium's diminished role in dictating the mode's effective index. The period of the grating serves as a knob for coarse tuning of the emission wavelength, over a range that spans almost the entire C-band of wavelength division multiplexing (WDM)-based optical communications. Resonator design parameters, such as the photonic well depth V can serve as additional knobs for fine positioning of the emission in the C-band grid. Current-mediated tuning of $75\,\mathrm{GHz}$ is more than adequate for tuning of the emission within the $50\,\mathrm{GHz}$ channel bandwidth of dense WDM (DWDM).

Figure 5.21 presents a more detailed view of the evolution of the optical spectrum of a hybrid laser with the pump current. Shortly over 4 times threshold, the blue side mode starts to lase, result of spatial hole burning (SHB). The maximum operating current is limited either by thermal roll-off, as described in the previous section, or by SHB. The latter is especially pronounced in the case of undercoupled resonators, as the ones these hybrid lasers are based on. Reduction of the undercoupling, along with improvements on the facet AR-coating and more uniform current injection could
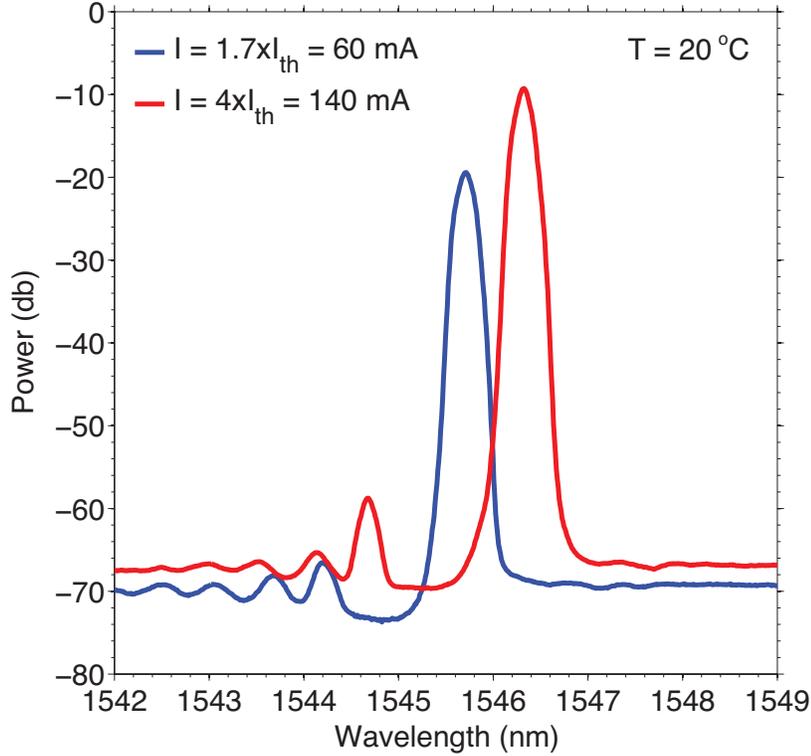
Figure 5.20. Optical spectrum of a high-Q hybrid laser as a function of the pump current. ($V = 100\,\mathrm{GHz}$, $L_d = 200\,\mathrm{\mu m}$.)

help push the onset of SHB to higher currents.

5.2.3 Frequency Noise

5.2.3.1 Measurement Setup

The benchmark metric for the high-Q hybrid laser is, naturally, its spectral purity and specifically the component of it pertaining to the spontaneous emission-induced phase noise, quantified in the Schawlow-Townes linewidth. A method widely used to determine the spectral linewidth of a laser is the *self-heterodyne linewidth measurement method* [179]. In that method, a portion of the laser output is delayed (e.g., fiber delay line), usually by time that exceeds the laser's coherence time, while another portion of the output is frequency shifted ($\sim 10\,\mathrm{MHz}$) by means, for example, of a acousto-optic modulator (AOM). The two optical paths are interfered again on a
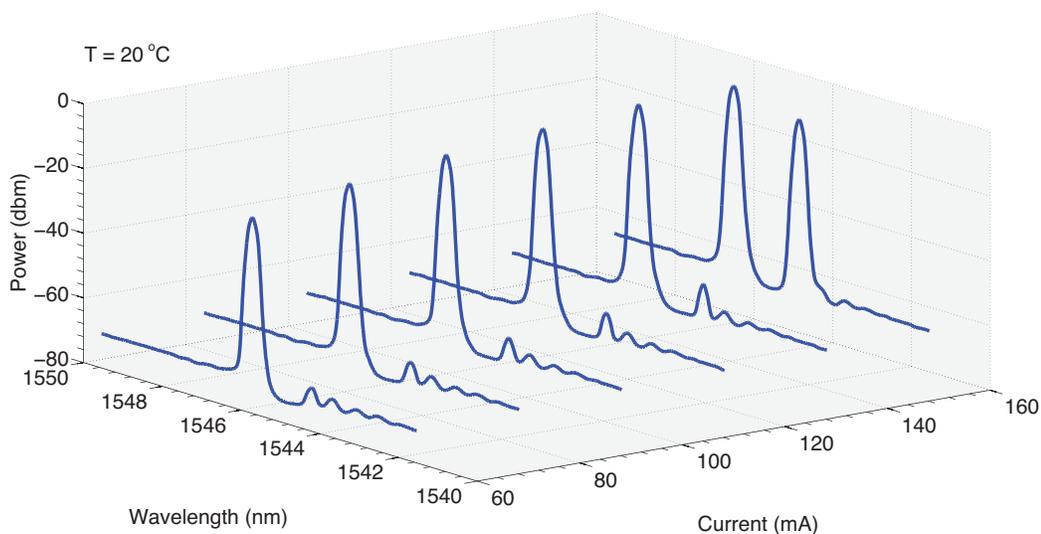
Figure 5.21. Optical spectrum of a hybrid laser as a function of the pump current. ($V = 100\,\mathrm{GHz}$, $L_d = 200\,\mathrm{\mu m}$.)

photodiode and the resulting beatnote at the AOM's offset is recorded on a RF spectrum analyzer. When the dominating source of phase noise is spontaneous emission, the resulting spectral lineshape is Lorentzian and its linewidth is twice the linewidth of the measured laser. However, when technical noise as in $1/f$-type of noise is present in the laser output, the resulting lineshape is less straightforward. For instance, in the case of coexisting white and $1/f$-type of noise the lineshape corresponds to the convolution between a Lorentzian (due to white noise) and a Gaussian (due to $1/f$) function, a lineshape also known as Voigt lineshape [180,181]. Although an aggregate linewidth can still be defined for the composite lineshape, accurate discrimination between the technical and white noise contribution to the linewidth is difficult. Variants of the above technique, utilizing subcoherent delay times [182] or without frequency shifting [183], all result in similar ambiguity at distinguishing between technical and white noise contributions.

In cases where the laser to be measured is inherently narrow linewidth or accurate determination of the fundamental, white noise linewidth is desired, measurement of the full frequency (or phase) noise spectrum is most useful. This is the case with the high-Q hybrid lasers developed in this work. The laser resonator was designed with

emphasis on maximizing its quality factor to reduce spontaneous emission-induced phase noise. Therefore, it of critical important to identify the effect of the resonator on the laser's quantum-limited (i.e., Schawlow-Townes) linewidth. Measurement of the laser's frequency noise spectrum can be done using a Mach-Zehnder interferometer (MZI), of subcoherent differential delay τ, as a frequency discriminator [184]. An MZI of subcoherent delay, biased in quadrature ($\omega\tau = \frac{\pi}{2}$), converts phase fluctuations to intensity fluctuations recorded on a photodiode. Monitoring the spectrum of the photodiode's output on a RF spectrum analyzer (SA), reveals the frequency (or phase) noise spectrum of the laser.

We implemented a frequency-discriminating scheme for the measurement of frequency noise in the configuration illustrated in figure 5.22. Light output from the laser is coupled into a lensed fiber and sent through a pair of optical isolators (ISO) in series, to suppress reflections back into the laser that could cause instability. Due to the relatively low output powers of high-Q hybrid lasers based on undercoupled resonators, as well as the significant insertion loss introduced by facet imperfections and the coupling into fiber, power levels in the fiber had to be increased to enhance the measurement's dynamic range. This was done by sending the signal through a C-band booster optical amplifier (ThorLabs BOA 1004, ex Covega BOA 6460). BOAs are single-pass, traveling-wave amplifiers based on InGaAsP/InP MQW, that typically feature bandwidths flatter than that of semiconductor optical amplifiers (SOA). A BOA was chosen in this case to provide amplification over the entire 45 nm span of the lithographically tuned lasers. Unlike SOAs though, BOAs amplify one polarization state. To optimize the amplification, a polarization controller (PC) was inserted in front of the BOA to tune the signal's polarization. The amplified signal out of the BOA was then passed through an unbalanced MZI with a free spectral range of FSR = 847 MHz, which corresponds to a differential delay of about $\tau = 1.2$ ns.

The laser's complex field can expressed as

$$e(t) = a(t)\exp\left(j\omega_o t + j\phi(t)\right), \tag{5.2}$$
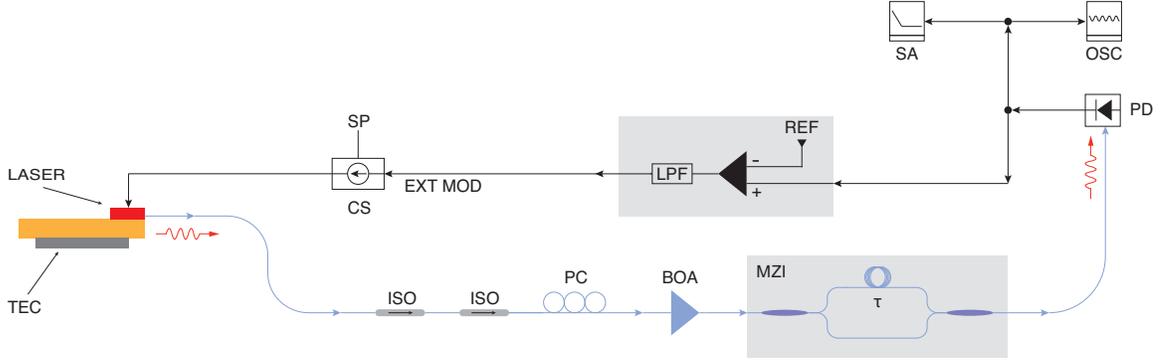
Figure 5.22. Laser frequency noise measurement setup.

where $a(t)$ is the field's amplitude, ω_o the center frequency of the laser and $\phi(t)$ the phase noise of the laser. The output of the MZI is given by

$$e_{\text{MZI}}(t) = e(t) + e(t - \tau). \tag{5.3}$$

For the conversion of the optical signal to electrical, we used a high-speed lightwave converter (PD, HP 11982A), with a bandwidth of $15\,\text{GHz}$. The voltage at the output of the photodetector is given by

$$v(t) = \rho \left| e(t) + e(t - \tau) \right|^2, \tag{5.4}$$

where ρ is the detector's responsivity in $[V/W]$. The intensity noise is typically much smaller than the phase noise of the laser, so the time-dependence of the field amplitude can be ignored. The voltage for the detected output of the MZI then becomes

$$v(t) = 2v_o + 2v_o \cos(\omega_o \tau + \Delta\phi(t, \tau)), \tag{5.5}$$

with

$$\Delta\phi(t, \tau) = \phi(t) - \phi(t - \tau) \tag{5.6}$$

being the accumulated phase noise over the time interval $t - \tau$ to t and v_o a voltage that has absorbed the detector responsivity and the field amplitude.

In practice, due to splitter imbalance, polarization mismatch between the two

arms, as well as the effect of phase noise, the MZI does not exhibit 100% fringe visibility. The frequency response of an actual MZI, recorded as voltage oscillations on a photodetector, is shown in figure 5.23. The photodetector voltage can then be
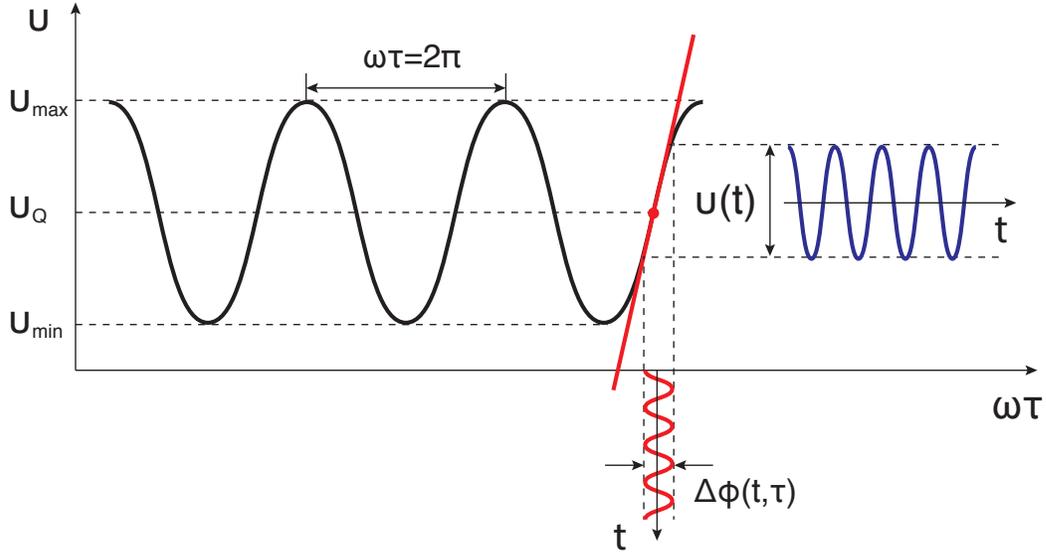
Figure 5.23. Frequency response of a Mach-Zehnder interferometer recorded as voltage on a photodetector.

expressed as [185]

$$v(t) = \left(\frac{v_{\max} + v_{\min}}{2} \right) + \left(\frac{v_{\max} - v_{\min}}{2} \right) \cos(\omega_o \tau + \Delta\phi(t, \tau)), \qquad (5.7)$$

where

$$v_Q = \frac{v_{\max} + v_{\min}}{2}, \qquad (5.8)$$

$$v_G = \frac{v_{\max} - v_{\min}}{2} \qquad (5.9)$$

are the voltage's DC offset and excursion amplitude respectively. When the interferometer is in quadrature ($\omega\tau = \frac{\pi}{2}$), the voltage fluctuation becomes (dropping the DC component)

$$v(t) = v_G \sin(\Delta\phi(t,\tau)). \tag{5.10}$$

For delay times τ much shorter than the laser coherence time, the accumulated phase noise is accordingly small enough and equation (5.10) can be further approximated with

$$v(t) = v_G \Delta\phi(t,\tau). \tag{5.11}$$

Equation (5.11) provides a direct and linear correspondence between phase noise and voltage fluctuations recorded on the photodetector, with the proportionality constant v_G serving as gain factor.

The photodetector output is split into two signals. One is monitored on an oscilloscope (OSC) to track the MZI's state relative to quadrature and to acquire v_Q, v_G, while the other is sent to a RF spectrum analyzer (SA, Agilent 4395A), with a scan range of $10\,\mathrm{Hz}$–$500\,\mathrm{MHz}$, to extract the frequency noise spectrum. When the spectrum analyzer and the oscilloscope are impedance-matched to the photodetector ($R_L = 50\,\Omega$), the fluctuating power at the input of the spectrum analyzer is given by

$$p(t) = \frac{v^2(t)}{R_L}. \tag{5.12}$$

The power reaching the analyzer is resolved into its spectral components with a given frequency resolution (or resolution bandwidth, RBW), yielding the power spectrum of the photodetector's output voltage. Using equations (5.11), (5.12), the power spectrum measured with the spectrum analyzer can be related to the phase noise spectrum via

$$W_{SA} = \frac{v_G^2}{R_L} S_{\Delta\phi}, \tag{5.13}$$

where $W_{SA}, S_{\Delta\phi}$ are power spectral densities (PSD) of the photodetector output and the phase noise respectively. We wish to find the power spectral density of the frequency noise $S_\nu(f)$ in [$\mathrm{Hz}^2/\mathrm{Hz}$]. Taking the autocorrelation of $\Delta\phi(t,\tau)$ and its Fourier

transform, a relationship between phase noise and frequency noise spectral density is established [186, 187]:

$$S_{\Delta\phi}(f) = 4\pi^2\tau^2 sinc^2(\pi f\tau)S_\nu(f). \tag{5.14}$$

For offset frequencies smaller than the MZI FSR, the *sinc* function in equation (5.14) can be approximated by unity, so the frequency noise PSD can be written as a function of the measured electrical power spectrum on the spectrum analyzer:

$$S_\nu(f) = \frac{R_L}{4\pi^2\tau^2 v_G^2}10^{W_{SA}/10}, \tag{5.15}$$

where W_{SA} is in [dbm/Hz] and $S_\nu(f)$ in [Hz^2/Hz].

Unlike the self-heterodyne linewidth measurement, the measurement of the frequency noise spectrum is an absolute type of measurement and as such, it requires to be carefully calibrated. This calibration is provided by equation (5.15) and specifically by the acquisition of the gain factor v_G, represented in figure 5.23 by the slope of the MZI's frequency response at quadrature. Practically, v_G is determined on the oscilloscope by forcing the MZI to oscillate through multiple FSRs and recording its maximum excursion.

Necessary requirement for the above scheme to yield meaningful results is not only that the MZI be biased at quadrature, but also that it remain there for time long enough, for a high-resolution scan of the spectrum analyzer to be completed. Interferometers are inherently prone to drift, typically due to temperature changes or mechanical vibrations, but additional instability can be caused by jittering of the laser's center frequency. Laser jitter is most commonly result of low frequency-induced pump current noise (60 Hz) and temperature fluctuations. To maximize stability for the frequency noise measurements, we pumped the lasers with a battery-powered ultralow-noise current source (CS, ILX LDX-3620) using a low-noise DC probe (Cascade Microtech DCQ). A low-pass filter (ILX LPF-320) was also used in line with the probe to further filter the current supply.

With all the electrical filtering applied, significant amount of temperature-induced jitter still remained, due to the exposure of the nonpackaged lasers to the ambient environment. To suppress the residual jitter and stabilize the interferometer at quadrature, a negative electronic feedback scheme was implemented. Part of the photodetector output was electronically subtracted from a reference voltage (REF) to create a correction signal for the source. This voltage signal, after being filtered of any excess noise imparted to it during the electronic processing, was supplied to the current source through its external modulation port, converted to a correction component superimposed on the pump current setpoint (SP) and fed back into the laser. The loop bandwidth was electronically controlled and kept low ($< 100\,\mathrm{Hz}$) to ensure that this artificial noise suppression was restricted to the low frequency temperature fluctuations and did not affect the bulk of the laser's frequency noise spectrum.

5.2.3.2 Results

Before we proceeded with the measurement of hybrid lasers, it was imperative that the integrity of the measurement scheme be verified. With regard to the BOA, we had to make sure that it was not adding excess phase noise and as for the feedback loop, that it was not interfering with the measurement, except only at very low frequencies. To perform those checks, we employed a commercial DFB laser (JDS Uniphase CQF-935/808), possessing enough output power and stability to be measured without BOA and feedback. Figure 5.24 presents frequency noise spectra of the JDSU laser taken with and without the use of BOA, while figure 5.25 spectra with and without feedback. In the case of the BOA, no significant difference between the two traces is observed, thus confirming that the BOA does not alter the frequency noise characteristics of the tested laser. In the case of the feedback, there is noticeable, though not substantial, discrepancy between the two traces in the low frequency end of the spectrum ($<$ $100\,\mathrm{Hz}$), with the noise under feedback being slightly reduced, as intended. There is further discrepancy between the two traces in a region of intermediate frequencies ($1\,\mathrm{kHz}$–$1\,\mathrm{MHz}$), with the noise with feedback this time being higher. This excess noise is attributed to the modulation circuit of the current source that is utilized in the
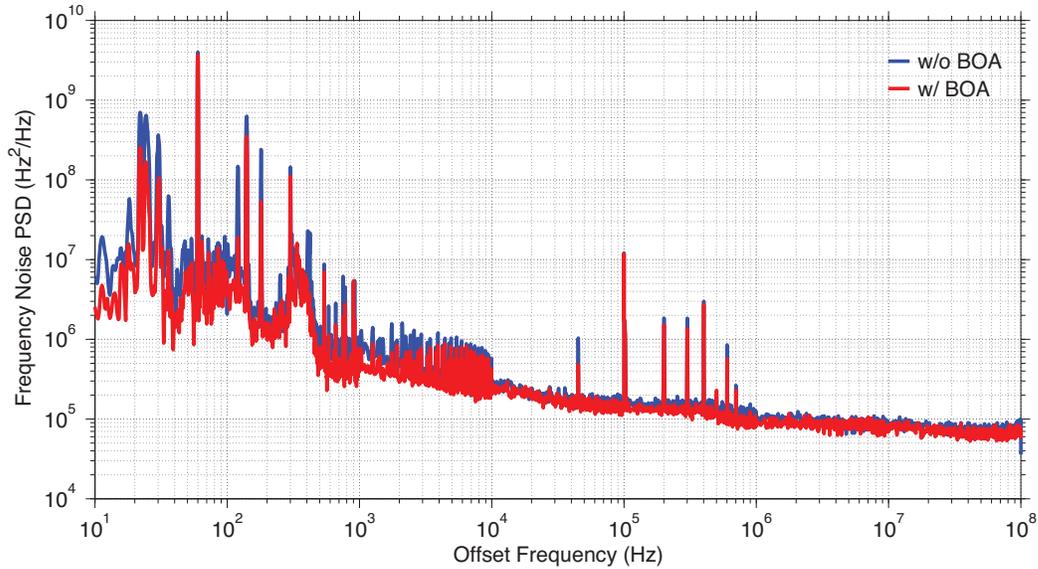
Figure 5.24. Frequency noise of the JDSU DFB laser with (red line) and without (blue line) BOA.
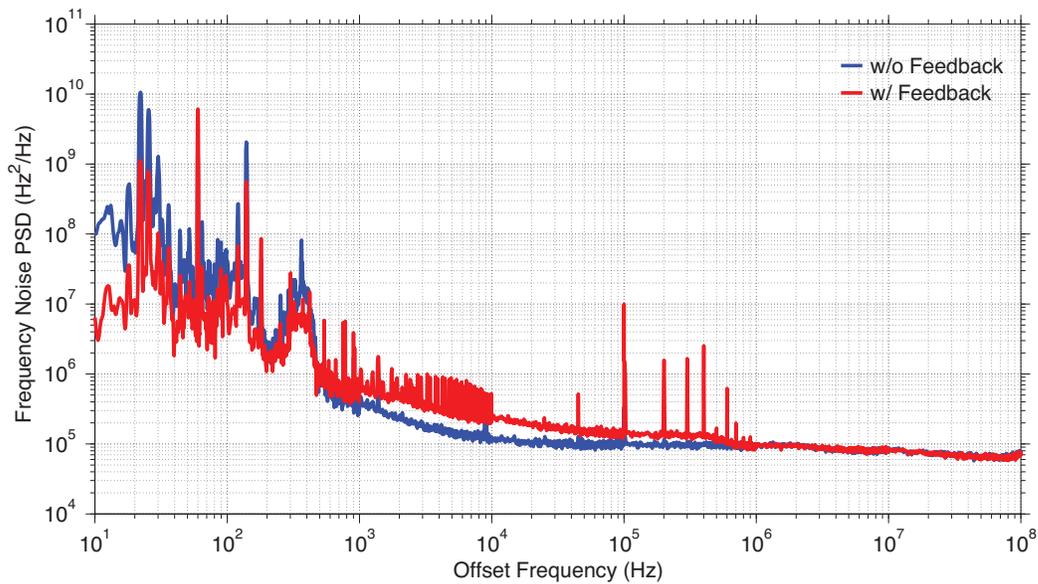
Figure 5.25. Frequency noise of the JDSU DFB laser with (red line) and without (blue line) feedback.

feedback scheme. Additional noise spikes are also present in the noise spectrum, also attributable to the current modulator. The two traces appear to match perfectly in the high frequency end of the spectrum ($> 1\,\mathrm{MHz}$), which, in the case of the JDSU

laser, is white noise. Therefore, the use of feedback stabilization was determined that it did not affect the extraction of the Schawlow-Townes linewidth.

As a further check of the integrity of the frequency noise measurement, we carried out a comparison of the relative contribution from sources of noise pertinent to the measurement configuration at hand. Figure 5.26 presents the electrical power spectra, as measured with the spectrum analyzer in [dbm/Hz], of four major noise components, laser frequency noise (blue), laser intensity noise (red), photodetector dark current noise (black) and spectrum analyzer noise (purple). The laser frequency noise measurement was taken with the MZI in the setup, while the laser intensity noise measurement with the MZI removed. For most of the pump currents used to drive the lasers, except only for those close to threshold, the intensity noise was found to be near or below the dark current noise. Therefore, the photodetector dark noise sets the noise floor, while the noise measured with no input into the spectrum analyzer defines the ultimate noise sensitivity. The measured laser frequency noise was consistently 10 db or higher above the noise floor, thus ensuring that no intensity or equipment-induced noise contribution was made to the frequency noise.

Using the configuration of figure 5.22, the electrical power spectrum corresponding to laser frequency noise was measured for high-Q hybrid lasers and via equation (5.15) converted to frequency noise power spectral density in [Hz^2/Hz]. Figure 5.27 shows a representative frequency noise spectrum of a high-Q hybrid laser. The inset shows the spectrum for the full frequency scan window (10 Hz–500 MHz), wherein the artificial noise suppression at low frequencies (< 100 Hz), as well as the onset of the MZI's roll-off (> 200 MHz) are evident. The noise spikes around 100 MHz correspond to FM radio noise. The truncated noise spectrum (1 kHz–100 MHz) can be divided into two main sections, a $1/f$-type section in (1 kHz–500 kHz) and a more gently sloped section in (500 kHz–100 MHz). In the scanned frequency range, the spectrum was never found to level off, to indicate the predominance of white noise. The scan window was limited by the length of the MZI and was the result of trade-off between frequency range and frequency gain, factored in through v_G in equation (5.11). This frequency noise pattern was consistently observed for all hybrid lasers tested. Therefore, we
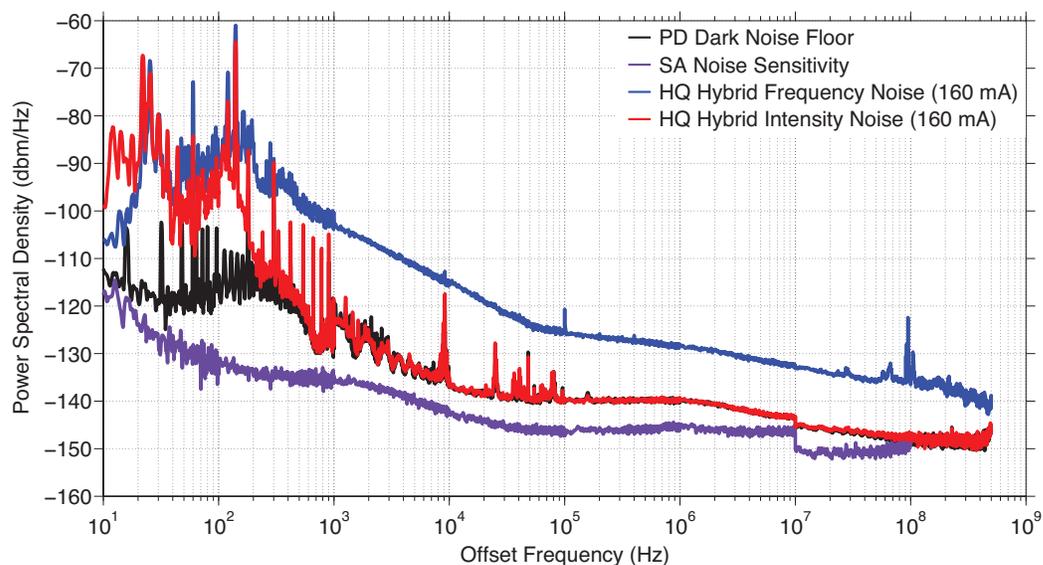
Figure 5.26. Frequency noise spectrum of a high-Q hybrid laser plotted against all relevant noise levels involved in the measurement: spectrum analyzer (SA) noise sensitivity, photodetector (PD) dark noise floor, high-Q hybrid laser intensity noise.

can conclude that the high-Q hybrid lasers frequency noise is dominated by technical noise for offset frequencies up to 100 MHz from the carrier. This noise pattern is, to
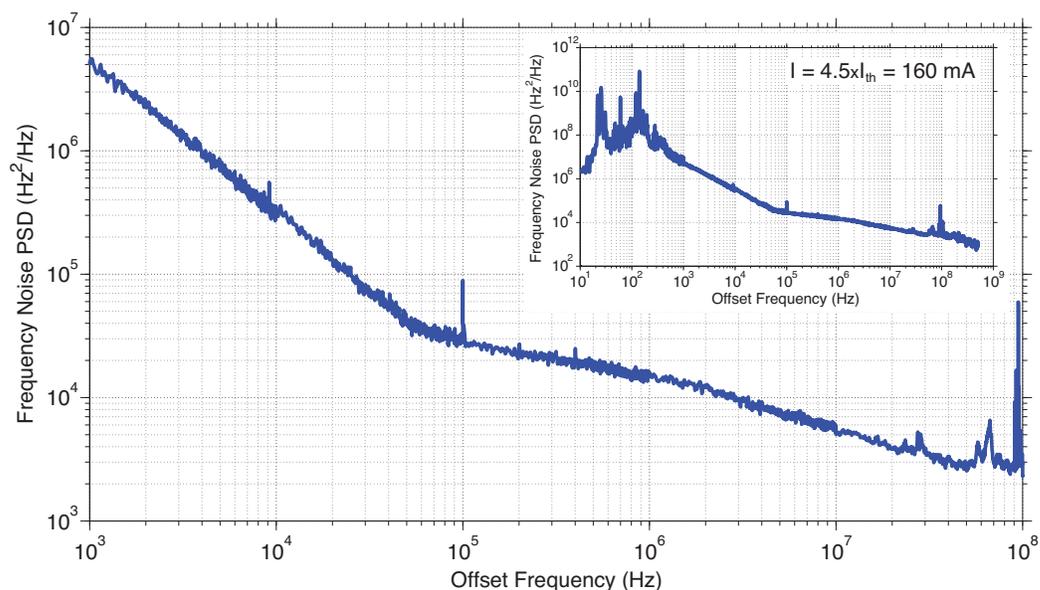
Figure 5.27. Frequency noise spectrum of a high-Q hybrid laser. Inset: same plot showing the full frequency scan range.

some extent, natural signature of the laser's internal dynamics and, to some other extent, result of the laser's technical and ambient environment (e.g., lack of packaging, current source noise, measurement equipment noise, etc.).

To the degree that the onset of a white noise floor was never well clearly observed, it is more accurate to speak in terms of an upper bound on the white noise linewidth, which is extracted from the power spectral density at the high end of the frequency noise spectrum ($\nu_{\max} \sim 100\,\mathrm{MHz}$) using

$$(\Delta\nu)_{ST} = 2\pi S_f(\nu_{\max}), \tag{5.16}$$

where the factor 2π is for a two-sided measured spectrum. This way, a minimum Schawlow-Townes linewidth of $18\,\mathrm{kHz}$ was found among all hybrid lasers tested and showcased in the frequency noise spectrum of figure 5.27. This result was for a laser based on a resonator with a photonic well design set of $V = 100\,\mathrm{GHz}, L_d = 200\,\mathrm{\mu m}$, driven at a pump current $4.5\times$ the threshold current of the particular device ($I_{th} = 35\,\mathrm{mA}$). This measurement, as well as all frequency noise measurements, were conducted at an operating temperature of $20\,^\circ\mathrm{C}$.

To calibrate the measurement scheme, as well as to contrast the high-Q hybrid lasers against a commercial laser standard, we measured the frequency noise of the JDSU DFB laser at different pump levels to find its minimum white noise linewidth. Figure 5.28 presents frequency noise spectra of a hybrid laser ($18\,\mathrm{kHz}$) and the JDSU DFB at drive currents $4\times$ ($100\,\mathrm{mA}$) and $12\times$ ($300\,\mathrm{mA}$) its threshold current ($I_{th} = 25\,\mathrm{mA}$). The JDSU DFB clearly exhibits white noise levels at all drive currents, with corresponding Schawlow-Townes linewidths of 500 and $160\,\mathrm{kHz}$ at $4\times$ and $12\times$ threshold respectively. The best hybrid laser is almost an order of magnitude better in linewidth than the JDSU laser, with the minimum linewidth for the hybrid achieved at only a fraction of the drive current required by the JDSU to achieve its own minimum.

We measured the frequency noise of a given high-Q hybrid laser as a function of the pump current. Figure 5.29 presents the minimum Schawlow-Townes linewidth extracted for each current, as a function of the normalized offset current from thresh-
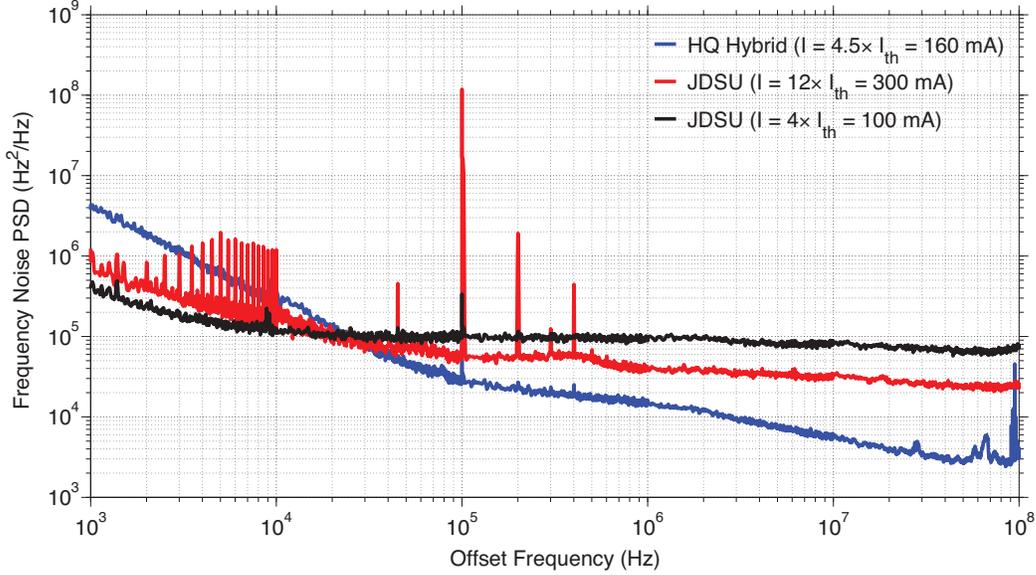
Figure 5.28. Frequency noise spectra of a high-Q hybrid laser and a JDSU DFB laser.

old, for a laser with threshold $I_{th} = 35\,\text{mA}$. The main figure presents the dependence of the linewidth on the offset current in linear scale, while the inset in log-log scale. Square solid markers denote measured data points. The fitting curve (red) in the linear plot illustrates the existence of a saturation floor for the white noise linewidth and the deviation from the dependence predicted by the Schawlow-Townes formula, expressed here in terms of the offset current as

$$(\Delta\nu)_{ST} = \frac{2\pi\eta e\nu_o^2}{Q^2 I_{th}\left(\frac{I}{I_{th}} - 1\right)}(1 + a^2). \tag{5.17}$$

A constant linewidth offset added to the above formula accounts for saturation. It was this linewidth offset that was recorded for every laser tested as its minimum linewidth. On the logarithmic scale, the linear fit denotes the range of validity of equation (5.17), with the deviation from it at higher offset values also evident. Upon further pumping, the linewidth starts to rebroaden, as documented in both scales of figure 5.29. In the case of the laser of figure 5.29, as well as in the case of several other lasers tested, this rebroadening was found to be the result of the onset of lasing of the dominant side mode (blue side mode). This occurrence was particularly pronounced
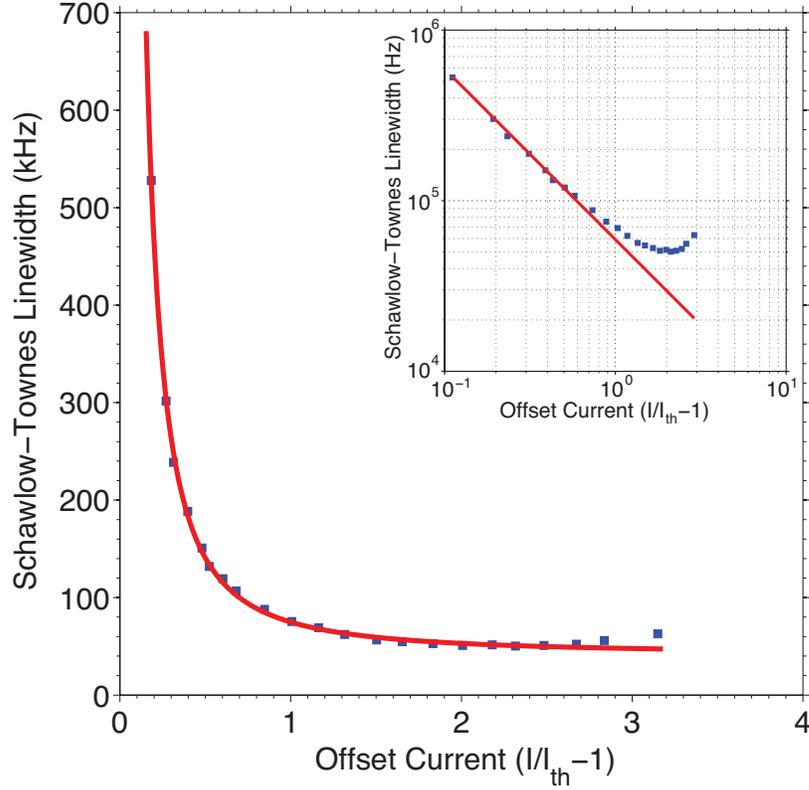
Figure 5.29. Schawlow-Townes linewidth as a function of offset pump current from threshold for a high-Q hybrid laser ($I_{th} = 35\,\text{mA}$). Inset: same plot in log-log scale.

on lasers based on the most undercoupled resonators, due to increased spatial hole burning at elevated pump currents. In other cases, rebroadening was found to be due to heating and the ensuing roll-off in the generated optical power.

The same current-dependent measurement was carried out for the JDSU DFB laser and the results for the two lasers are plotted against each other in log-log scale in figure 5.30. The linear fits on both data sets represent the region of compliance with the Schawlow-Townes formula. Frequency noise at threshold could not be measured reliably, though shortly above threshold, the JDSU laser exhibits a Schawlow-Townes linewidth over $10\,\text{MHz}$, whereas the hybrid laser a linewidth below $1\,\text{MHz}$. Over the linear regime, the two lasers are separated in linewidth by an average ratio of

$$\left(\frac{\Delta\nu_{Hybrid}}{\Delta\nu_{JDSU}}\right)_{ST} = \left(\frac{Q_{JDSU}}{Q_{Hybrid}}\right)^2 \frac{1 + a^2_{Hybrid}}{1 + a^2_{JDSU}} \simeq 25. \tag{5.18}$$

This reduction in linewidth is, as formulated in equation (5.18), the aggregate effect
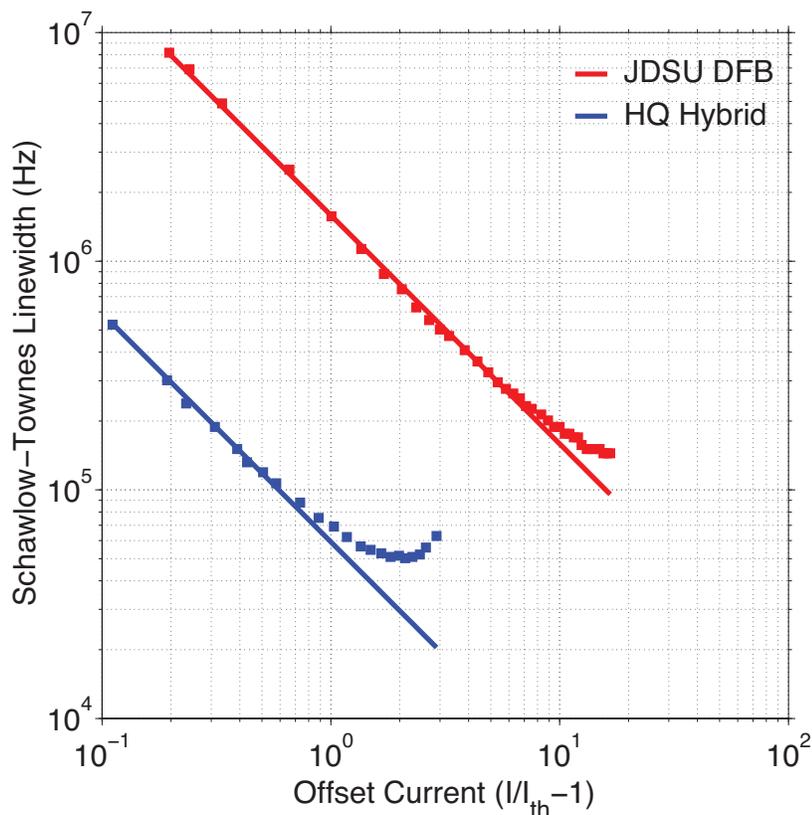
Figure 5.30. Schawlow-Townes linewidth as a function of offset pump current from threshold for a high-Q hybrid laser (blue line, $I_{th} = 35\,\mathrm{mA}$) and a JDSU DFB laser (red line, $I_{th} = 25\,\mathrm{mA}$) in log-log scale.

of improvement in loaded Q and linewidth enhancement factor a in the hybrid laser. The effect of the loaded Q itself is the combined result of reduced intrinsic losses in the hybrid resonator and of increased resonator undercoupling. Without further investigation, at this point, an exact breakdown of the contribution of each component to the linewidth reduction between the two lasers can only be of speculative nature. The JDSU laser also exhibits saturation in white noise linewidth, at about $12\times$ its threshold current and minimum linewidth of roughly $160\,\mathrm{kHz}$. Rebroadening on the JDSU was not observed, possibly due to its cavity's lesser degree of undercoupling, as a means to design against spatial hole burning.

As already mentioned in previous sections of this chapter, hybrid lasers were litho-

graphically tuned and single-mode, CW lasing was demonstrated over a wavelength span of 45 nm. Lasers of varying emission wavelength were also compared with respect to their frequency noise performance. Figure 5.31 presents the distribution of the Schawlow-Townes linewidth of an array of lithographically tuned hybrid lasers, all from a single chip. All lasers measured below 100 kHz, with a median linewidth of about 40 kHz. With the peak of the spontaneous emission spectrum located at approximately 1575 nm, the emission wavelength was tuned across the blue side of the peak, to utilize the linewidth enhancement factor's a decrease with blue detuning for additional linewidth reduction. [121–125, 188].
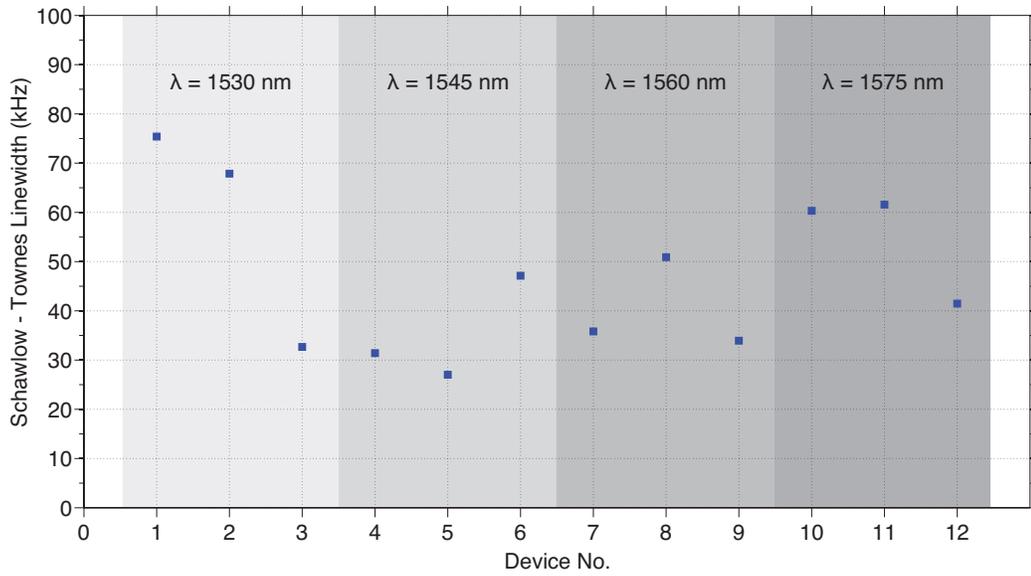
Figure 5.31. Distribution of the Schawlow-Townes linewidth of an array of lithographically tuned high-Q hybrid lasers from a single chip, spanning a wavelength range of 45 nm.

Chapter 6

Conclusion

6.1   Summary of the Thesis

In this work, we developed a new type of semiconductor laser with superior phase coherence to state of the art commercial DFB lasers. This breakthrough performance is enabled by a fundamentally new approach at laser cavity design. Separating the functions of photon generation and photon storage, naturally implemented on a hybrid Si/III-V material platform, offers previously unavailable degrees of freedom in laser cavity optimization, and specifically in the minimization of cavity losses. Minimizing cavity losses, quantified in the cold cavity quality factor Q, enables high photon-number storage with long photon lifetimes. This enhanced reservoir of coherent optical quanta acts as an optical flywheel, which by its inertia reduces the effect of spontaneous emission-mandated phase perturbations on the laser field. At the same time, enhanced cavity photon lifetimes reduce the temporal rate of spontaneously emitted incoherent quanta into the lasing mode. Conceptually, we approached the cavity design from a passive resonator optimization perspective, thereby redefining the way laser cavities are perceived and designed.

The single most critical aspect in the optimization process was the temporal loss rate of the resonator, as expressed through the quality factor Q. The resonator loss was analyzed into its constituent sources and each one was tackled individually. Oscillation frequency selection and mode control are provided by a specially designed 1D waveguide grating resonator. Radiation loss is suppressed via Fourier space engi-

neering. Longitudinal mode tailoring enables high side mode suppression ratios and increased tolerance against spatial hole burning under laser operation. Light absorption in the the active III-V medium is reduced by diluting the optical mode between the lossy active medium and the low absorbing Si. Key enabler for this optimization was the hybrid Si/III-V structure. Enabled by the optimized longitudinal mode engineering, these resonators were amenable to undercoupling to degrees unprecedented for conventional DFB laser resonators, thereby leading to enhanced photon-number storage and long photon lifetimes. The conceptual design optimizations were backed up by extensive and elaborate process development. Fabrication tools and methods were developed and refined with emphasis on high quality Si processing for ultra low-loss optical propagation and confinement. Designs and tools were both tested and demonstrated on purely Si 1D waveguide grating resonators for high photon-number storage, with loaded quality factors exceeding 1 million.

We demonstrated CW single-mode lasing on high-Q hybrid Si/III-V semiconductor lasers, over a temperature range of 10–70 °C, with threshold currents at room temperature as low as 30 mA for 1 mm long cavities. Side mode suppression ratios (SMSR) consistently exceeded 50 db. The laser resonators were intentionally undercoupled to maximize photon storage and lifetimes. Single-side output powers as high as 9 mW were collected for pump currents up to $5 \times I_{th}$. The critical benchmark metric for these lasers was their temporal coherence, quantified in the Schawlow-Townes linewidth. We performed thorough characterization of the frequency noise spectrum of the hybrid lasers and extracted white noise linewidths as low as 18 kHz at approximately $4.5 \times I_{th}$ (150 mA). The noise spectrum was found to be largely dominated at offset frequencies up to 100 MHz from the carrier by technical noise (e.g., $1/f$, sub-$1/f$, etc.) and no clear evidence of a white noise floor was observed. In that sense, the Schawlow-Townes linewidths cited in this work represent upper bounds on the phase noise due to spontaneous emission. The phase coherence metrics recorded for the high-Q hybrid lasers represent an order of magnitude improvement over the state of the art in coherence of DFB SCLs currently under deployment in coherent communication systems [189]. Even more remarkably, this breakthrough performance

was attained at just a fraction of the input power required by conventional DFBs to achieve lesser performance. This is direct consequence of the unprecedented high quality factors of the laser cavities developed in this work.

Consistently high-coherence performance was obtained for lithographically tuned high-Q hybrid lasers spanning a wavelength bandwidth of 45 nm (1530–1575 nm), while sustaining single-mode lasing with high SMSR (> 50 db). Emission wavelength fine-tuning was available via current, by approximately 1 nm (125 GHz) over the operating current range (30–150 mA), and additionally via temperature at a rate of 0.09 nm/K. Both tuning mechanisms more than suffice for the accurate positioning of an optical carrier within the 50 GHz of allotted channel bandwidth in WDM optical communications. Although not shown in this work, fine and precise spreading of wavelength carriers over extended bandwidth can be done lithographically using design parameters of the resonator (i.e depth of the photonic well V in [GHz]). This result is extremely promising for the prospect of densely integrated tunable laser assemblies (ITLA) for Tb/s-scale capacity links based on coherent optical communications [190].

6.2   Outlook

The result of this work represents a breakthrough in the field of communication lasers, especially in light of the potential afforded by DSP-enabled coherent systems. We believe that the future of optical communications lies in *optical coherent processing*. Already since the dawn of the DWDM era, the pivotal role of photonic integration started to be increasingly recognized [191]. As the number of components and the complexity of functions increases, large-scale integration emerges urgently as the only viable option for improved performance at reduced cost. Whether photonic integration remains anchored on InP [192] or finally transitions to Si-based CMOS platforms [193], certain technological challenges will need to be addressed. Communication lasers remain power-hungry devices and require constant and precise temperature control. This has been especially true for semiconductor lasers aiming at narrow linewidth performance. If SCLs are to be densely integrated in large numbers,

along with other optical components or even electronics, then power consumption and heat management have to be addressed.

In this work, we delivered breakout performance in laser coherence by redefining the way laser cavities are designed. As much of an enabler to that end the hybrid Si/III-V platform has proven to be, in terms of electrical efficiency and temperature dependence, these lasers are still largely restricted by the choice for the active medium. Quantum wells (QWs) ushered in outstanding characteristics, even so with regard to coherence, when they were originally introduced and have remained a staple in DFB SCL technology ever since. Yet, they do not represent the ultimate in potential afforded by quantum engineering. Quantum dots (QDs) in turn, with their full 3D quantum confinement (i.e., 0D dimensionality) have long held promise for superior laser characteristics [194]. In recent years, advances in the growth technology of QDs has brought this untapped potential within reach [195]. Three key features in particular stand out, extremely low thresholds [196, 197], high characteristic temperatures (i.e., threshold independence on temperature) [197–199] and low linewidth enhancement factors [200]. Early demonstrations of QD-based lasers are indicatively promising [201, 202]. We find the prospect of embedding a superior quantum emitter in a high-Q hybrid resonator, as the one developed in this work, extremely compelling and promising. The synergy between the two, we believe, can set a new standard in high-end semiconductor lasers. High-Q hybrid QD lasers operating at just a fraction of the current range of conventional QW SCLs, temperature robust and with improved coherence, can be the key to low power consumption, uncooled laser operation. Under these conditions, large-scale photonic integration or even on-chip convergence of photonics and electronics becomes a viable path toward coherent optical processing.

The second area wherein we envision great potential is that of *chip-based coherence purification*. While the coherence performance demonstrated in this work represents dramatic improvement for solitary semiconductor lasers, the golden standard in temporal coherence still belongs to non-semiconductor-based sources, such as those afforded by materials devoid of the broadening effect the amplitude to phase coupling, as in Er-doped glasses [203] or noninversion-type, nonlinear process, as in

stimulated Brillouin scattering (SBS) [204]. These sources are usually though available in complex and bulky, benchtop configurations, while most importantly, they require an independent optical seed. The availability of a coherent source of light on an ultralow-loss optical platform, especially with the degree of coherence achieved in this work, creates a natural and ideal testbed for optical diversification. For instance, coupling a solitary hybrid laser to an on-chip high-Q resonator in an optical injection configuration, can provide frequency stabilization and further phase noise reduction [205]. This locking scheme can then be readily utilized to harness the stabilized source as an optical seed (i.e., pump) for chip-based, resonant Erbium- or SBS-driven lasing, at extremely low threshold, enabling access to extreme coherence on chip scale.

Appendix A

Fabrication

Here, we detail the fabrication of high-Q hybrid Si/III-V semiconductor lasers. This is done in two sections. The first covers the process flow on the passive (SOI) platform and represents the fabrication of both Si-only resonators as well as of the passive counterpart of hybrid Si/III-V resonators. The second section describes the steps involved in the integration of Si and III-V for the realization of hybrid lasers.

A.1 Fabrication of High-Q Si Resonators

The passive platform is based on a Silicon-on-insulator (SOI) wafer, with Si device layer thickness of 500 nm and buffer oxide (BOX) thickness of 1.0 μm. The Si handle is typically thicker than 500 μm. The device layer is p-doped (Boron), with resistivity higher than $10\,\Omega\,$cm. The Si layer on the SOI wafer used in this work was thinned down, from originally 700 nm, by thermal oxidation and subsequent oxide etching.The process flow, illustrated in figure A.1, begins at the oxide-capped wafer.

Prior to the removal of the oxide cap, the sample surface (9 cm × 18 cm) is cleaned of organic contaminants in a hot Piranha bath. The Piranha solution is prepared out of $H_2SO_4 : H_2O_2$ at a volume ratio of 3 : 1. 3 parts of H_2SO_4 (typically 90 ml) are poured into a beaker and set on a hot plate to heat up to 90 °C. Once the desired temperature is reached, 1 part of H_2O_2 (e.g., 30 ml) is added to the mix, while the solution is kept on the hot plate at the set plate temperature. The reaction between H_2SO_4 and H_2O_2 is exothermic and leads to the rise of the solution temperature
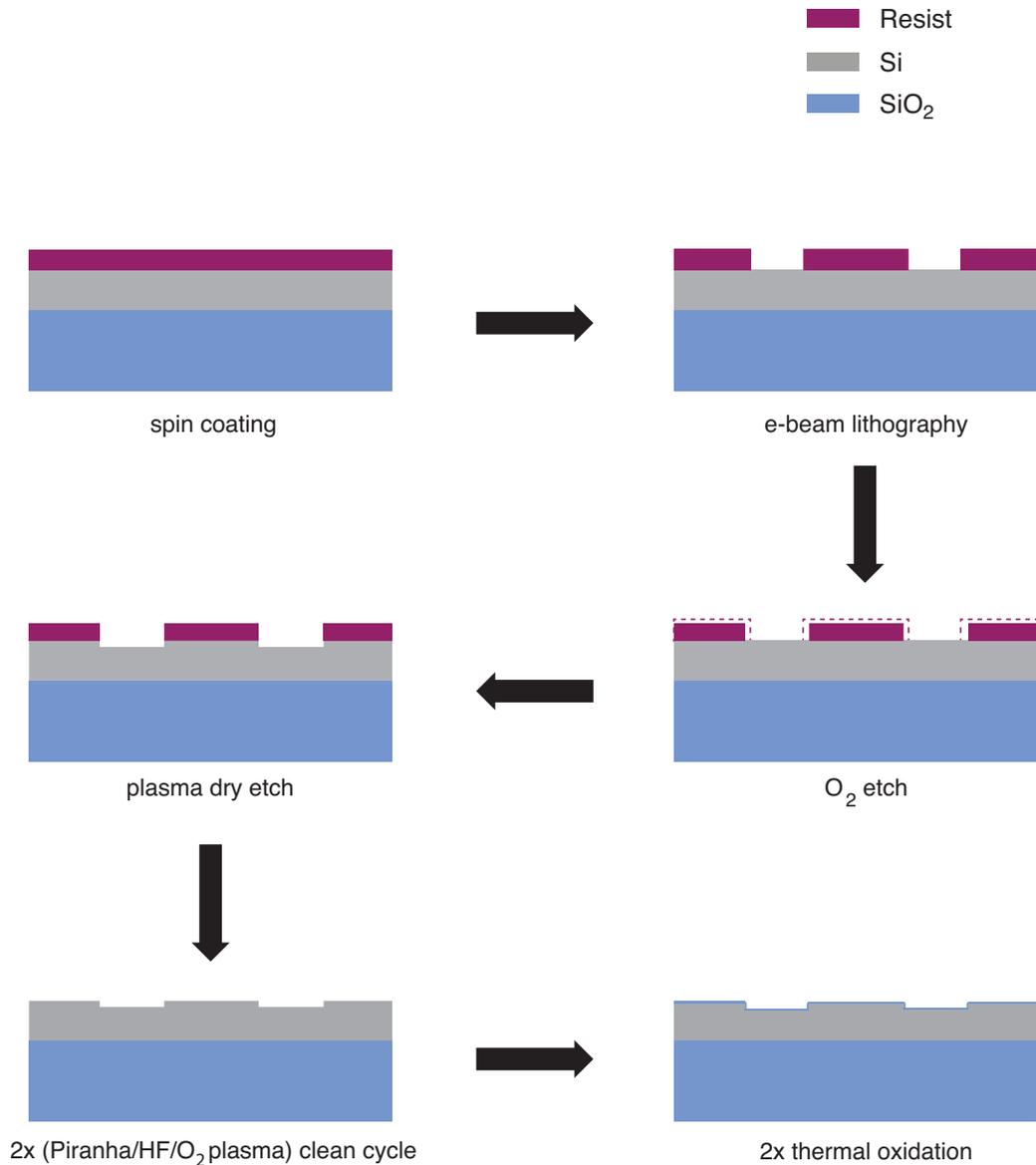
Figure A.1. High-Q Si resonator fabrication process flow.

to about 130 °C. The reactivity of the solution, manifested with the formation of bubbles, lasts for about 10–15 min, after which the sample is removed from the bath and rinsed under running deionized (DI) water for at least 2 min. This is important for washing off the surface the otherwise viscous H_2SO_4. The sample is then blow dried with N_2 and ready for the oxide removal.

The approximately 400 nm of thermal oxide (TOX) are removed by immersion in buffered oxide etch (BOE) hydrofluoric acid (Buffer HF improved) for 6 min. The

oxide-etched sample is then rinsed in DI water and blow dried. Complete removal of the oxide is evidenced by the perfect hydrophobicity of the surface following the water rinse. Given that the oxide cap also serves as a protection layer for the underlying Si, no further cleaning is warranted. In the absence of initial oxide, the Si device layer would be cleaned first, as described above.

The SOI sample is now ready for electron-beam(e-beam) lithography, which starts with the application of a positive electron sensitive resist (e-beam resist, ZEP 520A). ZEP 520A is chosen for its increased dry-etch resistance, as well as for its high sensitivity. Dipping in HF for the removal of native oxide was found to be necessary for reducing defects in the resist during spinning. In terms of resolution, the aforementioned resist is comparable to the commonly used PMMA. Approximately 350 nm of resist are spun on the sample at 5000 RPM for 1.5 min, followed by a hot plate bake at 180 °C for 10 min.

Resonators are patterned on resist using e-beam lithography (Vistec/Leica EBPG 5000+). Waveguides and gratings are patterned in the same lithography step. Patterns are split into a fine resolution (sleeve) and a coarse part (bulk) to optimize for both exposure time and resolution of critical features (e.g., holes). Sleeves are typically exposed with doses between 250–280 μCb/cm^2, beam current of 300 pA, resolution and beam step size (BSS) of 2.5 nm each. Bulks are exposed with doses around 230 μCb/cm^2, beam currents on the order of 5.0 nA, resolution and beam step size of 10 nm. The exact resist clearing dose, as well doses required to achieve certain critical dimensions, are highly pattern-dependent and can also vary significantly with the preparation conditions of the resist. Therefore, special dose calibration is necessary at the beginning of every new process.

The splitting into sleeve and bulk is also important for another reason. Overexposure of the sleeve part was found to help minimize line-edge roughness (LER), an optimization critical for the reduction of scattering losses [206,207]. LER in e-beam lithography is result partly of the discrete nature of the e-beam shot placement, and partly of imperfections inherent to the resist's chemical structure [208–210]. Overexposure of critical areas (e.g., waveguide boundaries, holes) as well as optimization

of the beam current/BSS ratio help address both sources of LER. Naturally, as a result of the overexposure, critical dimensions are often distorted in both shape and size. This is corrected for by careful calibration and application of appropriate feature biasing factors in the design pattern.

Exposed samples are developed in ZED-N50 for 1 min, followed by a 30 sec rinse in MIBK (methyl-isobutyl-ketone) and a final rinse with IPA (iso-propyl-alcohol), after which they are blow dried with N_2. Patterns are transferred into Si by means of dry plasma etching on a inductively coupled plasma, reactive ion etcher (ICP-RIE) [211, 212]. ICP-RIE allows the independent control of the plasma density and of the ion acceleration, which along with the control of the stage temperature and chamber pressure, enable precise etch tuning. On the same etcher and prior to the Si etch, samples are subjected, under controlled plasma conditions, to a very short (~ 4 sec) and directional O_2 plasma etch. This etch trims the resist and specifically the sidewall bottom, where residual LER typically persists.

The gas mixture used for the etching of Si is SF_6/C_4F_8 [213, 214]. Upon plasma ignition, SF_6 dissociates into primarily fluorine radicals that etch Si chemically, creating an isotropic etch component, and heavy SF_x^+ ions that are accelerated toward the RF-biased stage/electrode, contributing to a physical and highly directional etch component (i.e., milling). At the same time, C_4F_8 dissociates and polymerizes into a fluoro-carbon-based polymer ($\{C_xF_y\}_\nu$,Teflon-like) which is deposited everywhere on the exposed surface of the sample. Polymer deposited on horizontal surfaces (i.e., trench bottom) is readily removed under the effect of milling, thus allowing the etching of Si, both chemical and physical, to proceed in the vertical direction. Instead, on vertical surfaces (i.e., sidewalls), where no milling takes place, the polymer builds up, protecting (i.e., passivating) Si from being chemically etched. This interplay between milling and passivation, and specifically the relative rates of the two mechanisms, enable control over the anisotropy of the etch (i.e., angle of etched sidewalls). Highly anisotropic etches (i.e., vertical) are desirable for optical components such as waveguides and gratings. A gas flow rate ratio of 35 sccm : 45 sccm for SF_6 : C_4F_8 respectively, was found to provide the desired etch verticality, at an average total

etch rate of 400 nm/min [215]. A slightly enhanced isotropic component was found to help mask residual resist wall imperfections and reduce the line-edge roughness transferred to Si. The stage temperature and chamber pressure during the etch are set to 15 °C and 10 mTorr respectively. The ICP RF power controlling the density of the plasma is set to 1200 W, while the RF power applied to the stage electrode to 7 W. The latter is intentionally kept low to reduce the effective DC bias developed on the electrode, which controls the acceleration of ions toward the sample. A DC bias voltage between 20 and 30 V is found to provide the required milling component for the anisotropic etch, while keeping it at levels low enough to prevent mask erosion, that can cause severe roughness on the etched sidewalls.

Following the plasma etch, thorough cleaning is of critical importance. This is primarily due to the passivation polymer's extreme resistance to most commonly used solvents. Complete removal of the passivation was absolutely necessary, not only to free the fabricated devices of potential scatterers, but especially in preparation of the samples for thermal oxidation (see next step). An intricate cleaning process was developed for this purpose, comprising cycles of hot Piranha bath (as described above), immersion in HF and O_2 plasma. Alternating cycles of Piranha/HF, in addition to their organic contaminant removal effect, have been found to contribute to a gradual smoothing of Si surfaces, via the cycled chemical oxidation (Piranha) of Si and etching (HF) of the grown oxide, as well as to reduction of surface absorption states [216]. Yet, because the efficacy of Piranha/HF on the passivation polymer proved to be moderate, O_2 plasma was added to the cycle as the most effective way of removing the passivation. The O_2 plasma clean was performed on a ICP-RIE under precisely controlled conditions to minimize damage to Si.

After at least two cleaning cycles, samples are subjected to double dry thermal oxidation, as a means to further smooth Si surfaces and reduce scattering in the resonator. In principle, this method is equivalent to the chemical smoothing via Piranha/HF, only with more drastic effects. Cycles of thermal oxidation in the reaction-limited regime [217], followed by removal of the oxide in HF, has been found to significantly reduce surface roughness and improve propagation losses in waveg-

uides [218, 219]. In this case, dry oxidation is chosen over wet to more accurately control the amount of consumed Si. This is especially necessary to achieve the desired critical dimensions of nanoscale features (e.g., holes). The first oxidation is carried out for 10 min at 1000 °C, followed immediately by a 30 min anneal in N_2 atmosphere at the same temperature. The first oxide is removed in HF and samples are oxidized for a second time for 15 min, followed by another anneal. The final oxide (~ 20 nm) is left on to serve as a surface encapsulation layer [220]. Thermal oxide is of high optical quality, contributing negligible absorption loss, while the relatively higher refractive of SiO_2 (1.46) helps reduce the index contrast at the Si/air interface, thus reducing scattering [147, 221, 222]. The exact amount of Si consumed in each oxidation was calculated using Si oxidation kinetics, as modified by Massoud *et al* [223–226], to accurately account for the fast oxidation in the early thin-film regime. Theoretical calculations, combined with experimental calibration, was used to compensate for the total loss in Si in the original design.

Thermal oxidation is highly intolerant to organic contamination. Samples not perfectly cleaned of organic residues are severely damaged during oxidation. Organic residues, even of the smallest size, are believed to create hot spots, that lead to extreme local heating and to the final fracturing of the material attached to, as documented in figure A.2(a). Therefore, thorough cleaning prior to oxidation was deemed of absolute necessity. Figure A.2(b) shows section of the grating of a high-Q resonator from an as-oxidized sample, that was prior subjected through a 2 × (Piranha/HF/O_2 plasma) cleaning cycle. After the final oxidation, samples are ready, either for testing, in the case of Si resonators, or for hybridization, in the case of lasers.

A.2 Integration of Si and III-V for Hybrid Semiconductor Lasers

The hybrid integration process begins with two dies, a passive SOI one, patterned with devices and prepared through the process flow outlined in the previous section,
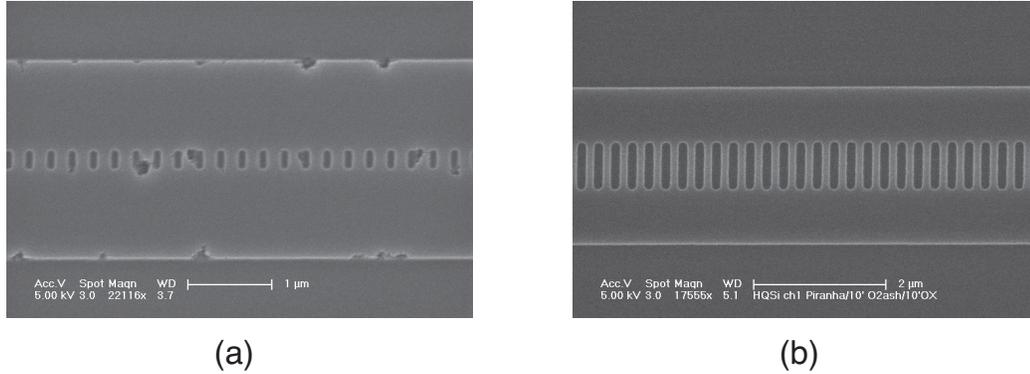
Figure A.2. Effect of organic contamination on Si during thermal oxidation. (a) Damage caused to contaminated sample. (b) Oxidized Si sample, treated with O_2 plasma prior to oxidation.

and an active III-V one (InGaAsP/InP) to provide the gain for the laser. The process is illustrated in figure A.3.

The two dies are first solvent cleaned (acetone/IPA/PG remover). To remove the native oxide from the surface, the active die is further immersed into a bath of $NH_4OH - DI\,H_2O$ at volume ratio of $1:15$ for $10\,min$, followed by a rinse with $DI\,H_2O$ and blow drying with N_2. The SOI die is intentionally not dipped in HF, to preserve the thermal oxide encapsulation layer. Instead, it is treated in Nanostrip for $1\,min$ for additional cleaning.

The two dies are now ready for bonding. The bonding method utilized in this work is often referred to as *plasma-assisted wafer bonding* [129, 227]. Treatment in O_2 plasma is known to grow a thin oxide, which in the case of the SOI die, already exists in the form of the thermal oxide encapsulation. Plasma treatment also activates the dies chemically, in that it creates a high density of dangling hydroxyl groups $(-OH)$ on the exposed surfaces, rendering them hydrophylic and chemically reactive in H_2O-based solutions. The dies are first brought to contact at room temperature and bond spontaneously via weak Van der Waals forces or hydrogen bonds, followed by strengthening of the bonding through the development of covalent bonds arising
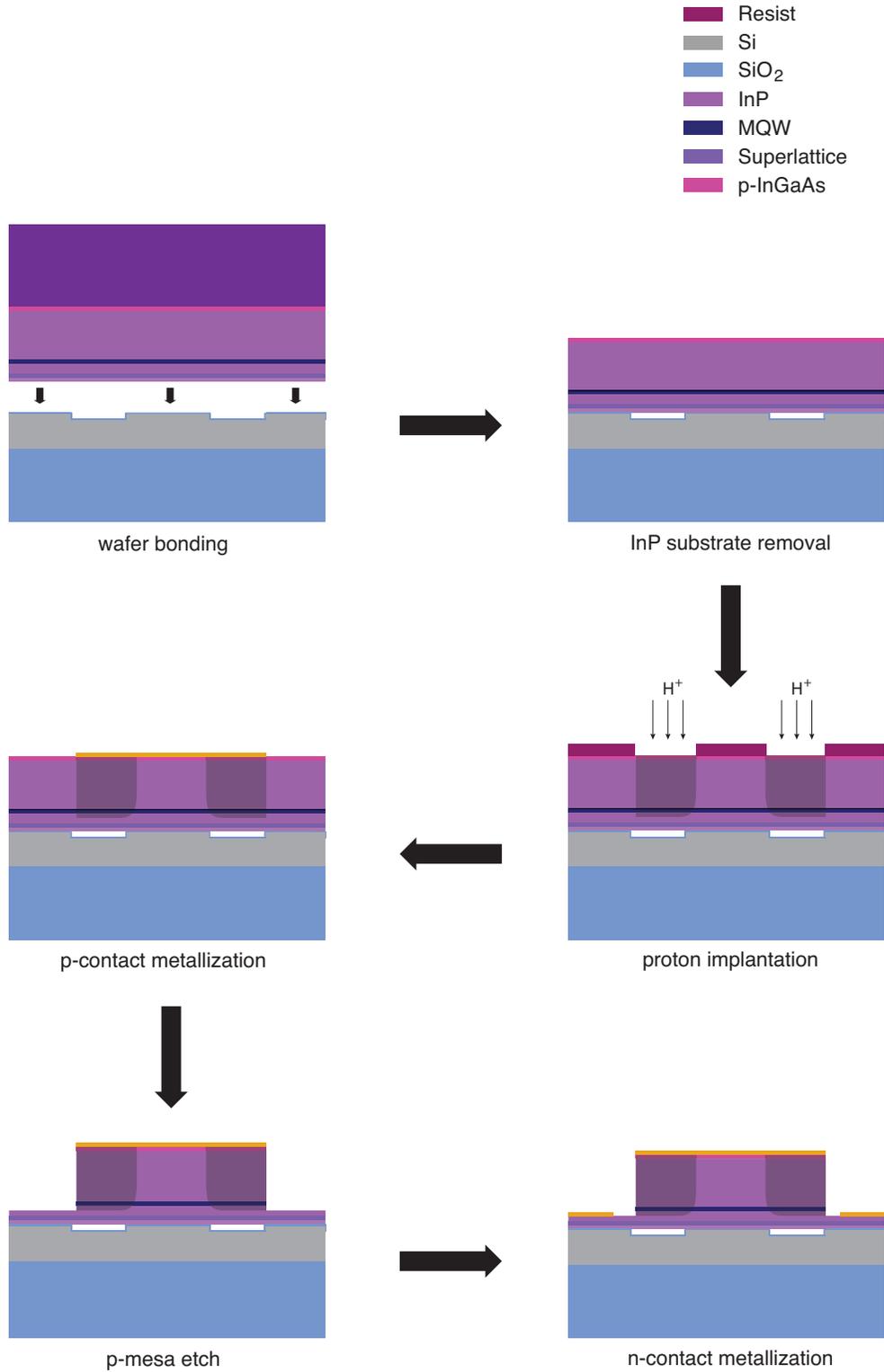
Figure A.3. High-Q hybrid laser fabrication process flow.

in Si-based hydrophylic bonding and described by the chemical reactions [228]:

$$\text{Si} - \text{OH} + \text{M} - \text{OH} \quad \longrightarrow \quad \text{Si} - \text{O} - \text{M} + \text{H}_2\text{O}_{(g)}, \tag{A.1}$$

$$\text{Si} + 2\text{H}_2\text{O} \quad \longrightarrow \quad \text{SiO}_2 + 2\text{H}_{2(g)}, \tag{A.2}$$
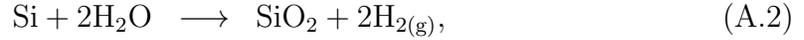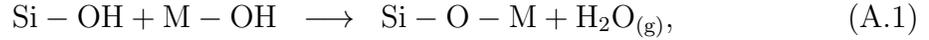
where M stands for metals of the III and V group. The above reactions are accelerated in a two-step annealing process, at $150\,°\text{C}$ for $1\,\text{h}$ and at $285\,°\text{C}$ for $5\,\text{h}$, under ambient pressure of $2 \times 10^{-2}\,\text{mbarr}$ and contact force of $1\,\text{N}$ over an approximate contact area of $0.5\,\text{mm}^2$. The choice of relatively low ($< 300\,°\text{C}$) temperatures is critical at enabling successful bonding between dissimilar materials, in terms of thermal expansion coefficients ($a_{Si} = 2.6 \times 10^{-6}\,\text{K}^{-1}, a_{InP} = 4.8 \times 10^{-6}\,\text{K}^{-1}$).

The gas byproducts H_2O and H_2 can get trapped at the bonding interface and create interfacial voids (i.e., bubbles), the size of which varies with wafer surface states, such as surface roughness and defect density [229]. Interfacial defects compromise the quality of the bonding interface and ultimately laser operation. Therefore, it is critical the gas byproducts be driven off effectively. The method utilized in this work to achieve this is the incorporation of vertical outgassing channels (VOCs) in the SOI die, prior to bonding [230]. VOCs are patterned in the Si layer, on the same lithography step with the functional devices, in the form of arrayed micron-wide square wells interleaved between devices. Gas byproducts of the bonding reactions (A.1, A.2) migrate toward the channels and get trapped in them. In the case where VOCs reach down to the BOX, gases can get absorbed in the oxide and gradually diffuse out through it. In devices fabricated in this work, VOCs were only partially etched into Si, due to the shallow waveguide depth, and therefore, the diffusion process is believed to proceed slower.

Following bonding, the InP substrate (typically a few hundred microns thick) of the III-V die is removed by wet etching in mixture of $\text{HCl} : \text{H}_2\text{O}$ at a ratio $1 : 3$. The etch lasts about $1\,\text{h}$ and its completion is evidenced by the termination of bubble generation in the solution. With the removal of the InP substrate, the remaining active epiwafer has a thickness of about $1.8\,\text{μm}$ and is subsequently patterned to create

the current injection functionality for the lasers. First, an injection confinement path for the current is created by means of proton (H^+) implantation. The implanted regions extend vertically through the p-side InP and and reach shortly below the MQW level, while laterally, they are symmetrically centered about the underlying waveguides in Si. This is achieved via alignment-assisted photolithography. Thick photoresist (Shipley 1813) masks the regions to be protected from ion bombardment. Protons raise the electrical resistivity of the implanted regions, thus preventing lateral current spreading and creating a narrow path for carriers, that overlaps with the guided optical mode. Typical widths of the injection path are on the order of $10\,\mu m$. The proton implantation is performed at acceleration energy of $170\,keV$, dose of $5 \times 10^{14}\,cm^{-2}$ and incident angle of $7°$.

A second photolithography step sets the sample up for p-side metallization. The p-contact is also centered about the the current injection window and spans laterally about $100\,\mu m$. A metal stack consisting of Ti/Pt/Au is deposited by e-beam evaporation in the same order and at thicknesses of $20\,nm/50\,nm/150\,nm$ respectively, followed by lift-off in acetone. With a third photolithography patterning, the sample is prepared for etching of the p-mesa, that provides access from the top to the n-side InP. Etching through the III-V epiwafer is performed in three sequential steps. A short $7\,sec$ dip in modified Piranha ($H_2SO_4 - H_2O_2 - H_2O$) at room temperature and ratio $1 : 1 : 10$ is used to etch through the uppermost p-InGaAs layer. The underlying p-InP serves as a natural etch stop. A second immersion in HCl for $17\,sec$ is used to etch through the p-InP, with an etch stop at the undoped InGaAsP, upper separate confinement layer (SCL). A final Piranha bath, as on the first step, is used to etch through the InGaAsP SCLs and MQW active region, coming to a stop at the n-InP. The width of the p-mesa is typically $150\,\mu m$.

A final photolithography and lift-off step patterns the sample with the n-side contacts. The metallization is performed again via e-beam evaporation and the stack is Ge/Au/Ni/Au with thicknesses $30\,nm/50\,nm/12\,nm/225\,nm$ respectively. Samples are subsequently thinned down to approximately $175\,\mu m$ by means of back-side (Si handle) lapping and cleaved into bars. Individual bars are annealed for contact alloy-

ing on a rapid thermal annealer (RTA) at 325–385 °C for 30 sec. The cleaved facets of bars are anti-reflection-coated (AR) via deposition (e-beam evaporation) of about 250 nm of alumina (Al_2O_3, $n = 1.78$), to suppress spurious reflections at the facets, that undermine mode stability, below 1%.

Bibliography

[1] A. H. Gnauck, R. W. Tkach, A. R. Chraplyvy, and T. Li, "High-capacity optical transmission systems," *J. Lightwave Technology*, vol. 26, no. 9-12, pp. 1032–1045, 2008.

[2] Y. Yamamoto, "Receiver performance evaluation of various digital optical modulation-demodulation systems in the $0.5\,\mu m - 10\,\mu m$ wavelength region," *IEEE J. Quantum Electronics*, vol. 16, no. 11, pp. 1251–1259, 1980.

[3] Y. Yamamoto and T. Kimura, "Coherent optical fiber transmission systems," *IEEE J. Quantum Electronics*, vol. 17, no. 6, pp. 919–935, 1981.

[4] K. Kikuchi, "Digital coherent optical communication systems: fundamentals and future prospects," *IEICE Electronics Express*, vol. 8, no. 20, pp. 1642–1662, 2011.

[5] S. Saito, Y. Yamamoto, and T. Kimura, "Optical heterodyne detection of directly frequency modulated semiconductor laser signals," *Electronics Lett.*, vol. 16, no. 22, pp. 826–827, 1980.

[6] E. Ip, A. P. T. Lau, D. J. F. Barros, and J. M. Kahn, "Coherent detection in optical fiber systems," *Optics Express*, vol. 16, no. 2, pp. 753–791, 2008.

[7] F. Favre and D. Leguen, "High frequency stability of laser diode for heterodyne communication systems," *Electronics Lett.*, vol. 16, no. 18, pp. 709–710, 1980.

[8] T. Okoshi and K. Kikuchi, "Frequency stabilization of semiconductor lasers for heterodyne-type optical communication systems," *Electronics Lett.*, vol. 16, no. 5, pp. 179–181, 1980.

[9] J. M. Kahn, A. H. Gnauck, J. J. Veselka, S. K. Korotky, and B. L. Kasper, "4 Gb/s PSK homodyne transmission system using phase-locked semiconductor lasers," *IEEE Photonics Technology Lett.*, vol. 2, no. 4, pp. 285–287, 1990.

[10] J. M. Kahn, A. M. Porter, and U. Padan, "Heterodyne detection of 310 Mb/s quadriphase-shift keying using 4th-power optical phase-locked loop," *IEEE Photonics Technology Lett.*, vol. 4, no. 12, pp. 1397–1400, 1992.

[11] L. G. Kazovsky, "Performance analysis and laser linewidth requirements for optical PSK heterodyne communications systems," *J. Lightwave Technology*, vol. 4, no. 4, pp. 415–425, 1986.

[12] L. G. Kazovsky, "Impact of laser phase noise on optical heterodyne communication systems," *Journal of Optical Communications*, vol. 7, no. 2, pp. 66–78, 1986.

[13] J. R. Barry and E. A. Lee, "Performance of coherent optical receivers," *Proc. IEEE*, vol. 78, no. 8, pp. 1369–1394, 1990.

[14] T. Y. Li, "The impact of optical amplifiers on long-distance lightwave telecommunications," *Proc. IEEE*, vol. 81, no. 11, pp. 1568–1579, 1993.

[15] P. J. Winzer and R. J. Essiambre, "Advanced optical modulation formats," *Proc. IEEE*, vol. 94, no. 5, pp. 952–985, 2006.

[16] J. M. Kahn and K. P. Ho, "Spectral efficiency limits and modulation/detection techniques for DWDM systems," *IEEE J. Selected Topics In Quantum Electronics*, vol. 10, no. 2, pp. 259–272, 2004.

[17] P. J. Winzer, "High-spectral-efficiency optical modulation formats," *J. Lightwave Technology*, vol. 30, no. 24, pp. 3824–3835, 2012.

[18] S. Tsukamoto, K. Katoh, and K. Kikuchi, "Coherent demodulation of optical multilevel phase-shift-keying signals using homodyne detection and digital sig-

nal processing," *IEEE Photonics Technology Lett.*, vol. 18, no. 9-12, pp. 1131–1133, 2006.

[19] S. Tsukamoto, K. Katoh, and K. Kikuchi, "Unrepeated transmission of 20 Gb/s optical quadrature phase-shift-keying signal over 200 km standard single-mode fiber based on digital processing of homodyne-detected signal for group velocity dispersion compensation," *IEEE Photonics Technology Lett.*, vol. 18, no. 9-12, pp. 1016–1018, 2006.

[20] M. G. Taylor, "Phase estimation methods for optical coherent detection using digital signal processing," *J. Lightwave Technology*, vol. 27, no. 5-8, pp. 901–914, 2009.

[21] K. Roberts, M. O'Sullivan, K. T. Wu, H. Sun, A. Awadalla, D. J. Krause, and C. Laperle, "Performance of dual-polarization QPSK for optical transport systems," *J. Lightwave Technology*, vol. 27, no. 16, pp. 3546–3559, 2009.

[22] M. Taylor, "Coherent detection method using DSP for demodulation of signal and subsequent equalization of propagation impairments," *IEEE Photonics Technology Lett.*, vol. 16, no. 2, pp. 674–676, 2004.

[23] E. Ip and J. M. Kahn, "Digital equalization of chromatic dispersion and polarization mode dispersion," *J. Lightwave Technology*, vol. 25, no. 8, pp. 2033–2043, 2007.

[24] E. M. Ip and J. M. Kahn, "Fiber impairment compensation using coherent detection and digital signal processing," *J. Lightwave Technology*, vol. 28, no. 4, pp. 502–519, 2010.

[25] S. J. Savory, G. Gavioli, R. I. Killey, and P. Bayvel, "Electronic compensation of chromatic dispersion using a digital coherent receiver," *Optics Express*, vol. 15, no. 5, pp. 2120–2126, 2007.

[26] C. R. S. Fludger, T. Duthel, D. V. den Borne, C. Schulien, E. D. Schmidt, T. Wuth, J. Geyer, E. D. Man, G. D. Khoe, and H. de Waardt, "Coherent

equalization and POLMUX-RZ-DQPSK for robust 100-GE transmission," *J. Lightwave Technology*, vol. 26, no. 1-4, pp. 64–72, 2008.

[27] V. Curri, P. Poggiolini, A. Carena, and F. Forghieri, "Dispersion compensation and mitigation of nonlinear effects in 111 Gb/s WDM coherent PM-QPSK systems," *IEEE Photonics Technology Lett.*, vol. 20, no. 17-20, pp. 1473–1475, 2008.

[28] P. P. Mitra and J. B. Stark, "Nonlinear limits to the information capacity of optical fibre communications," *Nature*, vol. 411, no. 6841, pp. 1027–1030, 2001.

[29] R. J. Essiambre, G. Kramer, P. J. Winzer, G. J. Foschini, and B. Goebel, "Capacity limits of optical fiber networks," *J. Lightwave Technology*, vol. 28, no. 4, pp. 662–701, 2010.

[30] K. Kikuchi, "Electronic post-compensation for nonlinear phase fluctuations in a 1000 km 20 Gbit/s optical quadrature phase-shift keying transmission system using the digital coherent receiver," *Optics Express*, vol. 16, no. 2, pp. 889–896, 2008.

[31] K. Roberts, C. D. Li, L. Strawczynski, M. O'Sullivan, and I. Hardcastle, "Electronic precompensation of optical nonlinearity," *IEEE Photonics Technology Lett.*, vol. 18, no. 1-4, pp. 403–405, 2006.

[32] E. Ip and J. M. Kahn, "Compensation of dispersion and nonlinear impairments using digital backpropagation," *J. Lightwave Technology*, vol. 26, no. 17-20, pp. 3416–3425, 2008.

[33] A. Yariv and P. Yeh, *Photonics - Optical Electronics in modern communications (6th Edition)*. New York, NY: Oxford University Press, 2007.

[34] A. Yariv and W. M. Caton, "Frequency, intensity, and field fluctuations in laser oscillators," *IEEE J. Quantum Electronics*, vol. QE10, no. 6, pp. 509–515, 1974.

[35] A. L. Schawlow and C. H. Townes, "Infrared and optical masers," *Phys. Rev.*, vol. 112, no. 6, pp. 1940–1949, 1958.

[36] S. Saito and Y. Yamamoto, "Direct observation of Lorentzian lineshape of semiconductor laser and linewidth reduction with external grating feedback," *Electronics Lett.*, vol. 17, no. 9, pp. 325–327, 1981.

[37] M. W. Fleming and A. Mooradian, "Fundamental line broadening of single-mode GaAlAs diode lasers," *Appl. Phys. Lett.*, vol. 38, no. 7, pp. 511–513, 1981.

[38] M. Lax, "Classical noise. V. Noise in self sustained oscillators," *Phys. Rev.*, vol. 160, no. 2, pp. 290–307, 1967.

[39] C. H. Henry, "Theory of the linewidth of semiconductor lasers," *IEEE J. Quantum Electronics*, vol. 18, no. 2, pp. 259–264, 1982.

[40] C. H. Henry, "Theory of the phase noise and power spectrum of a single-mode injection laser," *IEEE J. Quantum Electronics*, vol. 19, no. 9, pp. 1391–1397, 1983.

[41] C. H. Henry, "Phase noise in semiconductor lasers," *J. Lightwave Technology*, vol. 4, no. 3, pp. 298–311, 1986.

[42] K. Vahala and A. Yariv, "Semiclassical theory of noise in semiconductor lasers - Part I," *IEEE J. Quantum Electronics*, vol. 19, no. 6, pp. 1096–1101, 1983.

[43] K. Vahala and A. Yariv, "Semiclassical theory of noise in semiconductor lasers - Part II," *IEEE J. Quantum Electronics*, vol. 19, no. 6, pp. 1102–1109, 1983.

[44] K. Kikuchi and T. Okoshi, "Dependence of semiconductor-laser linewidth on measurement time - evidence of predominance of 1/f noise," *Electronics Lett.*, vol. 21, no. 22, pp. 1011–1012, 1985.

[45] K. Kikuchi, "Origin of residual semiconductor laser linewidth in high-power limit," *Electronics Lett.*, vol. 24, no. 16, pp. 1001–1002, 1988.

[46] K. Kikuchi, "Effect of 1/f-type FM noise on semiconductor laser linewidth residual in high-power limit," *IEEE J. Quantum Electronics*, vol. 25, no. 4, pp. 684–688, 1989.

[47] M. Okai, T. Tsuchiya, K. Uomi, N. Chinone, and T. Harada, "Effect of 1/f noise on the spectral linewidth of corrugation-pitch-modulated multi-quantum-well distributed feedback lasers at high output power," *IEEE Photonics Technology Lett.*, vol. 3, no. 5, pp. 427–429, 1991.

[48] M. Okai, T. Tsuchiya, A. Takai, and N. Chinone, "Factors limiting the spectral linewidth of CPM-MQW-DFB lasers," *IEEE Photonics Technology Lett.*, vol. 4, no. 6, pp. 526–528, 1992.

[49] K. Kikuchi, "Impact of 1/f-type FM noise on coherent optical communications," *Electronics Lett.*, vol. 23, no. 17, pp. 885–887, 1987.

[50] K. Kikuchi, T. Okoshi, M. Nagamatsu, and N. Henmi, "Degradation of bit-error rate in coherent optical communications due to spectral spread of the transmitter and the local oscillator," *J. Lightwave Technology*, vol. 2, no. 6, pp. 1024–1033, 1984.

[51] S. Yamazaki and K. Emura, "Feasibility study on QPSK optical heterodyne detection system," *J. Lightwave Technology*, vol. 8, no. 11, pp. 1646–1653, 1990.

[52] L. G. Kazovsky, G. Kalogerakis, and W. T. Shaw, "Homodyne phase-shift-keying systems: Past challenges and future opportunities," *J. Lightwave Technology*, vol. 24, no. 12, pp. 4876–4884, 2006.

[53] D. S. Ly-Gagnon, K. Katoh, and K. Kikuchi, "Unrepeated optical transmission of 20Gbit/s quadrature phase-shift keying signals over 210 km using homodyne phase-diversity receiver and digital signal processing," *Electronics Lett.*, vol. 41, no. 4, pp. 206–207, 2005.

[54] M. Taylor, "Accurate digital phase estimation process for coherent detection using a parallel digital processor," in *ECOC*, vol. 2, pp. 263–264, 2005.

[55] D. S. Ly-Gagnon, S. Tsukarnoto, K. Katoh, and K. Kikuchi, "Coherent detection of optical quadrature phase-shift keying signals with carrier phase estimation," *J. Lightwave Technology*, vol. 24, no. 1, pp. 12–21, 2006.

[56] K. Kikuchi, "Coherent detection of phase-shift keying signals using digital carrier-phase estimation," in *Optical Fiber Communication Conference*, 2006.

[57] S. Norimatsu and K. Iwashita, "Linewidth requirements for optical synchronous detection systems with nonnegligible loop delay time," *J. Lightwave Technology*, vol. 10, no. 3, pp. 341–349, 1992.

[58] J. R. Barry and J. M. Kahn, "Carrier synchronization for homodyne and heterodyne detection of optical quadriphase-shift keying," *J. Lightwave Technology*, vol. 10, no. 12, pp. 1939–1951, 1992.

[59] E. Ip and J. M. Kahn, "Carrier synchronization for 3-and 4-bit-per-symbol optical transmission," *J. Lightwave Technology*, vol. 23, no. 12, pp. 4110–4124, 2005.

[60] E. Ip and J. M. Kahn, "Feedforward carrier recovery for coherent optical communications," *J. Lightwave Technology*, vol. 25, no. 9, pp. 2675–2692, 2007.

[61] M. Seimetz, "Laser linewidth limitations for optical systems with high-order modulation employing feed forward digital carrier phase estimation," *Optical Fiber Communication Conference*, vol. 1–8, pp. 2470–2472, 2008.

[62] R. Wyatt and W. J. Devlin, "10 kHz linewidth $1.5\,\mu m$ InGaAsP external cavity laser with 55 nm tuning range," *Electronics Lett.*, vol. 19, no. 3, pp. 110–112, 1983.

[63] I. D. Henning, L. D. Westbrook, A. W. Nelson, and P. J. Fiddyment, "Measurements of the linewidth of ridge-guide DFB lasers," *Electronics Lett.*, vol. 20, no. 21, pp. 885–887, 1984.

[64] M. R. Matthews, K. H. Cameron, R. Wyatt, and W. J. Devlin, "Packaged frequency-stable tunable 20 kHz linewidth $1.5\,\mu m$ InGaAsP external cavity laser," *Electronics Lett.*, vol. 21, no. 3, pp. 113–115, 1985.

[65] E. Ip, J. M. Kahn, D. Anthon, and J. Hutchins, "Linewidth measurements of MEMS-based tunable lasers for phase-locking applications," *IEEE Photonics Technology Lett.*, vol. 17, no. 10, pp. 2029–2031, 2005.

[66] H. Kogelnik and C. V. Shank, "Coupled-wave theory of distributed feedback lasers," *J. Appl. Phys.*, vol. 43, no. 5, pp. 2327–2335, 1972.

[67] H. Kogelnik and C. V. Shank, "Stimulated emission in a periodic structure," *Appl. Phys. Lett.*, vol. 18, no. 4, pp. 152–154, 1971.

[68] M. Nakamura, H. W. Yen, A. Yariv, E. Garmire, S. Somekh, and H. L. Garvin, "Laser oscillation in epitaxial GaAs waveguides with corrugation feedback," *Appl. Phys. Lett.*, vol. 23, no. 5, pp. 224–225, 1973.

[69] M. Nakamura, A. Yariv, H. W. Yen, S. Somekh, and H. L. Garvin, "Optically pumped GaAs surface laser with corrugation feedback," *Appl. Phys. Lett.*, vol. 22, no. 10, pp. 515–516, 1973.

[70] M. Nakamura, K. Aiki, J. Umeda, A. Yariv, H. W. Yen, and T. Morikawa, "$\text{GaAs}-\text{Ga}_{1-\text{x}}\text{Al}_{\text{x}}\text{As}$ double-heterostructure distributed-feedback diode lasers," *Appl. Phys. Lett.*, vol. 25, no. 9, pp. 487–488, 1974.

[71] M. Nakamura and A. Yariv, "Analysis of threshold of double heterojunction GaAs-GaAlAs lasers with a corrugated interface," *Optics Comm.*, vol. 11, no. 1, pp. 18–20, 1974.

[72] M. Nakamura, K. Aiki, J. Umeda, and A. Yariv, "CW operation of distributed-feedback GaAs-GaAlAs diode lasers at temperatures up to 300 K," *Appl. Phys. Lett.*, vol. 27, no. 7, pp. 403–405, 1975.

[73] K. Aiki, M. Nakamura, J. Umeda, A. Yariv, A. Katzir, and H. W. Yen, "GaAs-GaAlAs distributed-feedback diode lasers with separate optical and carrier confinement," *Appl. Phys. Lett.*, vol. 27, no. 3, pp. 145–146, 1975.

[74] M. Nakamura, K. Aiki, J. Umeda, A. Katzir, A. Yariv, and H. W. Yen, "GaAs-GaAlAs double-heterostructure injection lasers with distributed feedback," *IEEE J. Quantum Electronics*, vol. QE11, no. 7, pp. 436–439, 1975.

[75] A. Yariv and M. Nakamura, "Periodic structures for integrated optics," *IEEE J. Quantum Electronics*, vol. 13, no. 4, pp. 233–253, 1977.

[76] H. A. Haus and C. V. Shank, "Antisymmetric taper of distributed feedback lasers," *IEEE J. Quantum Electronics*, vol. 12, no. 9, pp. 532–539, 1976.

[77] K. Sekartedjo, N. Eda, K. Furuya, Y. Suematsu, F. Koyama, and T. Tanbunek, "1.5 μm phase-shifted DFB lasers for single-mode operation," *Electronics Lett.*, vol. 20, no. 2, pp. 80–81, 1984.

[78] F. Koyama, Y. Suematsu, K. Kojima, and K. Furuya, "1.5 μm phase adjusted active distributed reflector laser for complete dynamic single-mode operation," *Electronics Lett.*, vol. 20, no. 10, pp. 391–393, 1984.

[79] K. Utaka, S. Akiba, K. Sakai, and Y. Matsushima, "Analysis of quarter-wave-shifted DFB laser," *Electronics Lett.*, vol. 20, no. 8, pp. 326–327, 1984.

[80] S. L. McCall and P. M. Platzman, "An optimized $\pi/2$ distributed feedback laser," *IEEE J. Quantum Electronics*, vol. 21, no. 12, pp. 1899–1904, 1985.

[81] K. Utaka, S. Akiba, K. Sakai, and Y. Matsushima, "$\lambda/4$-shifted InGaAsP/InP DFB lasers," *IEEE J. Quantum Electronics*, vol. 22, no. 7, pp. 1042–1051, 1986.

[82] S. Akiba, M. Usami, and K. Utaka, "1.5 μm $\lambda/4$-shifted InGaAsP/InP DFB lasers," *J. Lightwave Technology*, vol. 5, no. 11, pp. 1564–1573, 1987.

[83] Y. Kotaki, S. Ogita, M. Matsuda, Y. Kuwahara, and H. Ishikawa, "Tunable, narrow-linewidth and high-power $\lambda/4$-shifted DFB laser," *Electronics Lett.*, vol. 25, no. 15, pp. 990–992, 1989.

[84] M. Kitamura, H. Yamazaki, T. Sasaki, N. Kida, H. Hasumi, and I. Mito, "250 kHz spectral linewidth operation of $1.5\,\mu m$ multiple quantum-well DFB LDs," *IEEE Photonics Technology Lett.*, vol. 2, no. 5, pp. 310–311, 1990.

[85] H. Ishii, K. Kasaya, and H. Oohashi, "Spectral linewidth reduction in widely wavelength tunable DFB laser array," *IEEE J. Selected Topics In Quantum Electronics*, vol. 15, no. 3, pp. 514–520, 2009.

[86] H. Ishii, K. Kasaya, and H. Oohashi, "Narrow spectral linewidth operation (< 160 kHz) in widely tunable distributed feedback laser array," *Electronics Lett.*, vol. 46, no. 10, pp. 714–U74, 2010.

[87] L. P. Hou, M. Haji, J. Akbar, and J. H. Marsh, "Narrow linewidth laterally coupled $1.55\,\mu m$ AlGaInAs/InP distributed feedback lasers integrated with a curved tapered semiconductor optical amplifier," *Optics Lett.*, vol. 37, no. 21, pp. 4525–4527, 2012.

[88] K. Utaka, S. Akiba, K. Sakai, and Y. Matsushima, "Longitudinal-mode behavior of $\lambda/4$-shifted InGaAsP/InP DFB lasers," *Electronics Lett.*, vol. 21, no. 9, pp. 367–368, 1985.

[89] S. Ogita, Y. Kotaki, K. Kihara, M. Matsuda, H. Ishikawa, and H. Imai, "Dependence of spectral linewidth on cavity length and coupling coefficient in DFB laser," *Electronics Lett.*, vol. 24, no. 10, pp. 613–614, 1988.

[90] M. Okai, S. Tsuji, and N. Chinone, "Stability of the longitudinal mode in $\lambda/4$-shifted InGaAsP-InP DFB lasers," *IEEE J. Quantum Electronics*, vol. 25, no. 6, pp. 1314–1319, 1989.

[91] M. C. Wu, Y. H. Lo, and S. Wang, "Linewidth broadening due to longitudinal spatial hole burning in a long distributed feedback laser," *Appl. Phys. Lett.*, vol. 52, no. 14, pp. 1119–1121, 1988.

[92] R. Schatz, "Longitudinal spatial instability in symmetrical semiconductor lasers due to spatial hole burning," *IEEE J. Quantum Electronics*, vol. 28, no. 6, pp. 1443–1449, 1992.

[93] X. Pan, H. Olesen, and B. Tromborg, "Spectral linewidth of DFB lasers including the effects of spatial hole burning and non-uniform current injection," *IEEE Photonics Technology Lett.*, vol. 2, no. 5, pp. 312–315, 1990.

[94] A. Takemoto, Y. Ohkura, Y. Kawama, Y. Nakajima, T. Kimura, N. Yoshida, S. Kakimoto, and W. Susaki, "$1.3\,\mu m$ distributed feedback laser diode with a grating accurately controlled by a new fabrication technique," *J. Lightwave Technology*, vol. 7, no. 12, pp. 2072–2077, 1989.

[95] Y. Sakakibara, A. Takemoto, Y. Nakajima, M. Fujiwara, N. Yoshida, and S. Kakimoto, "Very narrow spectral linewidth of GaInAs MQW-DFB-PPBH laser diodes," *Electronics Lett.*, vol. 25, no. 15, pp. 988–990, 1989.

[96] T. Kimura and A. Sugimura, "Linewth reduction by coupled phase-shift distributed-feedback lasers," *Electronics Lett.*, vol. 23, no. 19, pp. 1014–1015, 1987.

[97] H. Soda, Y. Kotaki, H. Sudo, H. Ishikawa, S. Yamakoshi, and H. Imai, "Stability in single longitudinal mode-operation in GaInAsP-InP phase-adjusted DFB lasers," *IEEE J. Quantum Electronics*, vol. 23, no. 6, pp. 804–814, 1987.

[98] G. P. Agrawal, J. E. Geusic, and P. J. Anthony, "Distributed feedback lasers with multiple phase-shift regions," *Appl. Phys. Lett.*, vol. 53, no. 3, pp. 178–179, 1988.

[99] S. Ogita, Y. Kotaki, H. Ishikawa, and H. Imai, "Optimum design for multiple-phase-shift distributed feedback laser," *Electronics Lett.*, vol. 24, no. 12, pp. 731–732, 1988.

[100] T. Kimura and A. Sugimura, "Coupled phase-shift distributed-feedback semiconductor lasers for narrow linewidth operation," *IEEE J. Quantum Electronics*, vol. 25, no. 4, pp. 678–683, 1989.

[101] S. Ogita, Y. Kotaki, M. Matsuda, Y. Kuwahara, and H. Ishikawa, "Long-cavity, multiple-phase-shift, distributed feedback laser for linewidth narrowing," *Electronics Lett.*, vol. 25, no. 10, pp. 629–630, 1989.

[102] K. Kojima, K. Kyuma, and T. Nakayama, "Analysis of the spectral linewidth of distributed feedback laser diodes," *J. Lightwave Technology*, vol. 3, no. 5, pp. 1048–1055, 1985.

[103] Y. Arakawa, K. Vahala, and A. Yariv, "Quantum noise and dynamics in quantum well and quantum wire lasers," *Appl. Phys. Lett.*, vol. 45, no. 9, pp. 950–952, 1984.

[104] Y. Arakawa and A. Yariv, "Theory of gain, modulation response, and spectral linewidth in AlGaAs quantum well lasers," *IEEE J. Quantum Electronics*, vol. 21, no. 10, pp. 1666–1674, 1985.

[105] Y. Arakawa and A. Yariv, "Quantum-well lasers gain, spectra, dynamics," *IEEE J. Quantum Electronics*, vol. 22, no. 9, pp. 1887–1899, 1986.

[106] K. Kikuchi, M. Amano, C. E. Zah, and T. P. Lee, "Measurement of differential gain and linewidth enhancement factor of $1.5\,\mu m$ strained-quantum-well active layers," *IEEE J. Quantum Electronics*, vol. 30, no. 2, pp. 571–577, 1994.

[107] S. Takano, T. Sasaki, H. Yamada, M. Kitamura, and I. Mito, "Spectral linewidth reduction in metalorganic vapor-phase epitaxy grown $1.5\,\mu m$ separate-confinement-heterostructure quantum well distributed feedback laser diodes," *Appl. Phys. Lett.*, vol. 53, no. 21, pp. 2019–2020, 1988.

[108] M. Okai, T. Tsuchiya, K. Uomi, N. Chinone, and T. Harada, "Corrugation-pitch-modulated MQW-DFB laser with narrow spectral linewidth (170 kHz)," *IEEE Photonics Technology Lett.*, vol. 2, no. 8, pp. 529–530, 1990.

[109] M. Okai, T. Tsuchiya, K. Uomi, N. Chinone, and T. Harada, "Corrugation-pitch modulated MQW-DFB lasers with narrow spectral linewidth," *IEEE J. Quantum Electronics*, vol. 27, no. 6, pp. 1767–1772, 1991.

[110] M. Okai, M. Suzuki, and T. Taniwatari, "Strained multi-quantum-well corrugation-pitch-modulated distributed-feedback laser with ultra-narrow (3.6 kHz) spectral linewidth," *Electronics Lett.*, vol. 29, no. 19, pp. 1696–1697, 1993.

[111] M. Okai and T. Tsuchiya, "Tunable DFB lasers with ultra-narrow spectral linewidth," *Electronics Lett.*, vol. 29, no. 4, pp. 349–351, 1993.

[112] M. Okai, "Spectral characteristics of distributed-feedback semiconductor lasers and their improvements by corrugation-pitch-modulated structure," *J. Appl. Phys.*, vol. 75, no. 1, pp. 1–29, 1994.

[113] R. Sahara, R. Ranganathan, J. Dormail, R. Patterson, J. Coyne, S. Burroughs, and H. Lu, "Narrow linewidth, high speed, AlInGaAs, strained MQW, $1.55\,\mu m$, DFB laser diodes," in *IEEE 16th International Semiconductor Laser Conference*, pp. 75–76, 1998.

[114] L. D. Westbrook and M. J. Adams, "Simple expressions for the linewidth enhancement factor in direct-gap semiconductors," *IEE Proceedings - J. Optoelectronics*, vol. 134, no. 4, pp. 209–214, 1987.

[115] L. D. Westbrook and M. J. Adams, "Linewidth enhancement in quantum-well lasers," *Electronics Lett.*, vol. 23, no. 23, pp. 1223–1225, 1987.

[116] L. D. Westbrook and M. J. Adams, "Explicit approximations for the linewidth enhancement factor in quantum-well lasers," *IEE Proceedings - J. Optoelectronics*, vol. 135, no. 3, pp. 223–225, 1988.

[117] S. Takano, T. Sasaki, H. Yamada, M. Kitamura, and I. Mito, "Sub-MHz spectral linewidth in $1.5\,\mu m$ separate-confinement-heterostructure (SCH) quantum-well DFB LDs," *Electronics Lett.*, vol. 25, no. 5, pp. 356–357, 1989.

[118] M. Aoki, K. Uomi, T. Tsuchiya, S. Sasaki, and N. Chinone, "Stabilization of the longitudinal mode against spatial hole burning in $\lambda/4$-shifted DFB lasers by quantum size effect," *IEEE Photonics Technology Lett.*, vol. 2, no. 9, pp. 617–619, 1990.

[119] M. Aoki, K. Uomi, T. Tsuchiya, S. Sasaki, M. Okai, and N. Chinone, "Quantum size effect on longitudinal spatial hole burning in MQW $\lambda/4$-shifted DFB lasers," *IEEE J. Quantum Electronics*, vol. 27, no. 6, pp. 1782–1789, 1991.

[120] K. Uomi, S. Sasaki, T. Tsuchiya, M. Okai, M. Aoki, and N. Chinone, "Spectral linewidth reduction by low spatial hole burning in $1.5\,\mu m$ multi-quantum-well $\lambda/4$-shifted DFB lasers," *Electronics Lett.*, vol. 26, no. 1, pp. 52–53, 1990.

[121] K. Vahala, L. C. Chiu, S. Margalit, and A. Yariv, "On the linewidth enhancement factor a in semiconductor injection lasers," *Appl. Phys. Lett.*, vol. 42, no. 8, pp. 631–633, 1983.

[122] S. Ogita, M. Yano, and H. Imai, "Theoretical calculation of the linewidth enhancement factor of DFB lasers," *Electronics Lett.*, vol. 22, no. 11, pp. 580–581, 1986.

[123] K. Y. Liou, N. K. Dutta, and C. A. Burrus, "Linewidth-narrowed distributed feedback injection lasers with long cavity length and detuned Bragg wavelength," *Appl. Phys. Lett.*, vol. 50, no. 9, pp. 489–491, 1987.

[124] S. Ogita, M. Yano, H. Ishikawa, and H. Imai, "Linewidth reduction in DFB laser by detuning effect," *Electronics Lett.*, vol. 23, no. 8, pp. 393–394, 1987.

[125] K. Kikuchi, "Precise estimation of linewidth reduction in wavelength-detuned DFB semiconductor lasers," *Electronics Lett.*, vol. 24, no. 2, pp. 80–81, 1988.

[126] C. Harder, K. Vahala, and A. Yariv, "Measurement of the linewidth enhancement factor α of semiconductor lasers," *Appl. Phys. Lett.*, vol. 42, no. 4, pp. 328–330, 1983.

[127] K. Kikuchi and T. Okoshi, "Estimation of linewidth enhancement factor of AlGaAs lasers by correlation measurement between FM and AM noises," *IEEE J. Quantum Electronics*, vol. 21, no. 6, pp. 669–673, 1985.

[128] M. Osinski and J. Buus, "Linewidth broadening factor in semiconductor lasers - an overview," *IEEE J. Quantum Electronics*, vol. 23, no. 1, pp. 9–29, 1987.

[129] A. W. Fang, H. Park, Y. H. Kuo, R. Jones, O. Cohen, D. Liang, O. Raday, M. N. Sysak, M. J. Paniccia, and J. E. Bowers, "Hybrid silicon evanescent devices," *Materials Today*, vol. 10, no. 7-8, pp. 28–35, 2007.

[130] G. Roelkens, L. Liu, D. Liang, R. Jones, A. Fang, B. Koch, and J. Bowers, "III-V/silicon photonics for on-chip and inter-chip optical interconnects," *Laser & Photonics Rev.*, vol. 4, no. 6, pp. 751–779, 2010.

[131] D. Liang, A. W. Fang, H. W. Chen, M. N. Sysak, B. R. Koch, E. Lively, O. Raday, Y. H. Kuo, R. Jones, and J. E. Bowers, "Hybrid Siilicon evanescent approach to optical interconnects," *Appl. Phys. A - Materials Science & Processing*, vol. 95, no. 4, pp. 1045–1057, 2009.

[132] H. Park, M. N. Sysak, H. W. Chen, A. W. Fang, D. Liang, L. Liao, B. R. Koch, J. Bovington, Y. B. Tang, K. Wong, M. Jacob-Mitos, R. Jones, and J. E. Bowers, "Device and integration technology for Silicon photonic transmitters," *IEEE J. Selected Topics In Quantum Electronics*, vol. 17, no. 3, pp. 671–688, 2011.

[133] M. J. R. Heck, H. W. Chen, A. W. Fang, B. R. Koch, D. Liang, H. Park, M. N. Sysak, and J. E. Bowers, "Hybrid Silicon photonics for optical interconnects," *IEEE J. Selected Topics in Quantum Electronics*, vol. 17, no. 2, pp. 333–346, 2011.

[134] H. Park, A. W. Fang, S. Kodama, and J. E. Bowers, "Hybrid silicon evanescent laser fabricated with a silicon waveguide and III-V offset quantum well," *Optics Express*, vol. 13, no. 23, pp. 9460–9464, 2005.

[135] A. W. Fang, H. Park, R. Jones, O. Cohen, M. J. Paniccia, and J. E. Bowers, "A continuous-wave hybrid AlGaInAs-Silicon evanescent laser," *IEEE Photonics Technology Lett.*, vol. 18, no. 9-12, pp. 1143–1145, 2006.

[136] A. W. Fang, H. Park, O. Cohen, R. Jones, M. J. Paniccia, and J. E. Bowers, "Electrically pumped hybrid AlGaInAs-Silicon evanescent laser," *Optics Express*, vol. 14, no. 20, pp. 9203–9210, 2006.

[137] G. Roelkens, D. V. Thourhout, R. Baets, R. Notzel, and M. Smit, "Laser emission and photodetection in an InP/InGaAsP layer integrated on and coupled to a Silicon-on-Insulator waveguide circuit," *Optics Express*, vol. 14, no. 18, pp. 8154–8159, 2006.

[138] B. R. Koch, A. W. Fang, O. Cohen, and J. E. Bowers, "Mode-locked silicon evanescent lasers," *Optics Express*, vol. 15, no. 18, pp. 11225–11233, 2007.

[139] A. W. Fang, B. R. Koch, R. Jones, E. Lively, D. Liang, Y. H. Kuo, and J. E. Bowers, "A distributed Bragg reflector Silicon evanescent laser," *IEEE Photonics Technology Lett.*, vol. 20, no. 17-20, pp. 1667–1669, 2008.

[140] A. W. Fang, M. N. Sysak, B. R. Koch, R. Jones, E. Lively, Y. H. Kuo, D. Liang, O. Raday, and J. E. Bowers, "Single-wavelength Silicon evanescent lasers," *IEEE J. Selected Topics In Quantum Electronics*, vol. 15, no. 3, pp. 535–544, 2009.

[141] T. J. Karle, Y. Halioua, F. Raineri, P. Monnier, R. Braive, L. L. Gratiet, G. Beaudoin, I. Sagnes, G. Roelkens, F. van Laere, D. V. Thourhout, and R. Raj, "Heterogeneous integration and precise alignment of InP-based photonic crystal lasers to complementary metal-oxide semiconductor fabricated silicon-on-insulator wire waveguides," *J. Appl. Phys.*, vol. 107, no. 6, p. 063103, 2010.

[142] S. Srinivasan, A. W. Fang, D. Liang, J. Peters, B. Kaye, and J. E. Bowers, "Design of phase-shifted hybrid Siilicon distributed feedback lasers," *Optics Express*, vol. 19, no. 10, pp. 9255–9261, 2011.

[143] A. W. Fang, E. Lively, H. Kuo, D. Liang, and J. E. Bowers, "A distributed feedback Silicon evanescent laser," *Optics Express*, vol. 16, no. 7, pp. 4413–4419, 2008.

[144] S. Keyvaninia, G. Roelkens, D. V. Thourhout, C. Jany, M. Lamponi, A. L. Liepvre, F. Lelarge, D. Make, G. H. Duan, D. Bordel, and J. M. Fedeli, "Demonstration of a heterogeneously integrated III-V/SOI single wavelength tunable laser," *Optics Express*, vol. 21, no. 3, pp. 3784–3792, 2013.

[145] H. A. Haus, *Waves and fields in optoelectronics*. Solid state physical electronics series, Englewood Cliffs, NJ: Prentice-Hall, 1984.

[146] T. Asano, B. S. Song, and S. Noda, "Analysis of the experimental Q factors (similar to 1 million) of photonic crystal nanocavities," *Optics Express*, vol. 14, no. 5, pp. 1996–2002, 2006.

[147] F. P. Payne and J. P. R. Lacey, "A theoretical analysis of scattering loss from planar optical waveguides," *Opt. Quantum Electronics*, vol. 26, no. 10, pp. 977–986, 1994.

[148] J. P. R. Lacey and F. P. Payne, "Radiation loss from planar waveguides with random wall imperfections," *IEE Proceedings-J. Optoelectronics*, vol. 137, no. 4, pp. 282–288, 1990.

[149] E. Kuramochi, M. Notomi, S. Hughes, A. Shinya, T. Watanabe, and L. Ramunno, "Disorder-induced scattering loss of line-defect waveguides in photonic crystal slabs," *Phys. Rev. B*, vol. 72, no. 16, p. 161318, 2005.

[150] B. S. Song, S. Noda, T. Asano, and Y. Akahane, "Ultra-high-Q photonic double-heterostructure nanocavity," *Nature Materials*, vol. 4, no. 3, pp. 207–210, 2005.

[151] T. Asano, B. S. Song, Y. Akahane, and S. Noda, "Ultrahigh-Q nanocavities in two-dimensional photonic crystal slabs," *IEEE J. Selected Topics In Quantum Electronics*, vol. 12, no. 6, pp. 1123–1134, 2006.

[152] Y. Takahashi, H. Hagino, Y. Tanaka, B. S. Song, T. Asano, and S. Noda, "High-Q nanocavity with a 2-ns photon lifetime," *Optics Express*, vol. 15, no. 25, pp. 17206–17213, 2007.

[153] Y. Tanaka, T. Asano, and S. Noda, "Design of photonic crystal nanocavity with Q-factor of similar to 10^9," *J. Lightwave Technology*, vol. 26, no. 9-12, pp. 1532–1539, 2008.

[154] E. Kuramochi, M. Notomi, S. Mitsugi, A. Shinya, T. Tanabe, and T. Watanabe, "Ultrahigh-Q photonic crystal nanocavities realized by the local width modulation of a line defect," *Appl. Phys. Lett.*, vol. 88, no. 4, p. 041112, 2006.

[155] T. Tanabe, M. Notomi, E. Kuramochi, A. Shinya, and H. Taniyama, "Trapping and delaying photons for one nanosecond in an ultrasmall high-Q photonic-crystal nanocavity," *Nature Photonics*, vol. 1, no. 1, pp. 49–52, 2007.

[156] M. Notomi, E. Kuramochi, and H. Taniyama, "Ultrahigh-Q nanocavity with 1D photonic gap," *Optics Express*, vol. 16, no. 15, pp. 11095–11102, 2008.

[157] M. Notomi, "Manipulating light with strongly modulated photonic crystals," *Reports On Progress In Phys.*, vol. 73, no. 9, p. 096501, 2010.

[158] E. Kuramochi, H. Taniyama, T. Tanabe, K. Kawasaki, Y. G. Roh, and M. Notomi, "Ultrahigh-Q one-dimensional photonic crystal nanocavities with modulated mode-gap barriers on SiO_2 claddings and on air claddings," *Optics Express*, vol. 18, no. 15, pp. 15859–15869, 2010.

[159] O. Painter, K. Srinivasan, and P. E. Barclay, "Wannier-like equation for the resonant cavity modes of locally perturbed photonic crystals," *Phys. Rev. B*, vol. 68, no. 3, p. 035214, 2003.

[160] Y. Akahane, T. Asano, B. S. Song, and S. Noda, "High-Q photonic nanocavity in a two-dimensional photonic crystal," *Nature*, vol. 425, no. 6961, pp. 944–947, 2003.

[161] Y. Akahane, T. Asano, B. S. Song, and S. Noda, "Fine-tuned high-Q photonic-crystal nanocavity," *Optics Express*, vol. 13, no. 4, pp. 1202–1214, 2005.

[162] K. Srinivasan and O. Painter, "Momentum space design of high-Q photonic crystal optical cavities," *Optics Express*, vol. 10, no. 15, pp. 670–684, 2002.

[163] K. Srinivasan and O. Painter, "Fourier space design of high-Q cavities in standard and compressed hexagonal lattice photonic crystals," *Optics Express*, vol. 11, no. 6, pp. 579–593, 2003.

[164] J. W. John Carroll and D. Plumb, *Distributed feedback semiconductor lasers.* London, The United Kingdom: The Institution of Electrical Engineers, 1998.

[165] L. Lapidus and G. Pinder, *Numerical Solution of Partial Differential Equations in Science and Engineering.* New York, NY: J. Wiley, 1982.

[166] L. J. P. Ketelsen, I. Hoshino, and D. A. Ackerman, "The role of axially nonuniform carrier density in altering the TE-TE gain margin in InGaAsP-InP DFB lasers," *IEEE J. Quantum Electronics*, vol. 27, no. 4, pp. 957–964, 1991.

[167] G. P. Agrawal and A. H. Bobeck, "Modeling of distributed feedback semiconductor lasers with axially-varying parameters," *IEEE J. Quantum Electronics*, vol. 24, no. 12, pp. 2407–2414, 1988.

[168] J. I. Kinoshita and K. Matsumoto, "Yield analysis of SLM DFB lasers with an axially-flattened internal field," *IEEE J. Quantum Electronics*, vol. 25, no. 6, pp. 1324–1332, 1989.

[169] M. Usami and S. Akiba, "Suppression of longitudinal spatial hole-burning effect in $\lambda/4$-shifted DFB lasers by nonuniform current distribution," *IEEE J. Quantum Electronics*, vol. 25, no. 6, pp. 1245–1253, 1989.

[170] K. Tada, Y. Nakano, and A. Ushirokawa, "Proposal of a distributed feedback laser with nonuniform stripe width for complete single-mode oscillation," *Electronics Lett.*, vol. 20, no. 2, pp. 82–84, 1984.

[171] N. Satyan, A. Vasilyev, G. Rakuljic, V. Leyva, and A. Yariv, "Precise control of broadband frequency chirps using optoelectronic feedback," *Optics Express*, vol. 17, no. 18, pp. 15991–15999, 2009.

[172] N. Satyan, *Optoelectronic Control of the Phase and Frequency of Semiconductor Lasers.* PhD thesis, California Institute of Technology, Pasadena, California, 2011.

[173] A. Vasiliev, *The Optoelectronic Swept-Frequency Laser and Its Applications in Ranging, Three-dimensional Imaging, and Coherent Beam Combining of Chirped-seed Amplifiers.* PhD thesis, California Institute of Technology, Pasadena, California, 2013.

[174] T. Baba, "Slow light in photonic crystals," *Nature Photonics*, vol. 2, no. 8, pp. 465–473, 2008.

[175] W. Fang, M. Hattendorf, S. L. Chuang, J. Minch, C. S. Chang, C. G. Bethea, and Y. K. Chen, "Analysis of temperature sensitivity in semiconductor lasers using gain and spontaneous emission measurements," *Appl. Phys. Lett.*, vol. 70, no. 7, pp. 796–798, 1997.

[176] A. R. Adams, M. Asada, Y. Suematsu, and S. Arai, "The temperature-dependence of the efficiency and threshold current of $In_{1-x}Ga_xAs_yP_{1-y}$ lasers related to intervalence band absorption," *Japanese J. Appl. Phys.*, vol. 19, no. 10, pp. L621–L624, 1980.

[177] M. Asada, A. R. Adams, K. E. Stubkjaer, Y. Suematsu, Y. Itaya, and S. Arai, "The temperature-dependence of the threshold current of GaInAsP/InP DH lasers," *IEEE J. Quantum Electronics*, vol. 17, no. 5, pp. 611–619, 1981.

[178] M. Asada and Y. Suematsu, "The effects of loss and nonradiative recombination on the temperature-dependence of threshold current in 1.5–1.6 μm GalnAsP/InP lasers," *IEEE J. Quantum Electronics*, vol. 19, no. 6, pp. 917–923, 1983.

[179] T. Okoshi, K. Kikuchi, and A. Nakayama, "Novel method for high-resolution measurement of laser output spectrum," *Electronics Lett.*, vol. 16, no. 16, pp. 630–631, 1980.

[180] L. B. Mercer, "1/f frequency noise effects on self-heterodyne linewidth measurements," *J. Lightwave Technology*, vol. 9, no. 4, pp. 485–493, 1991.

[181] M. J. O'Mahony and I. D. Henning, "Semiconductor laser linewidth broadening due to 1/f carrier noise," *Electronics Lett.*, vol. 19, no. 23, pp. 1000–1001, 1983.

[182] L. E. Richter, H. I. Mandelberg, M. S. Kruger, and P. A. McGrath, "Linewidth determination from self-heterodyne measurements with subcoherence delay times," *IEEE J. Quantum Electronics*, vol. 22, no. 11, pp. 2070–2074, 1986.

[183] H. Ludvigsen and E. Bodtker, "New method for self-homodyne laser linewidth measurements with a short delay fiber," *Optics Comm.*, vol. 110, no. 5-6, pp. 595–598, 1994.

[184] W. V. Sorin, K. W. Chang, G. A. Conrad, and P. R. Hernday, "Frequency-domain analysis of an optical fm discriminator," *J. Lightwave Technology*, vol. 10, no. 6, pp. 787–793, 1992.

[185] B. Daino, P. Spano, M. Tamburrini, and S. Piazzolla, "Phase noise and spectral line shape in semiconductor lasers," *IEEE J. Quantum Electronics*, vol. 19, no. 3, pp. 266–270, 1983.

[186] K. Petermann, *Laser diode modulation and noise.* Dordrecht, The Netherlands: Kluwer Academic Publishers, 1991.

[187] L. S. Cutler and C. L. Searle, "Some aspects of theory and measurement of frequency fluctuations in frequency standards," *Proc. Institute Electrical Electronics Engineers*, vol. 54, no. 2, pp. 136–154, 1966.

[188] K. Vahala and A. Yariv, "Detuned loading in coupled cavity semiconductor lasers - effect on quantum noise and dynamics," *Appl. Phys. Lett.*, vol. 45, no. 5, pp. 501–503, 1984.

[189] R. Nagarajan *et al.*, "Terabit/s class InP photonic integrated circuits," *Semiconductor Science Technology*, vol. 27, no. 9, p. 094003, 2012.

[190] M. Ziari *et al.*, "Integrated laser sources for WDM coherent transmission," *IEEE Photonics Conference (IPC)*, pp. 324–325, 2012.

[191] R. Nagarajan *et al.*, "Large-scale photonic integrated circuits," *IEEE J. Selected Topics In Quantum Electronics*, vol. 11, no. 1, pp. 50–65, 2005.

[192] R. Nagarajan *et al.*, "InP photonic integrated circuits," *IEEE J. Selected Topics In Quantum Electronics*, vol. 16, no. 5, pp. 1113–1125, 2010.

[193] A. Mekis *et al.*, "Scaling CMOS photonics transceivers beyond 100 Gb/s," *Optoelectronic Integrated Circuits XIV*, vol. 8265, p. 82650A, 2012.

[194] Y. Arakawa and H. Sakaki, "Multidimensional quantum well laser and temperature dependence of its threshold current," *Appl. Phys. Lett.*, vol. 40, no. 11, pp. 939–941, 1982.

[195] Y. Arakawa and M. Sugawara, "Advances in quantum dot lasers for high-speed and temperature-stable operation," *Physics And Simulation Of Optoelectronic Devices XIII*, vol. 5722, pp. 45–48, 2005.

[196] G. T. Liu, A. Stintz, H. Li, K. J. Malloy, and L. F. Lester, "Extremely low room temperature threshold current density diode lasers using InAs dots in $In_{0.15}Ga_{0.85}As$ quantum well," *Electronics Lett.*, vol. 35, no. 14, pp. 1163–1165, 1999.

[197] O. B. Shchekin and D. G. Deppe, "Low-threshold high-T_o 1.3 μm InAs quantum dot lasers due to p-type modulation doping of the active region," *IEEE Photonics Technology Lett.*, vol. 14, no. 9, pp. 1231–1233, 2002.

[198] F. Klopf, R. Krebs, J. P. Reithmaier, and A. Forchel, "High-temperature operating 1.3 μm quantum dot lasers for telecommunication applications," *IEEE Photonics Technology Lett.*, vol. 13, no. 8, pp. 764–766, 2001.

[199] O. B. Shchekin and D. G. Deppe, "1.3 μm InAs quantum dot laser with $T_o = 161$ K from 0 to 80 degrees C," *Appl. Phys. Lett.*, vol. 80, no. 18, pp. 3277–3279, 2002.

[200] T. C. Newell, D. J. Bossert, A. Stintz, B. Fuchs, K. J. Malloy, and L. F. Lester, "Gain and linewidth enhancement factor in InAs quantum dot laser diodes," *IEEE Photonics Technology Lett.*, vol. 11, no. 12, pp. 1527–1529, 1999.

[201] K. Takada, Y. Tanaka, T. Matsumoto, M. Ekawa, H. Z. Song, Y. Nakata, M. Yamaguchi, K. Nishi, T. Yamamoto, M. Sugawara, and Y. Arakawa, "Wide temperature-range 10.3 Gbit/s operations of 1.3 μm high density quantum dot DFB lasers," *Electronics Lett.*, vol. 47, no. 3, pp. 206–U704, 2011.

[202] T. Kageyama, K. Takada, K. Nishi, M. Yamaguchi, R. Mochida, Y. Maeda, H. Kondo, K. Takemasa, Y. Tanaka, T. Yamamoto, M. Sugawara, and Y. Arakawa, "Long-wavelength quantum dot FP and DFB lasers for high temperature applications," *Novel In-Plane Semiconductor Lasers XI*, vol. 8277, p. 82770C, 2012.

[203] L. Yang, T. Lu, T. Carmon, B. Min, and K. J. Vahala, "A 4 Hz fundamental linewidth on-chip microlaser," *Conference On Lasers & Electro-optics/Quantum Electronics Laser Science Conference (CLEO/QELS)*, vol. 1–5, pp. 207–208, 2007.

[204] J. Li, H. Lee, T. Chen, and K. J. Vahala, "Characterization of a high coherence, Brillouin microcavity laser on Siilicon," *Optics Express*, vol. 20, no. 18, pp. 20170–20180, 2012.

[205] W. Liang, V. S. Ilchenko, A. A. Savchenkov, A. B. Matsko, D. Seidel, and L. Maleki, "Whispering gallery mode resonator-based ultranarrow linewidth external cavity semiconductor laser," *Optics Lett.*, vol. 35, no. 16, pp. 2822–2824, 2010.

[206] K. K. Lee, D. R. Lim, H. C. Luan, A. Agarwal, J. Foresi, and L. C. Kimerling, "Effect of size and roughness on light transmission in a Si/SiO_2 waveguide: Experiments and model," *Appl. Phys. Lett.*, vol. 77, no. 11, pp. 1617–1619, 2000.

[207] T. Barwicz and H. I. Smith, "Evolution of line-edge roughness during fabrication of high-index-contrast microphotonic devices," *J. Vacuum Science & Technology B*, vol. 21, no. 6, pp. 2892–2896, 2003.

[208] H. Namatsu, M. Nagase, T. Yamaguchi, K. Yamazaki, and K. Kurihara, "Influence of edge roughness in resist patterns on etched patterns," *J. Vacuum Science & Technology B*, vol. 16, no. 6, pp. 3315–3321, 1998.

[209] T. Yamaguchi, K. Yamazaki, M. Nagase, and H. Namatsu, "Line-edge roughness: Characterization and material origin," *Japanese J. Appl. Phys. Part 1-regular Papers Short Notes & Rev. Papers*, vol. 42, no. 6B, pp. 3755–3762, 2003.

[210] T. Yamaguchi, K. Yamazaki, and H. Namatsu, "Influence of molecular weight of resist polymers on surface roughness and line-edge roughness," *J. Vacuum Science & Technology B*, vol. 22, no. 6, pp. 2604–2610, 2004.

[211] S. J. Pearton and D. R. Norton, "Dry etching of electronic oxides, polymers, and semiconductors," *Plasma Processes Polymers*, vol. 2, no. 1, pp. 16–37, 2005.

[212] C. C. Welch, A. L. Goodyear, T. Wahlbrink, M. C. Lemme, and T. Mollenhauer, "Silicon etch process options for micro- and nanotechnology using inductively

coupled plasmas," *Microelectronic Engineering*, vol. 83, no. 4-9, pp. 1170–1173, 2006.

[213] C. C. Welch, A. L. Goodyear, G. Ditmer, and G. Tan, "Choice of silicon etch processes for opto- and microelectronic device fabrication using inductively coupled plasmas," *Conference On Optoelectronic And Microelectronic Materials And Devices, Proceedings*, pp. 13–16, 2005.

[214] R. Gunn, D. Stephens, and C. Welch, *Comparison of etch processes for patterning high aspect ratio and nanoscale features in silicon.* Bristol, UK: Oxford Instruments Plasma Technology Ltd., 2009.

[215] H. Jansen, M. Deboer, R. Legtenberg, and M. Elwenspoek, "The black silicon method - a universal method for determining the parameter setting of a fluorine-based reactive ion etcher in deep silicon trench etching with profile control," *J. Micromechanics Microengineering*, vol. 5, no. 2, pp. 115–120, 1995.

[216] M. Borselli, T. J. Johnson, and O. Painter, "Measuring the role of surface chemistry in silicon microphotonics," *Appl. Phys. Lett.*, vol. 88, no. 13, p. 131114, 2006.

[217] D. K. Sparacin, S. J. Spector, and L. C. Kimerling, "Silicon waveguide sidewall smoothing by wet chemical oxidation," *J. Lightwave Technology*, vol. 23, no. 8, pp. 2455–2461, 2005.

[218] L. Lai and E. A. Irene, "Limiting Si/SiO$_2$ interface roughness resulting from thermal oxidation," *J. Appl. Phys.*, vol. 86, no. 3, pp. 1729–1735, 1999.

[219] K. K. Lee, D. R. Lim, L. C. Kimerling, J. Shin, and F. Cerrina, "Fabrication of ultralow-loss Si/SiO$_2$ waveguides by roughness reduction," *Optics Lett.*, vol. 26, no. 23, pp. 1888–1890, 2001.

[220] M. Borselli, T. J. Johnson, C. P. Michael, M. D. Henry, and O. Painter, "Surface encapsulation for low-loss silicon photonics," *Appl. Phys. Lett.*, vol. 91, no. 13, p. 131117, 2007.

[221] D. Marcuse, "Mode conversion caused by surface imperfections of a dielectric slab waveguide," *Bell System Technical J.*, vol. 48, no. 10, pp. 3187–3215, 1969.

[222] T. Barwicz and H. A. Haus, "Three-dimensional analysis of scattering losses due to sidewall roughness in microphotonic waveguides," *J. Lightwave Technology*, vol. 23, no. 9, pp. 2719–2732, 2005.

[223] H. Z. Massoud, J. D. Plummer, and E. A. Irene, "Thermal oxidation of silicon in dry oxygen: growth-rate enhancement in the thin regime. I. Experimental results," *J. Electrochemical Soc.*, vol. 132, no. 11, pp. 2685–2693, 1985.

[224] H. Z. Massoud, J. D. Plummer, and E. A. Irene, "Thermal oxidation of silicon in dry oxygen: growth-rate enhancement in the thin regime. II. Physical mechanisms," *J. Electrochemical Soc.*, vol. 132, no. 11, pp. 2693–2700, 1985.

[225] H. Z. Massoud, J. D. Plummer, and E. A. Irene, "Thermal oxidation of silicon in dry oxygen - accurate determination of the kinetic rate constants," *J. Electrochemical Soc.*, vol. 132, no. 7, pp. 1745–1753, 1985.

[226] H. Z. Massoud and J. D. Plummer, "Analytical relationship for the oxidation of silicon in dry oxygen in the thin-film regime," *J. Appl. Phys.*, vol. 62, no. 8, pp. 3416–3423, 1987.

[227] D. Pasquariello and K. Hjort, "Plasma-assisted InP-to-Si low temperature wafer bonding," *IEEE J. Selected Topics In Quantum Electronics*, vol. 8, no. 1, pp. 118–131, 2002.

[228] Y. L. Chao, Q. Y. Tong, T. H. Lee, M. Reiche, R. Scholz, J. C. S. Woo, and U. Gosele, "Ammonium hydroxide effect on low-temperature wafer bonding energy enhancement," *Electrochemical Solid State Lett.*, vol. 8, no. 3, pp. G74–G77, 2005.

[229] X. X. Zhang and J. P. Raskin, "Low-temperature wafer bonding: A study of void formation and influence on bonding strength," *J. Microelectromechanical Systems*, vol. 14, no. 2, pp. 368–382, 2005.

[230] D. Liang and J. E. Bowers, "Highly efficient vertical outgassing channels for low-temperature InP-to-silicon direct wafer bonding on the silicon-on-insulator substrate," *J. Vacuum Science & Technology B*, vol. 26, no. 4, pp. 1560–1568, 2008.